THE UNIVERSITY *of* EDINBURGH

Direct Drive Wind Turbines:

The Effect of Unbalanced Magnetic Pull on Permanent Magnet Generators and Bearing Arrangements

Kaswar Mostafa

Thesis submitted towards the degree of

Doctor of Philosophy (Ph.D.)

The University of Edinburgh

2018

Abstract

Wind energy has been the fastest emerging renewable energy source over the last decade. The overriding provisos to minimise greenhouse emissions and increasing concerns regarding energy security have been the major inducements for many countries to make a resolute transition to new and non-conventional power sources.

Direct-drive systems for wind turbines are potentially a more reliable alternative to gearbox driven systems. Gearboxes are liable to significant accumulated fatigue torque loading with relatively high maintenance costs. It is with this in mind that the primary focus of this research is on direct-drive wind turbines.

Generators in direct-drive wind turbines tend to be of large diameter and heavier due to the support structure required to maintain as small air-gap as possible between the stationary and rotating parts of the generator. Permanent magnet generators (PMGs) are the most common type to be used within direct-drive wind turbines nowadays.

Generators and other drive-train components in wind turbines experience significant varying loads, which may lead to a bearing failure. These varying loads can lead to misalignment within the drivetrain producing eccentricity between the generator rotor and stator. Rotor eccentricity generates a magnetic force referred to as Unbalanced Magnetic Pull (UMP). The induced UMP for the same rotor eccentricity is much higher in PMGs than induction generators because of the higher permanent magnet magnetic field. UMP is an important issue requiring further research. A part of this study provides a more detailed treatment of UMP under varying rotor eccentricity regimes for various permanent magnet machine topologies.

The effect of UMP in direct-drive PMGs on the lifetime of the main bearing is a topic that requires more research aimed at proposing design improvements and solutions. The hope being that the availability of such solutions can be applied to practical reductions in operating costs. In brief, identification of the root causes of failure and impacts on component lifetime remain a subject of research. Establishing analytical tools for studying the impact of UMP on component lifetime in direct drive wind turbines and identifying the prospects for air gap winding machines using single bearing configuration are the two key areas for further research.

Firstly, this research aims to establish the relationship between bearing forces and different types of eccentricities and UMP in direct drive machines. It is intended to use such models for

predicting bearing wear and fatigue. Secondly, this research aims to establish the analytical tools for studying static, dynamic and tilting eccentricity in air-gap winding direct drive generators. Such tools are used to increase the understanding of the dynamics of direct drive PM generators. The final step of this study is using a multi-body simulation software (SIMPACK) to initiate investigations and comparison by providing assessments of electromagnetic interaction and internal drive-train loading for four possible designs for a proposed 5MW direct-drive wind turbine in response to the loads normally seen by a wind turbine. The four designs include: (a) iron-cored PM direct-drive generator supported by two main bearings, (b) airgap winding PM direct-drive generator supported by two main bearings, (c) iron-cored PM direct-drive generator supported by a single main bearing, (d) airgap winding PM direct-drive generator supported by a single main bearing. An aero-elastic simulation code (HAWC2) is used to extract the hub loads for different wind speeds corresponding to the normal operation of the wind turbine. The dynamic eccentricity and its influence on the electromagnetic interaction and consequential effects on bearing loading for all four designs is examined to determine the most optimal support structural configuration for a direct-drive system.

In summary, the main aim of this thesis is studying the effect of different types of rotor eccentricities in different types of direct drive PMGs on the main bearing arrangements. The results show that static rotor eccentricity has the maximum impact compared to the other types of eccentricities. The main result of an eccentricity is the induced UMP which applies directly as an extra force on the bearings. The influence of UMP on bearing wear is studied. This influence is found to be significant in PM machines and should be considered when designing the bearing stiffness. A 20% static rotor eccentricity in a PM machine is found to induce an UMP that roughly equals third the total weight of the machine. A single bearing design for a direct-drive wind turbine is proposed and compared with a conventional two-bearing design. The results show that the Iron-cored PM direct-drive generator supported by two main bearings design and airgap winding PM direct-drive generator supported by a single main bearing design have advantages over the other two designs in this study.

Declaration

I hereby declare that this thesis has been composed by myself and that except where stated, the work contained is my own. I also declare that the work contained in this thesis has not been submitted for any other degree or professional qualification except as specified.

Kaswar Mostafa

2018

Acknowledgments

To my beloved country “Syria”... With love and hope of a quick recovery...

First of all, I would like to thank my principal supervisor, Prof. Markus Mueller. He gave me the idea, opportunity, support and freedom to carry out my research. Without him, this work would not be possible.

I would like to thank Prof. Kamal Naji (Damascus University) for his support. Many thanks to my best friend Zoalfekar Zrekka.

I also would like to thank Dr. Latha Sethuraman for the very effective support and help. I am grateful to Siraj Sabihuddin for his valuable support. Special thanks go to my friends and officemates at The University of Edinburgh – especially Joe, Nacho, JenHao, Alberto, Reza, Mahdi, Helen, Maggie, Dr. JP, Dr. Ozan Keysan, Dr Aristides Zavvos, Will, Ricardo, John, Obi, Nissar, Marios, Monika, Dr. David Forehand, and Dr. Jonathan Shek.

Finally, I would like to dedicate this work to my parents “Marwan and Jumana”... Also, to my siblings Sylvan, Mohammad, and Yousef. To my brother in law Rani, my nephew Kaswara and my niece Noura.

Table of Contents

List of Figures

List of Tables

Abbreviations

ABB	Angular Ball Bearings
AFPMG	Axial Flux Permanent Magnet Generator
BEM	Boundary Element Methods
BLDC	Brushless Direct Current
CFD	Computational Fluid Dynamics
CoE	Cost of Energy
CRB	Cylindrical Roller Bearing
DFIG	Doubly-Fed Induction Generator
DOF	Degree of Freedom
EESG	Electrically Excited Synchronous Generator
emf	Electromotive Force
EPSRC	Engineering and Physical Sciences Research Council
FDM	Finite Difference Method
FEA	Finite Element Analysis
FEM	Finite Element Method
FFT	Fast Fourier Transform
FID	Final Investment Decision
FVM	Finite Volume Method
GWEC	Global Wind Energy Council
MAG	Multi-AirGap
MEC	Magnetic Equivalent Circuit
MMF	Magneto-Motive Force
MTBF	Mean Time Between Failures
NCKU	National Cheng Kung University
NdFeB	Neodymium-Iron-Boron
NREL	National Renewable Energy Laboratory
PCB	Printed Circuit Board
PM	Permanent Magnet
PMG	Permanent Magnet Generator
PMM	Point Mirroring Method
PVC	Polyvinyl Chloride

RFPM	Radial Flux Permanent Magnet Generator
SCIG	Squirrel Cage Induction Generator
SRB	Spherical Roller Bearing
TFPMG	Transverse Flux Permanent Magnet Generator
TRB	Tapered Roller Bearings
UMP	Unbalanced Magnetic Pull

Nomenclature

Chapter 1		
Symbol	***Unit***	***Description***
ρ	kg/m^3	Air Density
σ_g	N/m^2	Airgap Shear Stress
n	rpm	Blade Rotational Speed
K_{rad}	-	Generator Aspect Ratio
p	-	Pole Pair Number
C_p	-	Power Coefficient
l_r	m	Rotor Core Length
r_r	m	Rotor Radius
T	Nm	Torque
A	m^2	Turbine Rotor Swept Area
V	m/s	Wind Speed
P	W	Wind Turbine Power
Chapter 3		
Symbol	***Unit***	***Description***
g	m	Airgap Length
e	m	Rotor Eccentricity
w_e	rad/s	Rotor Rotational Speed
Chapter 4		
Symbol	***Unit***	***Description***
g_{dy}	m	Airgap Length with Dynamic Eccentricity
g_{dte}	m	Airgap Length with dynamic tilting Eccentricity
g_{se}	m	Airgap Length with Static Eccentricity
g_{ste}	m	Airgap Length with static tilting Eccentricity
g_{til}	m	Airgap Length with tilting Eccentricity
θ	deg	Angular Coordinate
k_c	-	Carter factor

Symbol	***Unit***	***Description***
μ_0	H/m	Free Space Permeability
Φ	Weber	Magnetic Flux
B	T	Magnetic Flux Density
A	m^2	Magnetic Path Cross-Sectional Area
$\mathcal{P}$	H	Magnetic Permeance
Λ	H/ m^2	Magnetic Permeance in a Cross-Sectional Area
mmf	V	Magneto-Motive Force
h_m	m	Magnet Height
σ	N/m^2	Maxwell Stress Tensor
b_n	T	Normal magnetic flux density
Λ_n	-	Normalized Magnetic Permeance in a Cross-Sectional Area
d_m	m	Permanent Magnet Axial Length
H_c	A/m	Permanent Magnet Field Intensity
b_m	m	Permanent Magnet Pitch
ε	-	Relative Eccentricity
B_{rem}	T	Remnant Flux Density
b_d	m	Slot Width
b_t	T	Tangential magnetic flux density
λ	m	Tooth Pitch
τ	m	Tooth Width
Chapter 5		
Symbol	***Unit***	***Description***
e	V	Electromotive Force
N	-	Number of Turns
K_{w_1}	-	Winding Factor
λ	Weber	Winding Flux Linkage
Chapter 6		
Symbol	***Unit***	***Description***
C_b	kN	Bearing Basic dynamic load
C_{0b}	kN	Bearing Basic Static load
P_{ub}	kN	Bearing Equivalent dynamic load

Symbol	***Unit***	***Description***
d_{ib}	m	Bearing Inner diameter
m_b	ton	Bearing Mass
d_{ob}	m	Bearing Outer diameter
$\acute{l}_{bl}$	m	Blade centre of gravity position
δ_{bl}	-	Blade configuration
l_{bl}	m	Blade length
C_L	-	Blade lift coefficient
l_{blch}	m	Blade max chord length
O_{bl}	-	Blade orientation
$\emptyset_{bl}$	degree	Blade precone
m_t	ton	Blade set & hub weight
A_{bl}	m^2	Blade swept area
r_{bl}	m	Blade swept radius
m_c	ton	Converter mass
ω_{ibl}	rpm	Cut-in blade speed
v_{iw}	m/s	Cut-in wind speed
v_{ow}	m/s	Cut-out wind speed
$\acute{l}_g$	m	Generator rotor/stator/shaft centre of gravity position
g	m/s^2	Gravitational acceleration
d_{hub}	m	Hub diameter
h_{hub}	m	Hub height
m_{nh}	ton	Nacelle housing mass
P_g	W	Nominal generator power
τ_{rg}	m	Pole pitch
$\acute{l}_c$	m	Power converter centre of gravity position
ω_{bl}	rpm	Rated blade speed
v_{tbl}	m/s	Rated blade tip speed
v_w	m/s	Rated wind speed
m_{rg}	ton	Rotor mass
d_{iS}	m	Shaft Inner diameter

Symbol	***Unit***	***Description***
l_S	m	Shaft Length
m_S	ton	Shaft Mass
M_S	-	Shaft Material
d_{oS}	m	Shaft Outer diameter
σ_{US}	MPa	Shaft Shear stress
t_S	degree	Shaft Tilt
γ_{US}	MPa	Shaft Ultimate tensile stress
$\acute{l}_b$	m	Single bearing centre of gravity position
m_{sg}	ton	Stator mass
τ_{sg}	m	Stator slot pitch
m_{tot}	ton	Total mass
m_{tw}	ton	Tower weight
$\acute{l}_t$	m	Turbine centre of gravity position
P_T	W	Turbine power
v_{lbl}	m/s	Wind velocity lower blade
v_{ubl}	m/s	Wind velocity upper blade

Chapter 1. Introduction

1.1. Background

Since the opening of the first coal power plant in Britain in 1882, coal was the backbone of the industrial revolution and the primary fuel for electricity generation. The time of relying on coal to generate electricity has come to an end. In Britain, on the 21st of April 2017, no electricity was generated from coal, marking a huge turning point for power supply [1]. Power from coal-fired power stations is mainly being substituted with renewable energy sources; especially wind energy, natural gas and nuclear. 27% of the UK's electricity was generated from renewable energy sources in the last quarter of 2015 [2]. Germany, on the other hand, supplied almost 100% of its power demand of 45.8GW from renewable energy sources for the first time on Sunday the 15th of May 2016 [3]. On the 9th of July 2015, Denmark generated 140% of its electricity needs from wind farms [4] with the surplus going to Germany, Norway and Sweden via grid interconnects.

Wind energy has been the fastest emerging renewable energy source with an annual growth rate of about 32% over the last decade [5]. The need to minimise greenhouse emissions and the increasing concerns regarding energy security have been the major inducements for many countries to make a resolute transition to new and non-conventional power sources. Wind energy has developed towards a mainstream, competitive and reliable power technology. More countries are becoming active in wind energy industry causing an increase in the annual installed capacity and investments. According to the most recent Global Wind Energy Council (GWEC) report, the total installed wind power capacity exceeded 432GW by the end of 2015 [6]. Reducing the cost of energy is the biggest challenge facing the wind energy industry. The estimated wind turbine capital cost is €1.6m/MW for onshore turbines and about double that number for offshore ones [7]. Given that installation and maintenance costs remain relatively fixed with increasing power ratings, in general, an increase in turbine power rating can be regarded as favourable. Wind turbine power rating and size, therefore, have been dramatically increasing in the last few decades [8]. Figure 1-1 [9] illustrates the growth and future predicted developments of offshore wind turbines. As shown in this figure, the current offshore wind turbine technology has grown up significantly. An example for that is Vestas wind turbine

company, which has developed V66 (2MW with 66m rotor radius) in 2000 and V164 (9MW and 164m rotor radius) in 2017, showing the considerable improvement.

Offshore wind is an attractive energy proposition for countries with long coastlines and with major demand centres located in proximity. Offshore wind blows about 40% more often than onshore on average thus allowing a wind turbine to be about 50% more productive than if it is placed onshore [10]. With lesser turbulence and steady wind flows, offshore turbines are expected to have a longer lifetime and require less maintenance. As of 2015, the cumulative global offshore wind capacity installed is over 12 GW. The UK has been the world leader in offshore wind since 2008, with as much capacity already installed as the rest of Europe combined. With more than 5 GW of installed power, representing nearly 42% of global total capacity, the UK has continued to attract new investment over the last year [6].

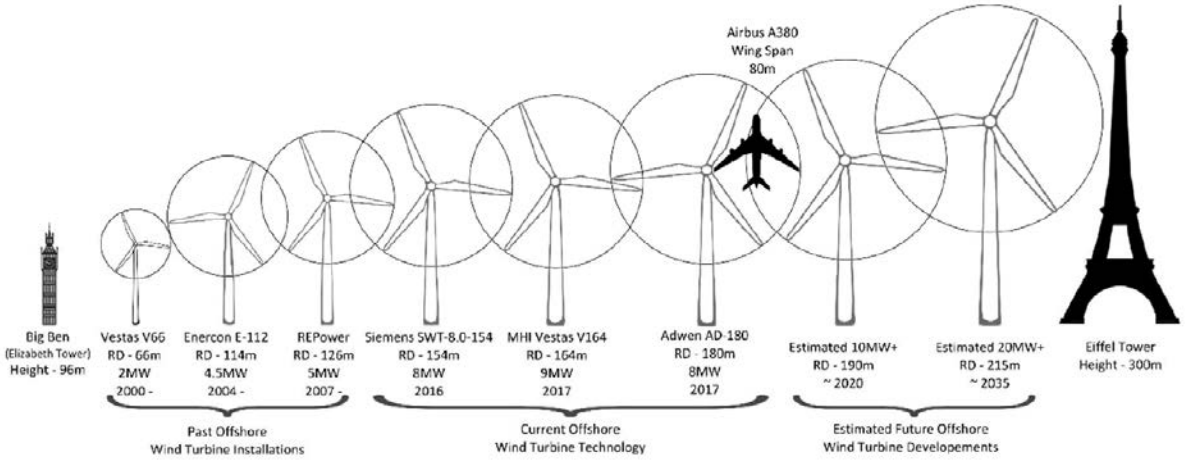

Figure 1-1 Increase in offshore wind turbine power rating and size [9]

Despite the great leaps, the energy production cost for offshore wind is still not competitive with other practical energy sources thus providing a major impediment to large-scale commercialization. According to the Bloomberg New Energy Finance research group, the average cost of energy from offshore wind farms was about £142/MWh in 2010-2011 [11]. Offshore wind costs, however, have fallen sharply through the adoption of larger turbines, increased competition and lower cost of capital. Projects were reaching a Final Investment Decision (FID) in 2015-2016 with an average Cost of Energy (CoE) of £97/MWh [11]. This is still more than double the CoE of new coal and gas power stations, which can cost as little as €45/MWh [12]. Across the world, the lowest cost of energy from offshore wind farms was off the coast of Denmark at €103/MWh until Denmark's Dong Energy has won a bid to build two offshore wind farms off the Dutch coast that industry experts claim will be the cheapest

schemes of their kind with €72.70/MWh [13]. It should, however, be pointed out that onshore wind turbines do much better at €56/MWh [14] suggesting that wind power can indeed compete with at least some fossil fuel generation technologies. Reducing the unit costs of energy is urgent and depends on the reliability and availability of the offshore wind turbines. The major cost drivers for offshore wind come from unplanned maintenance expenditure incurred due to component failures and the associated expenditure for logistics, transport and labour [15].

As the UK delivers its offshore wind programme, it is important that cost savings are delivered in order to protect UK consumers and help secure the UK position as a global leader in the offshore wind sector. The industry has a target of cutting costs by 30% by 2020 [16] which requires accelerated measures to improving efficiency and reliability that can help significantly drive down operation and maintenance costs which form a significant portion of offshore wind expenses. The UK government and industry have been working together, therefore, through the Offshore Wind Programme Board since 2012, taking forward the recommendations of the Offshore Wind Cost Reduction Taskforce in order to support the offshore wind industry [17].

Improving the reliability of offshore wind turbines is the key to reduce the cost and, hence, push the technology forward. Electrical generators and other drive-train components in offshore wind turbines experience significant varying loads, which may lead to different types of failures reducing the overall reliability. The varying loads induced by the varying high wind speed and harsh offshore environment can lead to misalignment within the drivetrain. Any misalignment is directly applied to the electrical generator producing so-called eccentricity between the generator rotor and stator. The rotor eccentricity generates unbalanced magnetic forces directly applied as extra loads on the main bearings. The extra loads may lead to bearing wear and bearing failure which is one of the main failures in wind turbines. Studying and improving the reliability of drive-train components in wind turbines provides the key and the motivation of this thesis.

1.2. Wind Energy and Wind Turbines

1.2.1. Historical Context

Throughout history, humankind has harnessed wind for energy; ships and boats were driven by wind using sails, grain-grinding mills were energised by wind, and water was pumped by wind energy. No clear record for the origin of using wind for mechanical power exists in the

literature. Figure 1-2 (a) shows an ancient windmill in British Isles and (b) shows ancient windmills in Spain.

In 1888 in Cleveland, Ohio, the first wind turbine to generate electricity was manufactured, with a step-up gearbox (a first for this design) and an electric generator with a 17m picket-fence rotor. This wind turbine is shown in Figure 1-3 [18][19]. The turbine was in operation for 20 years generating its 12kW rated power [20].

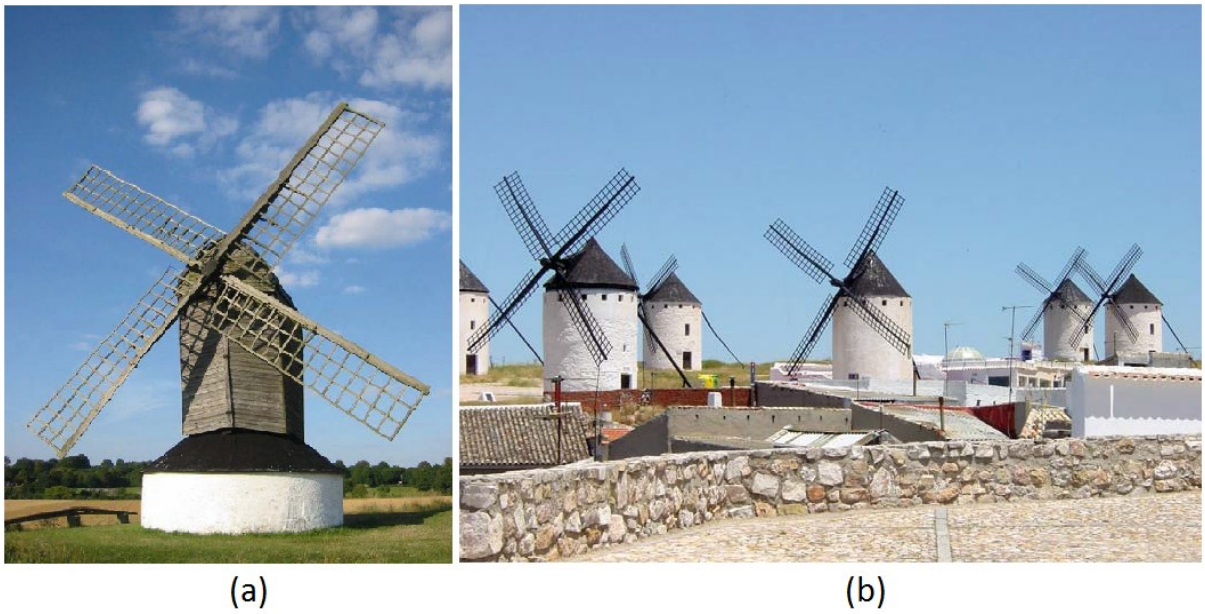

Figure 1-2 Ancient windmills. (a) In British Isles (Author: Michael Reeve). (b) in Spain (Author: Lourdes Cardenal). Source: Wikipedia, http://wikipedia.org. GNU Free Documentation License applies to this image.

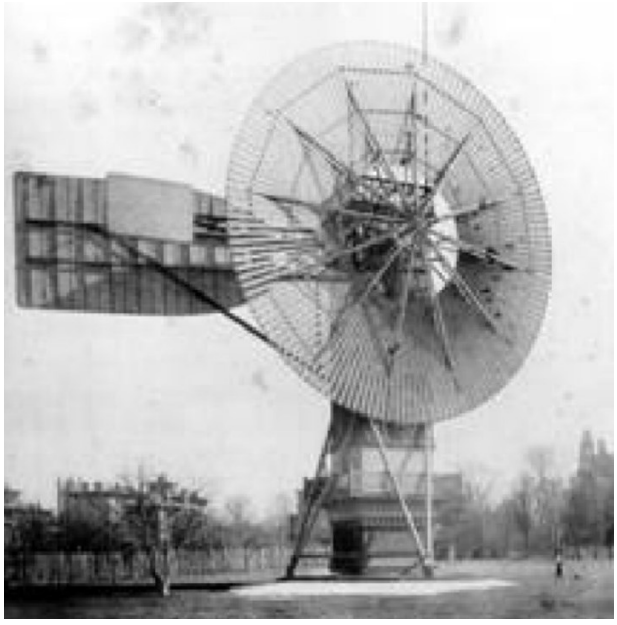

Figure 1-3 The first wind turbine used to generate electricity in the world (Ohio, 1888) [18]

Two years later, in 1890, Poul La Cour a pioneer in the area of aerodynamics and someone who is widely known for his development of windmills for electricity generation developed his theory for the ideal windmill blade profile. His theory also discovered that the airflow behind the blades was just as crucial as the wind's forward pressure. A photo of this windmill is shown in Figure 1-4 [21].

Figure 1-4 Askov Laboratory in Denmark. Poul La Cour Wind Turbine [21]

By 1910, electricity in Denmark was being supplied by several hundred wind turbines, and by 1925 wind turbines had become commercially available on the USA market [6].

Development continued in much of Europe with small 25 kW turbines becoming ubiquitous in places like Denmark by the end of World War 2. The development of the turbines of this day and age, especially for USA based development, was strongly influenced by the design of aircraft propellers [19].

By the 1960s, wind turbine power ratings had increased by a factor of 10 to sizes of 200kW. The emergence of large wind farms truly came about in the 1970s and 1980s with the oil crisis. The first large wind farms were installed in California [19]. By the 1990s, wind energy was here to stay. While the end of the oil crisis showed a reduction in investment towards wind energy in the EU, development still continued to rise at an exponential rate with the rest of the world demonstrating an increasing interest in the technology [19].

The extensive research into wind energy in the last century has resulted in many lessons being learned. A greater awareness of the environmental impact of human development has seen more careful analysis with regards to siting and installation and leading to the development of

lower impact designs. Along with this, there has been a push towards offshore installation. The first offshore wind farm with 11 wind turbines was established in Denmark in 1991. The first in the UK was deployed in the tidal waters of the North Sea at Northumberland in 2001 [22].

1.2.2. Current Status

The 1973 oil crisis and the threat of global warming gave the wind energy industry a big forward push leading to growth in wind farms across the USA. As mentioned earlier, modern wind turbines have expanded rapidly since then, and now, into the new millennia, exceed the level of 540GW installed wind capacity. According to the most recent Global Wind Energy Council (GWEC) report [6], as presented in Figure 1-5 showing the global cumulative installed wind capacity, 2015 was a record year for wind industry with over 63GW of annual new installed wind power capacity.

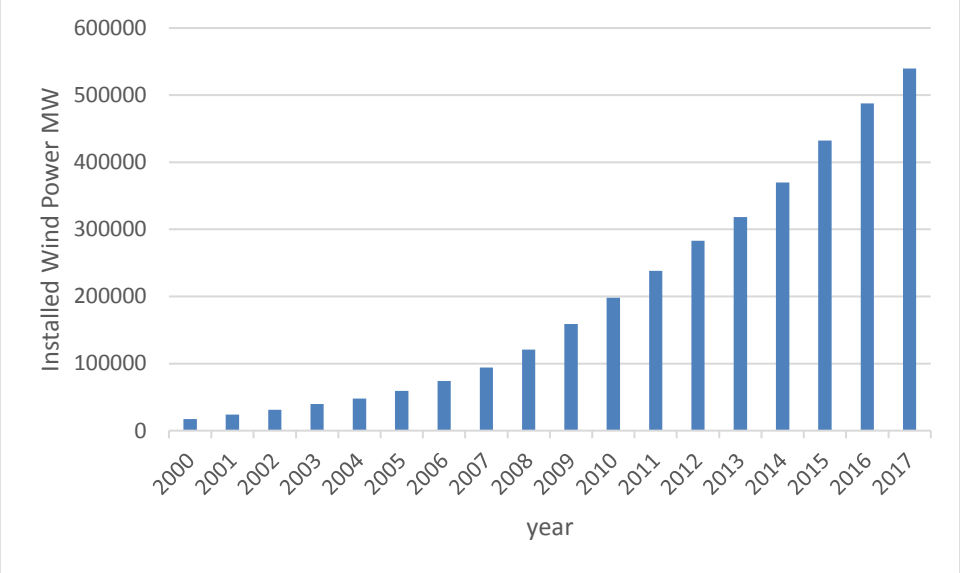

Figure 1-5 Global cumulative installed wind capacity 2000-2017 [6]

The dramatic growth in the Chinese market cannot be disregarded; China is the largest market for wind energy since 2009. 2014 and 2015 saw 23GW and 30.5GW new installed capacity, and approximately 45% of the total global installed capacity. In 2014 total wind energy capacity in China was over 114GW, as shown in Figure 1-6, and they aim to double capacity to over 200GW by the end of 2020 [23].

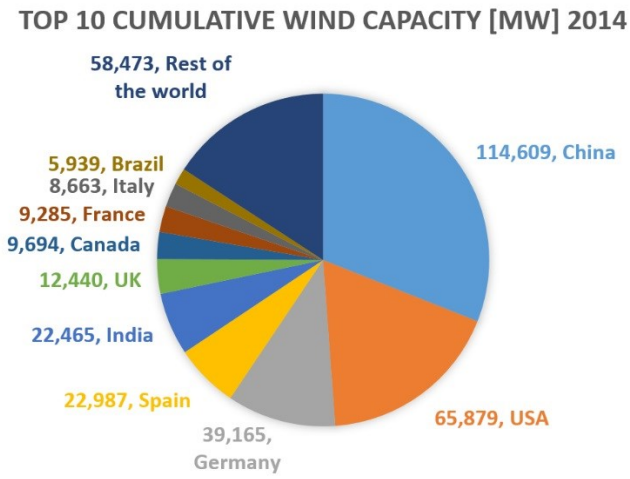

Figure 1-6 Regional distribution of top 10 global installed wind power capacity in MW in Dec 2014 [23]

Offshore wind energy capacity in Europe at the beginning 2015 was approximately 8GW out of total 134GW. Around 55% of all offshore installation in Europe is in the UK [23]. The wind energy market in Europe is stable in the short term with 5.1% annual growth.

1.3. Reliability of Wind Turbines

Reliability is essential for large and complex product, such as offshore wind turbines [24]. The reliability of wind turbines in general is improving rapidly. According to Tavner *et al*. [25], the reliability of maintained onshore wind turbines in Germany and Denmark is now higher than the reliability of diesel generating sets in the USA and almost approaching the reliability of the UK combined cycle gas turbines. Wind turbines, on the other hand, still have relatively high failure rates compared to conventional power stations due to the aggressive operating environment and the variable load [26].

The reliability of a machine in general can be defined as the probability of the machine to operate without failure for a certain period of time. Wind turbines usually operate in a harsh high wind speed environment. Access to offshore wind turbines in order to process maintenance or a repair is more difficult than to onshore ones due to the sea and weather condition and the availability of transportation. For a major replacement, weeks or even months are required, which means a loss of energy income plus the repair cost. Improving the reliability of wind turbines, therefore, is very important. The main challenge of wind turbine reliability studies is extracting information from existing operation data in order to predict and improve the reliability of large wind turbines, particularly offshore ones.

1.3.1. Historical Reliability of Modern Wind Turbines

In August 1985, the first recording of wind turbine reliability in Europe commenced [27]. Monthly inflow operational data of more than 3500 individual wind turbines and wind farms in Europe were collected for statistical analysis with the financial support of the Commission of the European Community. The data included total number of turbines, installed capacity, specific power, wind speed, component weights and mean turbine size. The statistical analysis provided information on capacity factor, operational time, failure analysis, economics and energy payback time. The reliability recording for wind turbines in the United States started in 1987 [22].

In the past, reliability problems in wind turbines have been attributed to gearboxes [28]. Tavner *et al*. [25] used 10 years of historic data extracted (1994-2004) from Windstats for German and Danish onshore wind turbines to analyse the reliability of wind turbine components. Windstats is a commercial newsletter that records details of wind turbines operation in many countries. The analysis showed the effect of wind turbine configuration on reliability and suggested a potential for greater improvements in reliability for direct-drive configurations over gearbox configurations [29]. Tavner *et al.* [25] used Homogeneous Poisson Process (HPP) model to extract the failure rate for each subassembly in the two national population of turbines. As shown in Figure 1-7, the gearbox mean time between failures (MTBFs) for Danish turbines was about 200,000 hours over the review period, whereas the number was less than 100,000 hours for German wind turbine's gearboxes. Those MTBFs numbers are not low considering the life time of the wind turbine. When taking into account the high downtime period for a gearbox failure, however, gearbox's MTBFs is critical. Gearboxes were responsible for about 65,000 downtime hours for wind turbines operating in Germany between 2003 and 2007 as shown in Figure 1-8 [30] and that was the highest downtime number compared to any other wind turbine components.

The gearbox is a complex mechanical framework requiring accurate mechanical arrangement for reliable functioning. It has a complex lubrication system that needs continuous monitoring and maintenance. Gearbox and lubrication including levelized replacement cost account for 38% of the total parts usage cost for the entire turbine system [31]. This situation is one of the main reasons for wind turbine manufacturers to think about changing to direct-drive systems [32]. A detailed comparison between direct-drive and geared-drive wind turbines is presented in the next section.

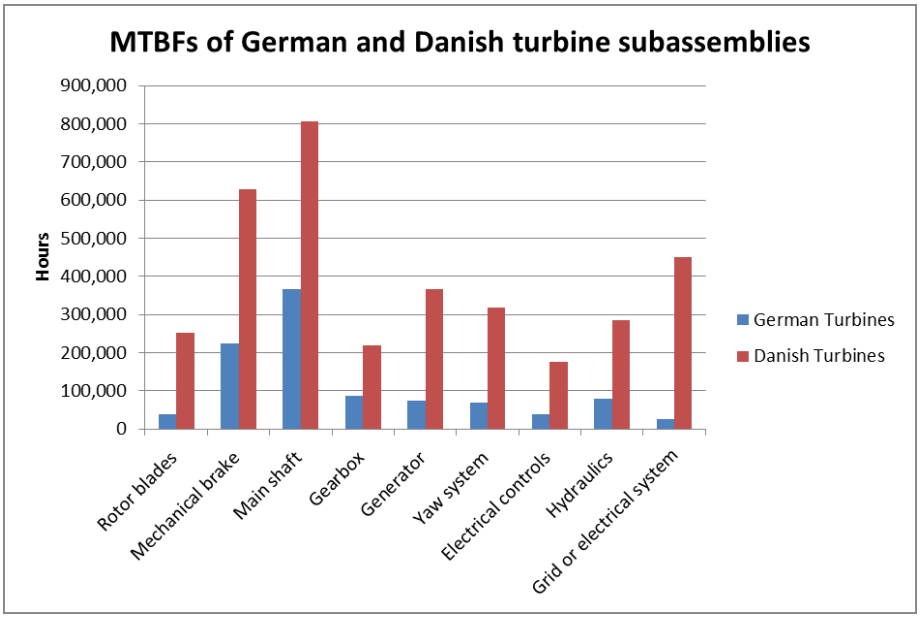

Figure 1-7 Mean time between failures (MTBF) of German and Danish turbine subassemblies (1994-2004) [25]

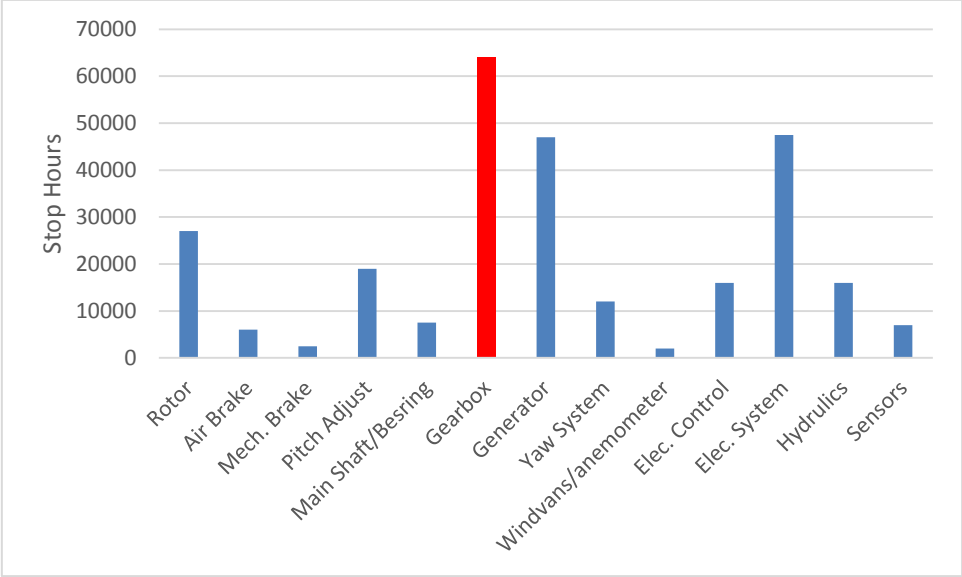

Figure 1-8 Downtime hours accumulated for wind turbines operating in Germany from 2003 to 2007 [30]

Finally, an interesting point of note is that, historically, in the early 2000s the downtime associated with coal power plants lay at roughly 6.5% as a result of failures [33]. Historic reliability issues of wind turbines have seen some drastic improvements even with gearbox systems. Current downtime of wind turbines can fall to roughly at 2% for onshore turbines and 5% for offshore turbines [33]. This suggests that, not only are turbines competing with respect to cost but also with respect to reliability when compared to some fossil fuel generation technologies.

1.3.2. Direct Drives and Geared Drives

Traditionally, the electricity generated from wind energy was made possible by gearbox operated wind turbines; Figure 1-9 shows the general layout of a typical geared wind turbine drivetrain. In these turbines, the main shaft is connected through a gearbox to the generator rotor. The gearbox is the component requiring the highest level of maintenance within a wind turbine due to its bearings and cogs which undergo high levels of stress [30]. A problem arising in one part of the gearbox can prevent the turbine from functioning properly, and lead to it coming to a breakdown. In offshore turbines, the gearbox has to withstand faster wind speeds and consequently wear can decrease lifespan significantly. The removal of the gearbox from the turbine has the potential to improve reliability and reduce repair costs. This is of particular importance in offshore wind turbines where maintenance cost is much higher.

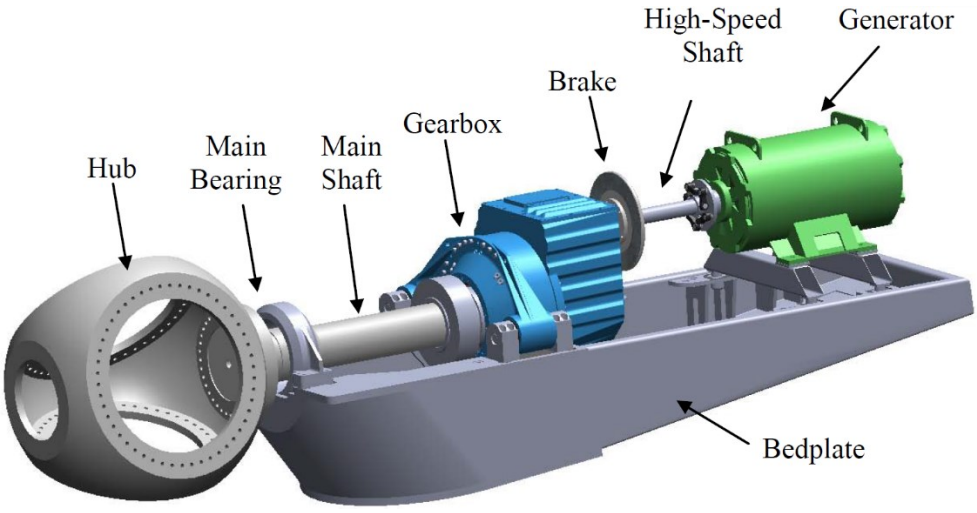

Figure 1-9 The illustration provides the general layout of a typical wind-turbine drivetrain [34][30]

Figure 1-10 Direct-Drive wind turbine (ENERCON E-82) [35]

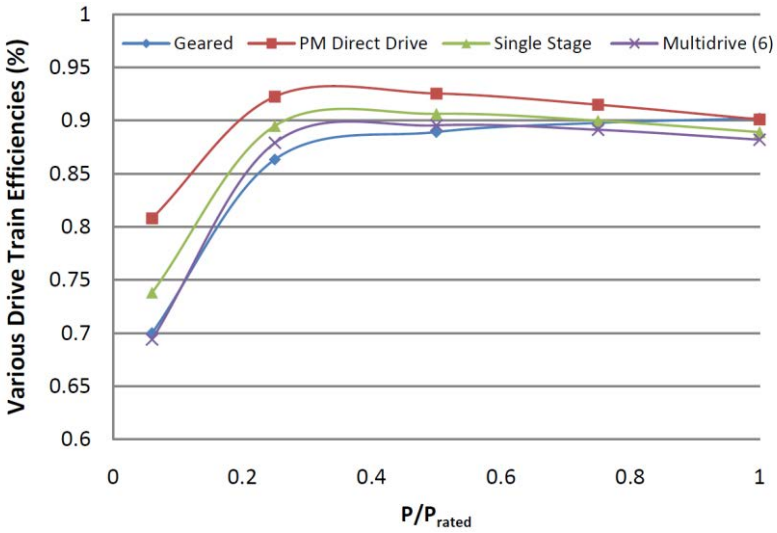

Figure 1-11 Drivetrain efficiencies for various drivetrain designs from 6% to 100% of rated power [36]

Many large wind turbines use multistage gearboxes. The rule of thumb is that 1% of the power applied at the input shaft is lost for each gearbox stage [37]. Hence, only about 97% of the input power is transmitted to a high speed generator through a three-stage gearbox. Such designs are the most common designs for gearbox drivetrain in large wind turbines. Even though high-speed generators are more efficient than direct drive low speed generators, the overall direct drive system efficiency is higher than that of geared systems. According to [38], there is 30% higher overall losses in a three-stage geared 3 MW wind turbine compared to a similar direct drive wind turbine.

The ENERCON E-82 3 MW direct drive wind turbine is shown in Figure 1-10. The generator in this wind turbine is a separately excited synchronous generator (annular generator) that is completely decoupled from the grid by a full-scale power converter located in the tower base. Many advantages for direct drive systems over geared drives can be summarized as [32][39]:

- Simplification of the transmission system
- Higher reliability [42]–[44] – Gearboxes are an important source of failure (Figure 1-7,8). They are liable to significant accumulated fatigue torque loading. Eliminating the gearbox potentially means longer lifetime and improves the reliability
- Higher efficiency – the friction between gears in gearboxes is a potential source of losses that reduce the efficiency. Figure 1-11 shows efficiency comparisons for different drivetrain designs. The efficiency of a geared drive generator is only comparable to a permanent magnet (PM) direct drive generator efficiency when the

generator is working at its rated power; otherwise, the PM generator efficiency is always higher.

- Reduced maintenance – regular maintenance is required for gearboxes in order to ensure lubrication and minimize friction
- Reduced weight – depending on the direct drive generator design, higher power direct drive systems are potentially lighter than geared drives if cleverly designed using permanent magnet topologies and multiple flux surfaces [43]
- Reduced noise – direct drive systems are less noisy with fewer mechanical parts

Even though, the total direct drive system has an advantage of reducing weight mainly because of eliminating the gearbox, direct drive generators face some challenges that are mainly related to the increased size and mass. For a given direct drive wind turbine's power, the low rotational speed means high torque in the direct-drive generator. The high torque produces a high magnetic shear stress in the airgap. Equation (1-1) gives the airgap shear stress [44]

$$\sigma_g = \frac{T}{2\,\pi\, r_r^2\, l_r} \tag{1.1}$$

Where T is the torque, r_r is the rotor radius, and l_r is the rotor core length. The magnetic flux density in the airgap is limited to approximately one Tesla. This limit is the result of the magnetic saturation of the generator core material and related topological considerations. Likewise, coil wiring and topology also act to limit this flux by putting an upper limit on the current density. These two factors acting together can be regarded as magnetic and electric loading, respectively [45]. The combination of these two components collectively determines the maximum shear stress possible on the stator-rotor assembly. Torque rather than power, therefore, has an influence in selecting the size of any given type of electrical machine for a given airgap flux density. Therefore, direct drive generators tend to be very large due to the high torque value compared to high-speed geared generators. As the turbine rating increases to multi-MW levels, the design challenge faced by direct drive becomes greater, and is explained as follows with reference to Equation 1.2, the general expression for wind turbine power.

$$P = \frac{1}{2} C_p\, \rho\, A\, V^3 \tag{1.2}$$

Here C_p is the power coefficient with a maximum value less than 16/27 defined by the Betz limit, but typically, ranging from 0.25 to 0.45. The value ρ is the air density, A is the wind

turbine's rotor swept area, and V is wind speed. P is proportional to A for a given wind speed, which means the higher the wind turbine power the bigger the turbine rotor diameter. Since the rotor's blade tip speed is limited to a certain value due to mechanical and environmental (noise) considerations, the rotational speed is lower with higher wind turbine capacity leading to higher torque requirement from the generator. This higher requirement, in turn, leads to larger direct drive generator size.

For example, comparing the size of a high-speed generator for a 3 MW geared wind turbine with a direct drive generator for a 3 MW wind turbine can better explain the size challenge. Making use of Equation 1.2 and assuming an average $n = 14$ rpm blade rotational speed, tangential stress value for the direct drive generator should be about $\sigma = 60$ kN/m^2. This can be compared to a high speed generator with a $n = 1000$ rpm gearbox output – such a machine would have a resulting stress of about $\sigma = 43$ kN/m^2 [46]. General Equation 1.3 gives the torque as a function of the power and the angular speed.

$$T = \frac{P}{w} = \frac{60\,P}{2\,\pi\,n} \tag{1.3}$$

The application of Equation 1.3 gives 2046 kNm and 28.6 kNm for the direct drive and high-speed generators respectively. The aspect ratio (length/diameter) of the generators can be calculated by Equation (1.4) [47]

$$K_{rad} = \frac{l}{2r} = \left(\frac{\pi}{4p}\right)^{\sqrt{p}} \tag{1.4}$$

Here l is the generator length, r is the generator radius and p is the pole pair number.

While across literature, direct drive pole pair numbers vary considerably, a median number of 60 can be chosen [47] to produce an estimate of 0.1 for the aspect ratio. Likewise, a simple high-speed generator can be typically regarded as having 3 pole pairs to produce an aspect ratio estimate of 0.45.

From this aspect ratio, the generator radius can be estimated. This radius is given by the expression shown in Equation (1.5) [47]

$$r = \sqrt[3]{\frac{T}{4\pi\sigma K_{rad}}} \tag{1.5}$$

Given the prior example of the 3 MW generator, the results of this calculation show a six times larger direct drive generator size of 3 m radius and a smaller 0.5 m radius high-speed generator. It is worth mentioning that, for this comparison, the length of the direct drive generator is 0.6 m, while it is 0.45 m for the high speed generator.

1.3.3. Root Causes and Failure Modes

For the purposes of this study, a failure of a generator can be defined as a complete failure to function. This is distinct from a partial failure where the machine continues to perform its primary function albeit at a considerable loss of efficiency.

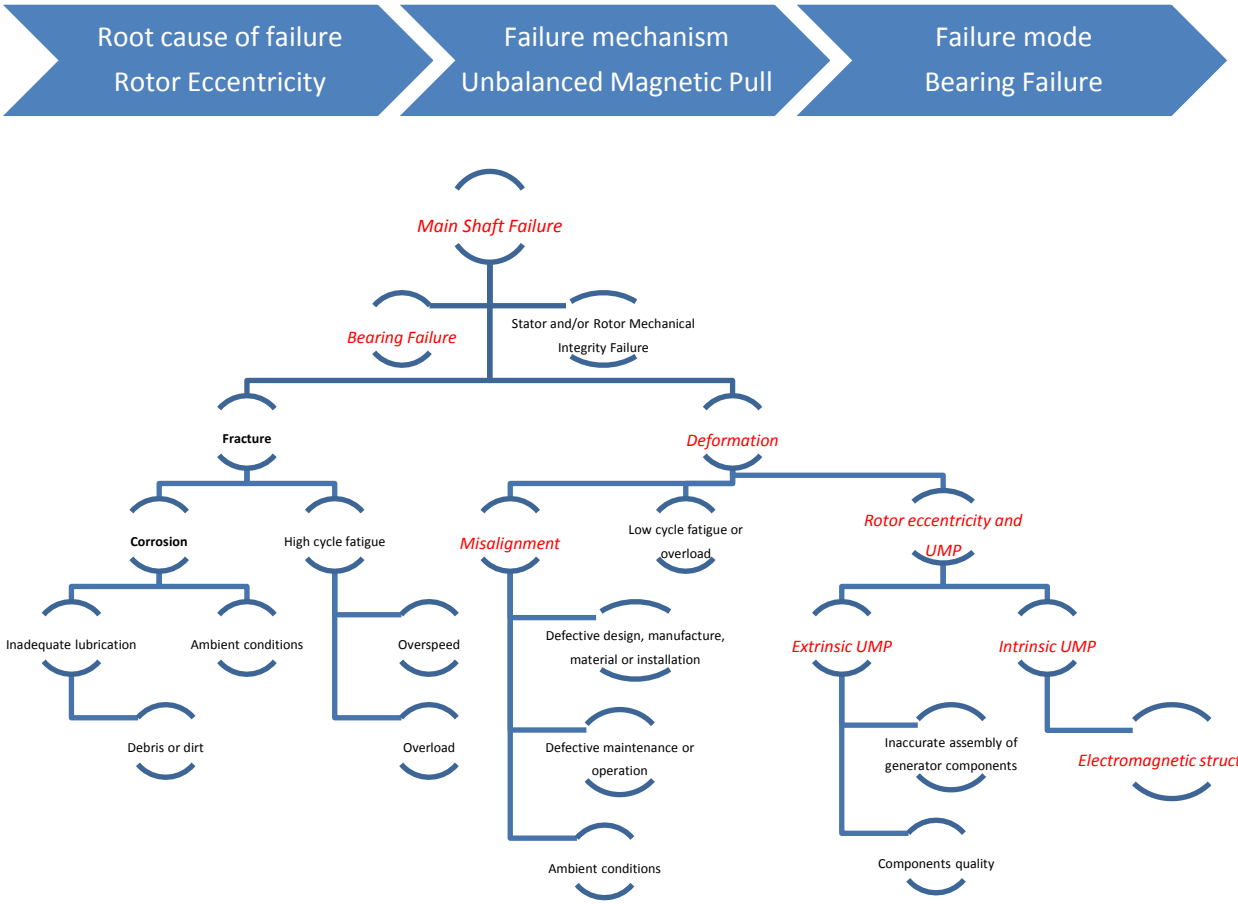

Figure 1-12 Example diagram for the root causes and main shaft failure modes

The way in which a failure occurs is referred to as the Failure Mode. Structural main shaft bearing failure for example is a failure mode for the main shaft connecting the generator assembly to the turbine. The way, in which a failure mode is initiated, is referred to as the Root Cause. Mechanical misalignment and rotor eccentricity for example are the root causes leading to a main shaft failure mode as shown in Figure 1-12. In order to prevent failure modes from occurring, root causes should be determined, monitored and treated. In some cases, a mutual

cause and effect relationship can be a root cause for a failure mode. For instance, the relationship between rotor eccentricity and bearing wear can lead to bearing failure.

1.4. Research Motivation

Following to the previous section (1.3. reliability of wind turbines), it has been proposed in literature that direct-drive systems for wind turbines are potentially a more reliable alternative to gearbox drive systems. Gearboxes are liable to significant accumulated fatigue torque loading with relatively high maintenance costs. It is with this in mind that the primary focus of this research will be on direct-drive wind turbines.

Generators in direct-drive wind turbines tend to be of large diameter and heavier due to the support structure required to maintain as small an air-gap as possible between the stationary and rotating parts of the generator. Published reliability data from existing direct drive offshore wind farms point towards the potential for the higher reliability of direct drive wind turbine systems when compared with geared drive wind turbine systems [22], [25], [29], [40]–[42]. This potential for higher reliability can have significant cost benefits in terms of maintenance where such maintenance costs are high, i.e. in offshore situations. Several concepts and alternative direct drivetrain configurations have emerged in the recent years. Permanent magnet generators (PMGs) are the most common type to be used within direct drive wind turbines nowadays. In spite of the low cost, the rugged manufacturing simplicity, and ease of maintenance, induction generators have been discounted in direct-drive wind turbine designs compared with synchronous generators. Induction generators in direct-drive systems would require a large pole number in order to meet the typical electrical system operating frequencies because of the low rotational speed. Increasing the pole number of induction generators reduces the efficiency, the power factor, the torque density, and the power throughput and increases the operating cost and the thermal losses that require adding complex cooling systems. The low power factor, moreover, increases the size, cost and weight of the power conversion equipment required to excite the induction generator with reactive power. The simplicity and the potential reduction in size, weight and cost of PMGs compared with direct drivetrains electrically excited synchronous generators, on the other hand, give a motivation to choose, review and improve the designs of permanent magnet generators used for direct drive wind turbines.

Unlike induction machines, PMGs typically do not suffer from power factor related issues associated with large air-gaps. This is fortunate since direct drive machines have a number of

significant challenges with maintaining small air-gaps. The large diameters of direct-drive generators (6 m for the example 3 MW turbine shown earlier) mean that mechanical tolerances must be extremely tight. This makes manufacturing processes challenging and expensive. Expanding on this, rotor eccentricity is likely to occur in direct-drive PMGs to a much greater extent as well. Factors such as bearing precision, shaft uniformity, shaft deflection and magnetostriction resulting (from high magnetic fields) all have a much greater effect with the larger diameters. A deeper discussion of some of these factors will follow in Chapter 3.

Rotor eccentricity generates a magnetic force referred to as Unbalanced Magnetic Pull (UMP). The induced UMP for the same rotor eccentricity is much higher in PMGs than induction generators because of the higher permanent magnet magnetic field. UMP is an important issue requiring further research. A part of this study will provide a more detailed treatment of UMP under varying rotor eccentricity regimes for various permanent magnet machine topologies.

There is a cause and effect relationship between UMP and bearing wear. This relationship, in spite of its importance (for more accurate bearing designs) has been neither widely considered nor studied in the literature in detail. This shows the importance of and provides the motivation for conducting research in this area and for presenting and analysing different designs for direct drive bearings.

The root cause of failures in direct drive generators has not been well established, hence, the possible causes and consequences of any generator failure on the remaining components of the drivetrain are not known. The following gaps were observed in the research activities that have so far been carried out in improving offshore wind turbine reliability:

Problem Statement 1: Improving Bearing life in direct drive generators

The existing design approach for permanent magnet direct drive applications accounts for structural integrity with the objective of achieving the lowest generator mass. Such design results in static eccentricity or permissible operating eccentricity limit of 2%. Misalignment based mechanical eccentricity is well known, but the impact of the such eccentricity on the rest of the components of the drive train, particularly the main bearings providing the structural support to the generator, is not well understood. Main bearing failure rates in direct drive wind turbines are relatively high (about 0.1 failure frequency per year) [29]. Studying the effect of UMP on main bearing failure will help reduce failure rates in direct drive wind turbines.

Problem Statement 2: Analytical and numerical tools to examine Air-gap winding machines

Air-gap winding machines are light and easier to manufacturing because of minimal forces between stator and rotor. Lower mass and reduced force are expected to be beneficial to improving the reliability of the main bearings. So far, limited research has been undertaken on the potential benefits of such a design. Very little emphasis has been placed on the impact of such a design on bearing/component life and the reliability of such a system. Analytical models to calculate induced forces are not available. A number of computational techniques employing different analytical tools are available for induction and iron cored PM machines. However, no such tools are available for air-gap winding machines. Such tools can help examine the influence of the UMP and eccentricity on bearing life.

Problem Statement 3: Single bearing design

The single bearing topology has many advantages such as reducing the rotating mechanical parts, the total weight, and the maintenance. While some single bearing design development is underway [48], so far, to the author's knowledge, there appears to be no significant publications about commercial presence of single bearing products in the market – at least not at a meaningful scale. The lack of established design tools, together with uncertainties related to reliability, have been major bottlenecks in taking the technology from conceptual designs to market. Having a multi-body design for the complete wind turbine drivetrain with a single bearing concept will push this technology forward.

1.5. Objectives and Aim of Thesis

The direct drive wind turbine market is expected to register a double-digit compound annual growth rate for the period 2016-2025 [49]. The effect of unbalanced magnetic pull in direct drive generators on the bearing has not been investigated in depth. With the expected increase in direct drive for offshore wind, this topic requires more research aimed at proposing design improvements and solutions. The hope being that the availability of such solutions can be applied to practical reductions in operating costs. In brief, identification of the root causes of failure and impacts on component lifetime remain a subject of research. Based on the research problems identified in previous section, establishing analytical tools for studying the impact of component lifetime in direct drive machines and identifying the prospects for air gap winding machine using single bearing configuration are the two key areas for further research.

Firstly, this research aims to establish the relationship between bearing forces and different types of eccentricities and UMP in direct drive machines. It is intended to use such models for predicting bearing wear and fatigue. Secondly, this research aims to establish the analytical tools for studying static, dynamic and tilting eccentricity in air-gap winding direct drive generators. Such tools will be used to increase the understanding of the dynamics of direct drive PM generators. Finally, the prospects of single bearing design as a reliable solution for direct drive generators will be examined.

In summary, the main aim of this thesis is studying the effect of different types of rotor eccentricities in different types of direct drive PMGs on the lifetime of bearing systems, showing the influence of unbalanced magnetic pull on bearing wear, and proposing a suitable single bearing design for a direct-drive wind turbine whilst comparing it with a conventional design.

1.6. Outline of Thesis

This thesis includes eight chapters. Chapter 1 gives a brief introduction about wind energy and reliability of wind turbines plus the motivation and the outlines of the thesis.

Chapter 2 presents a literature review for direct-drive permanent magnet generators for wind turbines including a review for permanent magnet materials and concentrating on radial flux PM machines.

Chapter 3 includes a detailed review of static, dynamic and tilting rotor eccentricities together with additional reviews of induced unbalanced magnetic pull in PM generators associated with direct-drive wind turbines.

Chapter 4 introduces analytical models to calculate unbalanced magnetic pull resulting from the various rotor eccentricity issues of direct drive PM generators. The output of this chapter is used as an input for chapter seven.

Chapter 5 presents numerical models that aim to validate the analytical approaches presented in chapter 4. Numerical models focus on the use of 2D finite element analysis software. Experimental test results are presented in this chapter to validate the iron-cored PM machine's numerical model.

Chapter 6 provides a design for a 5MW direct-drive wind turbine with two options of generators that are airgap winding PM generator and iron-cored PM generator and two options of main bearing that are single bearing design and double bearing design.

Chapter 7 presents multi-body simulation results for four direct drive generator and bearing arrangements for 5 MW wind turbine. The four designs include: (a) iron-cored PM direct-drive generator supported by two main bearings, (b) airgap winding PM direct-drive generator supported by two main bearings, (c) iron-cored PM direct-drive generator supported by a single main bearing, (d) airgap winding PM direct-drive generator supported by a single main bearing. The multi-body simulation aims to clarify the effect of the generator design on bearing system design.

Chapter 8 provides a summary and conclusion for this thesis including recommendations for future work.

Chapter 2. Review of Permanent Magnet Generators

2.1. Introduction

This chapter provides a review of different types of permanent magnet generator (PMG) designs for direct-drive wind turbines. A comparison of different PMGs is presented as a first step in the research process in section 2.2, starting with a review of permanent magnet (PM) materials which are used in such generator designs. The advantages, disadvantages, working principle and previous research into radial, axial and transverse flux PMGs is briefly presented with a focus on the three different types of radial flux PMGs: iron-cored, air-cored and air-gap wound. Later chapters will give further treatment to each of the generators.

2.2. Permanent Magnet Generators for Direct-Drive

Permanent magnet generators (PMGs) are favoured by the direct drive wind turbine industry due to their high power density and high efficiency under variable load conditions. However, the percentage of PMGs in the offshore wind turbines market share is low compared to the traditional geared drive induction generators as shown in Figure 2-1. PMGs have the potential to secure a much bigger portion of the market share in the near future as the main generator of choice for wind turbines.

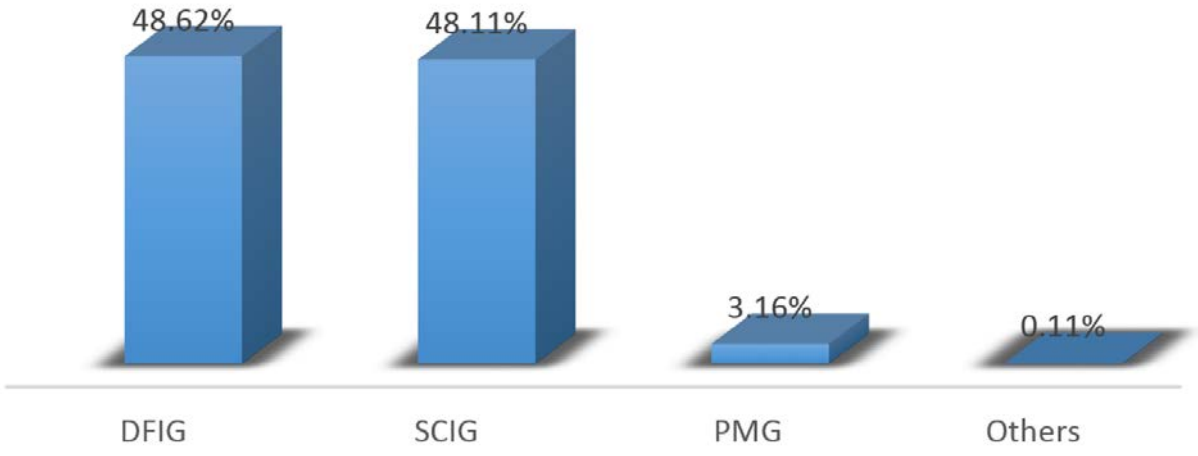

Figure 2-1 Offshore wind turbine market share of different machine types in 2012 [50]

For direct drive wind turbines, PMGs have higher efficiency and energy yield than electrically excited synchronous generators (EESGs) [47]. Using permanent magnets (PMs) eliminates the complexities of field excitation system, with improved reliability. This reliability increase is a result of the absence of physical contact components (slip rings and brushes). Moreover, PMGs have higher power to mass ratio compared with EESGs [47].

On the other hand, the strong attraction forces between the stator and the rotor in a PMG lead to difficulties in manufacture and maintenance. Demagnetisation at high temperatures or during short circuit fault conditions is also a challenge for PMGs in some applications. Typically, the operating temperature range recommended for such generators falls at an upper limit of 75 °C [43]. Under high torque conditions, induced by generator winding faults, temperature rise may occur faster. As well as generator short circuit faults, grid short circuit faults can lead to very high currents in the stator windings and core material due to induced eddy currents – the resulting temperatures can have an effect on the permanent magnets attached to the rotor [51]. It should be noted that while the upper temperature limit of many commercially manufactured magnets does fall within the recommended upper limit temperature of generators, there are a range of permanent magnet classes that can operate well above this temperature at values as high as 230 °C [52]. Of course, there is a cost premium associated with such performance.

Price instability exists with permanent magnets. This is particularly true for modern day high-energy product rare earth magnets. This unstable PM cost forms a disadvantage for PMGs in general.

Various PMGs can be classified according to topology. Four main PMG types are presented in the literature [53]:

- Radial or axial PMGs depending on the air-gap orientation with respect to the rotational axis.
- Longitudinal or transverse PMGs depending on the stator core orientation with respect to direction of movement.
- Surface-mounted or flux-concentration PMGs depending on the orientation of PMs with respect to air-gap.
- Slotted or slot-less PMGs depending on the windings housing.

Three configurations of PMGs, depending on the flux line direction crossing the air gap, have been reviewed in this section: radial flux PMGs, axial flux PMGs and transverse flux PMGs.

2.2.1. Permanent Magnet Materials

In the last few decades, the industry has succeeded in developing improved magnet characteristics as shown in Figure 2-2 [54]. Permanent magnets (PMs) are normally compared with regards to their maximum energy production $(BH)_{max}$.

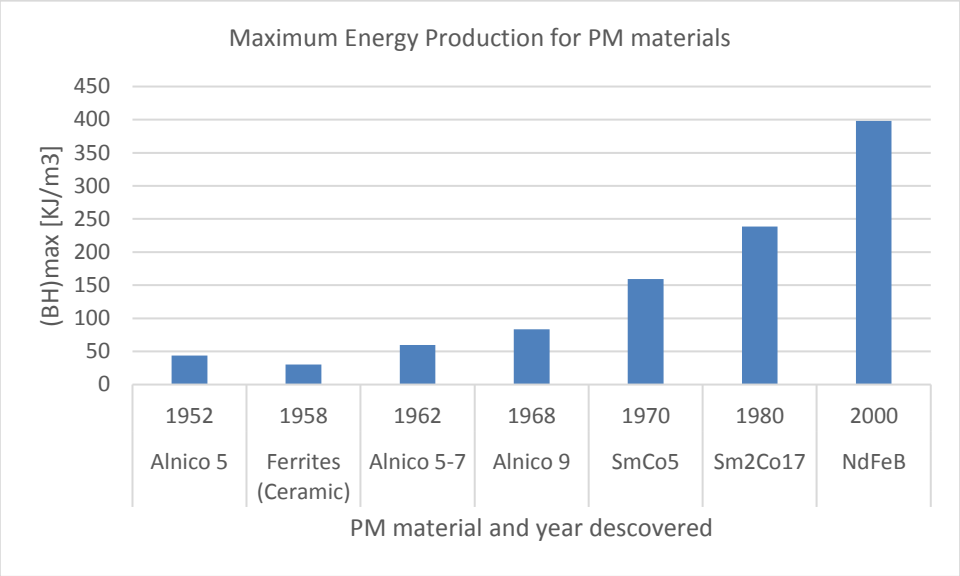

Figure 2-2 Development of PM materials in terms of maximum energy product [54]

Neodymium-iron-boron (NdFeB) is the industry standard PM type used today, e.g. in automotive, aerospace, acoustic and medical industries [55] as shown in Figure 2-3. It should be noted that the use of NdFeB has remained very small in the wind industry. The reasons for this is that NdFeB PMs are expensive compared to ferrite magnets, and price has been volatile in recent years. For example the price increased by more than 1000% from August 2009 to August 2011 due to export and mining regulations introduced by China [56]. This volatility makes it very difficult to plan ahead for any industrial sector, and in particular wind where cost margins are very tight. It is challenging to find clear numbers for pricing of NdFeB magnets as a whole, however, Figure 2-4 shows the rare earth export-prices from China at 2017 conversion rates between 2006 and 2016 [57] [58]. Although the prices of the rare earth in China are in the range of £2500/ton, the price of NdFeB in the UK has been in excess of £75/kg.

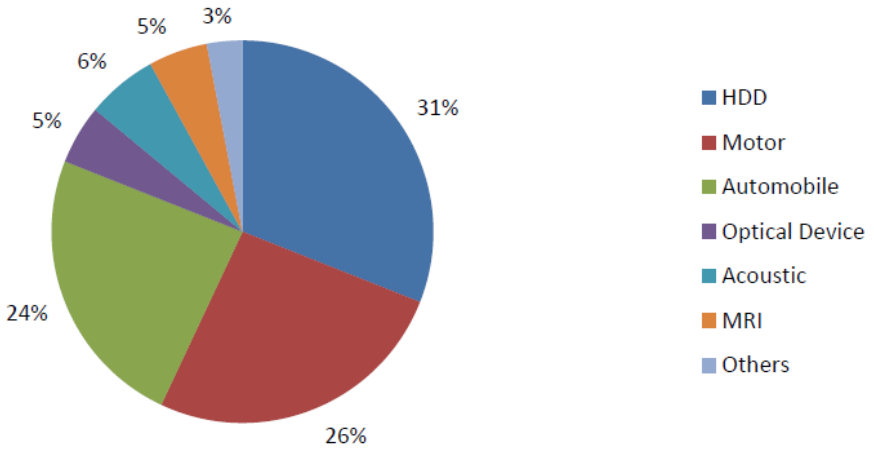

Figure 2-3 Neodymium magnet applications as of 2009. Data source: [59]

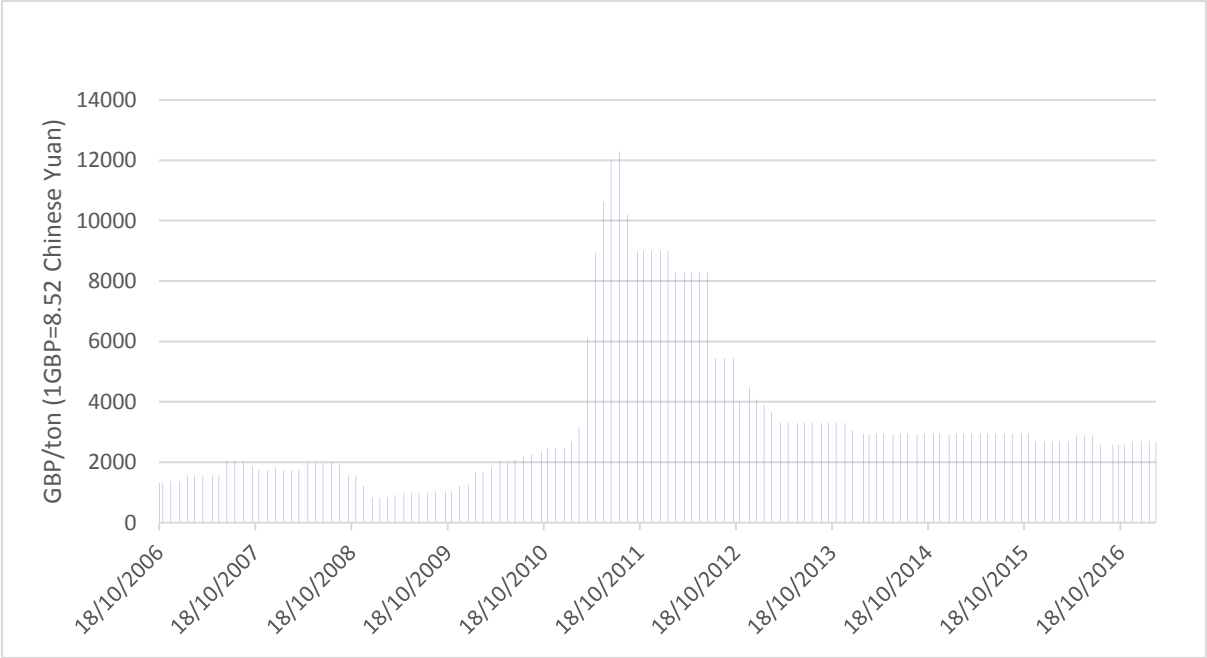

Figure 2-4 Rare earth price index according to the Association of China Rare Earth Industry [58]

Production by region [kTons]	*2012*	*2015*
China	50	65
Japan	10	8
Europe	1	1
USA	0	2
The rest of the world	2	2
Total	**63**	**78**

Table 2-1 NdFeB market [60]

The energy density of NdFeB suggests that it is likely that demand will continue to increase in the coming years. Production by region is presented in Table 2-1 [60]. About 83% of the whole

world rare earth elements are extracted and exported by China and the supply is already equalling demand within the country [56].

An accurate figure for the price of NdFeB is important when optimising machine designs with regards to cost of energy. Machine designs can be optimised to minimise PM content, but if the figure for PM price is inaccurate this will lead to optimistic forecasts of commercial viability.

2.2.2. Radial Flux Permanent Magnet generators (RFPMGs)

The magnetic flux in a RFPMG flows in the radial direction across the air-gap in order to link the stator windings.

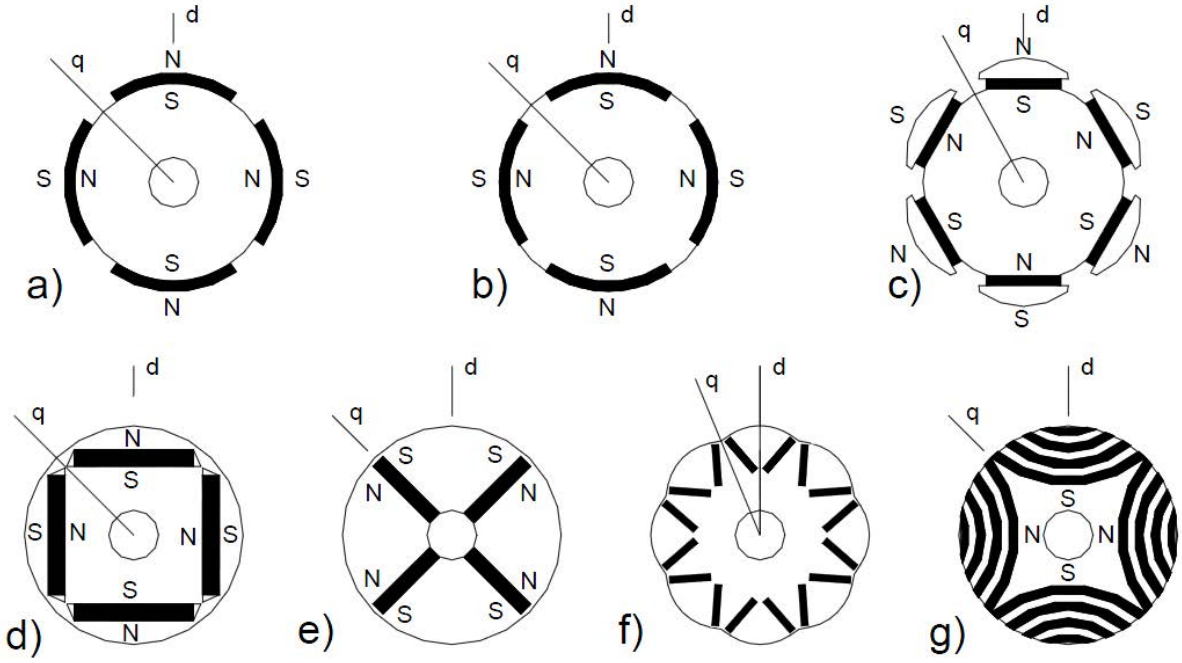

Figure 2-5 RFPMG types depending on rotor structure [61]

Different rotor constructions for RFPMGs can be distinguished in the literature as shown in Figure 2-5 [61], where, a) surface-mounted magnets, b) inset magnets, c) surface-mounted magnets with pole shoes, d) buried tangential magnets, e) buried radial magnets, f) buried inclined magnets with cosine shaped pole shoe, and g) permanent magnet assisted synchronous reluctance motor with axially laminated construction.

Regardless of topology, RFPMGs have good power factor and simple structure for manufacturing and maintenance compared with transverse flux PMGs, which have poor power factors and complex electromagnetic structures. Looking closer at the first three types of

generator shown in Figure 2-5, types a, b and c are the most common type of PMGs due to their simplicity and reliability. The length of these RFPMGs are relatively easy to vary from a manufacturing stand point, however, variations in diameter may be somewhat more constrained. Either solid rotor core or laminated rotor can be used in a, b and c types, whereas, only laminated rotor type is normally needed in the rest [62]. Surface-mounted magnets rotor construction is the most common design in direct-drive wind turbines because of manufacturing simplicity. Type (a), therefore, was selected in all designs and comparisons of PM generators for direct-drive wind turbines. While the figure only shows radial flux configurations, it is also possible to produce axial flux versions of PMGs. Such axial flux variants can be used with fewer diametric constraints. As a result, such configurations have the potential to be preferred for large diameter machines [47].

Different stator designs for surface-mounted PM generators already exist in the direct drive generator industry. Iron-cored stator design is the most common design for RFPM generators. However, a few other designs such as air-cored and air-gap winding RFPM generators are tested and yet to be commercialised [63].

2.2.2.1 Iron-cored (Slotted) RFPM generators

An iron-cored RFPM machine, also known as slotted RFPM machine, could have any rotor structure of those shown in Figure 2-5. The stator, however, consists of slotted iron cored laminations packed together with windings. Figure 2-6 shows an 11kW iron-cored surface-mounted RFPM generator with the magnetic flux density distribution using a finite element analysis.

Various rotor designs of iron-cored RFPM generators for low-speed direct-drive wind turbines including curved and rectangular surface-mounted magnets as well as rectangular magnets equipped with pole shoes were discussed and optimised in [64] . The optimisation showed that curved surface-mounted iron-cored RFPM generators have the lowest cost of active materials and the highest pull-out torque per the cost of active materials between other surface-mounted designs. The advantage of the pole-shoe rotor, according to this research, is that the magnets can be reliably protected mechanically and magnetically.

A design and optimisation of a 20kW outer rotor iron-cored surface-mounted RFPM machine, as shown in Figure 2-7, is discussed in [65]. The primary purpose of the outer rotor is to ensure stronger glue joints between the permanent magnets and the core material via centrifugal

effects. This machine aims at reducing cogging torque and improving performance by looking at optimizing the magnetic arc width of the PMs attached to the outer rotor and the width of the stator slot opening. While a variety of approaches exist for reducing cogging torque, this was found to be the most effective combination of changes. Finite element methods were used in this research to optimise the design for different number of poles and different lamination types.

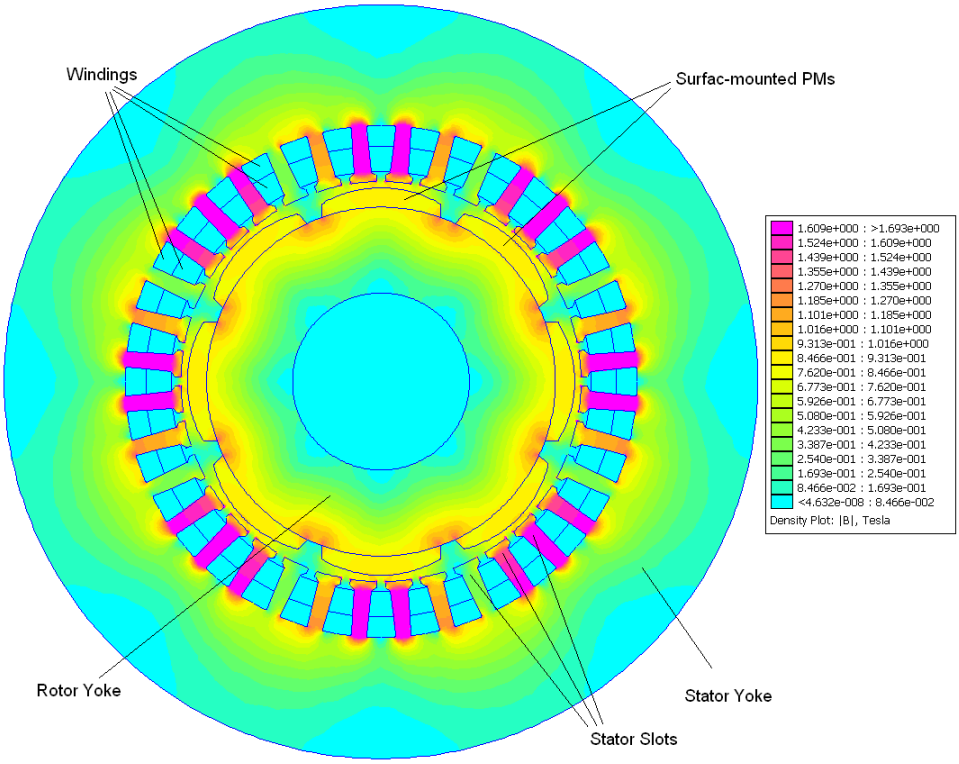

Figure 2-6 11kW Iron-cored surface-mounted RFPM machine showing magnetic flux density

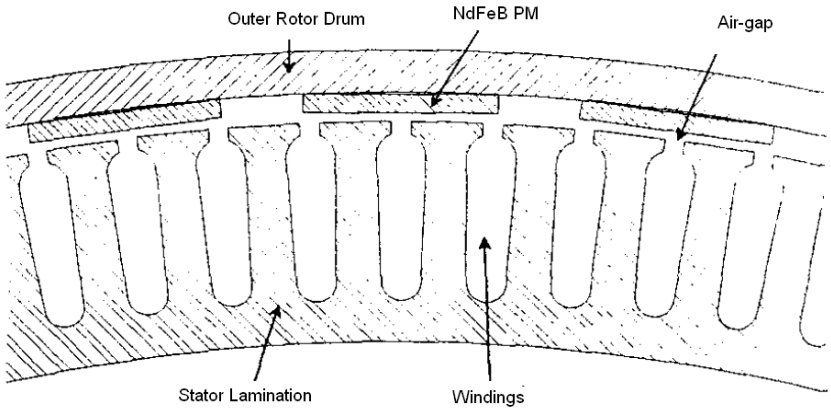

Figure 2-7 Layout of outer rotor iron-cored surface-mounted RFPM generator [65]

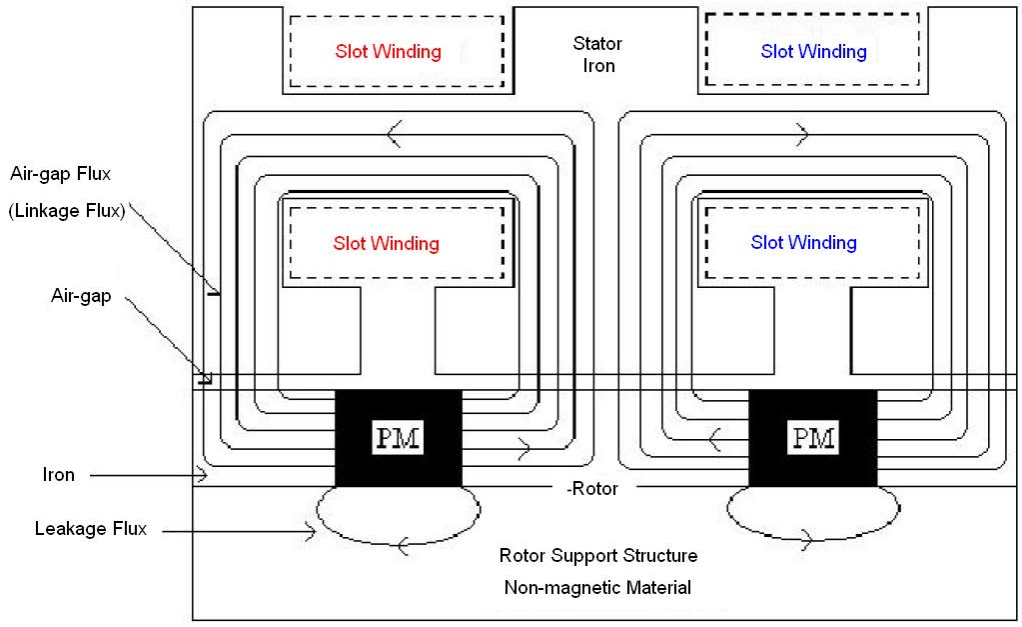

Figure 2-8 Schematic diagram of flux-concentrating iron-cored RFPM machine [66]

Flux-concentrating iron-cored RFPMG designs were discussed, optimised, constructed and tested in [66]. The rotor support structure in this design is made of a non-magnetic material, as shown in Figure 2-8. The PMs are attached to a soft magnetic core to form an easy flux path and fixed on the rotor support structure. The windings are of toroidal type, placed in flat slots with short ends. Such an arrangement allows for more compact designs and further allows for higher efficiency, lower weight and lower active material costs. The prototype presented in [66] exhibited about 84.6% efficiency at 1,270 W output power and 250 rpm rotational speed. While quite a small generator, this design demonstrates the possibilities and potential advantages of such a design for larger scale low speed variants as well.

2.2.2.2 Air-cored (Iron-less) RFPM generators

Spooner *et al*. [67][68] in 2004 proposed a new lightweight air-cored iron-less RFPM generator for direct-drive wind turbines. As shown in Figure 2-9, the generator consists of an outer rotor and inner stator. The rotor is connected with the wind turbine shaft from one side and with the nacelle structure through an auxiliary thrust bearing from the other side by a spoked structure. The stator is connected directly to the nacelle structure through a spoked structure also. The rotor is made of steel rim with surface mounted NdFeB PMs and the stator consists of non-metallic lightweight rim (such as glass fibre) and air-gap windings. An underlying structure in steel for the stator rim was suggested as an alternative by the author for stiffer construction with a clearance of about two pole pitches from the PMs in order to ensure no magnetic

attraction forces or eddy currents. This design has many advantages mainly related to the absence of iron in the stator structure. There are no radial magnetic attraction forces between the rotor and the stator, no cogging torque and no eddy currents in the iron structure. Manufacturing and maintenance for such a design are easier than other types of permanent magnet generators, which suffer from high magnetic attraction forces between the stators and rotors. Lower bearings stiffness is required because of the absence of unbalanced magnetic forces even when the rotor is eccentric with respect to the stator.

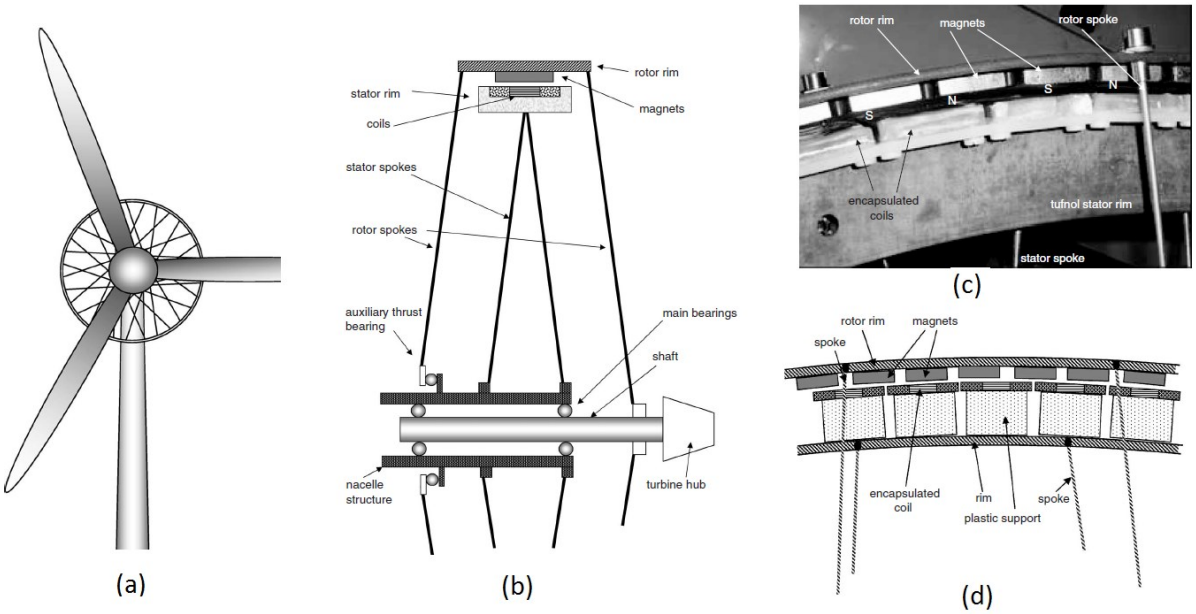

Figure 2-9 Air-cored RFPM generator design. (a)- Wind turbine with proposed generator. (b)- Overall generator cross-section. (c)- Prototype. (d)- Cross-section of rotor and stator rim [68].

The mass of active materials and the mass of structural materials in terms of shear stress and efficiency for 5MW air-cored, iron-cored and air-gap wound RFPM generators were compared in [68]. The results of the proposed air-gap RFPM generators showed best power to mass ratio for a fixed diameter and shear stress.

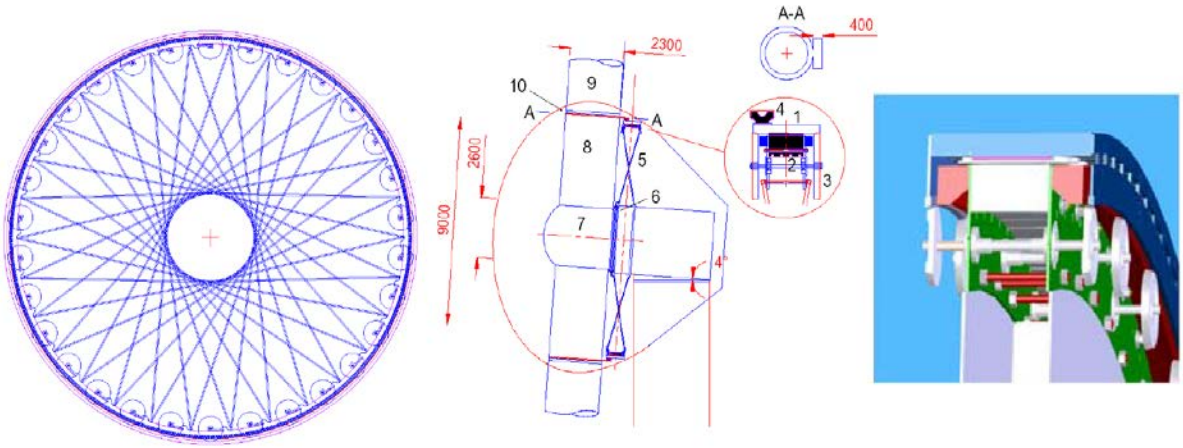

Figure 2-10 4MW New-Gen air-cored RFPM generator with 9m diameter. 1. The rotor, 2. The stator, 3. Bearing wheel, 4. Flexible connection, 5. Spokes, 6. Stator center with a single turbine rotor bearing, 7. Hub, 8. Hub extension, 9. Blade, 10. Blade pitch bearing [69][8]**.**

A new type of air-cored RFPM generator for wind turbines was proposed by Engstrom in 2006 [69][8], the New-Gen generator. The main idea of this design is to place the bearings adjacent to the machine's air-gap for large diameter generators, as shown in Figure 2-10. The goal here is to reduce the stiffness demand. Further, it removes the load path from the rotor, the stator and the shaft through the air-gap bearings. Large mass saving is gained in this case which also leads to mass reduction in electrically active parts. The first prototype was a 140 kW pilot scale generator with 1.6 m diameter. Good results from the prototype testing led to further investigations for the 4 MW, 19 rpm, 9 m diameter generator discussed in [69]. Depending on the particular configurations, it can be seen from [69] that about 70% of the mass of a 4 MW conventional direct-drive PM generator can be saved by this alternative New-Gen 4 MW design, as shown in Figure 2-11. It appears that this generator at some point until 2011 was in the process of commercialization with funding secured. Unfortunately, it is not clear what has become of this design in recent years [70]. Moreover, the large diameter of the support bearing would have made this solution not feasible in large wind turbine applications [71].

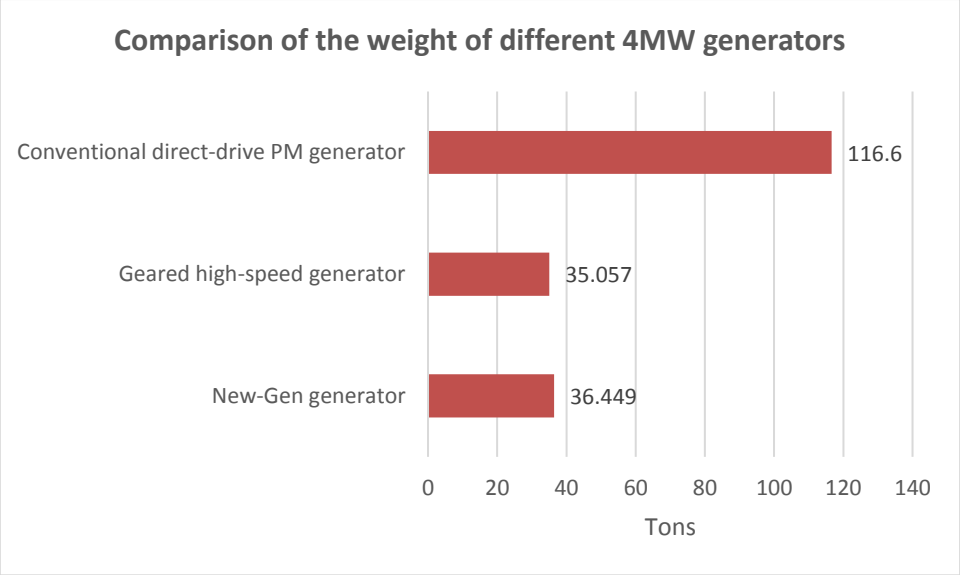

Figure 2-11 Comparison of the weight of different 4MW, 19rpm, drive-train alternatives. Source [69].

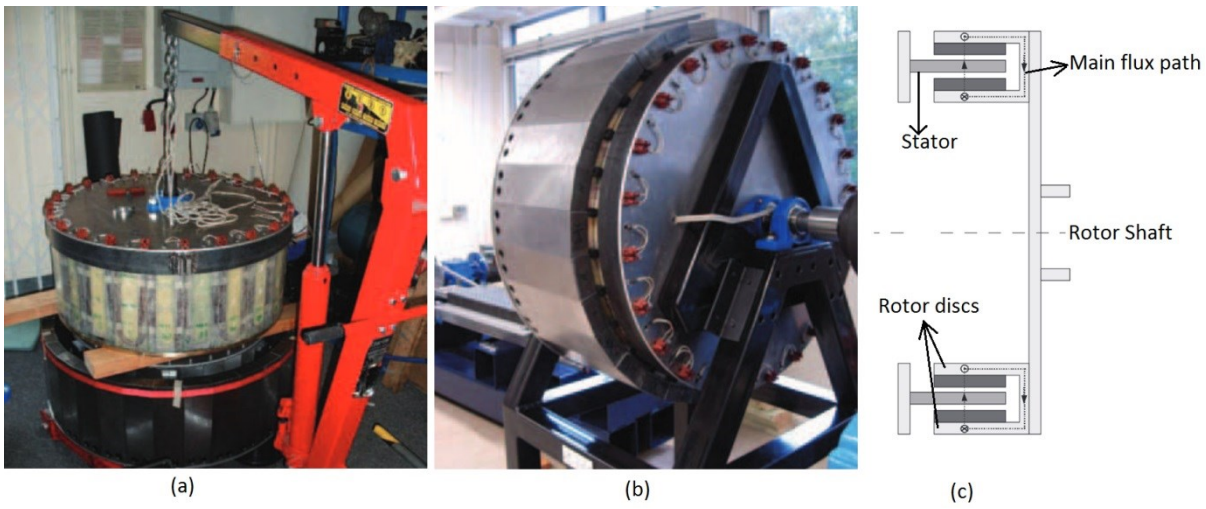

Figure 2-12 The 20 kW, 100 rpm C-core air-cored generator. (a) Lowering the 'C' core stator to meet the rotor, (b) The prototype test rig at the University of Edinburgh, (c) Cross section diagram of the radial flux C-core generator [72].

Mueller and McDonald in 2008 presented a new lightweight low-speed air-cored PM generator concept for direct-drive wind turbines, referred to as C-GEN [72] (Figure 2-12). C-GEN is a permanent magnet generator that has a number of unique selling points: – it is highly modular; – easy to assemble requiring only an overhead crane and lift, which benefits O&M operations as only the faulty module need be removed not the whole machine, this improves availability and hence reduces cost of energy; and – it exhibits zero cogging torque. As with all PM machines C-GEN exhibits high efficiency over all loads, which is beneficial at part load. The technology has been demonstrated at lab scale 20-50kW, a 15kW machine has been installed on a turbine, and the technology has been successfully scaled from 25kW to 1MW in one step,

which demonstrates the scalability of this technology. C-GEN is at TRL (Technology Readiness Level) 4-5 for small wind, as it has been demonstrated in a relevant environment – 15kW wind turbine.

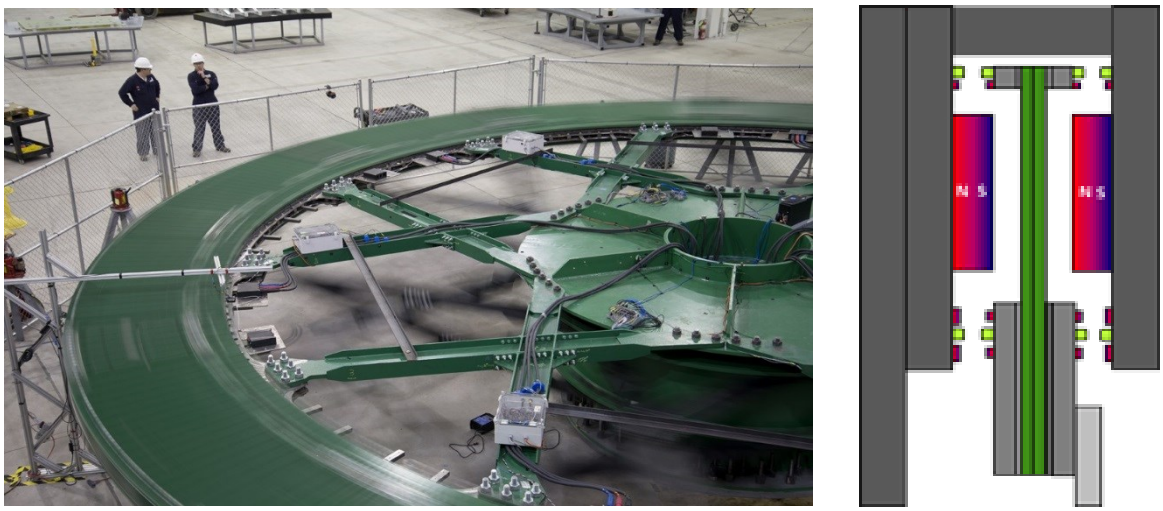

Figure 2-13 Boulder Wind Power's air cored generator assembly. Left image shows an isometric view of their 3 MW device, while the right image shows a cross-sectional CAD drawing [75]

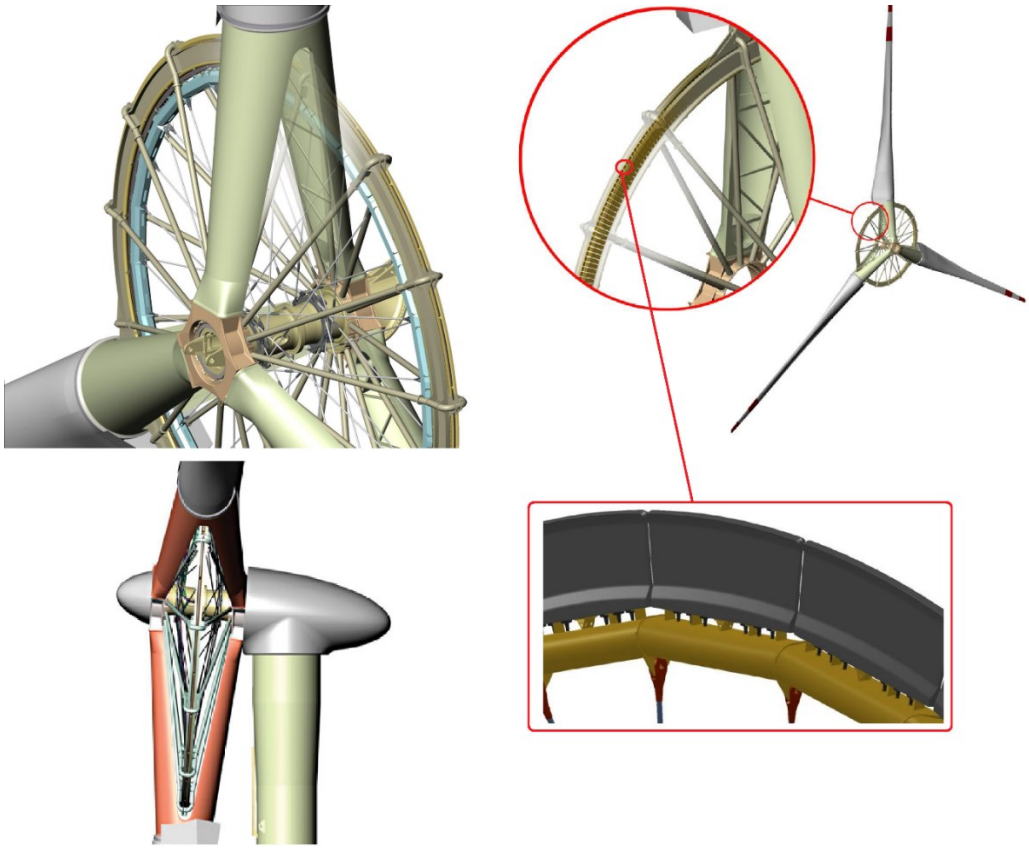

Figure 2-14 The Sway 10MW turbine showing the distinctive 'bicycle wheel' and stator and rotor segments [73][74]

Another contender for air-cored generator designs is a company called Boulder Wind Power [75]. Figure 2-13 shows an image of their turbine. They achieve light weight and reliable generation by making use of PCB technology to manufacture stator coils combined with a simple back iron. They further eliminate the need for expensive electrical steel laminations and use dynamic structural designs to maintain optimally positioned air-gaps of high stiffness.

Plans for a commercial 10 MW iron-less RFPM offshore wind turbine were unveiled in 2012 by the Norwegian Company Sway Turbines as shown in Figure 2-14 [73][74]. The company takes advantage of light weight structural components that resemble bicycle spokes to significantly improve the power to mass ratio over other direct-drive systems.

As a new company, they appear very much in early commercialization phase – it is unclear how far they have progressed with the technology however.

Most permanent magnet generators usually consist of one air-gap layer. However, some machines make use of multiple layers of air gap. Such machines make use of multiple stators and rotors and may not have iron yokes – the high axial force in iron cored machines of this nature produce high forces and increase mechanical complexity, as demonstrated in the earlier chapter. However, the multiple air gaps can lead to somewhat different considerations from a harmonic analysis point of view. Valavi *et al* [71] discussed details of multi air-gap (MAG) machines. Electromagnetic characteristics of a double-stator radial-flux PM generator were studied using FE analysis. Two design variant with magnetic and nonmagnetic rotor yokes were compared with regards to airgap flux density, induced voltage, electromagnetic torque and output electrical power. The results showed higher induced voltage and output power in the case of the magnetic rotor yoke. Figure (2-15) [71] includes: (a) which shows a direct drive PMSG by TheSwitch [76], (b) shows a schematic presentation of active parts (red colour is stator and green colour is rotor) in traditional design, (c) shows MAG machine with two levels of active parts, which is designated by letter “A” and one side rotor support structure, which is designated by letter “C”. The yellow triangles designate the extra supporting parts introduced to support the second stator.

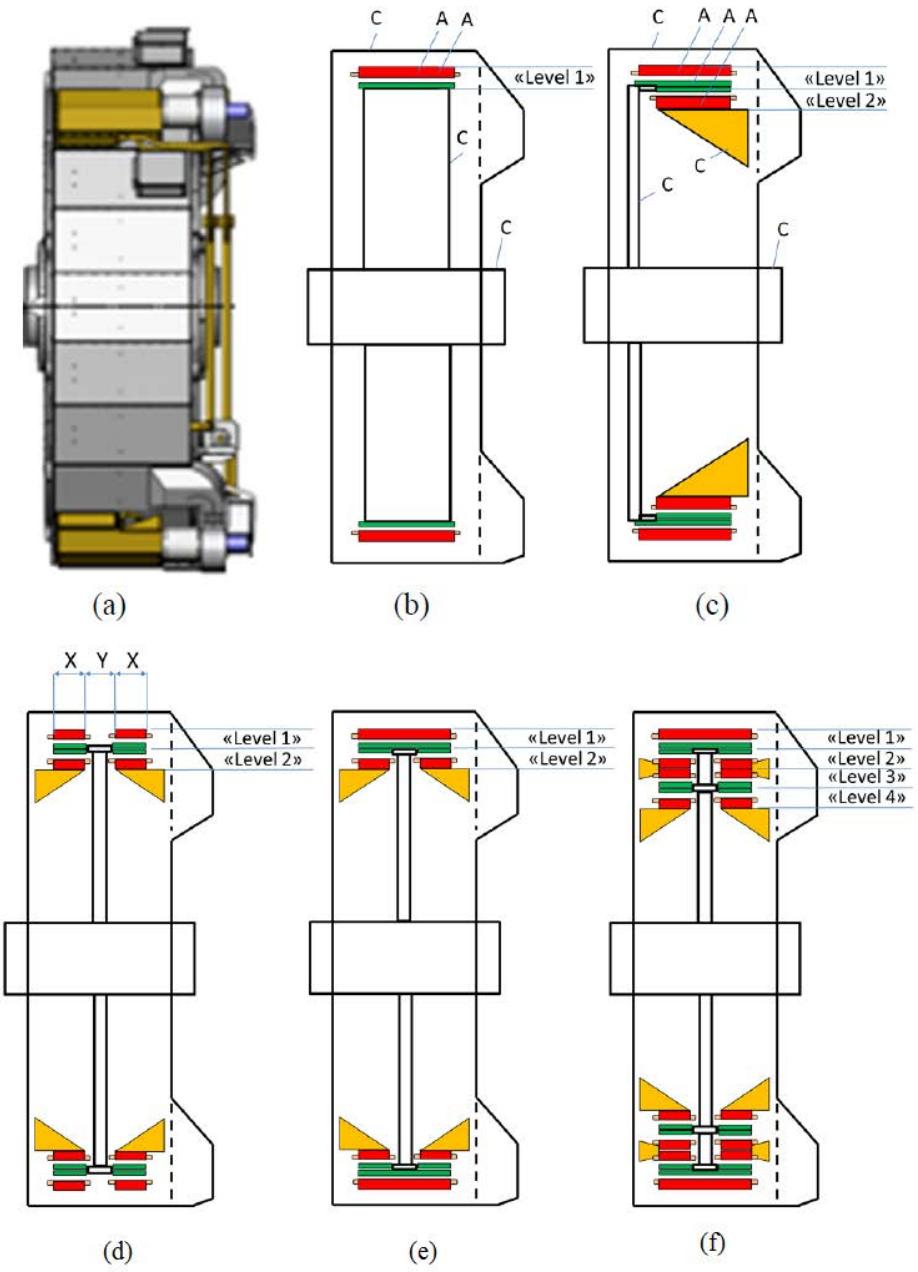

Figure 2-15 Illustration of Multi-Air-Gap (MAG) concept application by TheSwitch [76]**: (a) Direct drive PMSG (b) schematic presentation of active parts in traditional design (c) MAG with two levels of active parts and one side rotor support structure (d) MAG with two levels of active parts with rotor supporting structure in the middle (e) MAG with two levels of active parts with middle rotor supporting structure and full use for energy conversion (f) MAG with four levels. A is active parts and C is supporting structure. Modified from** [71]

The main challenge with the MAG RFPM machines is the high radial forces between the stator(s) and the rotor(s) in case of any eccentricity. There will always be some misalignment due to manufacturing inaccuracies which will result in high unbalanced magnetic forces. Eliminating these unbalanced forces requires either a massive supporting structure should or adopting a special design. In Figure 2-15: (d) shows MAG with two levels of active parts with rotor supporting structure located in the middle of the electrical machine and with the active parts are arranged on both sides, seen in the axial direction. This solution solves the problem

of supporting the active parts in case of misalignment, as the active parts located on each side of the supporting structure are shorter than in the case where the active parts are supported from one side only. On the other hand, the area at the periphery of the supporting structure (designated "Y" in Figure 2-15 (d)) is not used for energy conversion. A solution eliminating the mentioned drawback was proposed in [77] and shown in Figure 2-15 (e). Figure 2-15 (f) shows the same solution expanded with four levels.

2.2.2.3 Air-gap winding (slot-less) RFPM generators

Traditional iron-cored RFPM generators exhibit high magnetic attraction forces between the permanent magnet rotor and the iron-cored slotted stator. Alternatively, the coils can be directly attached to the stator surface toward the air-gap as shown in Figure 2-16. The machine, in this case, referred to as an air-gap wound or slot-less RFPM machine. Two kinds of air-gaps can be distinguished in this design. The mechanical air-gap is the distance between the PMs and the windings and should be as small as possible. The distance between the rotor surface and the stator surface is the magnetic air-gap. Due to a relatively large magnetic air-gap, such machines are easier to manufacture, assemble and maintain during operation but the magnetic field in the airgap is lower than in a slotted machine. On the other hand, the increase in the magnetic air-gap is compensated for by an increase in the core length, which in turn results in an increase in material mass. The slot-less design means no cogging torque losses.

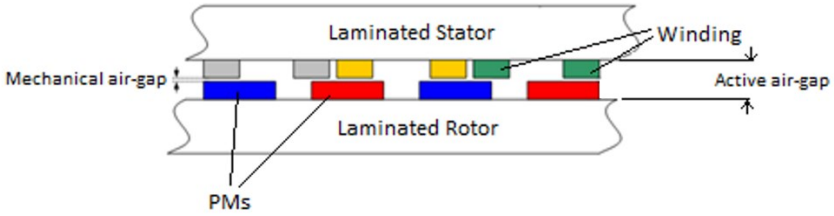

Figure 2-16 Schematic drawing for an air-gap wound RFPM generator.

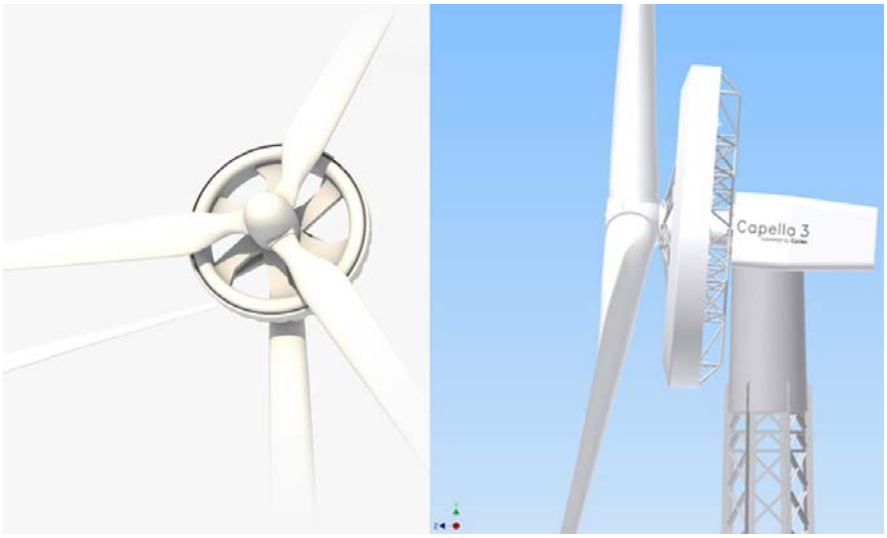

Figure 2-17 Goliath Wind Power's machine design for a 3.3 MW turbine [78][79]

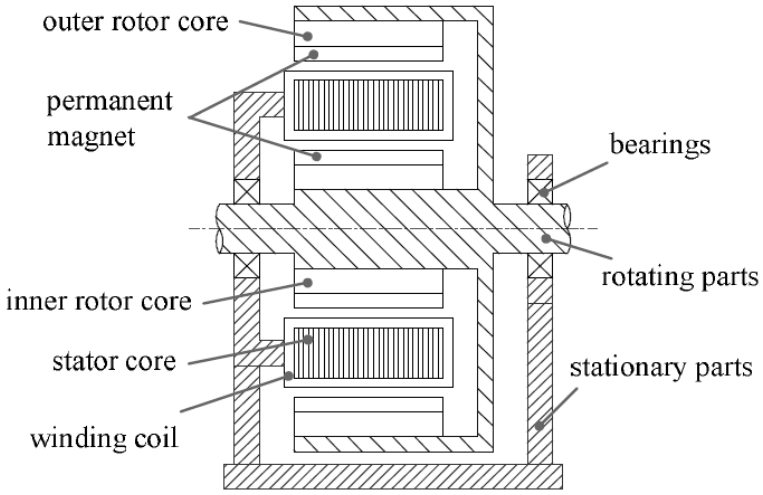

Figure 2-18 An air-gap wound RFPM generator with one stator and two rotors [47]

Goliath Wind Power, another new company based in Tallinn Estonia, has made use of this technique in 2008. In 2016, Goliath wind has signed a partnership with Indian's Steelite Engineering company to develop Capella 3.3MW wind turbine shown in Figure 2-17 [78] [79]. There are a number of interesting innovations in Goliath's work. The design is simple and modular, so it can be manufactured cost-efficiently locally, near to the site. The efficiency of this design is about 94%. The replaceable/redundant units and elimination of high risk components maximizes performance and facilitates localisation.

Considering the very large diameters required for Spooner design [67] to compensate the low airgap flux density, such a modification helps to increase shear stress in the machine without impractical size requirements.

Korouji [47][80] discussed air-gap wound RFPM machine with two rotors, as shown in Figure 2-18, in his thesis. Finite element methods were used for the design and optimization. The results showed high efficiency and low active material cost for this concept.

2.2.3. Axial Flux Permanent Magnet generators (AFPMGs)

The magnetic flux in an AFPMG crosses the gap in the axial direction, while the winding is installed in the radial direction as shown in Figure 2-19. A basic AFPMG normally consists of two discs: the stator disk with windings installed in the slots and the rotor disk with PMs installed on the surface.

Many AFPMG designs and configurations have been discussed in the scientific literature. AFPMGs can be classified depending on the electromagnetic configurations into three main categories [47]: slotted surface-mounted, slot-less with toroidal-stator (TORUS) and air-cored.

Slotted surface-mounted AFMGs, Figure 2-20, were discussed as better choice where compactness is more important for some applications [47][53][62][81][82]. However, this topology poses challenges due to the relatively strong balanced or unbalanced axial forces between the stator and the rotor; therefore, stiffer bearing arrangements and thicker rotor disks are required. Depending on the topology, a slotted surface-mounted AFPMG can have one rotor and one stator, Figure 2-20 (a), one rotor and two stators, Figure 2-20 (b), or two rotors and one stator, Figure 2-20 (c).

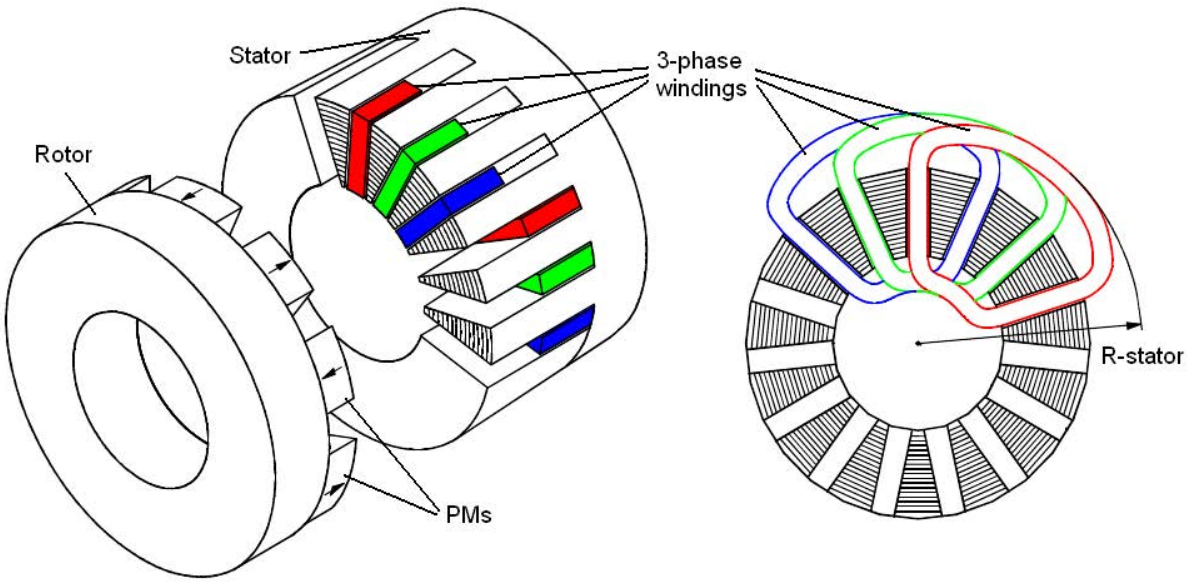

Figure 2-19 A slotted surface-mounted AFPM machine [53]

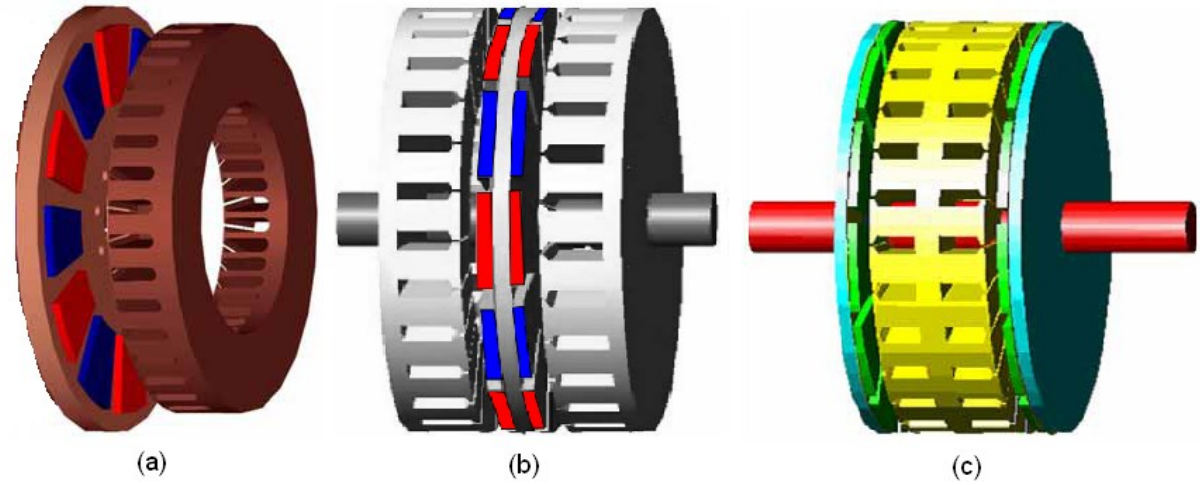

Figure 2-20 Slotted surface-mounted AFPM machines. (a) one rotor and one stator [62]**, (b) one rotor and two stators** [81]**, (c) two rotors and one stator** [82]**.**

The slot-less TORUS machine was introduced by Spooner and Chalmers in 1991 [83] [84]. It was initially developed for use in a portable generator providing low voltage DC output. The power density and machine efficiency were improved in this design by the short end-windings of the toroidal wound phases [62]. As shown in Figure 2-21, the machine consists of two rotor yoke disks with surface-mounted PMs and a toroidal stator, with a laminated steel tape and wound coils, between the two disks [85]. The stator windings in a TORUS machine can work safely under high electric loading because of the ensured natural cooling system by the rotor disks acting as fans [84]. The slot-less design reduces the magnetic forces which is of benefit to manufacturing and maintenance. Unfortunately, this comes at a cost – namely, the airgap magnetic flux density is lower due to a larger magnetic gap. The values of phase self and mutual inductances are low because of the slot-less winding with large magnetic gap [84]. The power to weight ratio of a TORUS machine tends to be quite high and suggests the possibility of scalability into the MW range [86].

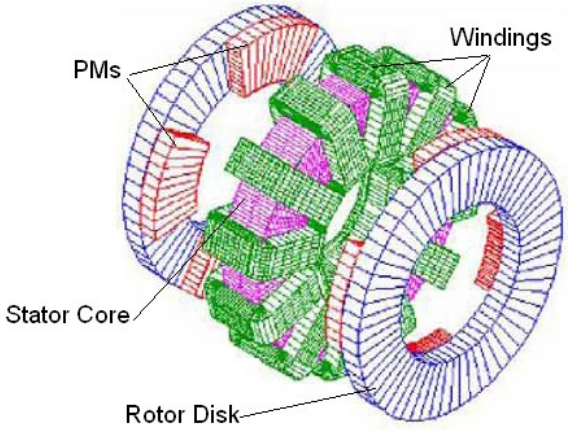

Figure 2-21 A slot-less TORUS machine [85]

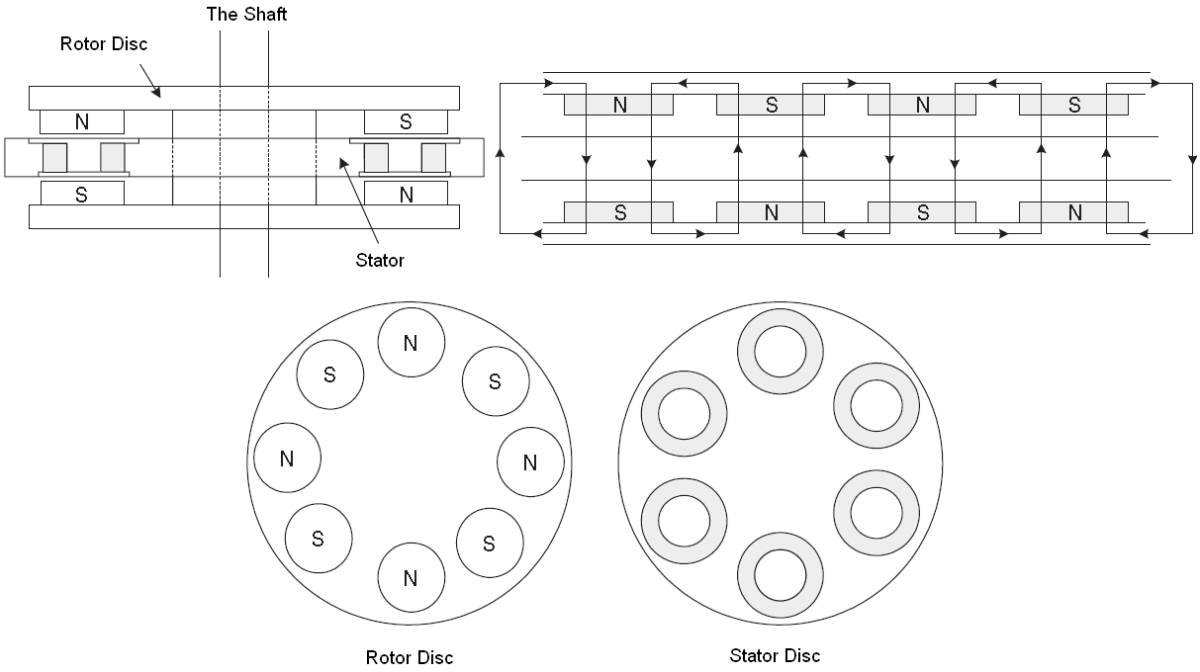

Figure 2-22 An air-cored AFPMG configuration [87]

Bumby and Martin [87] described in 2005 the design and development of an air-cored AFPMG for a direct-drive small-scale wind turbine. The design as shown in Figure 2-22 simply consists of a stator disc between two rotor discs. The stator is made of non-metallic non-conducting material (PVC or Tufnol) and has concentrated armature coils around its periphery. No axial magnetic forces exist between the stator and the rotor in this design because of the stator structure, which benefits manufacture and maintenance and there is no cogging torque. Such design, hence, is cost effective, reliable and simple to manufacture. Despite this, the design,

unfortunately, remains unproven. The high power density and lowered costs of this design suggest that scalability may be much less of an issue.

2.2.4. Transverse Flux Permanent Magnet generators (TFPMGs)

The path of the magnetic flux is perpendicular to the rotor rotation direction in TFPMGs. The ability to build TFPMGs with very small pole pitches, when compared with other types of generators, results in higher force density. Torque to active mass ratio in TFPMGs is relatively high because of the small amount of non-active copper winding compared with other generators [47].

However, TFPMGs configurations are complicated and hence exhibit high manufacturing cost. The cogging torque is high in TFPMGs resulting in high torque ripple [88]. The leakage inductance is also relatively large which causes low power factor in normal operation [89].

Two configurations were presented in [90] in order to reduce the torque ripple in the TFPMG. The approach used in the study aimed at eliminating certain torque waveform harmonics by symmetrical and asymmetrical stator element shifting. Both shifting methods, as shown in the paper, result in an almost sinusoidal torque curve.

TFPMGs can be classified into two main categories depending on the type of excitation, namely; electrically excited or magnetically excited.

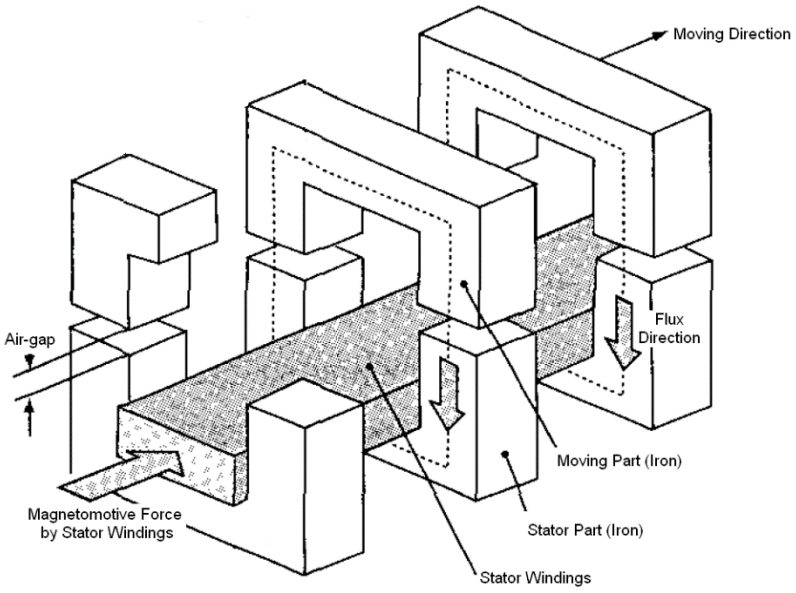

Figure 2-23 Basic configuration of electrically excited transverse flux linear machine [91]

A basic configuration of an electrically excited transverse machine is depicted in Figure 2-23. The primary magnetic flux is induced by the stator winding magneto-motive force. The flow direction of the flux is perpendicular to the direction of motion of the rotor relative to the windings [91].

Figure 2-24 shows a basic arrangement for a magnetically excited single-sided transverse flux topology. PMs are installed on a mover core and form the moving part or the rotor, which is separated from the stator part by an air-gap. The stator part in this basic topology is made up of C-shaped iron cores of laminated steel; the winding is inside the cores. A magnetically excited machine normally has a smaller moving part and lighter weight compared with an electrically excited machine [92].

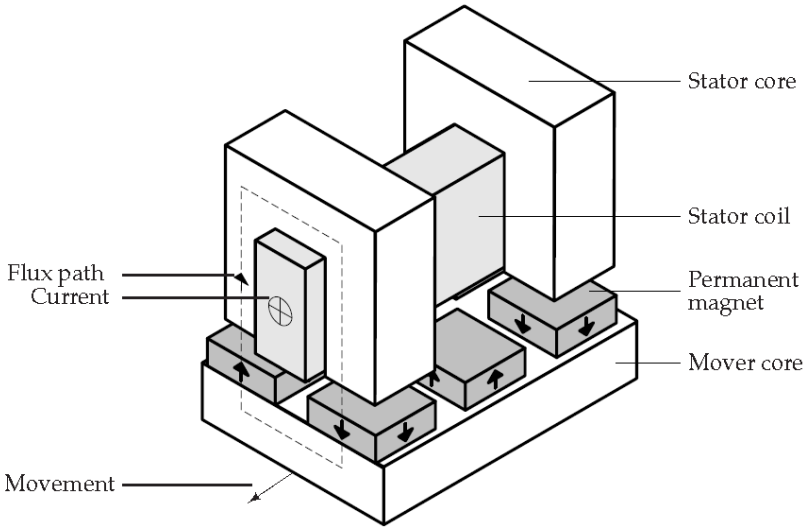

Figure 2-24 Basic single-phase TFPM topology[92]

There are a number of interesting works related to transverse flux machines. For instance, Bang *et al.* [93] focus on minimizing the mass of direct drive generators by making use of a ring

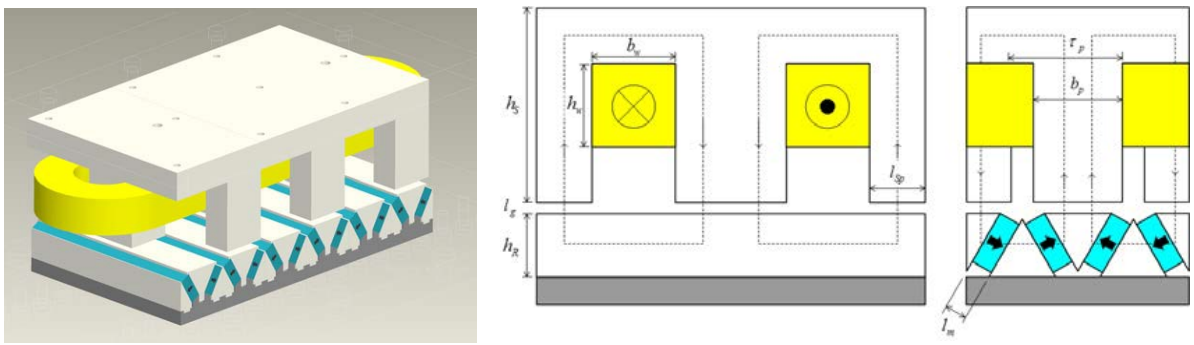

Figure 2-25 Bang et al transverse flux direct drive machine segment view. On the left a view of a single segment, on the right a cross-sectional view [93]

shaped axial flux TFPMG as shown in Figure 2-25. This generator addresses some key issues by proposing a design with the following characteristics: single-sided / single-winding with racetrack-shaped topologies ideal for large diameter machines, large iron core area claw pole configuration for higher induced voltage, reduced active material by decreasing slot pitch and height, segmented and modular structures for the rotor and stator for easy manufacture and maintenance.

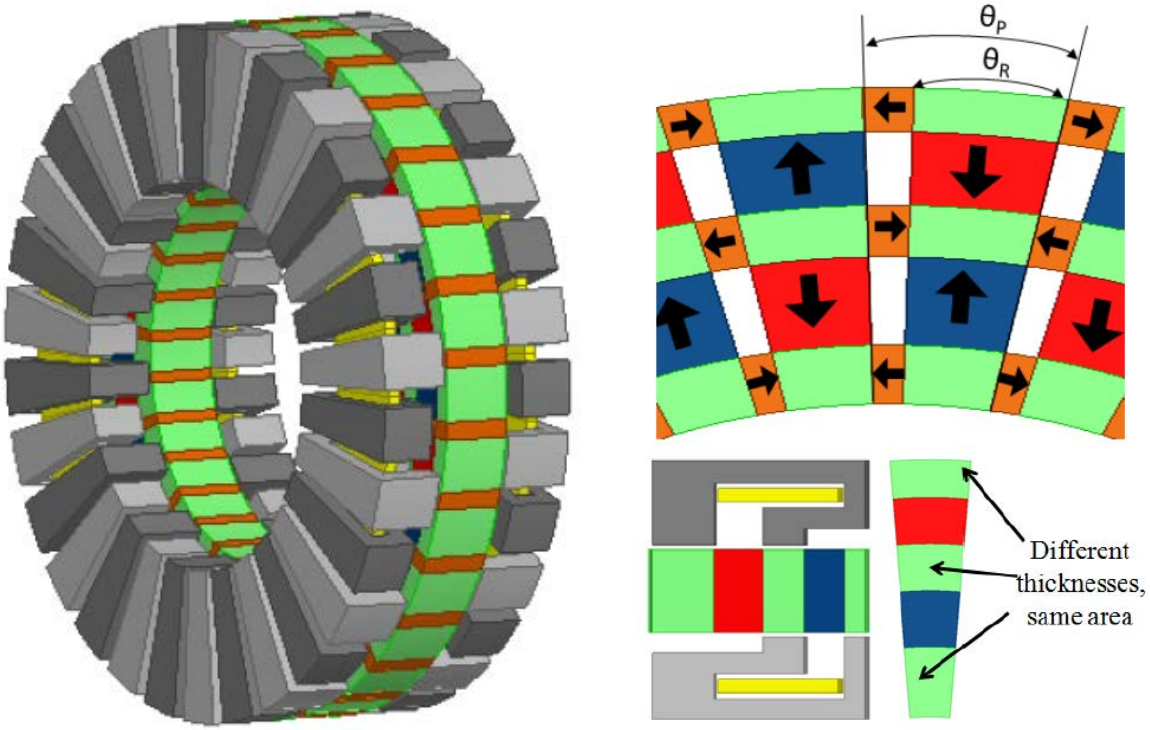

Figure 2-26 NREL halbach configuration based direct drive transverse flux machine. On the left a complete isometric view. On the right, a cross sectional top and side view of permanent magnets [94]

Another interesting design, presented by Wan *et al.* at NREL proposes a more complex geometry for the permanent magnet array while maintaining the modularity concept [94]. Specifically, it aims to combat the highly variable costs of rare earth permanent magnets by concentrating the flux of ferrite magnets using Halbach array configurations. The design is shown in figure 2-26.

2.3. Conclusion

According to the comparison of different types of PM generators, RFPM generators have been mostly installed in large direct-drive wind turbines due to their higher power density and the simple and stable structure design. In spite of the advantages of both AFPM and TFPM

generators, on the other hand, they have not been used for large direct-drive wind turbines yet and their designs require more development and research. AFPM generators have simpler winding, lower cogging torque and noise, and a higher torque/volume ratio than RFPM generators. TFPM generators have high force density, simple winding and low copper losses. The main drawbacks for AFPM generators are the large outer diameter with a large number of PMs and the lower torque/mass ratio, whereas, the relatively complicated construction with large air-gap is the main disadvantage for TFPM. Iron-cored surface-mounted RFPM generators are commonly used in large direct-drive wind turbines. Other stator designs for surface-mounted RFPM generators, however, have many advantages and ready to be widely commercialised.

In terms of large scale wind turbine applications, we note that among the various generator types, transverse flux varieties remain in early stages of development. While excellent for high power to weight ratio, they struggle with issues of complexity and associated manufacturing challenges. This means that they are likely to be less suited to large MW scale applications. Axial varieties likewise require stiffer structural consideration to account for the axial topologies. In comparison, radial flux permanent magnet machines provide a relatively simple solution with ease of manufacture and further simplicity in analysis.

Chapter 3. Review of Rotor Eccentricity and Unbalanced Magnetic Pull

3.1. Introduction

An electrical machine produces both tangential and radial electromagnetic forces. In a radial flux permanent magnet RFPMG machine (see section 2.2.2.), the tangential force generates a beneficial rotating torque while the radial force produces wasted torque. In theory, the radial electromagnetic forces in a perfectly centred rotor in a symmetrical RFPMG machine are cancelled out and the machine generates zero net radial force. In practice, however, a net radial electromagnetic force always exists and most machines run with some degree of rotor eccentricity.

This chapter provides a literature review of different types of rotor eccentricities in generators for wind turbine applications and concentrates on the induced unbalanced magnetic pull (UMP) as the main outcome of this eccentricity. General causes and consequences of air-gap eccentricities in wind turbine generators are reviewed in section 3.2. Analytical, numerical and experimental methods for calculating and measuring the UMP in the literature are reviewed in section 3.3.

3.2. Rotor Eccentricity in Wind Turbines

Electrical machines are designed to have as small air-gaps as possible in order to optimise performance and hence reduce magnetic losses (see section 4.6.). Any offset of the rotor from the stator bore can be considered as a serious problem as it generates a net radial force or UMP that increases the eccentricity. Severe damage to both stator and rotor; therefore, can occur when the eccentricity produces high UMP resulting in contact between the rotor and the stator. UMP is not the only result of rotor eccentricity, increasing the magnitude of air-gap magnetic field harmonics or generating extra harmonics can also cause issues. The mutual cause and effect relationship between rotor eccentricity, bearing wear, and rotor shaft deformation means that rotor eccentricity can be the root cause for other failures.

Rotor eccentricity in electrical machines can be a result of many reasons. Low manufacturing tolerances, which relate strongly to lower machine costs, lead to a decrease in the uniformity of the air-gap and some degree of eccentricity. The greater the tolerance, the lower the

performance and the efficiency of the machine. Rotor shaft bending and bearing wear are also the main reasons for the varying degree of rotor eccentricity [95].

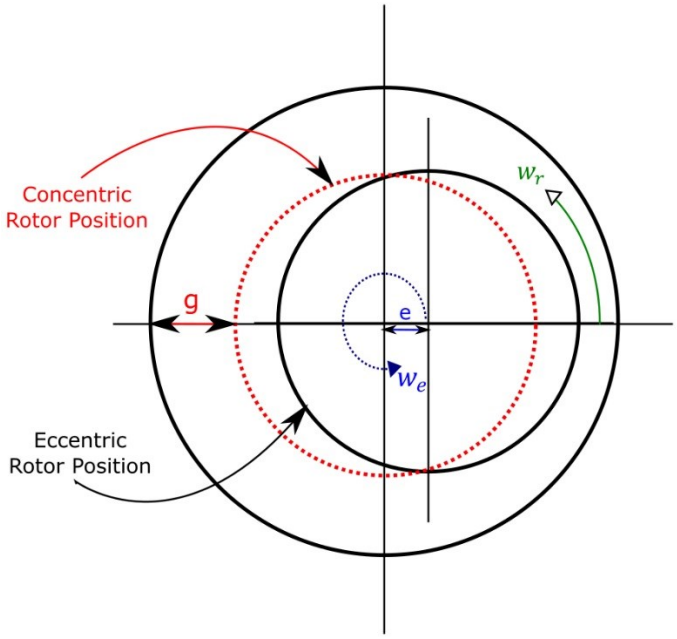

Figure 3-1 Schematic drawing for a rotor eccentricity

Several types of rotor eccentricities can be distinguished[96]. Static, dynamic, and mixed rotor eccentricities are the main types considered in the literature. Figure 3-1 shows a schematic drawing for the rotor position inside the stator bore before and after a dislocation. Here the value w_r is the rotor rotational speed around its own axis, g is the uniform mechanical air-gap length when the rotor is concentric, e is the rotor eccentricity and w_e is rotor axis rotational speed around the stator axis.

Ideally, the rotor should be concentric and its rotational axis is identical to the stator bore axis, i.e., $e = 0$. However, when the rotor is rotating around a shifted axis relative to the stator bore axis, by some fixed distance e, then a static eccentricity is said to exist. Essentially, static rotor eccentricity occurs when $e = constant$ and $w_e = 0$.

If the rotor rotational axis is not stable and moving around the stator bore axis with constant angular velocity w_e and constant distance e the scenario illustrated in Figure 3-2 occurs. The eccentricity can be considered as a uniform dynamic eccentricity. The value w_e is normally less than or equal to the rotor angular velocity w_r.

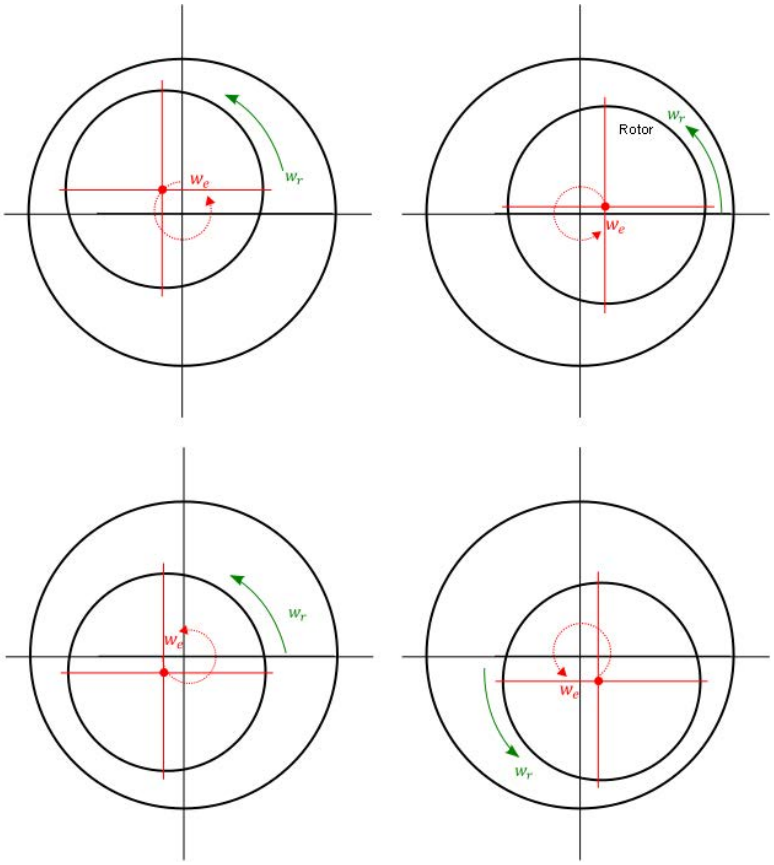

Figure 3-2 Schematic drawing for dynamic eccentricity

The most realistic rotor eccentricity type is a mix of static and dynamic variants. In such scenarios, the variable, e, changes over time. As long as $e(t) < g$, there is no severe or catastrophic failure as a result of contact between the rotor and the stator. Bearing wear, however, is a possibility where $e(t) > 0$, and one expects increasing wear with larger $e(t)$ values.

3.3. Unbalanced Magnetic Pull

When the rotor in an electrical machine is eccentric, a net radial force is generated. This force pulls the rotor off-centre leading to an asymmetric load on the bearings. As noted earlier, such a force is referred to as unbalanced magnetic pull (UMP) [97]. UMP can be classified into two main types. Extrinsic UMP is the first type, which could be caused by the inaccurate assembly of the generator's components leading to eccentric rotor positioning. It could also be induced by a component's quality – for instance, issues such as the asymmetric magnetization of magnets , inaccurate magnet placement and incorrect dimensions of the stator bore [98]. Intrinsic UMP is the second type, which could be the result of the electromagnetic forces resulting from coil energization. This UMP occurs regardless of whether motor or generator

components are perfect. Intrinsic UMP can be avoided by using an even number of magnetic pole-pairs and even slot numbers [99]. The history of electrical machines shows many different approaches developed for the analysis of magnetic fields and electromagnetic forces under eccentric conditions. Analytical, numerical and experimental methods are the main ways these can be categorised.

3.3.1. Analytical methods

There are a number of analytical approaches to calculate magnetic fields in generator systems. These approaches can roughly be divided into analytical and numerical approaches. Here, for the moment, primary focus will be given to analytical approaches. Numerical approaches will be discussed later in this chapter, but it should be noted that numerical methods may intersect with analytical approaches and further than analytical approaches may be augmented by semi-empirical requirements.

Among analytical methods, solutions can be roughly divided into four main approaches, namely: the Maxwell stress tensor approach, the co-energy approach, the rate of change of field energy approach and the Lorentz force approach [100].

The use of analytical methods to determine magnetic fields and associated forces, can be a tool for understanding UMP. The causes of UMP have been studied extensively and a number of computing models have been developed to analyse UMP specifically. A review of UMP in electric machines was published as early as 1918 [101]. Rosenberg [102] in 1918 used $B-H$ curves of the eccentric rotor machine to quantify the UMP by calculating the difference in the air-gap magnetic flux densities over opposite poles. The magnetisation curves were used to extract flux densities. In his paper, Rosenberg noted the effect of UMP on critical speed as an important issue to consider in machine design. He also mentioned that a displacement of the machine's rotor and stator centres might occur because of uneven thermal expansion even if they are concentric when the machine is cold. Rosenberg's paper, as a pioneer UMP piece of work, was used as a reference in most UMP research in the future. With the advent of computational fluid dynamics (CFD), however, it became possible to take his work on thermal expansion significantly further. The use of high speed computers to perform the required thermal design calculations gave a better illustration of UMP related effects and allowed for more accurate designs.

Robinson [103] in 1943 analytically calculated the induced UMP in a synchronous motor from static rotor eccentricity effects. He used the same model developed for an induction machine adding a new factor considering the difference in magnetic field shape between the two machines. Robinson, basically, implemented the same method used by Rosenberg, which simply calculated the UMP as a product of the magnetic flux density squared, stator bore area, and a certain factor that takes into account the different shape of synchronous and asynchronous magnetic fields.

Although there have been many papers published on UMP in electrical machines, with some dating back more than a century, the theory of UMP was basically developed in 1955 by Summers, using rotating field components in a two-pole induction machine [104]. He concluded that static and dynamic UMP induced by motor deformation and rotor irregularities respectively generate a vibration pulsation in the machine, an effect similar to torque ripple in some ways. A number of procedures to be followed in order to eliminate vibration pulsation were introduced in his paper. The rotating field method of modelling machines, which was initially developed by Summers, can be considered as the most common way of predicting UMP.

Subsequently, Frohne [105] carried out an extensive study in the field, concentrating on the induced magnetic field harmonics resulting from rotor eccentricity. UMP occurrence, according to Frohne, is a result of the interaction between fundamental magnetic field components with magnetic field harmonics. A graphical representation is shown in [106].

3.3.1.1 Conformal Transformation

Given the radial geometry of the generator stator and rotor being analysed, there are significant challenges in the calculations of air-gap fields. Air-gap MMF is usually assumed to be sinusoidal in the air-gap permeance method. This assumption can be considered as a poor approximation in case of rotor eccentricity. A key approach that is used to make these calculations somewhat simpler and more accurate involves the use of conformal mapping and transformation. The conformal mapping technique transforms the machine from being magnetically asymmetric to one which is magnetically symmetric but electrically asymmetric (non-uniformed winding distribution). A simple depiction of this form of transformation is shown in Figure 3-3 below [107]. The main idea is finding a transformation matrix that gives a relationship between Z-Plane and T-Plane. By finding proper values of d in Z-Plane and c in T-Plane, the eccentric rotor machine represented in Z-Plane can be mapped onto the T-Plane

using the transformation matrix as two concentric circles. The slotted pattern in T-Plane will become irregular, so the method accommodating conformal transformation technique must be capable of dealing with asymmetrical windings. The machine represented in the T-plane can be used to find an impedance matrix linking the stator currents and the terminal voltages. A detailed explanation of conformal transformation techniques is given by Dorrell and Smith [108].

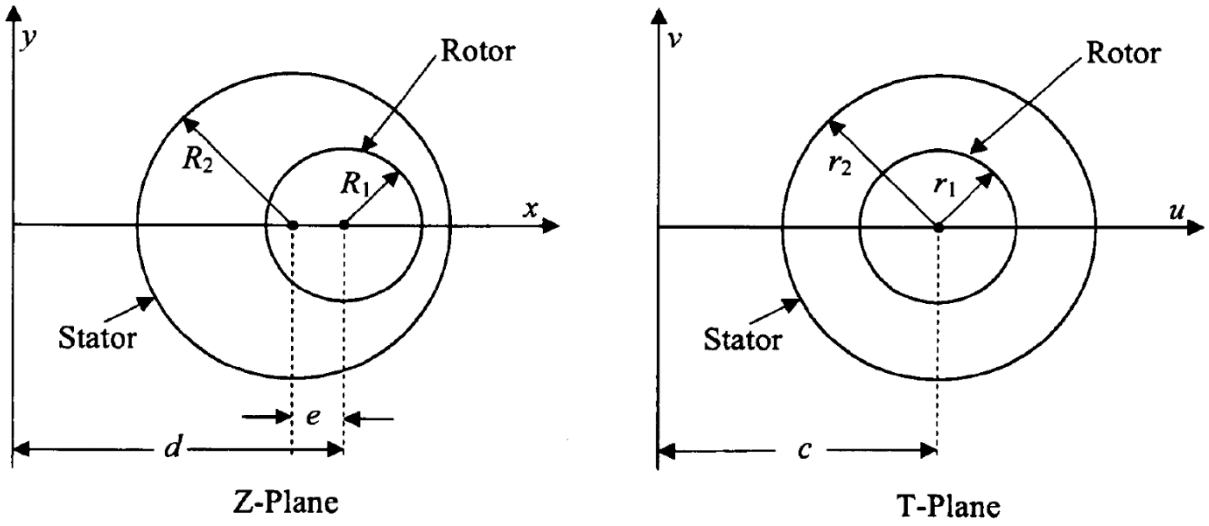

Figure 3-3 Conformal transformations between Z-Plane and T-Plane [107]

Starschich *et al* [100] utilize this approach to model magnetic fields in 3 phase permanent magnet machines. They note a specific application to BLDC style machines by expanding the Maxwell stress tensor approach (see subsection 5.2.3.) with conformal mapping.

Swann [109], more relevantly, developed a method to calculate magnetic fields in the air-gap of non-salient-pole machines with eccentric rotors. Conformal transformation was used to relate the eccentric annulus of the air-gap to a concentric air-gap annulus when the rotor is displaced. The goal here was to calculate the complex magnetic potential at any point in the eccentric air-gap. Simplifying assumptions were applied in this method and the basic case of an idealized concentric machine was considered first.

3.3.1.2 Harmonic Analysis

Understanding the spatial harmonics and amplitudes in the air gap are particularly important and can lead to a greater understanding of magnetic noise and harmonic torque related issues.

Williamson in the 1980s published a few papers with different co-authors [110]–[115] introducing a generalised harmonic analysis method. This method uses the calculation of

coupling impedances to relate voltages across windings to the currents flowing within the machine. Williamson's publications showed success in studying faults in stator winding and rotor cages using the generalised harmonic analysis. Dorrell and Smith in 1994 [108] presented a general analytical method for determining the induced UMP in induction motors using both Williamson's generalised harmonic analysis and Swann's developed method. The effect of using parallel stator winding paths on reducing the induced UMP because of rotor eccentricity was investigated and the results proved a significant reduction of the unbalanced winding currents, which means less UMP.

Some machines make use of multiple layers of air gap. Such machines make use of multiple stators and rotors and may not have iron yokes – the high axial force in iron cored machines of this nature produce high forces and increase mechanical complexity, as demonstrated in the earlier chapter. However, the multiple air gap (MAG) machines (see 2.2.2.2) can lead to somewhat different considerations from a harmonic analysis point of view. Valavi *et al* [71] take these considerations into account and discuss details of MAG machines.

3.3.1.3 Air-gap Permeance

In 1996, Smith and Dorrell published a paper [116] introducing a novel analytical model to calculate UMP in cage induction motors with eccentric rotors. The model was basically based on Williamson's general harmonic method [110] and used an air-gap permeance approach including stator and rotor magneto-motive force (MMF) harmonics. The effect of rotor load currents and different types of stator winding connections can be accommodated in the model to give more accuracy. Rotor skew and high order winding harmonics were found to have influence on UMP magnitude. The model, on the other hand, did not take saturation or slotting permeance into account. Experimental verification of the method was provided in [117].

This approach was taken further by Misir *et al* [118]. Noting the importance of harmonic analysis, Misir *et al*, thus take the idea of air-gap permeance based analysis even further by making a more integrated harmonic analysis for existing analytical models. Their model further explicitly takes into account slotting related issues. Generally, such issues are difficult to model with an air-gap permeance approach as they make calculations challenging at the edge of the poles of the machine. In order to account for this an empirical function is introduced for the slot region with calculations for pole shoe being performed separately. The resulting permeance calculation then uses the superposition of the two for an estimate. A Fourier representation is then used to incorporate aspects of frequency and harmonic modelling.

A further attempt by Ilhan *et al* [119], notes a similar discontinuity problem with slotting in doubly salient pole machines. The approach taken, rather than working with an empirical model, focuses more on discretizing the discontinuous air gap region. They particularly choose this approach because of the challenges noted in the previous approach by Misir *et al*. The work examines the use of semi-discrete spatial methods, namely the Schwarz-Christoffel (SC) mapping approach and the Tooth Contour Method (TCM). These methods are specifically designed for the analysis of doubly salient machines. In addition to this, attention is given to the traditional spatial discrete method as embodied by modern day finite element analysis (FEA). A further discussion of FEA is provided later in this chapter.

Li *et al*. [120] in 2007 introduced an analytical model to calculate UMP and cogging torque in slotted PM motors under rotor eccentricity situations. Static and dynamic rotor eccentricity were analysed using the model. Computed results were used to verify the analytical results of the model. An orthogonal coordinate system was used to find the distorted flux density distribution. The main step was deriving the relative permeance function by solving the Laplace field problem associated with the motor structure. A conformal mapping technique was also used in this circumstance and was originally introduced by Swann [109] in 1963 for a slot-less (non-salient-pole) machine structure.

3.3.1.4 Rotor Cage Skewing & Damper Windings

When discussing analytical approaches to computing UMP, situations where the machine is modified to adjust for this unbalanced pull must also be discussed. One such adjustment may take the form of damper windings [121]. Such windings tend to be found in the rotor poles of synchronous machines and into slots as short circuits in induction machines. Especially in induction machines, the rotor squirrel cage can also be regarded as damper windings and in some cases act more effectively in reducing UMP [122]. The two approaches are shown in Figure 3-4.

Since 1993 [123], Dorrell has been publishing valuable papers with different co-authors such as [106], [117], [122], [124]–[134] in the field of UMP estimation. In [95] and [105], Dorrell examined the influence of rotor cage skewing on the UMP. The magnitude of the induced UMP in a loaded machine was proven by Dorrell to be increased with skewed rotors, whereas, the skewing effect on the UMP can be disregarded under no load conditions.

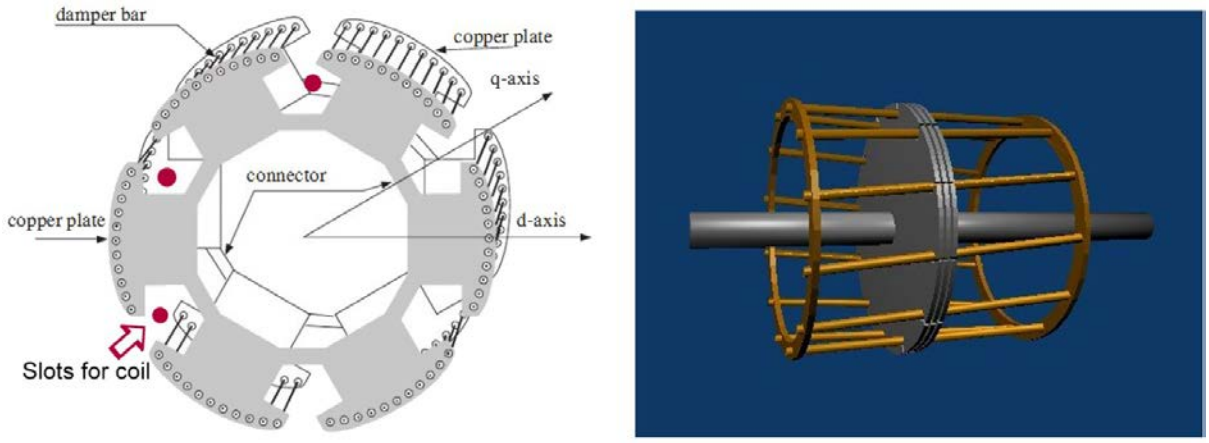

Figure 3-4 Damper windings (left), squirrel cage rotor skew (right) [121]

In most of his publications, Dorrell used the Maxwell stress tensor method and rotational field theory to calculate the UMP and present analytical models to investigate all types of rotor eccentricities in a wide range of electrical machines. In [126], Dorrell *et al.* investigated the possibility of reducing the UMP and the bearing wear using damper windings in induction machines. The study showed a significant damper windings effect on the UMP in wound rotor induction machines. Such damper windings were less effective under certain circumstances in cage induction machines. Damper winding effects in synchronous machines were investigated by Burakov and Arkkio [136][137]. Dorrell [130] used a permeance factor λ_{ecc} to represent the eccentricity in a PMSG as a function of the air-gap length.

3.3.1.5 Modelling a Change in Air-gap Length

Other studies have looked at specifically modelling changes in air gap length and as a result related eccentricity. Airgap length calculation can be considered as the first step requires in any analytical model because calculation the instant airgap length is a condition to calculate magnetic fields required to calculate UMP.

Kallaste *et al.* [138] in 2012 investigated and analysed the causes for static, elliptic, dynamic, and mixed rotor eccentricities in a slot-less permanent magnet wind turbine generator. Figure 3-5 (a) shows a schematic drawing for the considered slot-less PMG. Basic analytical equations were developed for calculating the eccentric airgap length and UMP. A 5 kW prototype machine, as shown in Figure 3-5 (b), was built to perform experiments in order to verify the analytical methodology.

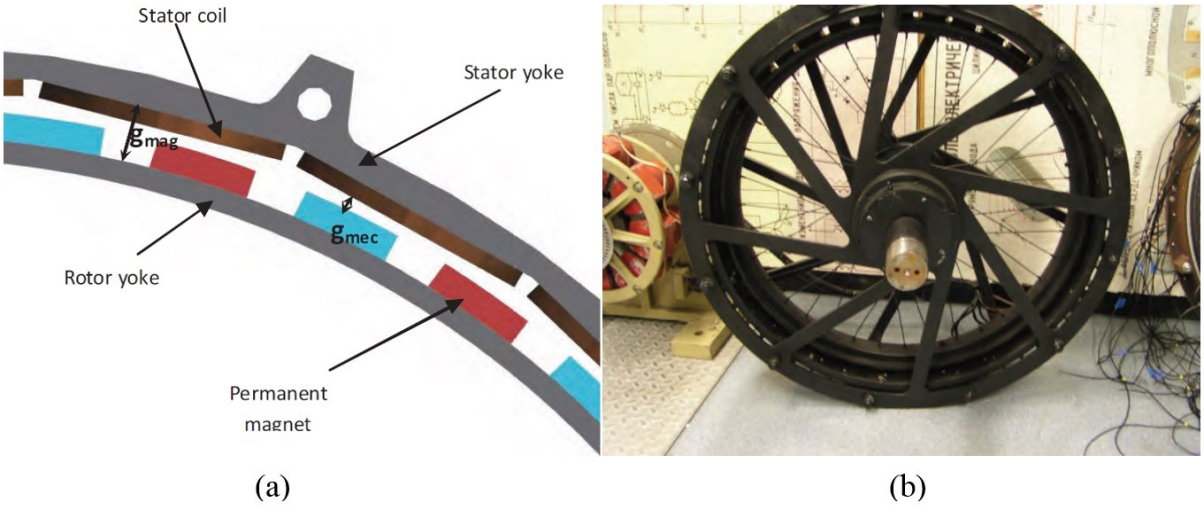

Figure 3-5 (a) Slot-less PMG schematic construction drawing (b) Photo of the constructed 5 kW prototype machine [138]

Results showed one difference between static and dynamic eccentricities, which is additional vibration in the generator. Extra stresses were found to be induced by all types of eccentricities on the generator structure. Such stresses have to be taken into account in the design process of the generator mechanical support. Similar to iron-cored PMGs, a linear relationship between the UMP and the rotor eccentricity was found in this research.

3.3.2. Numerical methods

The dramatic computational development in the last few decades significantly helped solving complicated mathematical and numerical problems, and widely spreading numerical calculation techniques. Regarding the UMP issue, the Finite Element Method (FEM) is still the dominant paradigm used in engineering analysis software to solve electromagnetic problems. FEM is a general numerical technique that is used to find approximate solutions for differential and integral equations. There are a few other numerical methods such as Finite Volume Methods, Boundary Element Methods, Finite Difference Methods, Spectral Methods, and Meshless Methods. Chari and Silvester [139] have published a comprehensive reference from the 1980s for the basic FEM principles and applications for electromagnetic fields in electrical machines.

3.3.2.1 Finite Element Method

The basis of FEM is the need to solve problems with complex geometries taking material characteristics into account, where there is no easy analytical solution. The primary means of doing this numerical solving is via discretization. The process consists of three main steps:

simplification of the real world into an ideal physical model, generation of a core mathematical model, and discretization of the model into a mesh [140] as shown in Figure 3-6.

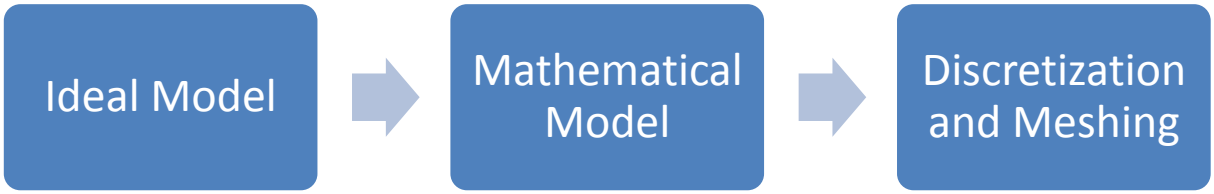

Figure 3-6 The steps involved in the Finite Element Method

The main advantages of FEM include the ability of handling complex geometry and varying boundary conditions, the possibility of generating a general code that handles different types of problems. The fact that there are many tested and easy to use software packages with user-friendly interfaces also helps make it an excellent solution.

A detailed treatment of FEM aimed at electromagnetic problems has been provided by a number of authors. For instance, Bastos *et al.* [141] provide a general explanation. More detailed and specific explanations are available for induction machines in Williamson *et al.* [142].

Arkkio has published several research papers based on numerical solutions of magnetic vector potential for analysing induction machines [143]–[147]. In his thesis [143], Arkkio assumed the magnetic field to be two dimensional and used a finite element method to discretize the two dimensional magnetic field formulation. The induction machine was divided into slices and the magnetic field of each slice was solved separately by the two-dimensional step-by-step model. This two-dimensional sliced model considers three dimensional features of the induction machine in some cases as well. For example, the end windings were modelled in the voltage equations as constant impedances, the machine was divided into slices and the winding currents were assumed to be continuous from slice to slice.

Arkkio found that the step-by-step method was a very time consuming calculation so he significantly decreased the computational time by introducing a simplified method that assumes sinusoidal field quantities despite the core materials and rotor rotation nonlinearity. Step-by-step methods and later simplified methods showed very close results, however, the measured and computed results had about 15% disagreement. Fortunately, this disagreement could be careful accounted for by the various simplifying assumptions of the analysis.

Later on, Arkkio [144] extended the numerical model to include UMP from static and dynamic rotor eccentricities, broken rotor bars, and varying rotor slot numbers. More attention was given to the effect of parallel branches in the stator winding, saturation, and machine loading. As a result, it was shown that a motor with closed rotor slots generates more UMP than the semi-open slots motor for same rotor eccentricity. Arkkio *et al.* in [145] studied the UMP acting on a whirling cage rotor 15 kW four-pole induction machine, shown in Figure 3-7 (a), using time-stepping FEA.

The machine was equipped with calibrated active magnetic bearings to allow the generator of a whirling motion and measure the induced UMP. Figure 3-7 (b) shows the axial rotor geometry of the test-rig. Good agreement was shown between the measured and the numerically computed UMP results, which verified the proposed UMP calculation method and implied that a simple UMP model can be used as a first approximation when studying the UMP effects.

In 2010, Arkkio *et al.* [146] introduced a new method for modelling a rolling-rotor electrical machine within FEA. The rolling-rotor machine works with no bearings, where the rotor rolls along the stator bore. The rotary motion is generated by the magnetic field and force produced from the stator windings. The magnetic force F_{em} also maintains the contact line between the rotor and the stator and the friction has to be large enough to prevent slipping. Figure 3-8 (a) shows the operation principle of the rolling-rotor machine, where F_r, F_t are the radial and tangential friction forces. The geometry, stator windings, and magnetic field of the machine equipped with five-phase stator winding are shown in Figure 3-8 (b). The load angle δ defines the phase of the excitation with respect to the rotor position. The new method used an element structure of radial bands in the airgap for modelling the motion instead of the conventional moving band technique. A prototype machine, as shown in Figure 3-8 (c), was constructed to validate the numerical method results.

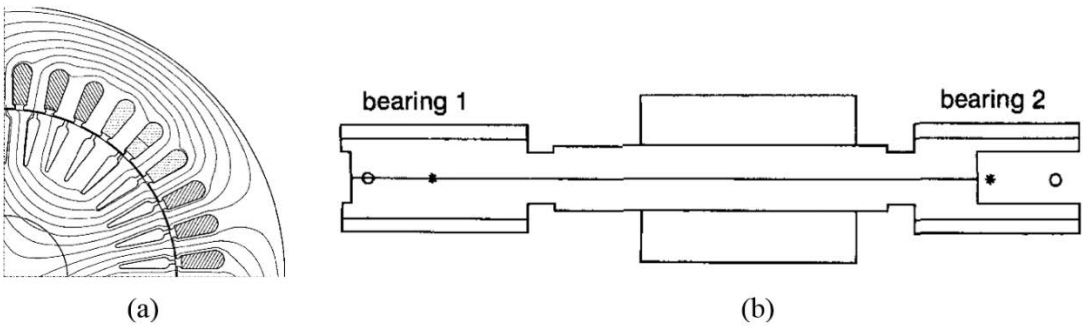

Figure 3-7 Arkkio et al. (a) Cross-sectional geometry of the 15 kW cage induction machine, (b) Axial rotor geometry of test machine. Where (*) centres of bearing magnets, (o) centres of position sensors [145]

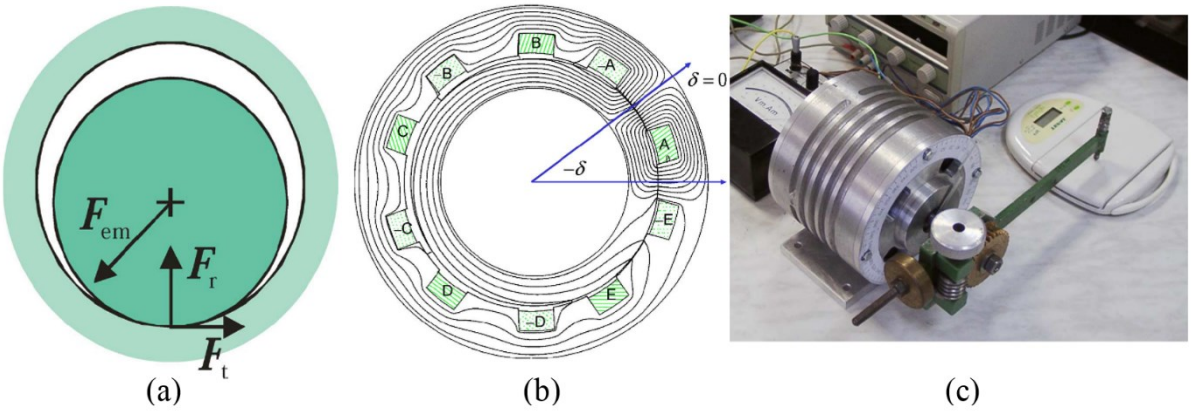

Figure 3-8 (a) Operating principle of the rolling-rotor machine (b) Geometry of the prototype with 99% eccentricity (c) The machine prototype under a static test [146]

In [148], Michon *et al.* used finite element analysis to determine and compare the UMP induced in a permanent magnet generator and a wound field synchronous generator. Both generators have similar power (3 MW), speed (365 rpm), airgap diameter (1.24 m), airgap length (1.24 mm), number of pole pairs (8), and airgap flux density to allow comparison. The results exhibited a linear relationship between the average UMP and the rotor eccentricity in both generators, in both no load and load cases. The load effect on average UMP was shown to be insignificant. This was explained as being a result of the relatively small armature reaction field. This small reaction field, itself, was a result of a large effective airgap in the permanent magnet generator and the saturation in the smallest airgap regions of the wound field generator. For a similar rotor eccentricity, the induced UMP in the wound field generator was found to be about three times the UMP value in the PM generator. The authors attributed this higher UMP to the smaller axial length and larger effective PM generator airgap. This air-gap is the sum of the physical airgap length and the magnet height, the so-called magnetic gap. Furthermore, the results showed significant UMP effect on shaft deflection and bearing wear. Only static rotor eccentricity in the gravitational direction was considered in this research, which over simplifies the model.

3.3.2.2 Other Numerical Methods

A number of numerical methods other than FEM were noted earlier in this section. The first of these is the Finite Volume Method (FVM). FVM remains somewhat in their infancy when compared to FEM. The method is based on Maxwell's curl equations, with integrations taking place over some volume. A key advantage of this process is that it can be applied to virtually any polyhedral mesh structure and works well across changing mesh structures [149]. There

has been very little research looking into solving UMP related electromagnetic problems using FVM. This is an area for a future research.

Another approach is the Boundary Element Methods (BEM). One of the challenges with FEM has been its slow computational processing for many engineering problems The BEM approach attempts to resolve this issues especially for infinite domain models and models with high stress concentration [150]. Solutions tend to be more accurate under these conditions as well, when compared to other techniques. The BEM approach generally works by modelling the object boundaries only. As with the FVM technique, little research appears to be done with regards to UMP. Generally, the mathematics associated with the method remain relatively unfamiliar.

The Finite Difference Method (FDM) attempts to approximate the differential equations in our UMP model as a finite difference, making it an extremely simple implementation. This simplicity comes at the cost of inaccuracy however. FDM solutions have had some application to electrical machine modelling for hydroelectric application [151]. Yet, given that software is often available for FEM, these solutions are used less often for electromagnetic solutions.

Two other final approaches for numerical analysis are Spectral Methods (SM) and Meshless Methods (MM). Both these methods are rarely used. The first of these makes use of Fast Fourier Transforms (FFT) while the second eliminates the mesh and instead focuses on the interconnectivity of nodes. Mesh free approaches are useful in dynamic simulations.

3.3.2.3 Combining Electrical and Mechanical Models

A particularly challenging aspect of UMP is the need to combine mechanical and electrical models together. The mutual coupling of these models plays a significant role in the overall behaviour of the system. A few researchers have made attempts at this coupling in the past.

For instance, in 1982, Fruchtennicht *et al.* [152] developed an analytical model of the rotor interacting with the stator under circular whirling action. Largely this work was confined to squirrel cage style induction machines however. This work was developed further to produce a model for a two pole induction machine by Belmans *et al.* [153]. Essentially Belmans treated the relationship between the rotor and stator as a damped spring system with electromagnetic coupling. Unfortunately, neither approach has been particularly successful at modelling real systems.

At this stage it would be prudent to point out the work of Guo *et al.* [154] Here there is some return to the idea of making use of air-gap permeance and harmonic analysis. A vibratory model was used to look at a wide variety of pole-pair configurations and demonstrated some success. The ideas of Guo were taken further by Holopainen *et al.* [155] to extend his work to a parametric force model. The resulting quasi-displacement interactions of this model had some link to damping, stiffness terms and the basic motion equations and associated circulatory terms.

3.3.3. Experimental methods

Unlike the analytical and numerical studies, the difficulty in creating and measuring UMP has limited experimental studies. A few techniques, however, were developed for measuring the UMP. Load cells were used in [97] to support bearing housings in order to measure the UMP. Whereas, a piezoelectric force table was used in [117] to measure the forces between the stator and rotor by mounting the stator on the table and supporting the rotor separately. The radial displacement of a flexible shaft was applied in [156] to assess the degree of UMP.

From 1968-1971, Bradford and Rai [97][157] from the Electrical Research Association ERA carried out broad studies concentrating on building equipment to accurately measure the rotor eccentricity. Strain gauges were used within the bearing housing in order to measure the induced UMP. A 6-pole 10 kW induction motor was built for a chain of steady-state and transient experiments of the UMP magnitude. The measurements indicated a critical magnetic circuit saturation effect on UMP value. The experiments also concluded that the UMP magnitude in the wound-rotor motor is much higher than the cage-rotor motor that damps the UMP. Inaccuracy in predicting the transient UMP during starting was noted after making use of analytical models. For considerable time after publication, the studies offered the best available experimental data for rotor eccentricity based UMP. However, experiments did not investigate the effect of parallel stator winding configuration on UMP which resulted in a significant UMP reduction as proven later by Dorrell and Smith in 1994 [108] and more investigated by Burakov and Arkkio [158][137].

Belmans *et al.* [156] in 1987 used the assumption that a constant UMP acts as an electromagnetically induced spring constant and electromagnetically induced damping coefficient, which result in a lowering of the electromagnetically influenced natural frequency and the electromagnetically influenced total damping ratio respectively. The radial rotor vibrations become unstable when the total damping ratio is negative. It was suggested that

lowering both the electromagnetically induced spring constant and damping coefficient, and therefore stabilising the vibrations can be achieved by using nonmagnetic end shields or by installing nonmagnetic rings surrounding the machine bearings. The test was limited for a homo-polar 10 kW induction machine as shown in Figure 3-9(a). External rotor eccentricity was not mechanically applied to the motor but the vibration, slip and eccentricity were increased by increasing the rotational speed. When studying the stability of this vibrational method, the airgap flux density was linearized by assuming a very small rotor eccentricity as a percentage of the airgap length., A figure of this setup is shown in Figure 3-9(b) where a coil on the end shield was used to measure the flux density. The study concluded that the radial rotor vibrations become unstable when the ratio of the induced electromagnetic spring constant and the induced electromagnetic damping coefficient is negative.

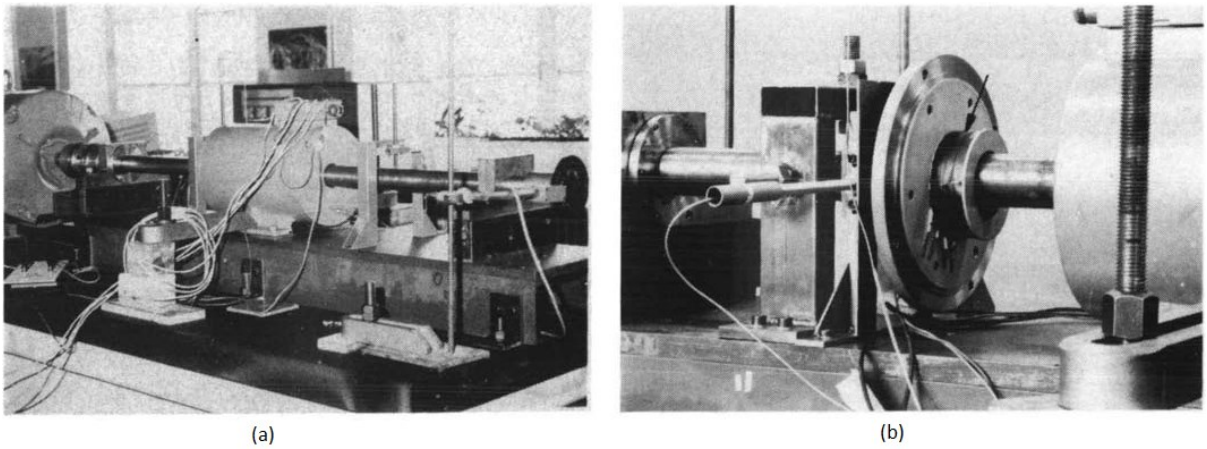

Figure 3-9 Test-rig with 10 KW motor introduced by Belmans *et al.* in 1987 where (a) The machine model, (b) Coil on the end shield for measuring the homo-polar flux [156]

Mueller [159], Williamson *et al.* [114][111], Dorrell and Smith [117], and other researchers used piezoelectric transducers to directly measure the UMP. The main idea was to support the rotor separately and place the stator, through the piezoelectric transducers, on a mounting table for measurement. This experimental method is the most common one to measure induced UMP from different causes such as pole changing in two-speed motors [159] and broken rotor bars [111].

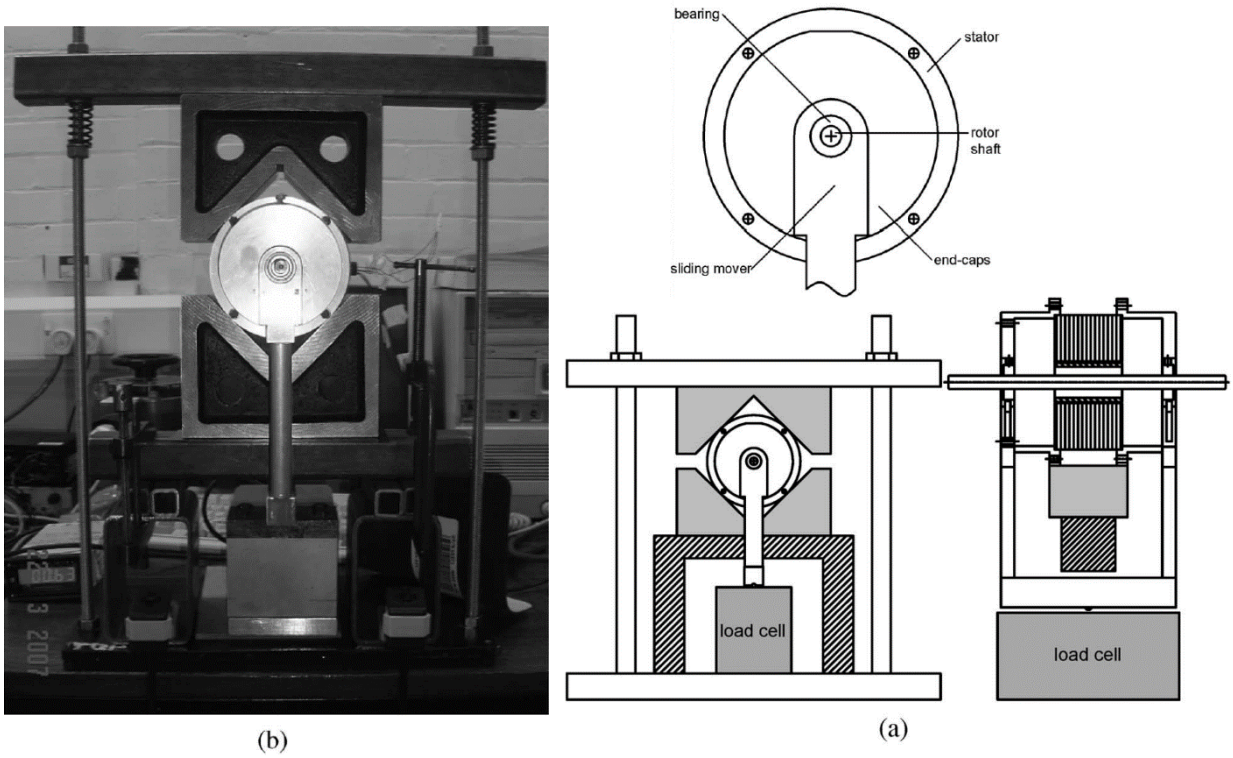

Figure 3-10 Zhu *et al*. test rig for UMP measurement. (a) Schematic drawing. (b) Experimental setup [161]

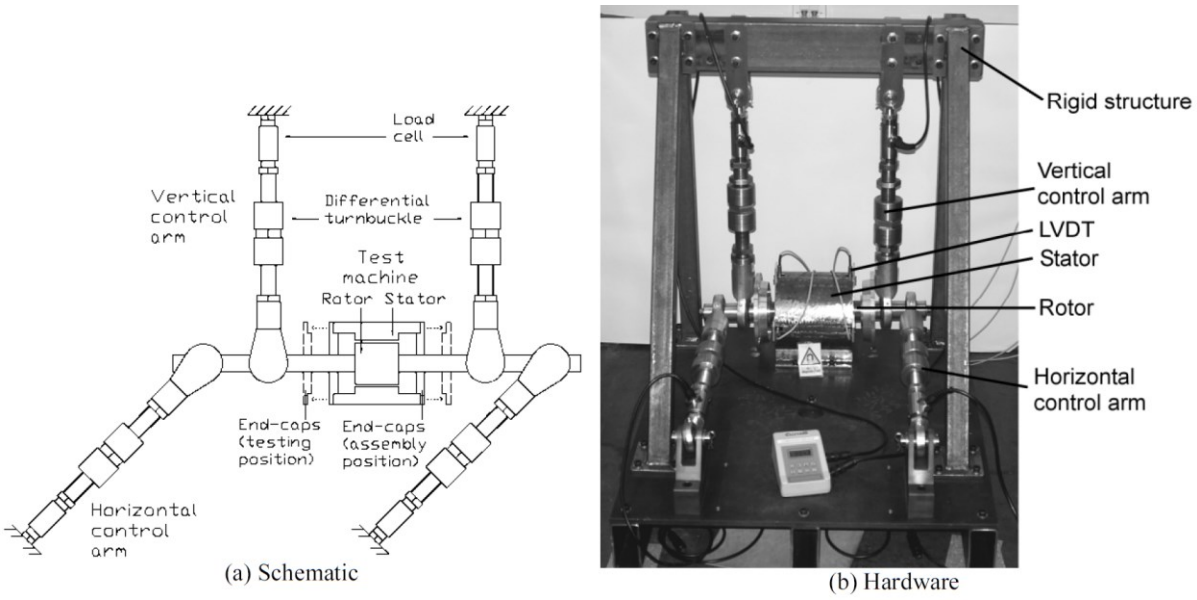

Figure 3-11 Michon *et al*. unbalanced Magnetic Pull test-rig [160]

Zhu *et al.* [161] in 2007 built a 3-slot/2-pole prototype PM brushless motor mounted on a specially designed test rig in order to verify the UMP prediction analytical model proposed in their publication. This test rig was claimed by the authors to be the first to provide UMP measurements in PM brushless machines. Figure 3-10 shows the experimental setup and the

schematic drawing of the test rig. The motor stator was rigidly held by a fixed structure, whereas the rotor was separately mounted on supports resting on a load cell. The rotor supports can move vertically to generate eccentricity, and then use the load cell to measure the induced UMP. In order to eliminate any rotor tendency while rotating, the rotor magnets were removed. Removing the rotor PMs is not well justified as the PMs are the main UMP source. Measured and predicted results without-rotor-PMs were not quite the same and had relatively large margins of error. As a result, the measurements produced significantly smaller UMPs than those predicted from machines with PMs. This suggests that some uncertainty exists with regards to the technical feasibility of the test rig used.

A novel and simple test-rig to validate predictions of UMP in a permanent magnet machine was introduced by Michon *et al.* [160][148][162] as shown in Figure 3-11. The test-rig consists of an iron-cored PM machine with a 50 mm air-gap radius, 100 mm axial length, 2mm air-gap length, and four control arms connected to a rigid structure. The two vertical and two horizontal control arms restrain the two ends of the rotor shaft and determine the accurate position generating the required eccentricity. The test-rig is under static conditions, which disregards the rotational speed, vibrations, saturation, cogging torque, armature reaction, and laminations effects on UMP and simplifies the UMP phenomena. However, those publications showed close analytical, 2D and 3D numerical, and experimental results.

3.4. Conclusion

The cause and effect relationship between UMP and bearing wear in addition to the influence of UMP on the wind turbine efficiency and the generator reliability illustrate the importance of studying and considering UMP in wind turbine designs. Reduction of UMP would greatly reduce bearing loads and subsequently reduce bearing wear. Especially for offshore wind turbines where maintenance cost is an important factor, it is essential that components are replaced or repaired prior to failure since a failed component can cause another component or other parts of the systems to fail. Hence, upon detection of imminent bearing wear or any airgap eccentricity, it is desirable to reduce the induced UMP in order to increase the generator and the main bearing time-to-failure. Reducing the induced UMP can be achieved by adopting new wind turbine generator designs. As an example, for similar conditions, the induced UMP in an airgap-winding permanent magnet synchronous generator is significantly smaller than the induced UMP in an iron-cored generator.

The first steps to understanding the extent of UMP involves the combination of analytical and numerical methods as well as experimentation. Several different analytical approaches were discussed in this chapter. These included some combination of conformation transformations, harmonic analysis, and air-gap permeance methods with augmentations looking at damping and rotor positioning effects. Unfortunately, in many cases solutions through purely closed form analytical equations isn't always possible.

A number of numerical solutions, were, thus, considered as well. Among the numerical solutions, the most popular have been finite element methods. These finite element approaches, however, require significant computational power and are only really useful for very simple applications. Alternatives to FEM were presented that made use of finite volume methods, boundary element methods, finite difference methods and other spectral and mesh-free methods. All these methods are fairly unused and mathematically unfamiliar in the field. An extensive effort would be required to take these methods and create a coupled electromagnetic-mechanical UMP model.

Problems of UMP were shown to require not only electrical modelling but also mechanical modelling. Much of this modelling uses harmonic and spring based coupling mechanisms to produce vibrational models.

No analytical or numerical approach is complete without experimental verification. UMP remains a challenging problem from the measurement perspective. Many approaches make use of vibration sensing and load cells attached to the main body of the test setup as a means of measuring and inferring UMP characteristics. These methods are not in any way ideal and further improvements can be made.

Chapter 4. Analytical Models to Calculate Unbalanced Magnetic Pull in Permanent Magnet Generators

4.1. Introduction

Unbalanced magnetic pull in electrical machines is a cause of noise and vibration in machines. The production of UMP is inherent in the operation of all electrical machines. In general, whenever a magnetic flux crosses from one iron surface to another across an airgap, a magnetic force is produced acting normal to the surfaces. In the case of a radial flux permanent magnet machine, and assuming the magnetic flux is normally crossing the surface between the airgap (free space) and the iron (infinite permeability), the normal force acting per unit surface area is obtained from the Maxwell Stress tensor as:

$$\sigma = \frac{B^2}{2\mu_0} \tag{4.1}$$

The total electromagnetic force, therefore, can be calculated by integrating the stress tensor over the surface area. The main key here is determining the magnetic flux density B which varies considerably with position and time.

This chapter presents basic electromagnetic field analysis and electromagnetic force calculation in air-gap winding and iron-cored permanent magnet generators suffering from rotor eccentricities. Three types of rotor eccentricities, static, dynamic, and tilting eccentricities, are studied. The models in this chapter are verified by numerical/computational models and experimental results presented in chapter 5. The analytical models are used in the direct-drive wind turbine multi-body model presented in chapter 7.

4.2. Air-gap length during rotor eccentricity

Calculating the UMP in a radial flux PM machine requires having the radial component value of the air-gap flux density, which is a function of both the permeance and the PM magneto-motive force MMF. Air-gap permeance cannot be determined without calculating the air-gap length, which is variable when the rotor is eccentric. The type of the rotor eccentricity regulates the analytical equations to calculate the air-gap length. This paragraph, therefore, presents the

air-gap length and permeance equations in radial flux machines with static, dynamic, and tilting rotor eccentricities.

4.2.1. Static Rotor Eccentricity

When the rotor in an electrical machine is rotating around its own axis which is shifted from the stator bore axis by constant distance e and angle α, then a static eccentricity occurs, as shown in Figure 4-1.

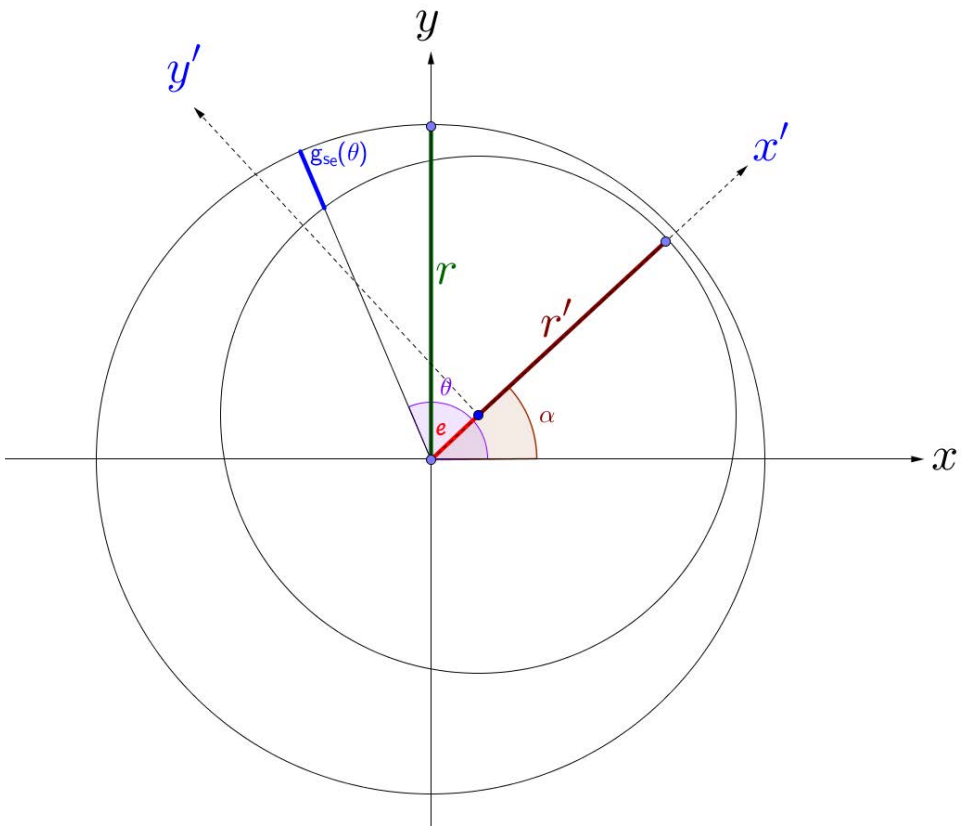

Figure 4-1 Static rotor eccentricity

The magnetic airgap length (magnetic path length) in the machine with static eccentricity g_{se} is no longer uniform and it becomes a function of the angular coordinate θ.

Assuming a coordinate system placed into Figure 4-1 with the origin on the stator bore centre, the stator inner surface radius in polar coordinates is:

$$R_s = r \tag{4.2}$$

and the equation of the outer rotor surface radius in Cartesian coordinates when $\alpha = 0$ is:

$$r'^2 = (x - e)^2 + y^2 \tag{4.3}$$

Converting and rearranging this equation into polar coordinates yields the following equation:

$$R_r^2 - 2R_r(e.\cos\theta) + (e^2 - r'^2) = 0 \tag{4.4}$$

Solving this equation in quadratic form results in the following equation:

$$R_r = e.\cos\theta + \sqrt{r'^2 - (e.\sin\theta)^2} \tag{4.5}$$

The airgap length is the difference between R_s and R_r:

$$g_{se}(\theta) = r - e.\cos\theta - r'\sqrt{1 - \frac{e^2}{r'^2}\sin^2\theta} \tag{4.6}$$

In practical cases $r' \gg e$, which means:

$$g_{se}(\theta) \approx (r - r') - e.\cos\theta \tag{4.7}$$

When $\alpha \neq 0$, the airgap length with static eccentricity can be expressed as:

$$g_{se}(\theta) \approx g - e.\cos(\theta - \alpha) \tag{4.8}$$

where g is the mean air-gap length when the rotor is concentric, α is the angle between the stator x axis and the rotor x' axis as shown in Figure 4-1. e, α are constants when the eccentricity is static, whereas, they are variables in a dynamic eccentricity case.

4.2.2. Dynamic Rotor Eccentricity

Dynamic eccentricity occurs when the rotor axis is moving with time, as shown in Figure 4-2, which could happen as a result of a bent shaft or bearing wear. Uniform dynamic eccentricity occurs when the rotor is rotating around its own axis that is shifted from the stator bore axis by a constant distance, e, and the angular velocity of the rotor rotational axis around the stator axis, w_e, is also constant, but not equal to 0.

The radial airgap length in this case is a function of time and space and can be described as

$$g_{dy}(t,\theta) = g - e.cos(\theta - \alpha - w_e t) \tag{4.9}$$

If the distance between the stator and the rotor axes is changing with time $e(t)$, and the angular velocity of the rotor rotational axis is also changing with time $w_e(t)$, then the eccentricity is non-uniform dynamic eccentricity, defined as,

$$g_{dy}(t,\theta,\alpha) = g - e(t).cos(\theta - \alpha - w_e(t).t) \tag{4.10}$$

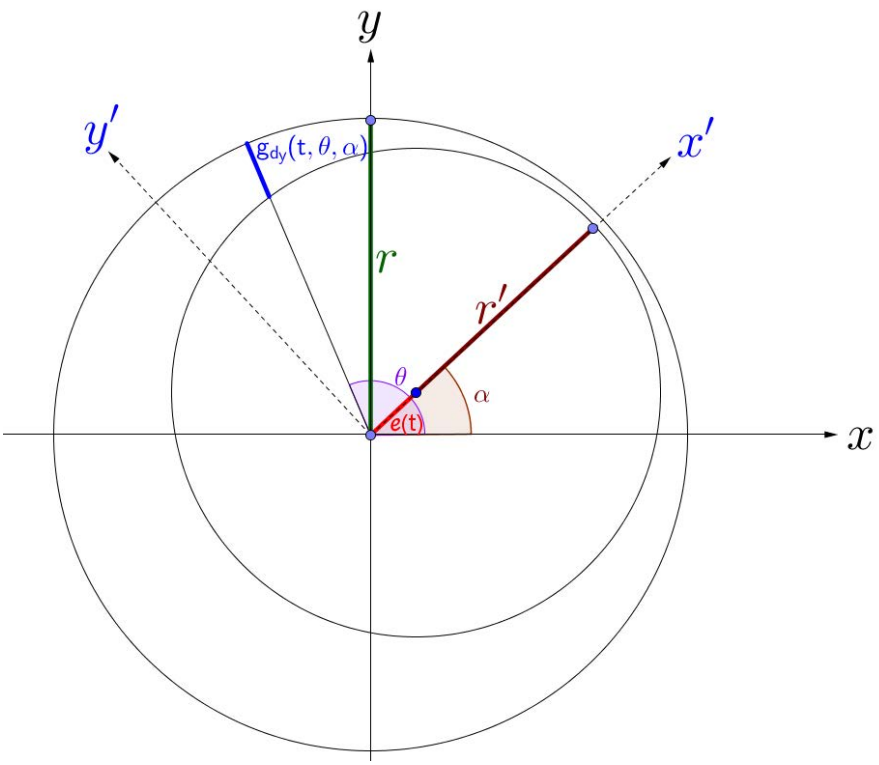

Figure 4-2 dynamic rotor eccentricity

4.2.3. Tilting Rotor Eccentricity

Tilting rotor eccentricity occurs when the stator and the rotor axes are not parallel as shown in Figure 4-3. It can be induced because of misalignment or bearing wear on either side of the generator. Tilting rotor eccentricity can be divided into both static and dynamic. The tilting

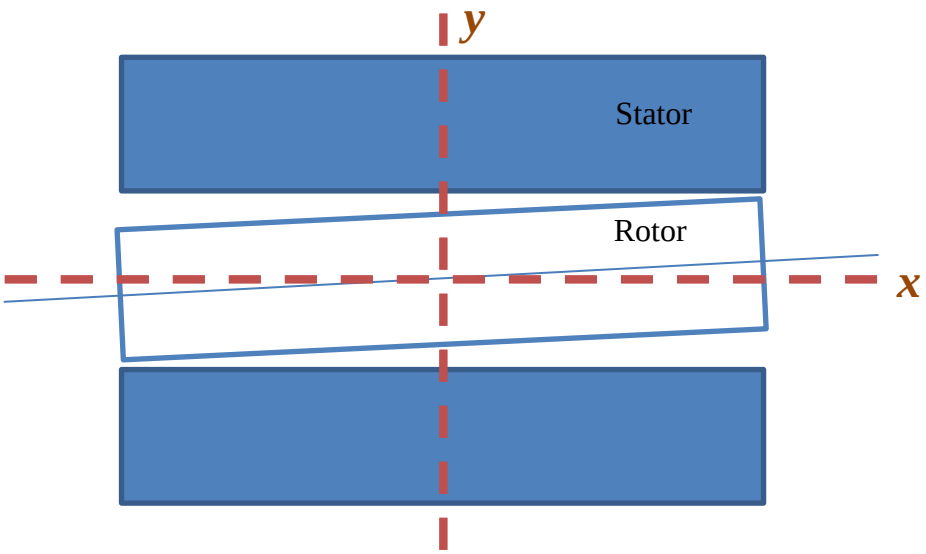

Figure 4-3 Schematic draw for tilting rotor eccentricity

eccentricity is static if the rotor is rotating around its stable axis, whereas, it is dynamic if the rotational axis is different from the rotor axis or if it is not stable.

Calculating the air-gap length in this case is more complicated than the static and dynamic rotor eccentricity cases. When tilting eccentricity is static and the maximum relative eccentricity is ε, using Cartesian coordinates and assuming the rotor and the stator axes are meeting at the point $(n, 0)$, the relative eccentricity at any point i on the x axis, which is limited between 0 and the axial generator length l, as shown in Figure 4-4, can be calculated as:

$$\varepsilon_i(x) = \frac{\varepsilon}{l-n}(i(x) - n); \quad 0 \le i(x) \le l \tag{4.11}$$

The air-gap length, therefore, given as:

$$g_{ste}(x, \theta) \approx g(1 - \varepsilon_i(x).cos(\theta - \alpha)) \tag{4.12}$$

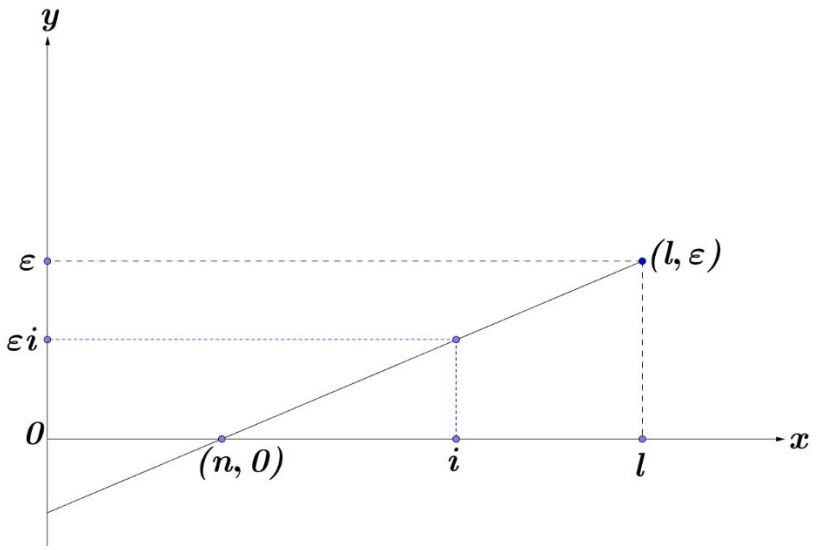

Figure 4-4 Cartesian coordinates for static tilting eccentricity

In order to demonstrate the change in airgap with tilting eccentricity consider the following special case where the rotor is supported by two sets of bearings, one on each side:

- there is excessive bearing wear in one set causing a maximum 0.8 relative rotor eccentricity in the same rotor side,
- while the other bearing set is in normal working order ensuring rotor concentricity at its side,
- and the tilting rotor eccentricity is static.

Figure 4-5 gives the normalized air-gap length at each point in the space under this condition.

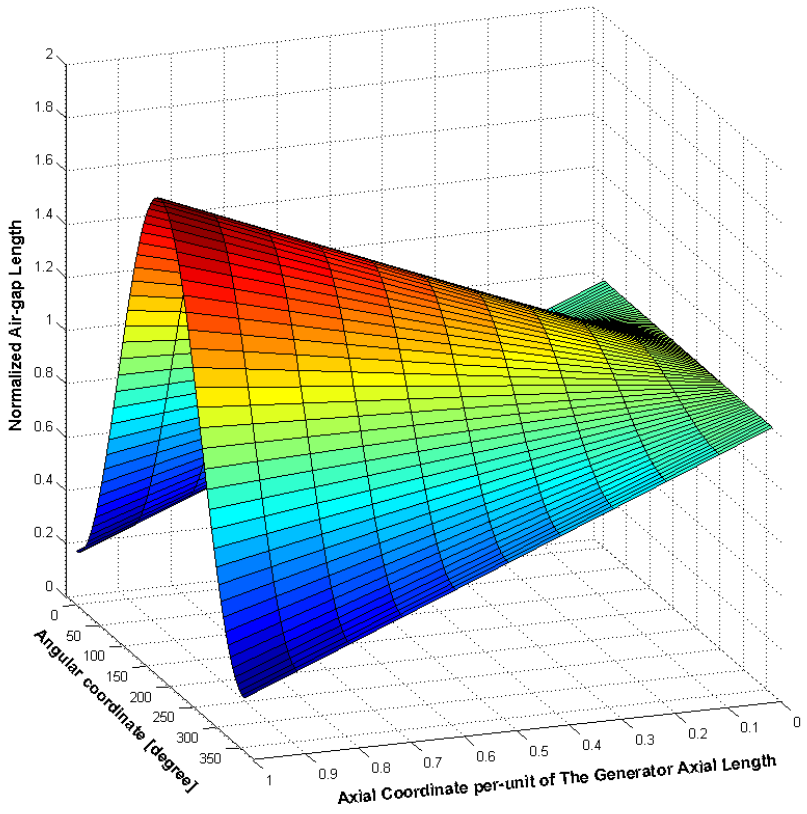

Figure 4-5 3D graph showing the normalized air-gap length at every point in the space with axial and angular coordinates when a static tilting rotor eccentricity occurs with 0 relative eccentricity at the first end of the rotor and 0.8 relative rotor eccentricity at the other end

It is even more complicated to calculate the air-gap length when the tilting rotor eccentricity is dynamic because the maximum relative rotor eccentricity and the stator and rotor axes meeting point become time-dependant variables. The relative rotor eccentricity can be calculated as:

$$\varepsilon_i(x,t) = \frac{\varepsilon(t)}{l-n(t)}\big(i(x,t) - n(t)\big); \quad 0 \le i(x,t) \le l \tag{4.13}$$

The air-gap length, therefore, can be calculated as:

$$g_{dte}(x,\theta,\alpha,t) \approx g(1 - \varepsilon_i(x,t).cos(\theta - \alpha - w_e(t).t)) \tag{4.14}$$

4.3. Permeance representation

The focus in this thesis is on the surface-mounted radial-flux permanent magnet generators, so no rotor slots. Hence, rotor slots are not considered and rotor yoke surface is assumed to be a smooth cylindrical surface. Under this condition, two cases can be distinguished here. Air-gap windings PM generators with no stator slots, as mentioned in chapter 2, are the first case. Iron-

cored PM generators with different slot shapes such as open, semi-closed, and closed slots are the second case.

4.3.1. Permeance of slot-less PM generators

Both the rotor and the stator surfaces are considered as two smooth iron surfaces. Figure 4-6 shows the magnetic flux paths in a slot-less PM generator. The magnetic permeance in a cross-sectional area unit is inversely proportional to the magnetic path length and, for an electrical machine with static rotor eccentricity, it can be written as

$$\Lambda_{se}(\theta) = \frac{\mathcal{P}(\theta)}{A} = \frac{\mu_0}{g_{se}(\theta)} = \frac{\mu_0}{g\left[1 - \frac{e}{g}.cos(\theta - \alpha)\right]} \tag{4.15}$$

Where $\mathcal{P}(\theta)$ is the magnetic permeance, μ_0 is the air permeance, A is the magnetic path cross-sectional area and ε is the relative eccentricity which is the proportion of the rotor eccentricity e out of the normal airgap length g.

$$\varepsilon = \frac{e}{g} \tag{4.16}$$

For a certain PM machine, μ_0 and g are constants so the normalized magnetic permeance can be written as

$$\Lambda_{n_{se}}(\theta) = \frac{\Lambda_{se}(\theta).g}{\mu_0} = \frac{1}{1 - \varepsilon.cos(\theta - \alpha)} \tag{4.17}$$

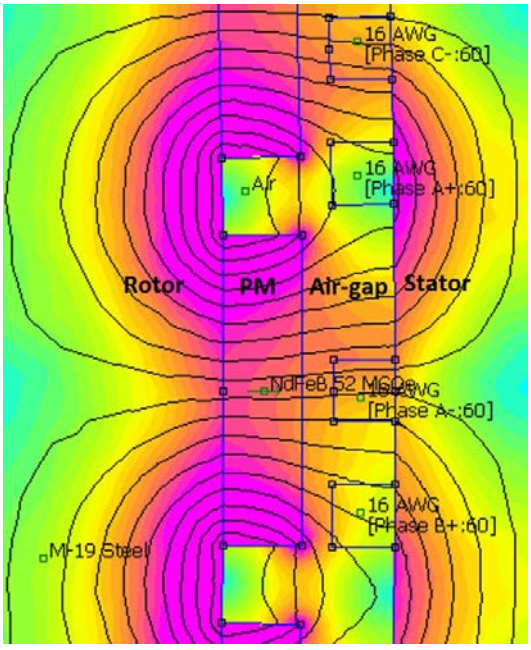

Figure 4-6 Magnetic flux paths in air-gap winding PM generator.

The graphical representation of Equation (4.17) is shown in Figure 4-7, which displays the variation of the normalized airgap permeance $\Lambda_{n_{se}}$ with different levels of relative eccentricity ε.

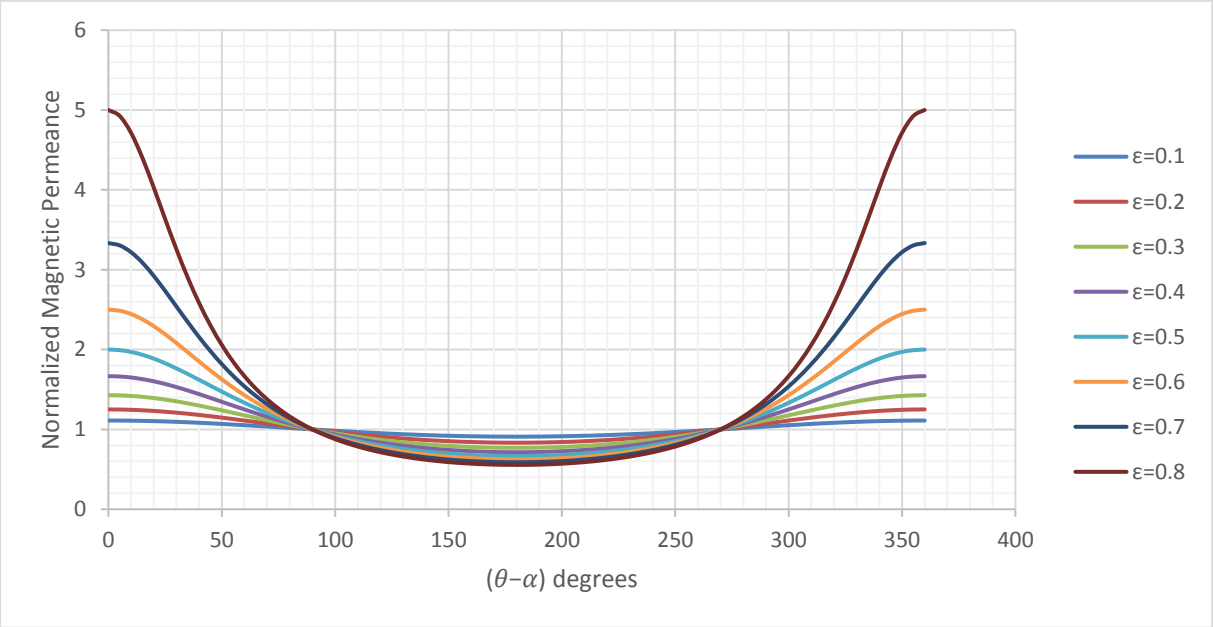

Figure 4-7 Variation of normalized airgap permeance waves with different relative eccentricities

In Equation (4.17), $\varepsilon.cos(\theta-\alpha) < 1$. Hence, the condition of using Maclaurin Series is applied, resulting in Equation (4.18), which is an option that was used in [163] and [154] to simplify the magnetic permeance equation .

$$\Lambda_{n_{se}}(\theta) = \sum_{i=0}^{\infty}[\varepsilon.cos(\theta-\alpha)]^i = 1 + \varepsilon.cos(\theta-\alpha) + \cdots \qquad (4.18)$$

Fourier series is the common analytical way to solve the magnetic permeance equation as applied in [95], [154], [164]. Equation (4.19) represents the general Fourier series for the normalized magnetic permeance.

$$\Lambda_{n_{se}} = \Lambda_0 + \Lambda_1\cos(\theta-\alpha) + \cdots = \sum_{i=0}^{\infty}\Lambda_{n_{se}}^{i}.\cos i(\theta-\alpha) \qquad (4.19)$$

$$\Lambda_0 = \frac{1}{2\pi}\int_{-\pi}^{\pi}\frac{1}{1-\varepsilon.cos(\theta-\alpha)}\,d\theta \qquad (4.20)$$

$$\Lambda_{n_{se}}^{i} = \frac{1}{\pi}\int_{-\pi}^{\pi} \frac{cos\, i\,(\theta-\alpha)}{1-\varepsilon.cos(\theta-\alpha)}\, d\theta \tag{4.21}$$

Fourier coefficients or the magnitude of normalized permeance harmonic waves for static eccentricity were found in [154], [164] by Fourier analysis as

$$\Lambda_0 = \frac{1}{\sqrt{1-\varepsilon^2}}\ ;\ i = 0 \tag{4.22}$$

$$\Lambda_{n_{se}}^{i} = \frac{2.\left(1-\sqrt{1-\varepsilon^2}\right)^{i}}{\varepsilon^{i}.\sqrt{1-\varepsilon^2}}\ ;\ i = 1,2,3,\ldots \tag{4.23}$$

The graphical representation of Equations (4.22) and (4.23) is shown in Figure 4-8, which exposes the relationship between the magnitude of normalized permeance harmonics $\Lambda_{n_{se}}^{i}$ and the relative eccentricity ε. Depending on Figure 4-8, Λ_0 dominates for small relative eccentricities. For most practical cases, when $\varepsilon < 0.3$, only Λ_0 and Λ_1 need to be considered. The other permeance harmonics are effective in higher relative eccentricity cases, especially when $\varepsilon > 0.6$.

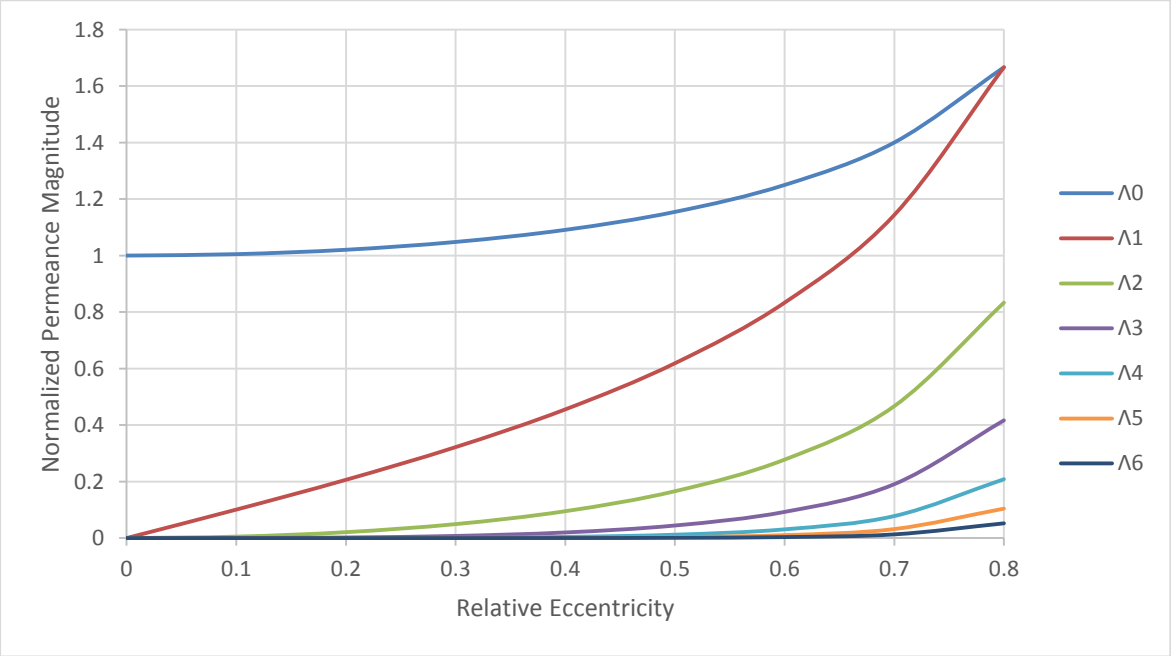

Figure 4-8 Amplitudes of normalized airgap permeance coefficient harmonics against the relative eccentricity

When the eccentricity is dynamic, using Fourier series [165], the normalized permeance at the point (t, θ) can be represented as

$$\Lambda_{n_{dy}}(t,\theta) = \Lambda_0 + \Lambda_1 \cos(\theta - \alpha - w_e t) + \cdots = \sum_{i=0}^{\infty} \Lambda_{n_{dy}}^{i} . \cos i(\theta - \alpha - w_e t) \quad (4.24)$$

$$\Lambda_{n_{dy}}^{0} = \frac{1}{2\pi} \int_{-\pi}^{\pi} \frac{1}{1 - \varepsilon . cos(\theta - \alpha - w_e t)} \, d\theta \quad (4.25)$$

$$\Lambda_{n_{dy}}^{i} = \frac{1}{\pi} \int_{-\pi}^{\pi} \frac{cos\, i\, (\theta - \alpha)}{1 - \varepsilon . cos(\theta - \alpha - w_e t)} \, d\theta \quad (4.26)$$

4.3.2. Permeance of iron-cored PM generators

The slots in this case can be open, semi-closed, or closed. When the slots are open or semi-closed, a part of the magnetic flux density enters the slot's tooth side normal to the slot surface instead of the top of the tooth as shown in Figure 4-9 and Figure 4-10, which causes flux concentration in the tooth tip. Flux concentration is normally associated with saturation which commonly occurs in semi-closed slots resulting in flux redistribution. The magnetic flux, when the machine works as a motor, induces forces that act on the tooth tips in a tangential direction to the air-gap. Integrating all tangential and radial forces, which are variable with time and position, around the air-gap, gives a total force independent of time that produces the mechanical machine torque. The magnetic flux, when the machine works as a generator, on the other hand, induces electrical current in the stator windings and produces the electrical torque. The tangential forces can produce pulsating torques and vibration in the teeth. Skewing the slots has very small effect on the vibration, since the main force wavelength is very big compared with the amount of skew [166]. The main advantage of skewing is in the reduction of voltage ripple and cogging torque.

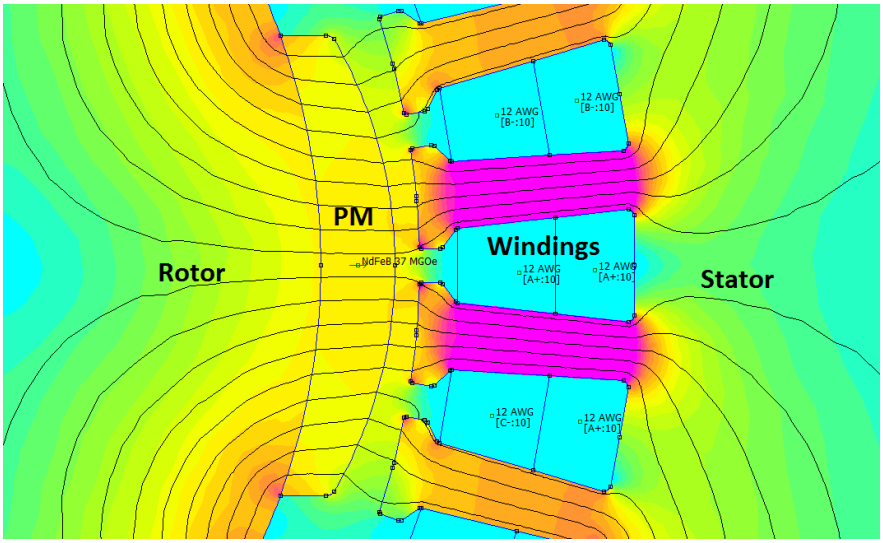

Figure 4-9 Magnetic flux paths in semi-closed slots PM generator.

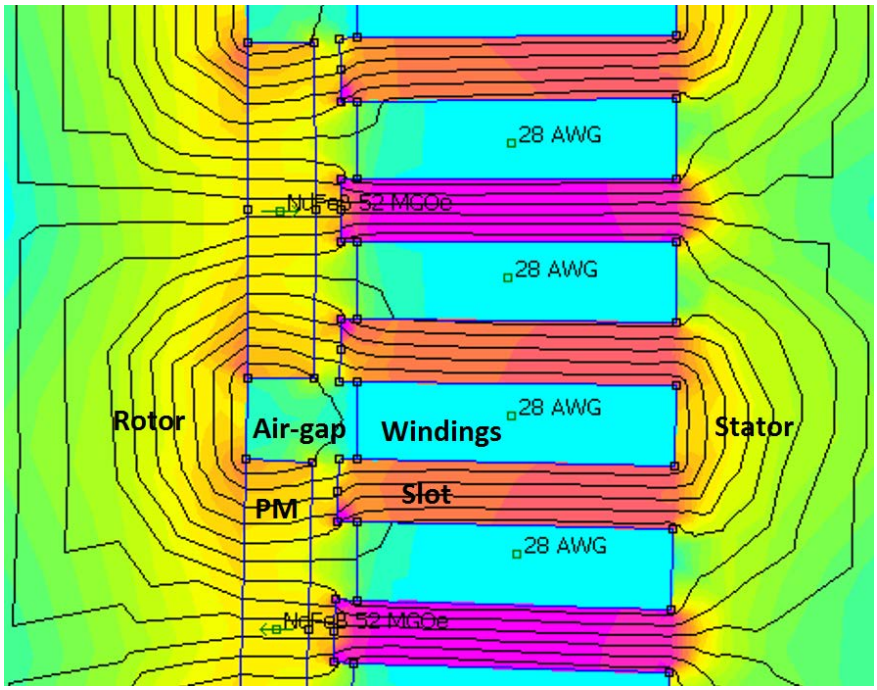

Figure 4-10 Magnetic flux paths in open slots PM generator.

Assuming an iron-cored PM machine with n number of teeth, as shown in Figure 4-11. The tooth width and pitch are τ and λ respectively. Slot depth can be assumed infinite with negligible error as long as the slot depth is more than 1.5 times the slot width, which is the common case in practice [167]. Therefore, the permeance can be considered to be zero when the slot is presented and it is equal $\frac{\mu_0}{g}$ when a tooth is presented as shown in Figure 4-11.

The airgap length g is constant when the rotor is concentric where as it is variable when eccentricity exists. The permeance wave in this case can be represented using Fourier analysis as:

$$\Lambda = \sum_{i=0}^{\infty} \Lambda_i \cos i(n\Phi) \tag{4.27}$$

$$\Lambda_0 = \frac{1}{2\pi}\left[\int_{-\pi}^{-\frac{\tau\pi}{\lambda}} 0\, d(n\Phi) + \int_{-\frac{\tau\pi}{\lambda}}^{+\frac{\tau\pi}{\lambda}} \frac{\mu_0}{g} d(n\Phi) + \int_{+\frac{\tau\pi}{\lambda}}^{+\pi} 0\, d(n\Phi)\right] = \frac{\mu_0\, \tau}{g\, \lambda} \tag{4.28}$$

$$\Lambda_{i\neq 0} = \frac{1}{\pi}\left[\int_{-\frac{\tau\pi}{\lambda}}^{+\frac{\tau\pi}{\lambda}} \frac{\mu_0}{g} \cos i(n\Phi)\ d(n\Phi)\right] = \frac{2\mu_0}{g\ i\ \pi} \sin\left(\frac{\tau\ i\ \pi}{\lambda}\right) \tag{4.29}$$

Assuming Λ_0 as an average permeance and basing the harmonic values on it gives:

$$\Lambda = \Lambda_0 \sum_{i=0}^{\infty} \Lambda_{i_{pu}} \cos i(n\Phi) \tag{4.30}$$

$$\Lambda_{0_{pu}} = 1 \tag{4.31}$$

$$\Lambda_{i_{pu}} = \frac{2\lambda}{\tau\ i\ \pi}\left[sin\left(\frac{\tau\ i\ \pi}{\lambda}\right)\right] \tag{4.32}$$

A graphical representation of Equation (4.32) is plotted in Figure 4-12 showing the per unit permeance harmonics against the ratio of the tooth width to tooth pitch τ/λ. This τ/λ ratio represents the air-gap coefficient. The higher the ratio, as shown in Figure 4-12, the lower the permeance harmonic values.

When the stator has closed slots, on the other hand, the iron permeability can no longer be assumed infinite since the slot bridges become saturated. Analytical calculations in this case are more complicated requiring different surface integral methods as explained in [168].

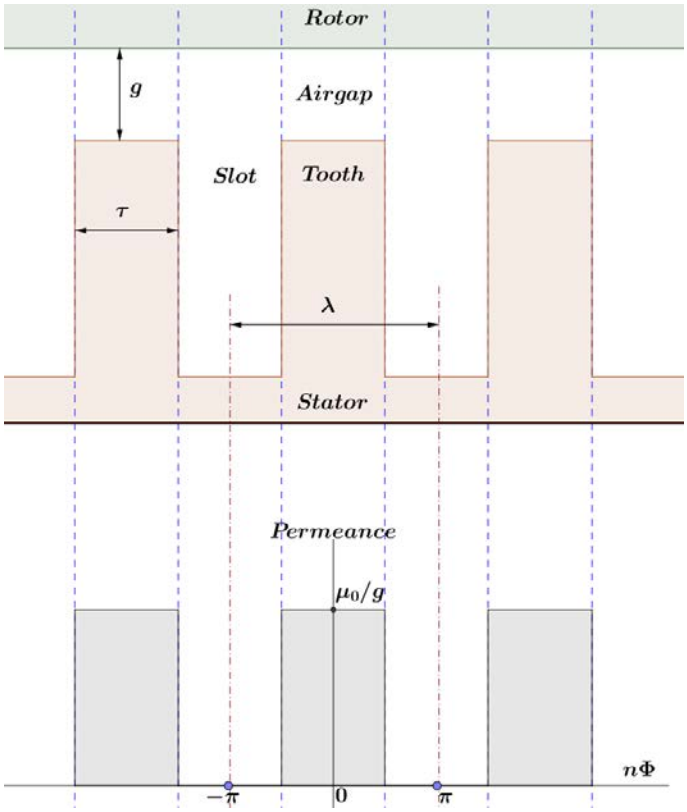

Figure 4-11 Permeance of PM generator with open slots stator.

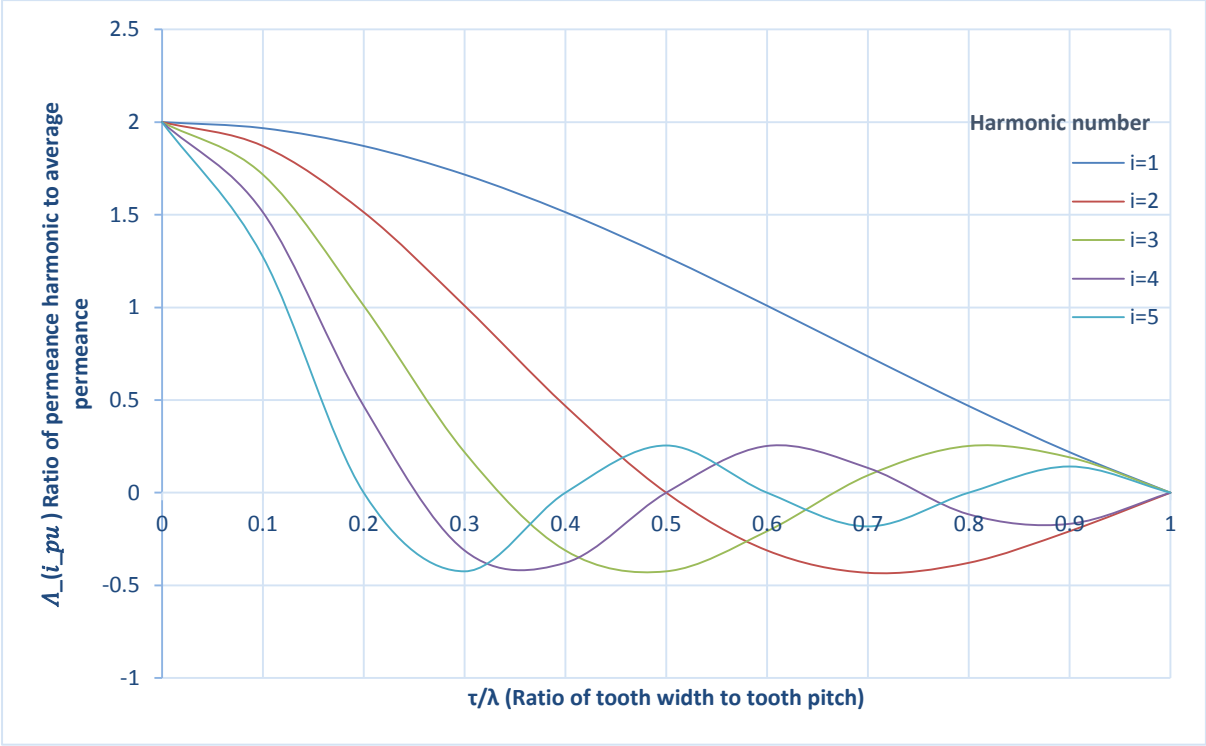

Figure 4-12 Various permeance harmonic numbers showing the per unit harmonic values against the ratio of tooth width to pitch.

4.4. Magnetic flux density

The magnetic flux distribution in the air gap can be obtained as a product of the air-gap permeance and the magneto-motive force (mmf) acting across the air-gap.

$$B(\theta,t) = \Lambda_{tot}(\theta,t).mmf_{tot}(\theta,t) \tag{4.33}$$

The following components should be considered while calculating the air-gap flux density in a radial flux PM generator:

1. Permeance harmonics of the air-gap eccentricity.
2. Stator slot permeance harmonics.
3. Permeance harmonics due to saturation.

Eccentricity and slot permeance harmonics have been discussed in the previous section. Heller and Hamata [169] studied permeance harmonics due to saturation. They concluded that a permeance wave with twice the number of poles and twice the frequency of the fundamental wave can efficiently represent saturation in an induction machine. The saturation effect, hence, can be expressed as:

$$\Lambda_{sa}(\theta,t) = \sum_{i_{sa}=0}^{\infty} \Lambda_{i_{sa}} \cos i_{sa}(2p\theta - 2w_1 t) \tag{4.34}$$

Total permeance can be represented as:

$$\Lambda_{tot}(\theta,t) = \sum_{i_{st}=0}^{\infty}\sum_{i_{s_{ecc}}=0}^{\infty}\sum_{i_{dy_{ecc}}=0}^{\infty}\sum_{i_{sa}=0}^{\infty} \Lambda_{i_{st},i_{s_{ecc}},i_{dy_{ecc}},i_{sa}} \cos\big[\big(i_{st} \pm i_{s_{ecc}} \pm i_{dy_{ecc}} \pm 2pi_{sa}\big)\theta - \big(i_{dy_{ecc}} \pm 2i_{sa}\big)\, w_r t\big] \tag{4.35}$$

The total mmf across the air-gap is the sum of both the permanent magnet mmf in the rotor and the armature reaction. Permanent magnet mmf can be represented by equation (4.36) which was also used in [170] and [171].

$$mmf_{pm} = H_c.h_m = \frac{B_{rem}}{\mu_0\,\mu_{rem}}\,.h_m \tag{4.36}$$

Fourier analysis can be used to represent the rotor mmf. that consists of a series of space and time harmonics as [164]:

$$mmf_{rt}(\theta,t)=\sum_{n\theta_r=1}^{\infty}\sum_{nw_r=-\infty}^{\infty} mmf_{n_{\theta r},n_{wr}}\cos(n_{\theta r}p\theta-(n_{wr}+n_{\theta r})pw_r t) \tag{4.37}$$

The fundamental mmf wave in the air-gap under no-load case, according to the theory of electrical machines [172], can be represented as:

$$mmf_{FD}(\theta,t)=MMF\cos(w\,t-p\,\theta) \tag{4.38}$$

Figure (4-13) shows the dimensions of a radial flux PM generator. Applying the same method introduced in the same paragraph and shown in Figure (4-11), MMF is the amplitude of the fundamental mmf_{rt}, and can be given as:

$$\begin{aligned} MMF&=\frac{1}{2\pi}\left[\int_{-\frac{\pi}{2}}^{-\frac{b_m\pi}{\tau_p}}0\,d(p\,\theta)+\int_{-\frac{b_m\pi}{\tau_p}}^{+\frac{b_m\pi}{\tau_p}}\frac{B_{rem}\,h_m}{\mu_0\,\mu_{rem}}d(p\,\theta)+\int_{+\frac{b_m\pi}{\tau_p}}^{+\frac{\pi}{2}}0\,d(p\,\theta)\right]\\ &=\frac{B_{rem}\,h_m\,b_m}{\mu_0\;\mu_{rem}\,\tau_p}\end{aligned} \tag{4.39}$$

The general form of the mmf for the stator, neglecting phase angle and skew, is given by [166]:

$$mmf_{st}(\theta,t)=\sum_{n\theta_s=1}^{\infty}\sum_{nw_s=-\infty}^{\infty} mmf_{n_{\theta s},n_{ws}}\cos(n_{\theta s}p\theta-n_{ws}w_s t) \tag{4.40}$$

Total mmf is the sum of rotor and stator magneto-motive forces:

$$mmf_{tot}(\theta,t)=mmf_{rt}(\theta,t)+mmf_{st}(\theta,t) \tag{4.41}$$

The air-gap flux density distribution in a radial-flux PM generator with static eccentricity under no load state can be obtained by substituting equations (4.19), (4.38) and (4.39) in (4.33) resulting:

$$\begin{aligned} B(\theta,t)&=\frac{1}{2}MMF\sum_{i=0}^{\infty}\Lambda_{n_{se}}^{i}\left[\cos\big(i(\theta-\alpha)-(w\,t-p\,\theta)\big)+\cos\big(i(\theta-\alpha)+(w\,t-p\,\theta)\big)\right]\\ &=\frac{1}{2}\,\frac{B_{rem}\,h_m\,b_m}{\mu_0\;\mu_{rem}\,\tau_p}\,\big[2\Lambda_0\cos(w\,t-p\,\theta)\\ &+\Lambda_1\left[\cos\big((p+1)\,\theta-(w\,t-\alpha)\big)+\cos\big((p-1)\,\theta-(w\,t-\alpha)\big)\right]\\ &+\Lambda_2\left[\cos\big((p+2)\,\theta-(w\,t-2\alpha)\big)+\cos\big((p-2)\,\theta-(w\,t-2\alpha)\big)\right]\\ &+\Lambda_3\left[\cos\big((p+3)\,\theta-(w\,t-3\alpha)\big)+\cos\big((p-3)\,\theta-(w\,t-3\alpha)\big)\right]+\cdots\big]\end{aligned} \tag{4.42}$$

The main observation from Equation (4.42) is that the air-gap flux density harmonic fields have different pole-pair numbers. When the eccentricity is small, as discussed previously and shown in Figure 4-8, Λ_0& Λ_1 dominate the other permeance harmonics, hence, only the fundamental flux density and $\pm$one pole-pair field harmonics need to be taken in account. More harmonics should be considered with large eccentricities.

The fundamental harmonic of the air-gap flux density induced by the permanent magnets [173] can be calculated as:

$$B_{g1} = \frac{4.B_{rem}.h_m}{\mu_{rem}.\left[k_c\left(g + \frac{h_m}{\mu_{rem}}\right)\right]}.sin\left(\frac{\pi.b_m}{2.\tau_p}\right) \tag{4.43}$$

where B_{rem} is the remnant flux density of the permanent magnets and for NdFeB, has the value of 1.2T. h_m , b_m are the magnet height and width respectively. τ_p is the pole pitch. μ_{rem} is the relative permeability of the magnets and for NdFeB, it is 1.05, as shown in Figure 4-13. Carter factor k_c can approximately represent the slot effect on the air-gap flux density [129] [169] and it is given as:

$$k_c = \frac{L_{tooth-pitch}}{L_{tooth-pitch} - \left(\frac{(slot\ opening)^2}{5.g_{actual} + slot\ opening}\right)} = \frac{\tau}{\tau - \left(\frac{(\tau - b_d)^2}{5g + \tau - b_d}\right)}$$
$$= \frac{5\,\tau\,g\ +\ \tau^2\ -\ \tau\,b_d}{5\,\tau\,g\ +\ \tau\,b_d\ -\ b_d^2} \tag{4.44}$$

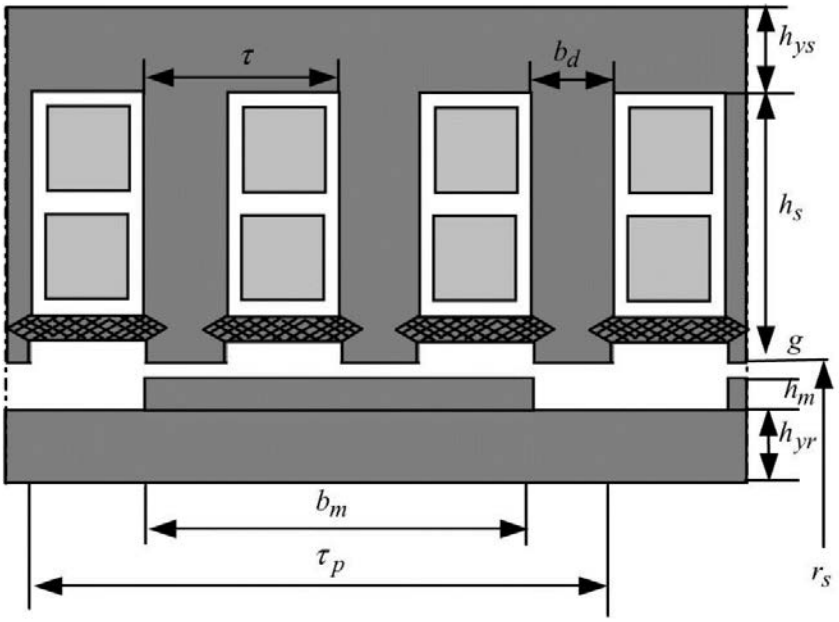

Figure 4-13 Dimensions of a radial flux PM generator pole [173].

The effect of winding connection in the stator can be significant while calculating the airgap flux density. The individual coil currents can be different in parallel winding connections while the coil voltages are fixed, that relatively maintains a sinusoidal airgap field and reduces the harmonics. However, this type of connection can lead to localised saturation of the leakage paths around the coils carrying the largest currents.

On the other hand, the coil currents are identical and coil voltages can vary in series winding connection. In this case, the magnetic airgap field will not be sinusoidal, thus causing localised saturation of the main magnetising paths around the area corresponding to the shortest airgap [174].

4.5. Unbalanced Magnetic Pull

UMP can be classified into two types. The first type is "Extrinsic UMP" which can be a result of the inaccurate assembly of the generator's components, such as the eccentric rotor positioning. It could also be induced by component quality issues, such as the asymmetric magnetization of the magnet rings and the incorrect dimensions of the stator's core[98]. The second type is "Intrinsic UMP" which can be caused by the electromagnetic structure itself. It even exists in a motor that has perfect components and production. The intrinsic UMP can be avoided by using even magnetic pole-pair and even slot number [98].

UMP has been measured using for example load cells in [97] to support bearing housings or a piezoelectric force table in [117] to measure the forces between the stator and rotor by mounting the stator on the table and supporting the rotor separately. The radial displacement of a flexible shaft was used in [156] to assess the degree of UMP.

Analytically, the Maxwell Stress tensor given in Equation (4.1) is normally used when calculating the UMP. Figures (4-14), (4-15), and (4-16) show schematic drawings for the induced UMP because of static, dynamic, and tilting rotor eccentricities respectively.

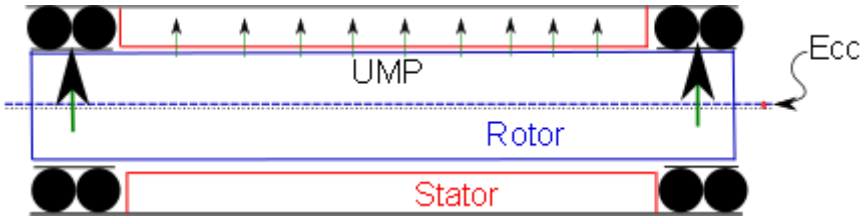

Figure 4-14 Schematic drawing for static rotor eccentricity

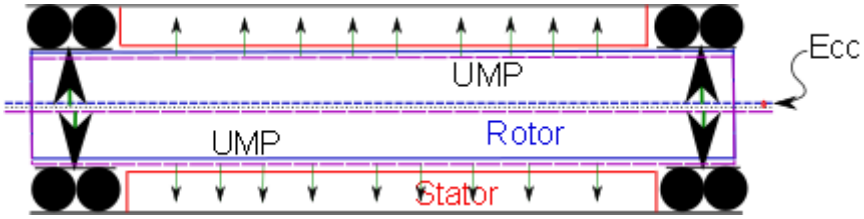

Figure 4-15 Schematic drawing for dynamic rotor eccentricity

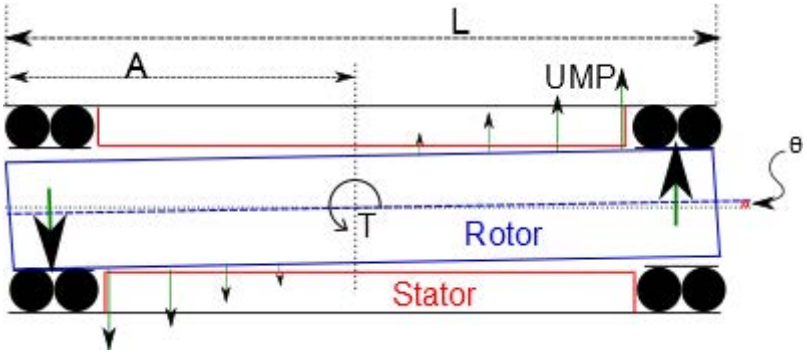

Figure 4-16 Schematic drawing for tilting rotor eccentricity

For cylindrical objects, such as the rotor of a radial flux PM generator, radial direction Maxwell Stress Tensor can be expressed as (see subsection 5.2.3):

$$\sigma_r = \frac{{b_n}^2 - b_t^2}{2\mu_0} \tag{4.45}$$

where $b_n$is the normal magnetic flux density, b_t is the tangential magnetic flux density in the air-gap and, μ_0 is the permeability of free space. The tangential component is conventionally negligible when calculating the UMP. The total radial magnetic force applied on the rotor of a generator is given by,

$$UMP = F_r = L \int_0^{2\pi} \frac{b_n(\theta, t)^2}{2\mu_0} d\theta \tag{4.46}$$

When the rotor is perfectly concentric, this force can be neglected. With rotor eccentricity, a considerable UMP force will be induced. The main factor required to calculate the UMP is the flux density distribution in the air-gap, which has been discussed in the previous section (4.4.).

When the eccentricity is static, the induced UMP is constantly applied directly and shared equally on the bearings as shown in Figure (4-14). The UMP is variable when the eccentricity is dynamic as shown in Figure (4-15) and it will be equally shared on the bearings. The case is totally different when the eccentricity is tilting, as shown in Figure (4-16). The UMP is not equally applied on the bearings. Dividing the rotor into large number of slices $(m + q)$ then

calculating the UMP induced on each slice due to the eccentricity is the analytical way chosen to calculate the force applied on the bearing due to tilting rotor eccentricity. Assuming the tilting is occurring around an imaginary axis, then m, q are the generator slice numbers on the two sides of the tilting axis. m & q are constants if the tilting eccentricity is static, whereas, they are variables with dynamic tilting eccentricity. Torque around the axis of rotation is given by:

$$T = \sum_{n=1}^{m} A_n F_n + \sum_{n=1}^{q} A_n F_n \tag{4.47}$$

Where, F_n is the net magnetic force induces on the slice number n because of the eccentricity and A_n is the distance between this slice and the axis of tilting. m is the number of slices in one side of the axis of rotation whereas q is the number of slices on the other side depending on the location of the axis of rotation. There is a linear relationship between rotor static eccentricity and the induced UMP and can be expressed as:

$$F_{UMP} = Bx + C \tag{4.48}$$

Where, B and C are constants related to the machine size and type. x is the rotor eccentricity as a percentage of the machine air-gap. Assuming the length of the rotor is L, then the length of each slice and the eccentricity x are:

$$dL = \frac{L}{m+q} \tag{4.49}$$

$$x = \frac{n.dL.\tan\theta}{a} \tag{4.50}$$

where, θ is the tilting angle and a is the normal air-gap length. Substituting Equations (4.48), (4.49), and (4.50) in (4.47) results:

$$T = \sum_{n=1}^{m} (n.dL)(B.n.dL.\frac{tan\theta}{a} + C) + \sum_{n=1}^{q} (n.dL)(B.n.dL.\frac{tan\theta}{a} + C) \tag{4.51}$$

When $(m = q)$, the torque becomes:

$$T = 2\sum_{n=1}^{m=q} B.n^2.dL^2.\frac{tan\theta}{a} + n.dL.C \tag{4.52}$$

The force applied on the bearing because of the tilting eccentricity will be:

$$F_{bearing} = \frac{2\sum_{n=1}^{m=q} B.n^2.dL^2.\frac{tan\theta}{a} + n.dL.C}{L} \quad (4.53)$$

4.6. UMP in an air-gap winding PM generator

The slot-less design of air-gap winding PM generators eliminates any slotting effect on the flux density distribution and consequently no effect on the induced UMP. Figure 4-17 shows a schematic drawing for the dimensions of an air-gap winding PM generator. It is important here to discriminate between the generator mechanical air-gap, which is $g(\theta)$ in Figure 4-17, and the magnetic air-gap which is $g(\theta) + l_c + h_m$. Similar to every electrical machine, the mechanical air-gap is manufactured to be as small as possible to enhance the machine efficiency. The magnetic air-gap in this design, however, is relatively large as the stator winding height is added anyway to the mechanical air-gap causing an increase in the leakage flux density and reduction in the induced electrical current. This is compensated by increasing the machine size.

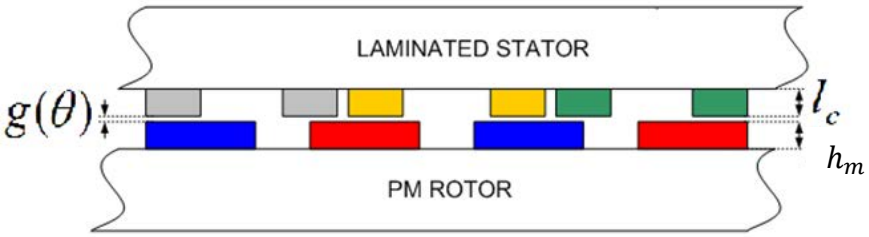

Figure 4-17 Air-gap dimensions for the radial flux PM machine

In this slot-less design, ignoring the saturation effect, the flux density in the air-gap is sinusoidal and can be expressed as:

$$B(\theta) = \hat{B}\, cos(P.\theta) \quad (4.54)$$

where, $B(\theta)$ is the normal magnetic flux density, $\hat{B}$ is the maximum magnetic flux density magnitude, P is the pole pair number. The maximum magnetic flux density magnitude, depending on Equation (4.36), is constant when the rotor is concentric and using a basic magnetic circuit design, it can be approximated as [175][176]:

$$\hat{B}_{con} = \frac{B_{rem}.h_m}{\mu_{rem}.(g + l_c) + h_m} \quad (4.55)$$

On the other hand, $\hat{B}$ is variable when there is static or dynamic rotor eccentricity. $\hat{B}$ is a function of space when the eccentricity is static and a function of both space and time when

the eccentricity is dynamic, as discussed previously. The maximum magnetic flux density magnitude with eccentric rotor can be approximated as:

$$\hat{B}_{ecc}(\theta,t)=\frac{B_{rem}.h_m}{\mu_{rem}.\left(g+l_c-e(\theta,t)\right)+h_m} \tag{4.56}$$

For static rotor eccentricity, the air-gap magnetic flux density can be represented as:

$$B(\theta)=\left[\left(\hat{B}_{ecc}-\hat{B}_{con}\right)cos\,\theta+\hat{B}_{con}\right]cos(P.\theta) \tag{4.57}$$

Equations (4.55) and (4.56) are simplified and can be enhanced by using a higher precision magnetic circuit design, as shown in Figure 4-18. The relative permeability of both copper and permanent magnet is very close to that of air and can be ignored when calculating the flux density, hence, the magnetic air-gap length $l_g=l_c+g$. Equation (4.57) can be rewritten as:

$$B(\theta)=\left[\left(\left(\frac{2.B_{rem}.h_m.e}{\left(l_g+h_m\right)^2-2e.\left(l_g+h_m\right)}\right)\cos\theta+\frac{B_{rem}.h_m}{l_g+h_m}\right)\right]\cos(P.\theta) \tag{4.58}$$

The first part of Equation (4.58), after expanding, represents the extra wave formula induced by the rotor eccentricity. It has smaller amplitude than the original one. Different pole-pair number by one generates it. The second part represents the concentric case flux density wave formula. The UMP, then, can be expressed as:

$$UMP=\frac{L}{2\mu_0}\int_0^{2\pi}\left(\left[\left(\frac{B_{rem}.h_m.e}{\left(l_g+h_m\right)^2-2e.\left(l_g+l_m\right)}\right)cos\left((P\pm1).\theta\right)\right]+\left[\frac{B_{rem}.h_m}{l_g+h_m}cos(P.\theta)\right]\right)^2 d\theta \tag{4.59}$$

Equation (4.59) is compatible with what Frohne showed in 1967 [174]. He said that the UMP is generated by the interaction of two magnetic fields with pole-pair numbers differing by one.

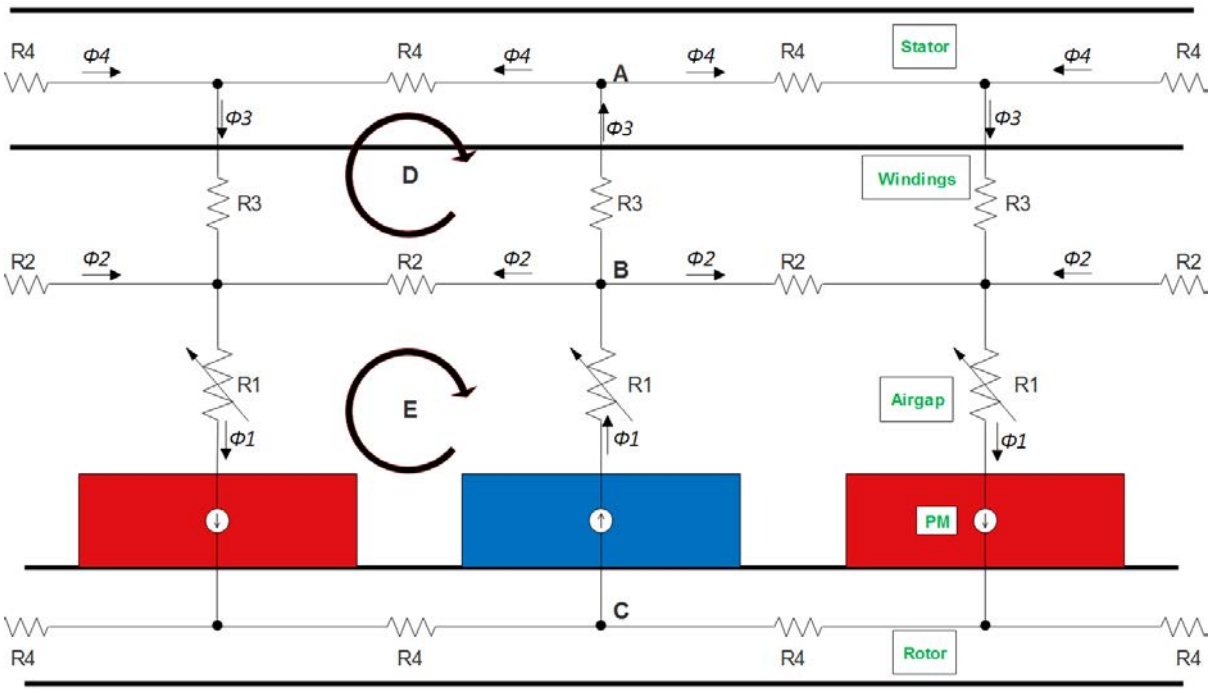

Figure 4-18 Schematic representation of a magnetic circuit model for an air-gap winding PM generator.

Figure 4-18 shows a basic magnetic circuit model for an air-gap winding PM generator. Where R1 represents the radial airgap magnetic reluctance. The smaller the R1, the more efficient the generator can be and the less magnetic flux leakage occurs, which shows the importance of the smaller airgap designs. R1 is constant when the rotor is concentric but it becomes variable when a rotor eccentricity occurs (change in the length of the mechanical airgap).

$$R1 = \frac{g}{\mu_0 \, b_m \, d_m} + c_1 \tag{4.60}$$

g is the mechanical air-gap length. b_m, d_m are the PM average pitch and axial length respectively. c_1 is a constant representing the PM magnet reluctance and mainly related to the PM design and dimensions.

$$c_1 = \frac{h_m}{\mu_0 \mu_{rem} \, b_m \, d_m} \tag{4.61}$$

R2 represents the airgap reluctance between the PMs. R2 is related to the generator design (specifically the distance between the PMs) and it determines the magnetic flux leakage so it should be significantly larger than R1.

$$R2 = \frac{\tau_p}{\mu_0 \, g \, d_m} \tag{4.62}$$

R3 represents the radial windings magnetic reluctance. The winding height determines R3 value, which is constant for a specific design. Assuming similar winding permeability to the air-gap permeability results:

$$R3 = \frac{l_c}{\mu_0 \, b_m \, d_m} \tag{4.63}$$

The main difference between the magnetic circuits of an iron-gap and an air-gap winding generators can be summarised by the existence of R3.

R4 is the iron reluctance of the stator and the rotor yoks.

$$R4 = \frac{\tau_p}{\mu_0 \, \mu_{ir} \, h_{ys,r} \, d_m} \tag{4.64}$$

μ_{ir} equals about 200000 for 99.95% pure iron and goes down to 5000 for 99.8% pure [177], therefore, R4 can be disregarded.

The permanent magnets are the mmf source in this magnetic circuit and can be modelled as [170][171]:

$$NI = \frac{B_{rem} h_m}{\mu_0 \, \mu_{rem}} \tag{4.65}$$

Assuming the air-gap flux Φ_1 is the same as the PM flux Φ_{pm}, the air-gap leakage flux is Φ_2 and the flux in the stator yoke is Φ_4, then applying Kirchoff's Magnetic Flux Equivalent Law (Current Law) at node B, as shown in Figure 4-18, results:

$$\Phi_3 = \Phi_1 - 2\Phi_2 \tag{4.66}$$

And applying Kirchoff's Law at node A gives:

$$\Phi_3 = 2\Phi_4 \tag{4.67}$$

Applying Kirchoff's m.m.f. Equivalent Law (Voltage Law) for loop E results:

$$2\frac{B_{rem} h_m}{\mu_0 \, \mu_{rem}} = 2 \, R1 \Phi_1 + R2 \, \Phi_2 \tag{4.68}$$

Applying Kirchoff's m.m.f. Equivalent Law for loop D gives:

$$R2 \, \Phi_2 = 2 \, R3 \, \Phi_3 \tag{4.69}$$

Subtracting Equation (4.69) from Equation (4.68) results:

$$2\frac{B_{rem}h_m}{\mu_0\,\mu_{rem}} = 2\,R1\,\Phi_1\ + 2\,R3\,\Phi_3 \tag{4.70}$$

Combining Equations (4.66), (4.68) and (4.70) leads to Equation (4.71):

$$2\frac{B_{rem}h_m}{\mu_0\,\mu_{rem}}\begin{bmatrix}1\\1\end{bmatrix} = \begin{bmatrix}2R1+\frac{1}{2}R2 & -\frac{1}{2}R2\\ 2R1 & 2R3\end{bmatrix}\begin{bmatrix}\Phi_1\\ \Phi_3\end{bmatrix} \tag{4.71}$$

Solving Equation (4.71) results:

$$\Phi_1 = 2\frac{B_{rem}h_m}{\mu_0\,\mu_{rem}}\left(\frac{2R3+\frac{1}{2}R2}{2R1\,R3+R2\,R3-R1\,R2}\right) \tag{4.72}$$

$$\Phi_3 = 2\frac{B_{rem}h_m}{\mu_0\,\mu_{rem}}\left(\frac{4R1+\frac{1}{2}R2}{2R1\,R3+R2\,R3-R1\,R2}\right) \tag{4.73}$$

At no load case, air-gap flux densities are found by dividing the flux values by the minimum cross section area:

$$B1 = \frac{\Phi_1}{b_m\,d_m} \tag{4.74}$$

$$B3 = \frac{\Phi_3}{b_m\,d_m} \tag{4.75}$$

Substituting Equations (4.60-63,72) in Equation (4.74) results the total magnetic flux density in the airgap:

$$B_1 = B_{g_{tot}} = \frac{B_{rem}h_m\,(4\,l_c\,g+\ \tau_p\,d_m)}{2\,g\,l_c(g+h_m)+\ \tau_p\,d_m(l_c-g-h_m)} \tag{4.76}$$

Substituting Equations (4.60-63,73) in Equation (4.75) results the effective magnetic flux density crossing the stator windings:

$$B_3 = B_{g_{eff}} = \frac{B_{rem}h_m\,(8\,g^2+8\,g\,h_m+\ \tau_p\,d_m)}{2\,g\,l_c(g+h_m)+\ \tau_p\,d_m(l_c-g-h_m)} \tag{4.77}$$

Replacing Equation (4.55) by Equation (4.77) results Equation (4.59) to become:

$$UMP\ = \frac{L}{2\mu_0}\int_0^{2\pi}\left(\begin{matrix}\left[\left(\frac{1}{2}.\frac{b\,c-a\,d}{c^2+d\,c}\right)\cos\left((P\pm1).\theta\right)\right]\\ +\left[\frac{a}{c}\cos(P.\theta)\right]\end{matrix}\right)^2 d\theta \tag{4.78}$$

Where:

$$
\begin{aligned}
a &= B_{rem} h_m \left(8\, g^2 + 8\, g\, h_m + \tau_p\, d_m\right) \\
b &= B_{rem} h_m \left(8\, e^2 - 16\, g\, e\right) \\
c &= 2\, g\, l_c (g + h_m) + \tau_p\, d_m (l_c - g - h_m) \\
d &= 2\, e\, l_c (e - 2\, g - h_m) + \tau_p\, d_m e
\end{aligned}
\tag{4.79}
$$

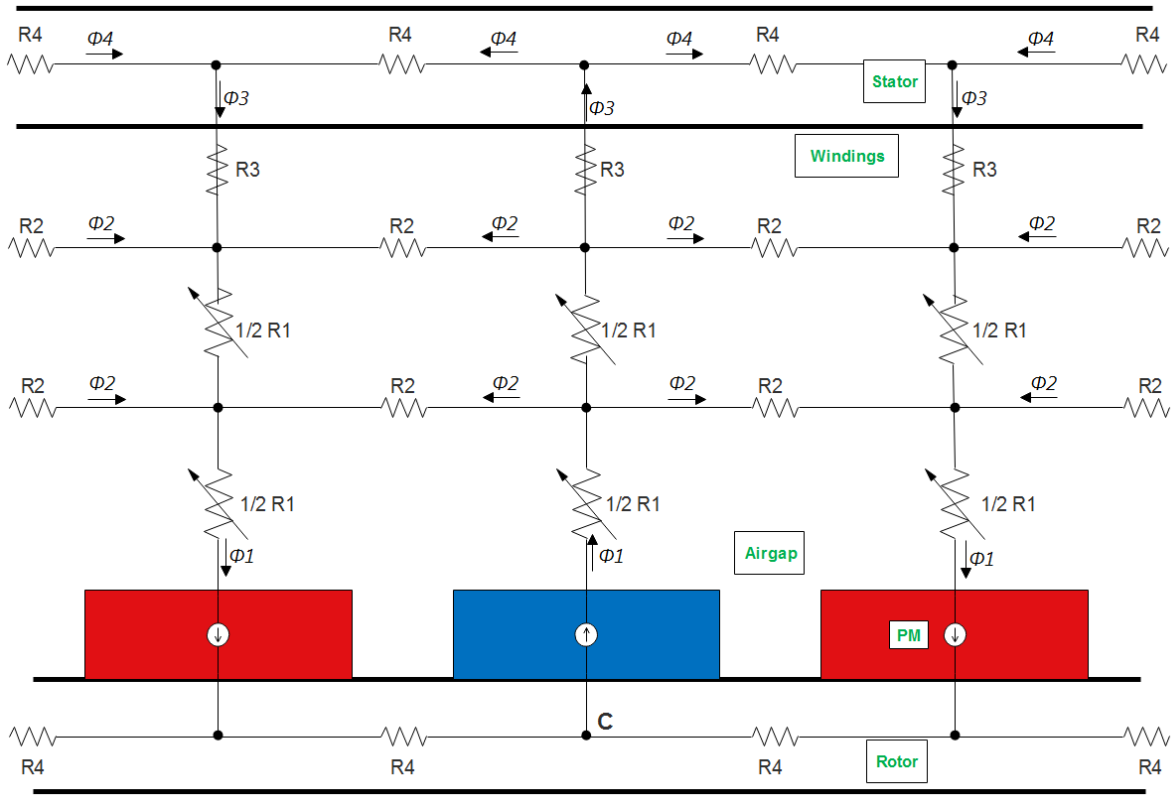

Figure 4-19 Schematic representation of a more accurate magnetic circuit model for an air-gap winding PM generator with rotor eccentricity.

The accuracy of this magnetic circuit model decreases with higher eccentricity values, which can be justified as the magnetic air-gap would significantly increase at one side of the air-gap and larger air-gap means more flux density leakage. The magnetic circuit model can be improved be dividing the mechanical air-gap into sections. The more sections, the higher the accuracy but the complexity increases also. Figure 4-19 shows the magnetic circuit model for an air-gap winding PM generator with two air-gap sections.

4.7. Conclusion

Analytical models to calculate UMP in PM machines with rotor eccentricity were presented in this chapter. Calculating the UMP requires determining the magnetic flux density in the PM machine, which cannot be calculated without knowing the airgap length in the machine. During a rotor eccentricity, the machine airgap is not unfirmed anymore. Analytical models to calculate the airgap length in a PM machine with eccentric rotor were presented in this chapter. Three types of rotor eccentricities were distinguished and reviewed in details, which are static, dynamic, and tilting rotor eccentricities. There was concentration on analytically studying the air-gap winding PM machine in this chapter trying to cover the research gap regarding this type of machine in the literature.

The analytical models introduced in this chapter are validated by numerical simulations using Finite Element Analysis FEA. The results and comparisons are provided in the next chapter. The permeance method of calculating the UMP wave magnitude can be applied to most types of electrical machines. The redistribution of magnetic flux density due to fringing and saturation, however, is not taken in account, which reduces the results accuracy especially for the higher harmonics. The air-gap winding machine UMP model is simplified to generate quick estimations of the magnetic forces. The model can be improved using more detailed magnetic circuits.

Chapter 5. Numerical Models and Experimental Test Rig to Calculate Unbalanced Magnetic Pull in Permanent Magnet Generators

5.1. Introduction

The main goal of this chapter is to validate the analytical models presented in the previous chapter. Two machines are analysed in this chapter: the first machine is a 47.7 kW air-gap winding PM generator and the second machine is an 11 kW iron-cored PM generator. Both machines were modelled using the 2-D open source finite element analysis software, FEMM. The results of the comparison between the numerical models and the analytical models are presented. Validating both the numerical and analytical results required building a test-rig and comparing those results with the experimental results. The test-rig is introduced in this chapter with the experimental results for only the 11 kW iron-cored PM generator.

5.2. Numerical Modelling

The numerical computation of magnetic fields in electrical machines has become a standard design requirement during the past few decades. The material characteristic where the magnetic field exists determines the relationship between the magnetic flux density B and the magnetic field intensity H.

$$B = \mu H \tag{5.1}$$

In a PM generator, the total airgap magnetic field consists of two components: the field produced by the permanent magnets and the field produced by the induced electrical currents in the stator winding. These currents are induced according to Faraday's Law, due to the rotating magnetic field produced by the rotating PM rotor. Induced currents only flow if the machine is connected to a load. The voltage that drives these induced currents is calculated from the PM field under the no-load case. Computing B for a given H is a static magnetic field problem that can be solved numerically using different methods. The common methods are detailed in [178] and listed below:

1. Finite Element Method (FEM)

2. Finite Difference Method (FDM)
3. Boundary Element Method (BEM)
4. Magnetic Equivalent Circuit (MEC)
5. Point Mirroring Method (PMM)

Table 5.1 gives a comparison between the above methods. In engineering analysis generally and electromagnetics especially, the FEM is extensively used. FEM currently represents the state-of-the-art in the numerical magnetic field computation relating to electrical machines

METHOD	*PRINCIPLE OF DISCRETISATION*	*GEOMETRY APPROXIMATION*	*NON-LINEARITY*	*COMPUTATIONAL COSTS*
FEM	Triangles	Extremely flexible	Possible	High
FDM	Rectangles	Inflexible	Possible	High
BEM	Polygons	Extremely flexible	Troublesome	High
MEC	Magnetic circuit	Specific geometries	Possible	Very low
PMM	Points mirroring	Simple geometries	By constant factors	Low

Table 5-1 Numerical field computation methods

FEM allows the modelling of complex geometries, and with today's computational power, 2D FEM is very fast and flexible. However, there is still computational challenges for 3D FEM modelling.

The FEM is a method for solving partial differential equations of a continuum domain. This method divides and separates the continuum domain into finite number of parts called elements using approximate functions. The solution of the element problem is similar to the standard discrete problem. The simple elements' equations are then assembled into a large system of equations to model the entire problem. FEM is widely detailed and discussed in [179]–[181].

Once a solution has been obtained from FEM there are three methods for post-processing that solution to obtain the forces acting between the rotor and the stator in an electrical machine [107]. The next subsections discuss these methods.

5.2.1. Lorentz force

Lorentz force can be defined as the induced force in a current-carrying conductor in an external magnetic field. The differential force equation can be written as:

$$\partial F = I(\partial l \times B) \tag{5.2}$$

Where ∂l is the elementary length in the direction of the current I. Equation (5.2) can be simplified to Equation (5.3) in a 2D finite element model where the current is perpendicular to plane of the magnetic flux density components.

$$F = BIl \tag{5.3}$$

For simplicity, B is normally considered as the average value of the magnetic flux density, but this does leads to a loss of accuracy, as the local information about the field is not taken into account [107].

5.2.2. Coulomb method

This technique, sometimes also called the co-energy variation method or the virtual work method, was originally presented in 1983 by Coulomb based on virtual work for calculating electromagnetic forces from a finite element solution. This method has a limited application area due to the fact it can only be employed to calculate forces in DC electrical machines [141]. The force acting along the virtual displacement direction is calculated as a partial derivative of the co-energy functional which is defined by the integral:

$$W_{co} = \int_V \left[\int_0^H B \, dH \right] dV \tag{5.4}$$

Where, V is integration volume, W_{co} is the co-energy functional. The component of the force F_x acting along the x-direction is:

$$F_x = \frac{dW_{co}}{dx} \tag{5.5}$$

Solving Equation (5.5) requires two magnetic field solutions, therefore, calculation of the electromagnetic force in electrical machines supplied by power converters becomes very difficult using this technique [182].

5.2.3. Maxwell stress tensor

This method is commonly used in the calculation of forces and torques in the finite element analysis of electrical machines as it simplifies understanding the relationship between the directions and magnitudes of the magnetic fields and the induced forces [183]. Applying this method requires [182]:

- The studied body has to be located in the air.
- The magnetic field has to be identified on the whole surface surrounding the body.

Simplified form of Maxwell stress tensor is given in Equation (4.1) and radial component of Maxwell stress tensor in RFPMG is given in Equation (4.45). Moreover, in terms of flux density components, Maxwell stress tensor is given as [183]:

$$\sigma = \frac{1}{\mu_0}\begin{bmatrix} B_x^2 - \frac{1}{2}B^2 & B_xB_y & B_xB_z \\ B_yB_x & B_y^2 - \frac{1}{2}B^2 & B_yB_z \\ B_zB_x & B_zB_y & B_z^2 - \frac{1}{2}B^2 \end{bmatrix} \tag{5.6}$$

Here, $B_x, B_y \; and \; B_z$ are the magnetic flux density components in $x-, y- \; and \; z-$ directions respectively. The total electromagnetic force is calculated by integrating the divergence of Maxwell stress tensor over the volume surrounding the body [107][182]:

$$F = \int_V \nabla.\sigma \; dV = \oint_S \sigma.n \; dS \tag{5.7}$$

where, S is the boundary of the region V, n is unit-vector normal to S.

It is common to assume no z-component for the magnetic flux density in RFPMGs and resolving the other two components as two orthogonal components:

$$B = B_n \, n + B_t \, t \tag{5.8}$$

where, B_n, B_t are the normal and tangential components to the boundary S respectively, t is unit vector tangential to the boundary S. The surface integration in Equation (5.7) is reduced to a line integration along the airgap in a two dimensional model resulting in the simplified Equation (4.46) after disregarding the tangential magnetic flux density which is significantly smaller than the radial component.

Fruchtenicht *et al.* [152] suggested solving the flux density distribution using harmonic analysis of the airgap fields or by using the conformal transformation technique then integrating the Maxwell stress tensor around the rotor in order to calculate the total electromagnetic force.

5.3. Air-gap winding PM machine case study

This machine is a slot-less 88 pole air-gap winding machine using NdFeB magnets. It was designed for a direct drive application. The parameters are shown in Table 5-2 and the dimensions are shown in Figure 5-1.

Main Machine Parameters	
Stator Outer diameter [m]	2.1
Number of poles	88
Number of coils	66
Mechanical Air-gap [mm]	10
Core length [m]	0.6
V_{ph} (rms) [V]	440
I_{ph} (rms) [A]	36
P_{out} [kW]	47.7
Speed [rpm]	21
Mass of Active Material	
Copper [kg]	427
Steel [kg]	1850
Permanent Magnets [kg]	597
Total active mass [kg]	2874

Table 5-2 Air-gap winding PM generator parameters

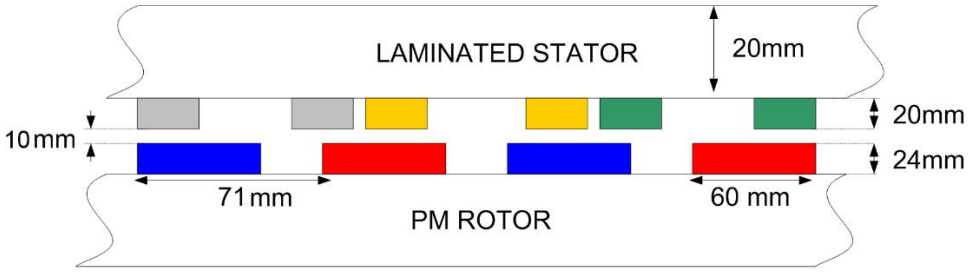

Figure 5-1 Dimensions for a 47.7 kW air-gap winding radial flux PM machine

Two-dimensional finite element method (FEM) open-source software called FEMM was used to study the effect of rotor eccentricity on the magnetic flux density in the generator air gap and hence the induced UMP for different levels of eccentricity. The software is particularly suitable for solving low frequency electromagnetic problems on two-dimensional planar and axisymmetric domains [184] ; therefore, no-load cases of permanent magnet machines are simple to model and simulate. However, loading cases are more complex to simulate and required additional instruction using a scripting language. The meshing size is controllable and

30° minimum meshing angle has been chosen for accurate analysis. A two-dimensional diagram of the studied machine showing the flux density lines is illustrated in Figure 5-2. In the next subsections, two cases are distinguished: no-load case and different loads case.

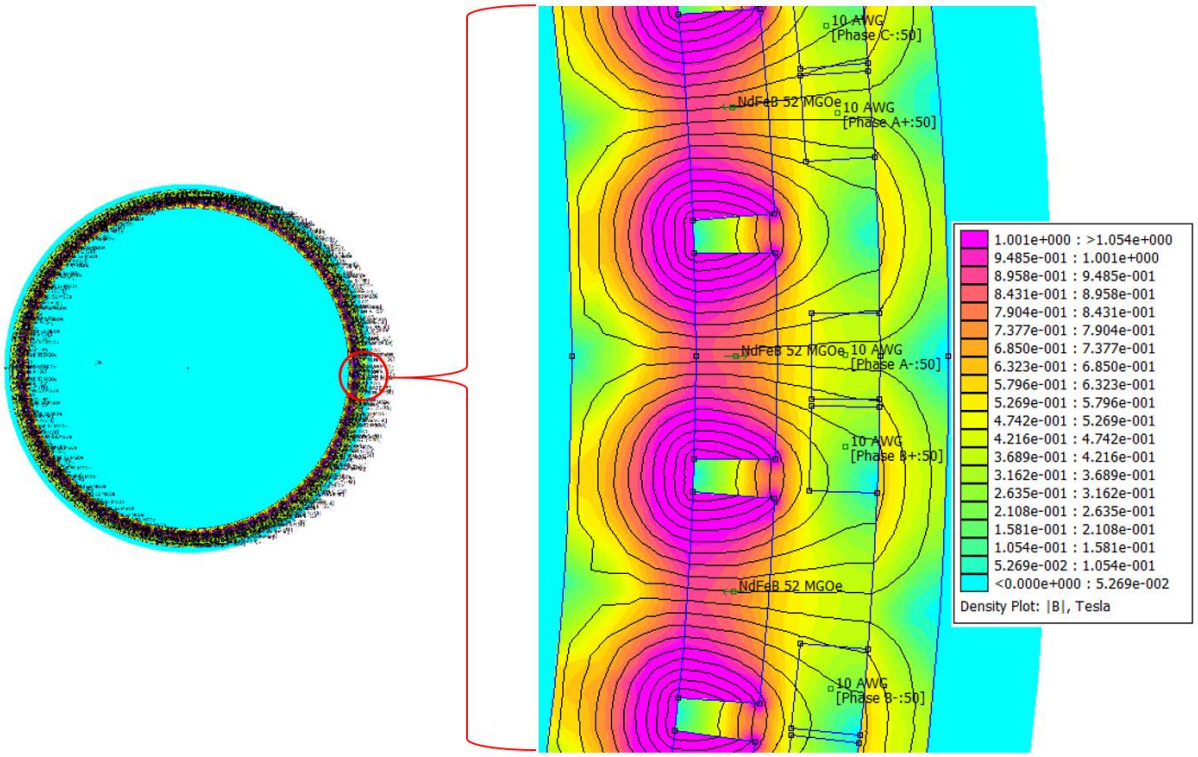

Figure 5-2 Magnetic flux density in the air-gap winding machine using FEMM

Using FEMM package in this study consists of eight steps:

- Machine description including dimensions and properties.
- Model analysis.
- Boundaries definition using the pre-processor, which is limited to five modes: the point, the segment, the arc segment, the block, or the group mode. The first four modes define the machine geometry and material properties, and the fifth mode is used to gather different objects into parts so that entire part can be manipulated more easily.
- Material description by identifying the block material properties, which exist in the FEMM built-in library.
- Boundary conditions: property specification of the boundaries of the solution domain. Three boundary conditions are used in FEMM, which are: 1- The Dirichlet where the value of the vector potential is explicitly defined on the boundary. 2- The Neumann where the normal derivative of the vector potential is specified along the boundary. 3-

The Robin where the boundary condition is linear combination between the other two boundary conditions [185].

- Mesh generation: FEMM divides the problem into large number of triangles. Mesh size values can be controlled in each area to increase the accuracy.
- Numerical solution: According to Meeker [186], FEMM uses the finite element method to obtain approximate solutions to the partial differential equations. The work concept, basically, depends on dividing the full studied region into small non-overlapping sub-regions called finite elements where simple approximations may be sufficed. The simple geometry (triangles) of a finite element allows approximating a solution for the partial differential equation by a simple polynomial function. The polynomial functions have to be pieced together in order to maintain the continuity of the field. The variation integral then is evaluated as a sum of contributions from each finite element. The result will be a finite algebraic system for the approximate solution of the infinite dimensional partial differential equation [185].
- Post processing: flux and current density plots, flux lines contour plots, flux density and intensity vector plots, and line and volume integral calculations along specified contour line and specified volume defined from a closed contour line respectively.

5.3.1. No-load case

The comparison between Equation (4.58) and FEM for different static rotor eccentricities displays similar outcomes for the magnetic flux density in the air-gap as shown in Figure 5-3. This verifies the accuracy of the analytical model proposed in Chapter 4 to be used later in the multi-body simulation in Chapter 7. Figure 5-4 illustrates the effect of rotor eccentricity on the magnetic flux leakage. The bigger the eccentricity, the higher the magnetic flux leakage at the maximum air-gap length side. That is expected according to Equation (4.60) where the magnetic reluctance is proportional to the mechanical airgap length (the distance between the magnets surface and the windings surface). The relationship between the air-gap length and the magnetic flux density whilst ignoring the magnetic flux leakage is expected to be linear and represented by the red dashed straight line in Figure 5-4, whereas, the numerical results, which are represented by the continuous blue line, illustrate the effect of the rotor eccentricities on the magnetic flux leakage.

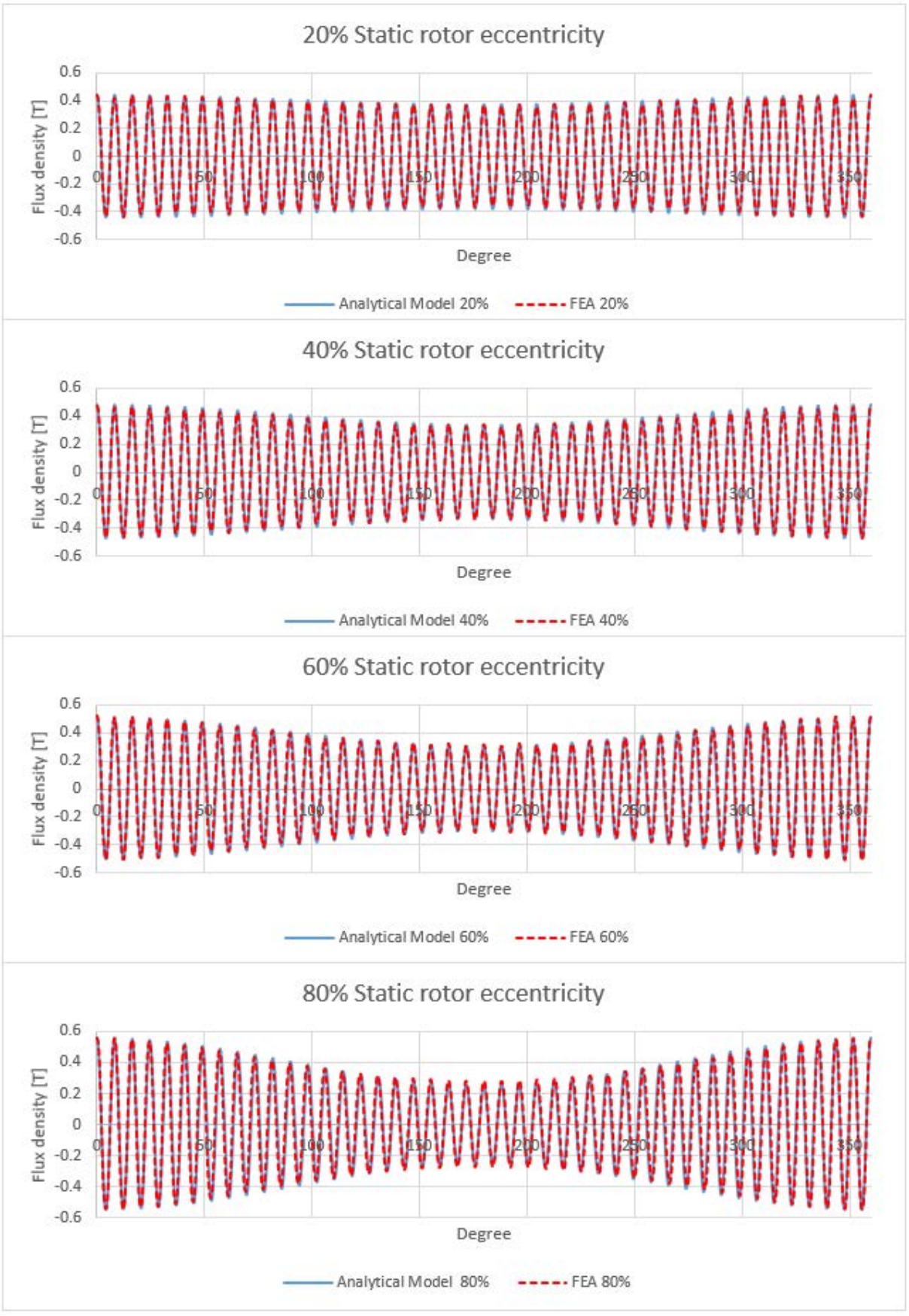

Figure 5-3 Air-gap flux density with different rotor eccentricities.

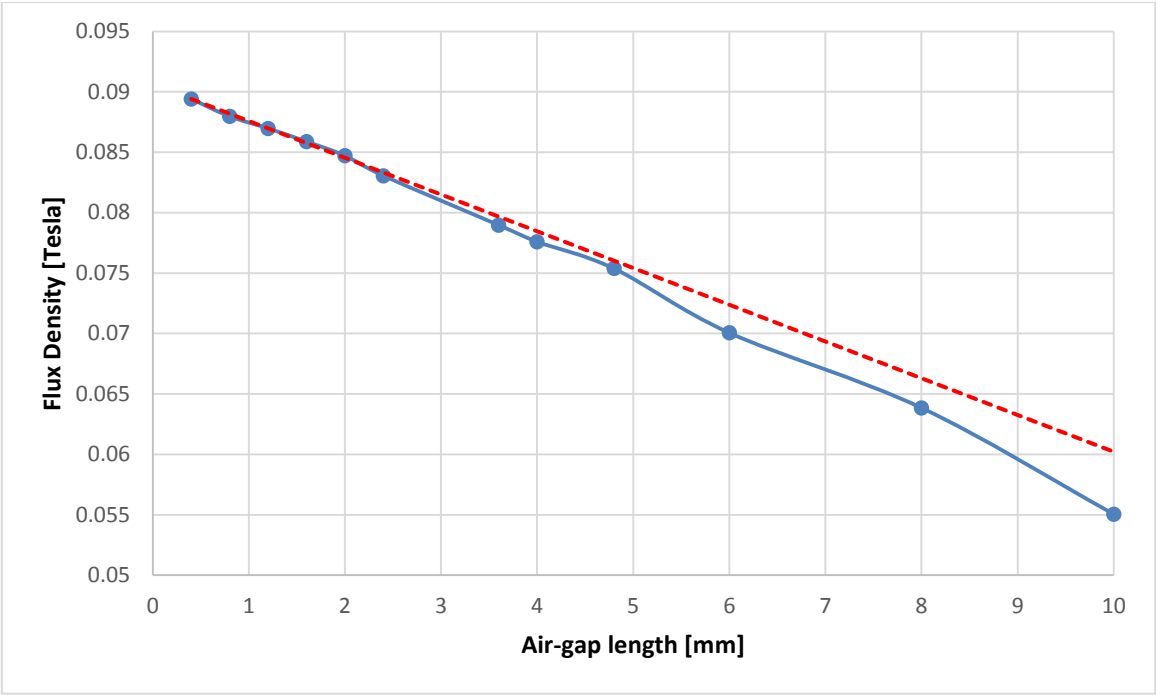

Figure 5-4 The effect of the air-gap length on the flux leakage in a 47.7 kW air-gap winding machine (The straight dashed red line represents the expected magnetic flux density in case of no leakage).

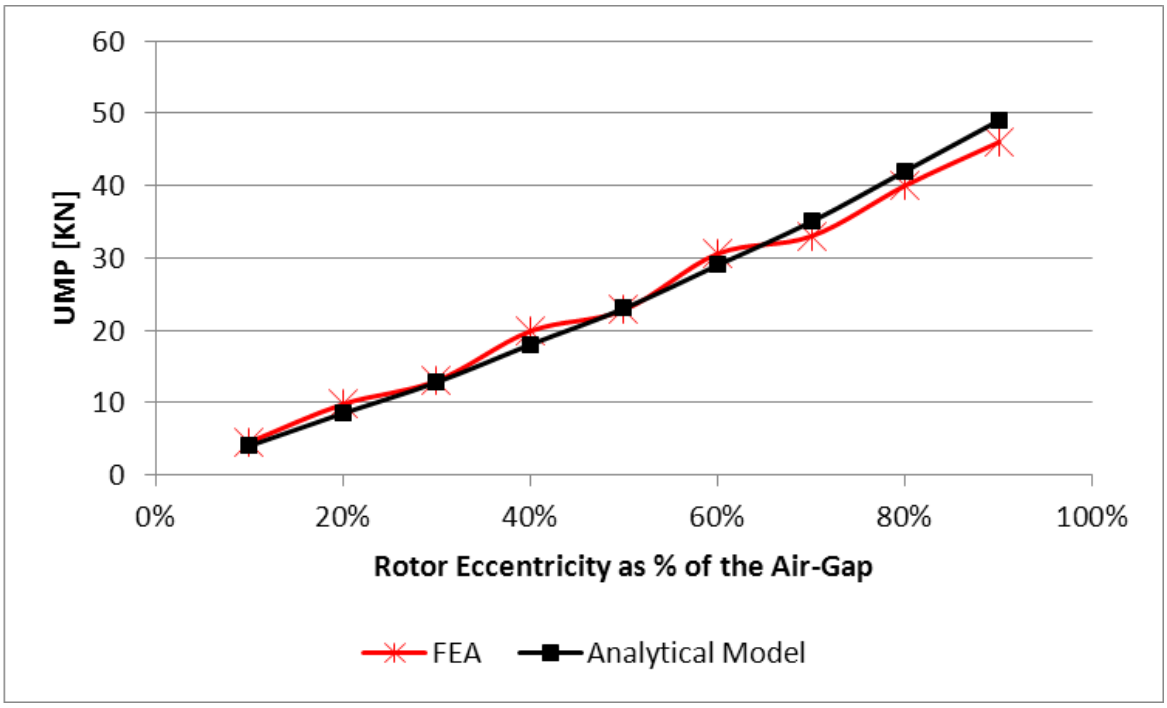

Figure 5-5 UMP for different rotor eccentricity results for both the FEA and the analytical model.

The difference between the FEA results and Equation (4.59) results for UMP calculations for different static rotor eccentricities is small as shown in Figure 5-5. The results clearly indicate a linear relationship between the static rotor eccentricity and the induced UMP in the proposed air-gap winding PM machine, which agrees with the literature (see chapter 3). For quick

estimations, it could be beneficial to notice that the induced UMP for 20% static rotor eccentricity of the mechanical air-gap length is roughly equivalent to a third of the air-gap winding PM machine's weight.

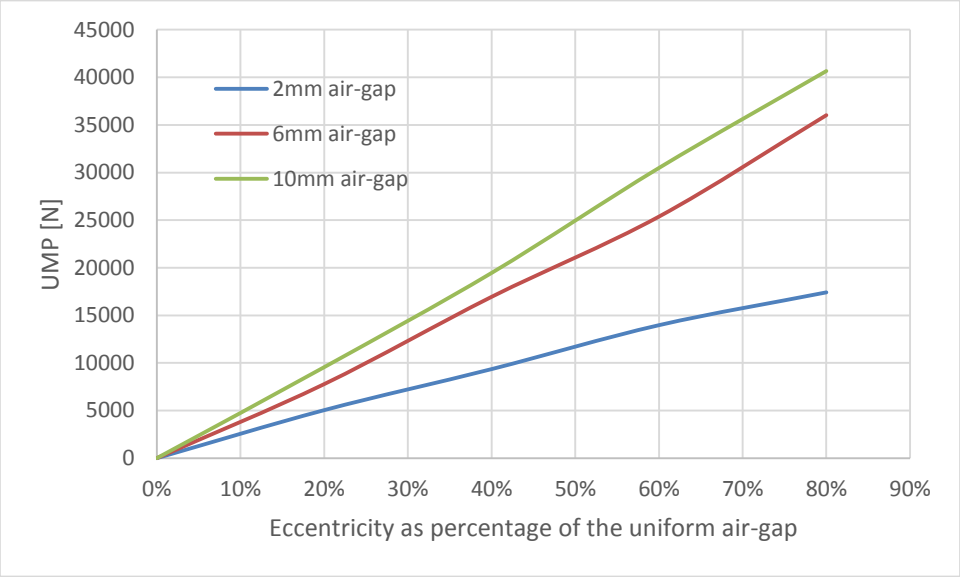

Figure 5-6 The induced UMP for different rotor eccentricity values in a 47.7kW air-gap winding PM generator under no load case with three different air-gap designs.

The mechanical air-gap length in the proposed air-gap winding PM machine is 10mm, which guaranties easier manufacture, assembly and maintaining stability during operation. Redesigning the machine with smaller mechanical air-gap length requires more complicated assembly mechanism but, on the other hand, provides a few advantages such as: - Reduction in material mass because an increase in air-gap is compensated for by an increase in the core length, which is reflected in the cost associated with the materials. - The impact of eccentricity on the UMP is more significant for a large air-gap compared to a small air-gap as shown in Figure 5-6, which was obtained using numerical FEM models, where the induced UMP at 2mm mechanical air-gap design is about half the induced UMP at 10mm mechanical air-gap design for the same relative eccentricities.

Spatial UMP variation for one full electrical cycle (which is repeated after each electrical cycle) for 10mm airgap design with 80% relative static eccentricity is shown in Figure 5-7. It can be noticed that the range is about ±15% of the average UMP value. This variation is directly applied on the bearing showing the importance of studying the dynamic loading effect on bearing wear and life time, and is detailed in chapters 6 and 7. In order to examine the effect of the meshing sizing on the results accuracy, the same process was repeated but changing the

minimum meshing angle from 30° to 20°. The maximum error between the fine meshing and coarse meshing was found to be less than 10% as shown in Figure 5-7.

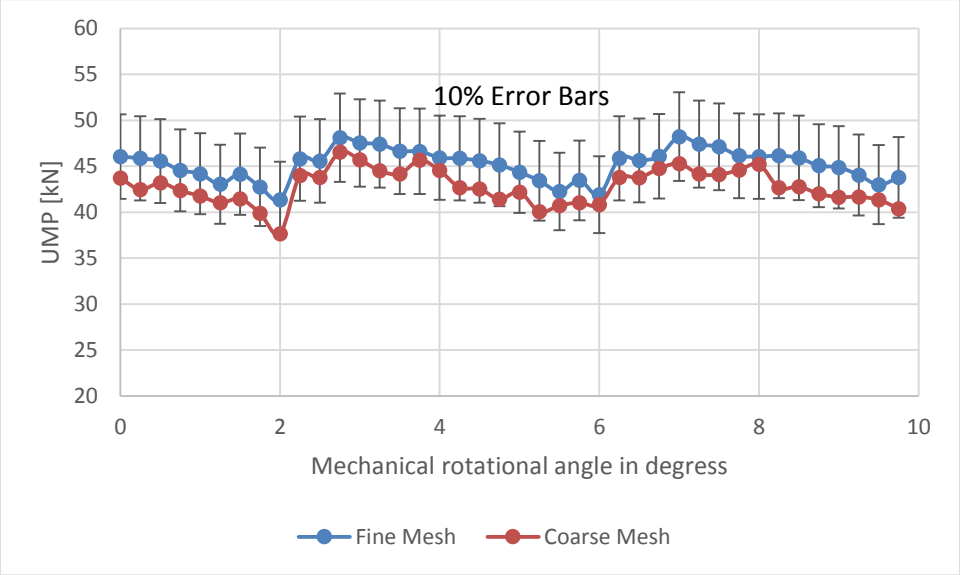

Figure 5-7 Spatial UMP variations for one electrical cycle for 10mm airgap design with 80% eccentricity

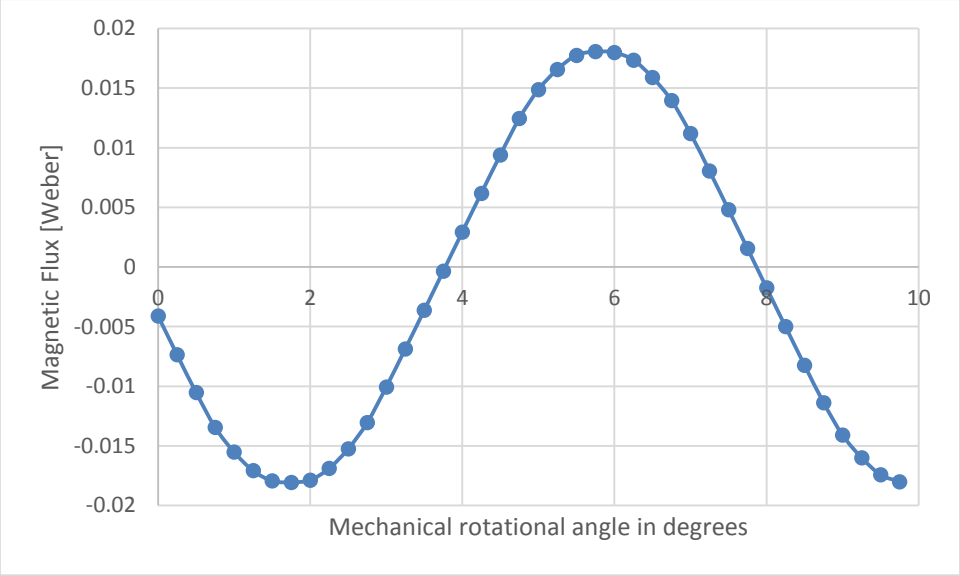

Figure 5-8 PM flux against mechanical rotor angle for 10mm airgap design with 80% eccentricity

The curve of PM flux against mechanical rotor angle for 10mm air-gap design with 80% rotor eccentricity was obtained using FEM software at a series of rotor positions as plotted in Figure 5-8. It can be noted that the PM flux wave is close to a sinusoid. That also can be confirmed by applying Fast Fourier Transform FFT as shown in Figures 5-9, 10, 11, 12. FFT for both 10mm and 2mm air-gap designs reveals that 3^{rd}, 5^{th} and 7^{th} harmonics are a small percentage

of the fundamental component. The harmonics are more noticeable in the smaller air-gap design. The bigger the relative eccentricity, the higher the harmonics amplitude.

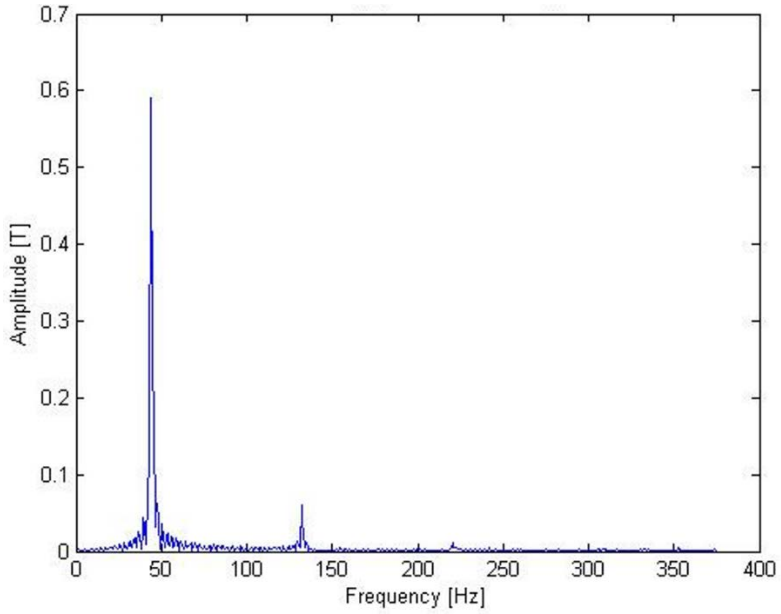

Figure 5-9 FFT for the airgap flux density in a 10 mm airgap design with 20% rotor eccentricity

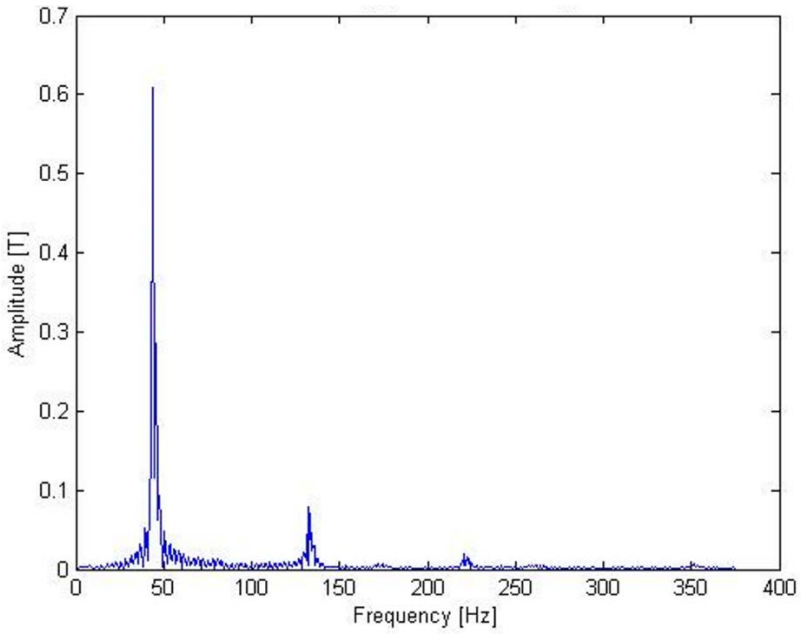

Figure 5-10 FFT for the airgap flux density in a 10 mm airgap design with 60% rotor eccentricity

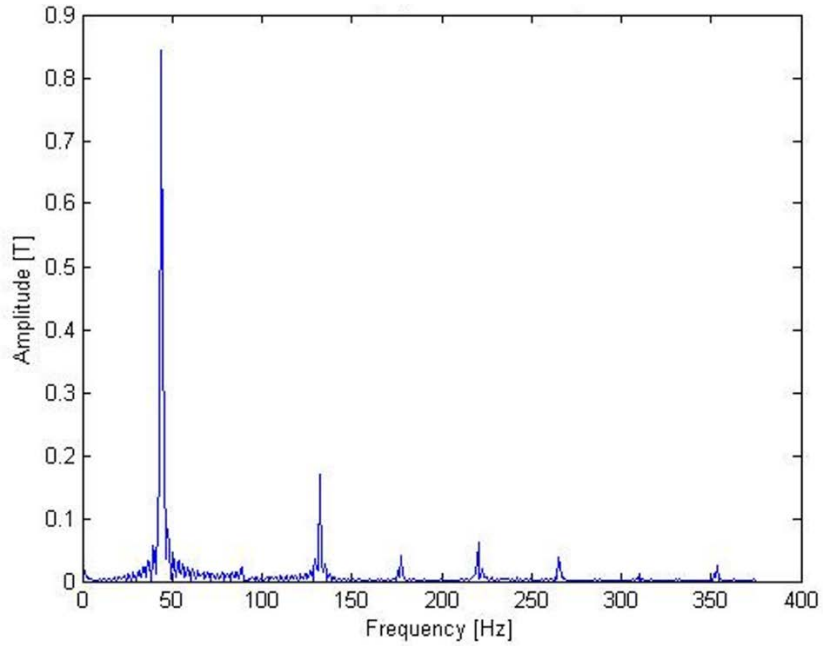

Figure 5-11 FFT for the airgap flux density in a 2 mm airgap design with 20% rotor eccentricity

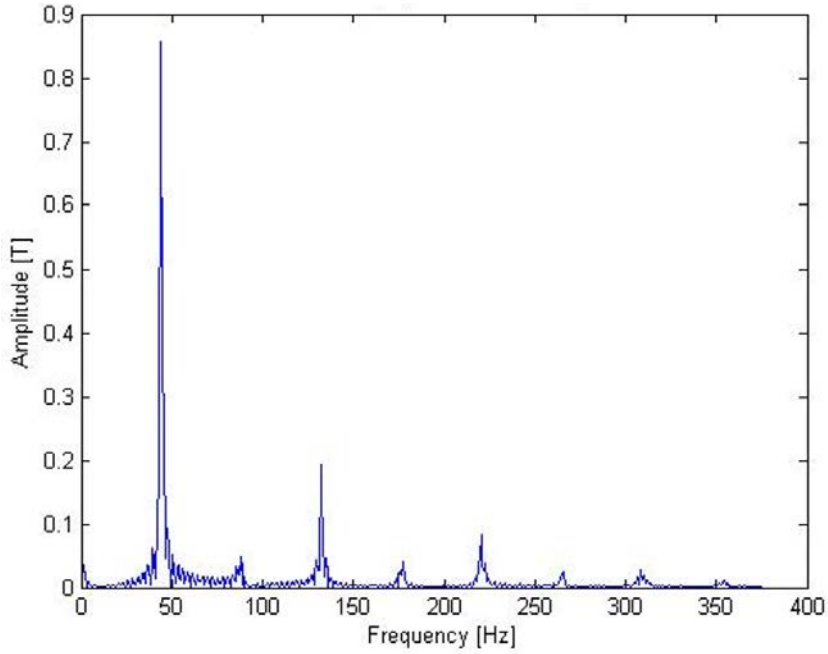

Figure 5-12 FFT for the airgap flux density in a 2 mm airgap design with 60% rotor eccentricity

5.3.2. Different loading cases

When the rotor rotates, a back Electromotive Force *emf* in the phase winding will be generated. The *emf* can be obtained by differentiating the PM flux against time (Faraday's Law) as

$$e_1 = \frac{d\lambda_1}{dt} = NK_{w_1}\frac{d\emptyset_1}{dt} = NK_{w_1}\frac{d\emptyset_1}{d\theta}\ pw_r \qquad (5.9)$$

Where λ_1, $\emptyset_1$, N and K_{w_1}, are phase winding flux linkage, flux, number of turns and winding factor respectively. θ, p, and w_r are the rotor angle in electrical radians, pole pair number, and the rotor rotational speed in mechanical radian per second.

The RMS (*Root-mean-square*) value of the fundamental *emf* is derived from Equation (5.9) as

$$E_1 = \sqrt{2}\pi f_1 N K_{w_1} \Phi_1 \qquad (5.10)$$

Where f_1 is the frequency of the *emf* and Φ_1 is the magnitude of the fundamental harmonic of the PM flux.

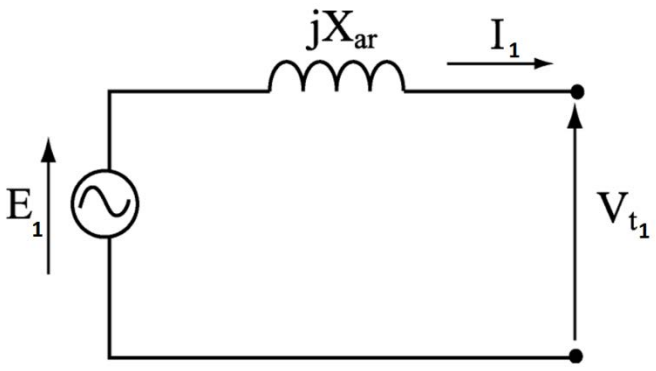

Figure 5-13 Equivalent circuit for one phase of the PM generator. X_{ar} is the armature phase winding impedance, ignoring the phase resistance

When no load is connected to the stator terminals, the rotor flux induces the *emf* E_1, which in this case equals the measured terminal voltage V_{t_1} as shown in Figure 5-13, and no electrical current will exist in the windings. When the stator starts to supply a load, an electrical current I_1 will flow in the windings. Assuming an inductive load or lagging power factor, the stator current I_1 will lag both the terminal voltage V_{t_1} and the *emf* E_1. This current flowing through the stator (or armature) windings produces a magnetic field that rotates at the same speed as the rotor. This flux $\Phi_{1_{ar}}$ associated with the armature current I_1 is in phase with this current. This magnetic flux $\Phi_{1_{ar}}$ will induce an *emf* $E_{1_{ar}}$ in the armature windings (commonly known

as armature reaction voltage), and this *emf* $E_{1_{ar}}$ is 90 electrical degrees lagging both the armature current I_1 and the armature flux $\Phi_{1_{ar}}$ as shown in the phasor diagram in Figure 5-14.

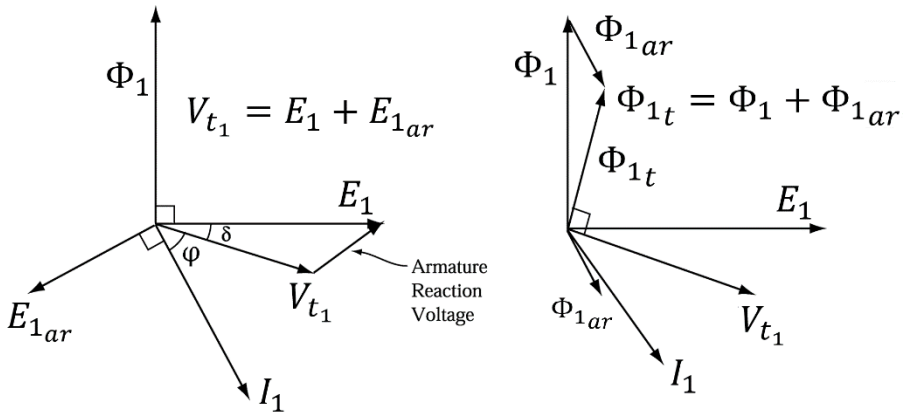

Figure 5-14 Phasor diagrams for PM generator

The total air-gap magnetic flux under any load condition can be calculated by summing the open-circuit flux produced by the rotor PMs and the armature reaction flux generated by the three phase induced currents.

$$\Phi_{1_t} = \Phi_1 + \Phi_{1_{ar}} \tag{5.11}$$

The angle between the phasors E_1 and V_{t_1} is known as the load angle δ.

The three phase generator electrical currents are given as

$$\begin{aligned} i_1 &= I_1 \cos w_r t \\ i_2 &= I_2 \cos(w_r t - 120) \\ i_3 &= I_3 \cos(w_r t + 120) \end{aligned} \tag{5.12}$$

The effect of armature reaction on magnetic flux distribution and UMP in both parallel and series winding connection cases with both static and dynamic eccentricities seems to be very small and can be disregarded as shown in Figures 5-15, 16. As the implemented open-source FEM software does not support the simulation of both the stator loading 3-phase alternating currents and the rotor permanent magnets simultaneously, Figures 5-15, 16 were obtained by loading the stator coils using instantaneous direct currents with different amplitudes. The direct current amplitude for each coil was calculated and applied automatically for each rotor rotation step using LUA scripting language (LUA is a powerful, efficient, lightweight, embeddable and open source scripting language supports FEMM [187]). For each instantaneous rotor position,

a new mesh and UMP calculation was implemented. The spatial UMP variation shown in Figure 5-7 is mainly due to the slotting effect and could cause vibration and noise in the machine. Figure 5-15 shows the magnetic flux passing throw two opposite stator winding circuits when an 80% relative static eccentricity is applied. The first circuit is located at the smallest airgap side and the opposite circuit is located at the biggest airgap side. The only effect for the armature reaction that can be noticed is a very small magnetic wave shifting without distorting the wave itself. That small effect can be justified by the small percentage of the magnetic field induced by the stator currents compared to the PMs field, and the no-distortion effect is a result of the synchronous rotor and stator magnetic fields.

The small effect of the armature reaction on the airgap magnetic flux is reflected as a small effect on the induced UMP as well as shown in Figure 5-16 where the loading effect can hardly be noticed comparing to the no-load case.

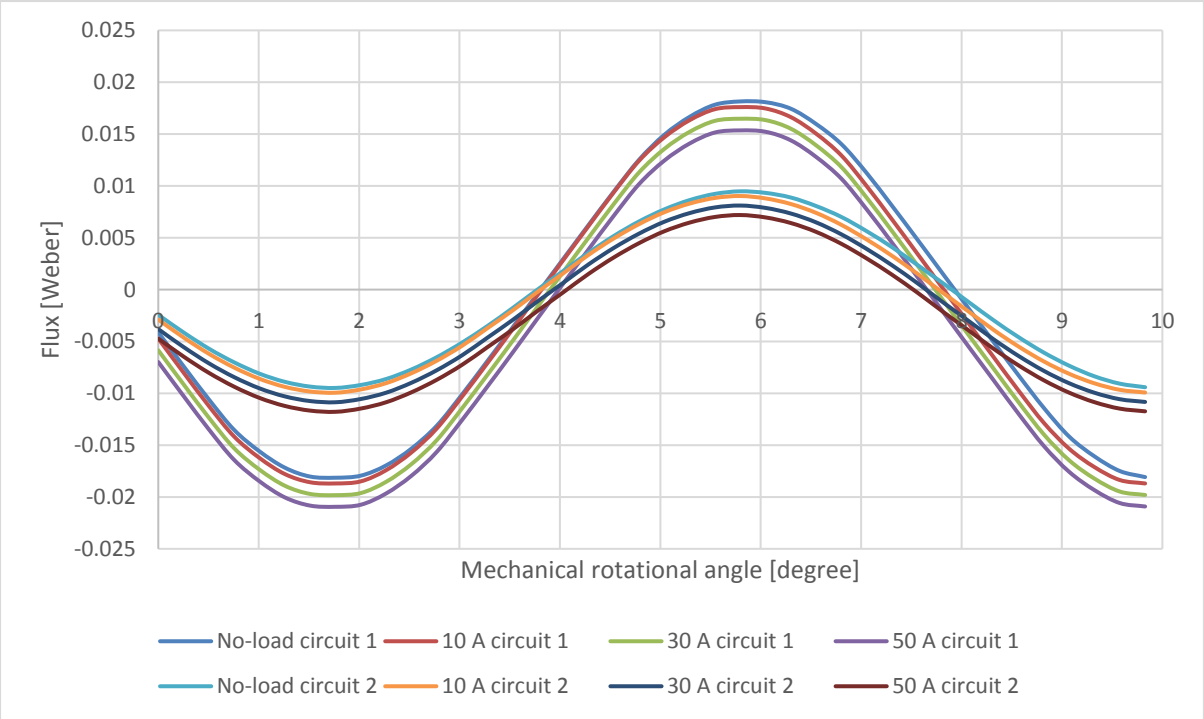

Figure 5-15 The effect of armature reaction with different loading cases on the flux distribution in two opposite side circuits in a 47.7 kW air-gap machine with 80% static rotor eccentricity and 10 mm air-gap design

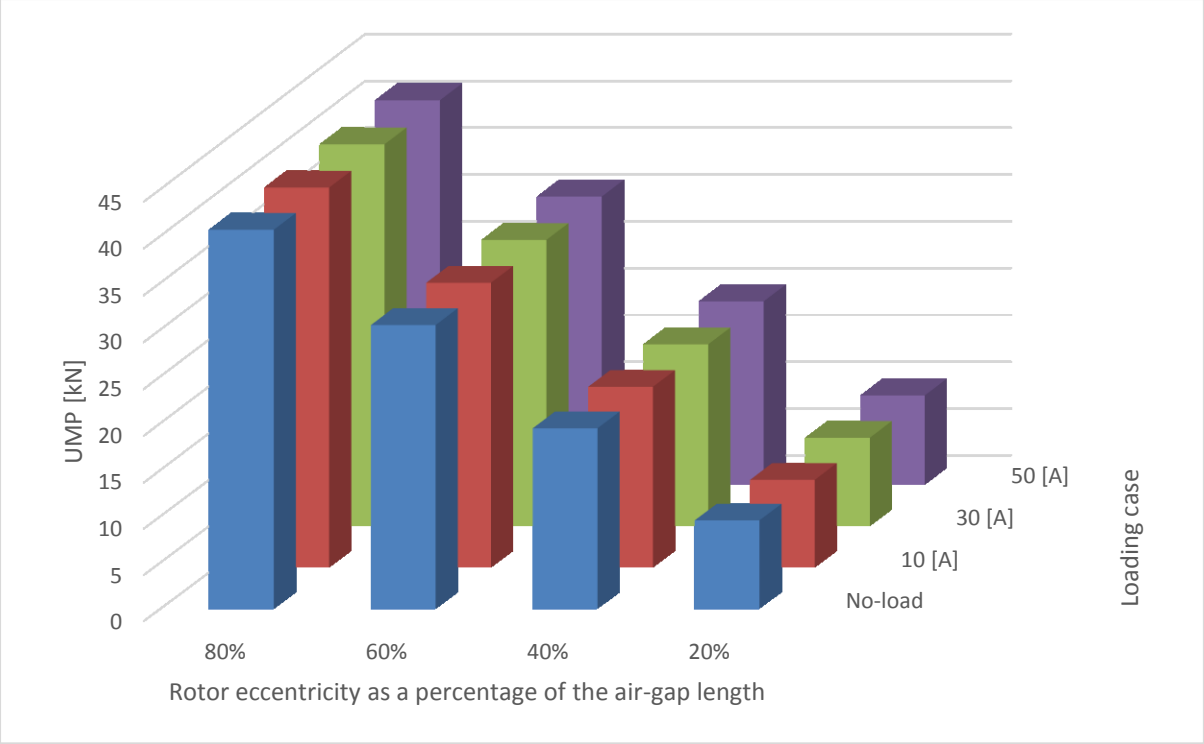

Figure 5-16 The effect of different loading cases and different rotor eccentricity values on the induced UMP

5.4. Iron-cored PM machine case study

In order to illustrate the effect of rotor eccentricity and armature reaction on the induced UMP in iron-cored permanent magnet machines, an 11kW slotted permanent magnet machine is modelled and simulated. The parameters of the machine are given in Table 5-3. The reason behind choosing this particular machine is the ability of validating this machine's numerical model results with experimental results shown in the section 5.5.

Rated power	11 kW
Axial length	111 mm
Nominal voltage	330 V
Nominal current	23.3 A
Nominal air gap	1.65 mm
Air gap diameter	104 mm
Magnet height	5 mm
Number of slots	36
Number of poles	8
Number of turns	10

Table 5-3 Permanent Magnet Machine Parameters

Similar to the steps taken to study the airgap winding machine, the same two-dimensional finite element method (FEM) open-source software was used to study the effect of rotor eccentricity on the magnetic flux density in this iron-cored generator's airgap and hence the induced UMP for different levels of eccentricity. 30° minimum meshing angle was also chosen for accurate analysis. A two-dimensional diagram of the iron-cored machine showing the flux density lines is illustrated in Figure 5-17.

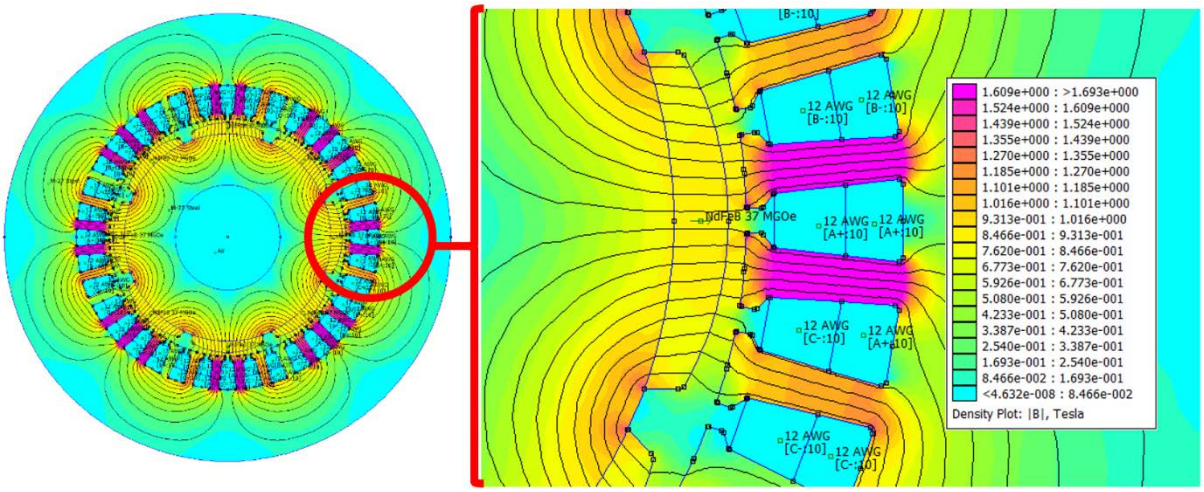

Figure 5-17 Cross-section of an 11kW permanent magnet machine with concentric rotor

In order to investigate the armature reaction effect on the induced UMP, results are presented for the no-load case and for loading up to 30A.

5.4.1. No-load case

It is shown in [164] that an increase in static eccentricity causes an increase in the magnitude of the permeance in one side of the air gap and a decrease on the opposite side. That leads to a corresponding change in the magnitude of the air gap flux density, which induces UMP. The relationship between static rotor eccentricity and UMP for the studied generator using FEM software is linear as shown in Figure 5-18. The flux density distribution in the air gap with 40% eccentricity is shown in Figure 5-19. The rotor was horizontally displaced on the x-axis; therefore, the flux density magnitude in the figure varies with the circumferential distance and it has a maximum peak where the airgap length is minimum, as shown in the Figure 5-19, and minimum peak where the airgap length is maximum. The slotting effect on the flux density distribution is clear in this figure as a wave distortion whereas the flux density wave was smooth in the airgap winding PM machine.

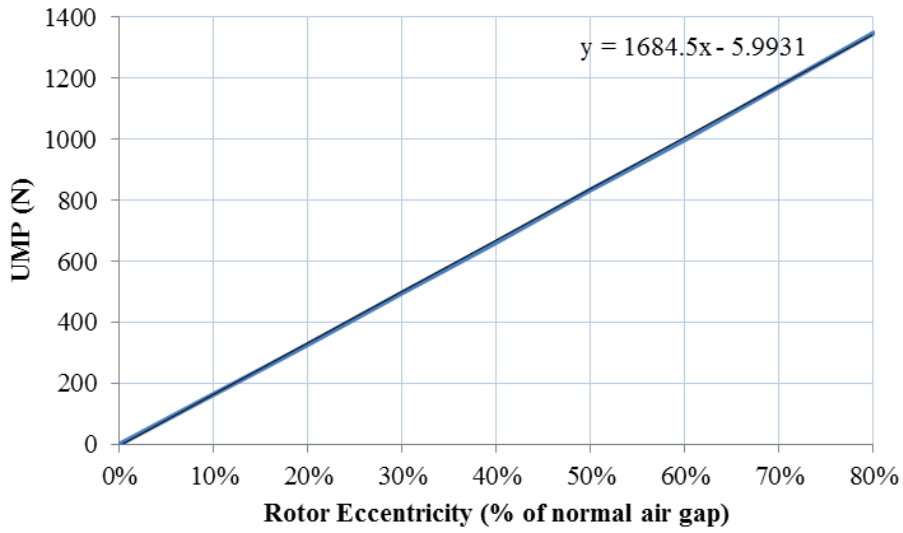

Figure 5-18 Graph of UMP versus rotor eccentricity for the modelled generator

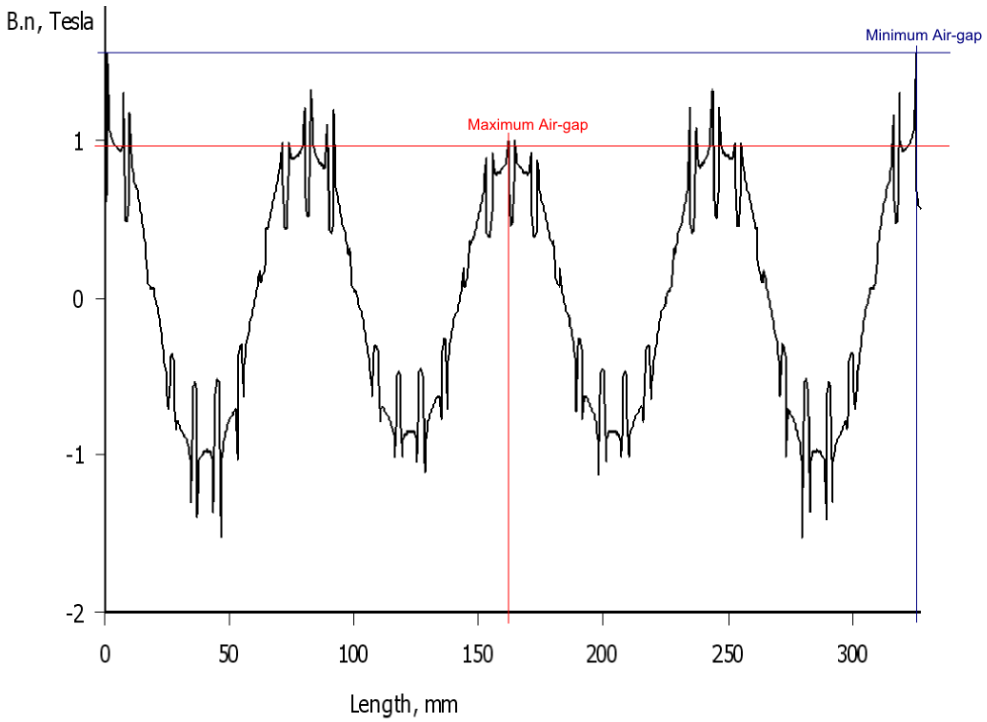

Figure 5-19 Flux density distribution in the air gap with 40% eccentricity

5.4.2. Different loading cases

Similar to subsection 5.3.2. for the airgap winding machine, the effect of armature reaction on UMP in both parallel and series winding connection cases with both static and dynamic eccentricities seems to be very small and can hardly be noticed as shown in Figure 5-20. As the open-source FEM software does not support the simulation of both the iron-cored stator loading 3-phase alternating currents and the rotor permanent magnets simultaneously, Figure

5-20 was obtained using the similar technique that was used with the airgap winding machine, which is loading the stator coils using instantaneous direct currents with different amplitudes. The direct current amplitude for each coil was calculated and applied automatically for each rotor rotation step using the LUA scripting language. For each instantaneous rotor position, a new mesh and UMP calculation were implemented. The spatial UMP variation shown in Figure 5-21 is for one full electrical cycle with 10% relative static eccentricity. This variation is a result of the rotor's pole width to pole pitch ratio and stator's slotting effect and it is a cause of slight vibrations and noise in the machine.

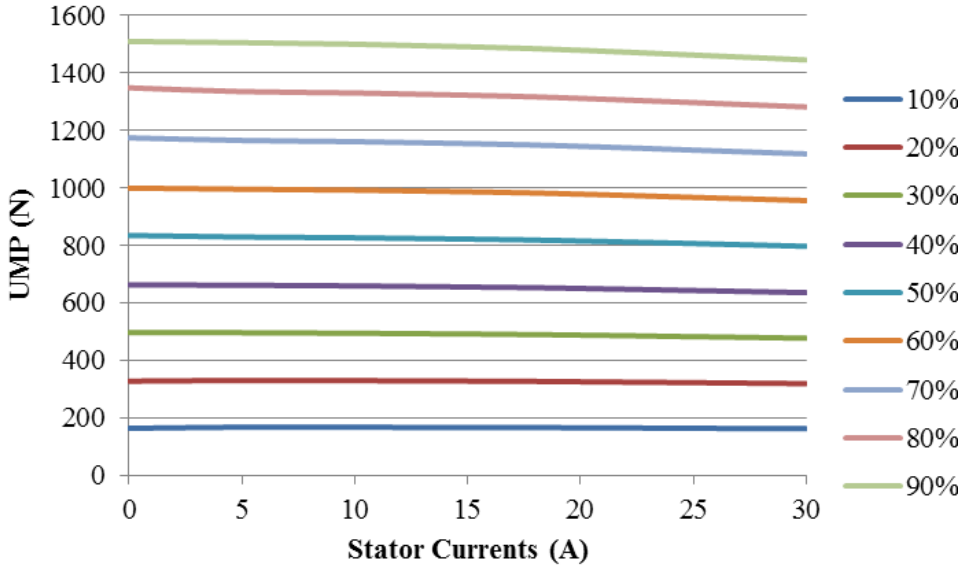

Figure 5-20 The effect of armature reaction on UMP, with different load cases and different rotor eccentricities.

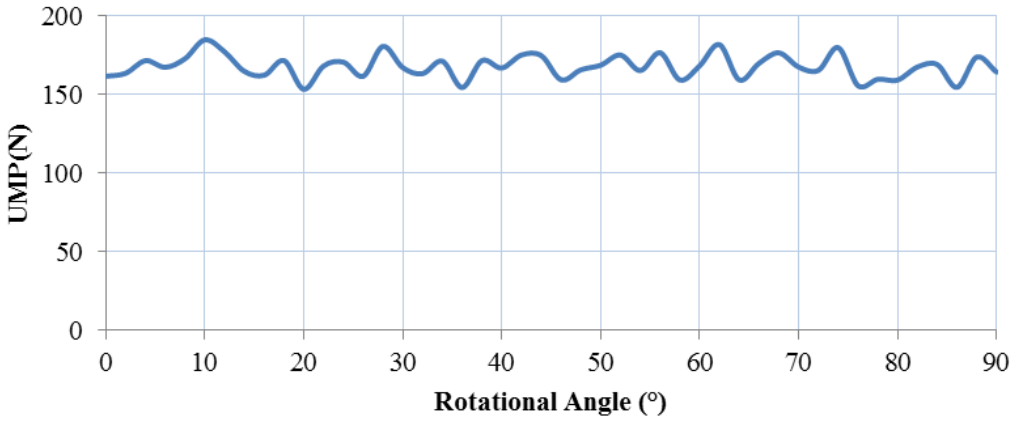

Figure 5-21 Spatial UMP variations for one electrical cycle with 10% eccentricity and 5A stator current

5.5. Test-Rig and Experimental Results

In order to verify the results obtained from both the Analytical and FEM numerical modelling, experimental work is required. Hence, this section describes an experimental test rig designed to introduce rotor eccentricity and measure unbalanced forces in the 11kW generator. Figure 5-22 shows a block diagram of the experimental test rig. The test generator is driven by a servo motor. A torque transducer connects the tested generator with the servomotor to measure the input mechanical power. The output of the generator is connected to a 3-phase load to control the power output from the generator. Measurement data from the torque transducer, force sensors, and power analyser all feed into a data acquisition unit [96].

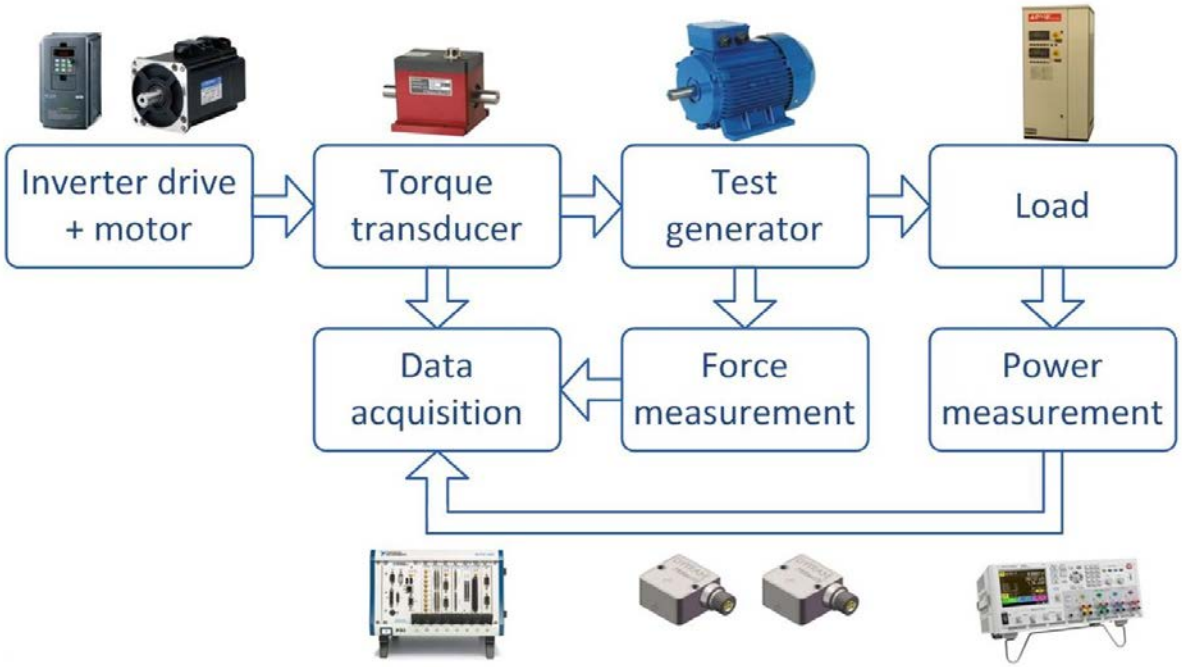

Figure 5-22 Block diagram of the experimental test rig for 11kW generator force measurement [96]

5.5.1. Creating Eccentricity

A certain eccentricity needs to be introduced into the generator in order to measure the induced unbalanced magnetic pull acting on the rotor. For experimental purposes, this can be created by physically moving the rotor in the radial direction relative to the stator. Electrical machines typically have a rotor, which is held in position by end caps mounted to the main body of the machine. Bearings in each end cap allow the rotor to rotate freely inside the machine. To create eccentricity, the rotor must be able to move independently from the stator. It is necessary, hence, to mount the rotor independently from the main body, which can be achieved by removing the end caps and mounting the rotor on external bearings. After mounting the rotor

on external bearings, eccentricity can be created by adjusting the rotor or the stator position. As the test generator is driven by a servo motor to emulate the input mechanical power from a wind converter, any adjustments for eccentricity should be made only to the stator. This allows the rotor to remain aligned to the rest of the drivetrain regardless of the amount of eccentricity created. Adjusting the vertical displacement of the stator is the simplest way of creating eccentricity. One way to achieved that is by inserting shims, tens of micrometres in thickness, between the main body of the generator and the platform to which it is secured. Hence, the addition or removal of each shim increments or decrements a fixed amount from the overall displacement of the stator. Alternatively, an adjustable micro-positioning platform can be used to lower or raise the height of the generator body.

5.5.2. Force Measurement

Unbalanced magnetic pull acts on the rotor in the direction of the narrowest air gap. This force needs to be measured with transducers that convert force into an electrical signal. The most widely used force transducers use either strain gauge or piezoelectric-based technology. Strain gauge load cells utilise the elastic range of the cell material to measure force. Strain gauges bonded to the material (such as steel or aluminium) change in electrical resistance as the material deforms under an applied force. Hence, strain gauge load cells require deformation in order to measure force. This is not desirable for measuring generator forces due to eccentricity as deformation causes a change in the air gap that leads to a change in eccentricity.

Piezoelectric force transducers require less deformation to generate an electrical signal. They utilise crystalline materials that generate an electric charge on the surface when a force is applied. They are inherently stiffer than strain gauge load cells and have a higher frequency response, which is more suitable for dynamic measurements. However, they are less suitable for static measurements compared to strain gauge load cells due to charge leakage in the charge amplifiers. Multiple piezoelectric crystals can be stacked to create a multi-component force transducer.

Piezoelectric force transducers were chosen due to their superior stiffness and characteristics under dynamic loading. Whilst the use of multiple single-axis transducers would have been a more cost-effective option, there is complexity in mounting multiple transducers without each transducer interfering with the force measurement of others. Hence, multi-axis transducers were chosen for the test-rig.

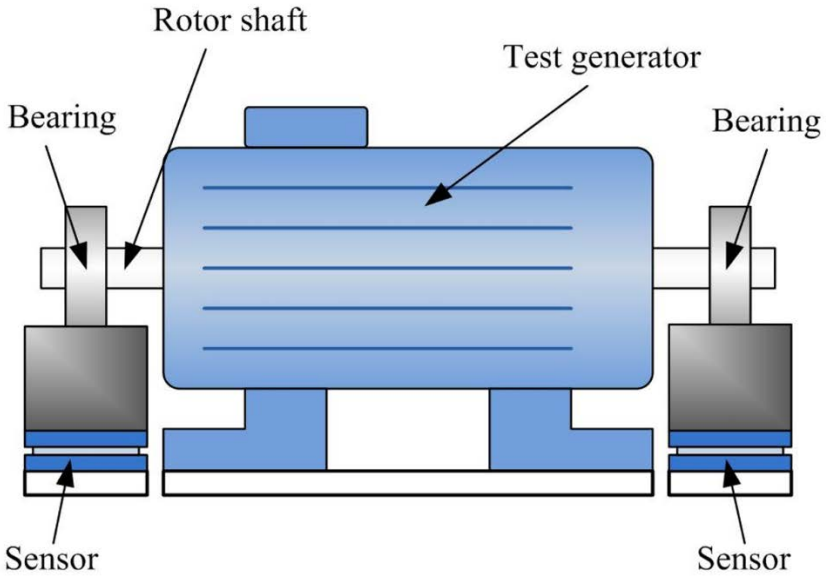

Figure 5-23 Diagram showing the rotor mounted on external bearings and force sensors beneath the bearing units [96]

From Newton's third law it can be deduced that UMP can be measured on the rotor or the stator given that the forces should be equal and opposite in nature. Hence, transducers can be mounted under the rotor or the stator, supporting the full weight of either, in order to measure the unbalanced force. Figure 5-23 shows a diagram of the rotor mounted separately from the stator on external bearings, with force transducers beneath the bearing units.

5.5.3. Actual Test-Rig

As a part of a collaborating project between The University of Edinburgh in the UK and National Cheng Kung University (NCKU) in Taiwan funded by Engineering and Physical Sciences Research Council (EPSRC) and Taiwanese National Science Council, the actual test-rig was funded and established. The parameters of the permanent magnet generator used in the test-rig are provided in Table 5-3. A schematic diagram for the full test rig is presented in Figure 5-24.

Figure 5-25 shows a photograph of the adjustable micro-positioning platform before installing the tested generator and Figure 5-26 shows a photograph of the experimental test-rig after installing the tested 11kW PM generator. The second photograph shows the test generator with the end cap removed. The original bearing is still located on the rotor shaft although it does not perform any function here. The larger external bearing is shown with one of the piezoelectric force transducers supporting the bearing housing. It should be noted that during operation, the

external bearing would be positioned closer to the original bearing in order to minimise flexibility in the rotor shaft, which may cause oscillations.

The piezoelectric force transducer has an output of 0.611mV/N and full specifications can be found in [188].

The experimental results are provided in Table 5-4. Comparing the experimental results with the numerical modelling results for the tested 11kW PM generator shows good level of similarity as illustrated in Figure 5-27. All results are under no-load condition. The experimental results are slightly different than the numerical results which can be justified by:

- The difficulty of taking very accurate measurements
- The accuracy of the measuring instruments
- The possible extrinsic UMP, which could be caused by the inaccurate assembly of the generator components (see section 3.3.) and that was not included in the analytical and numerical models.

The experimental results for this PM generator can verify the accuracy of the numerical modelling, which also showed similarity to the analytical model. Numerical results for other PM machines, hence, can confidently be adopted.

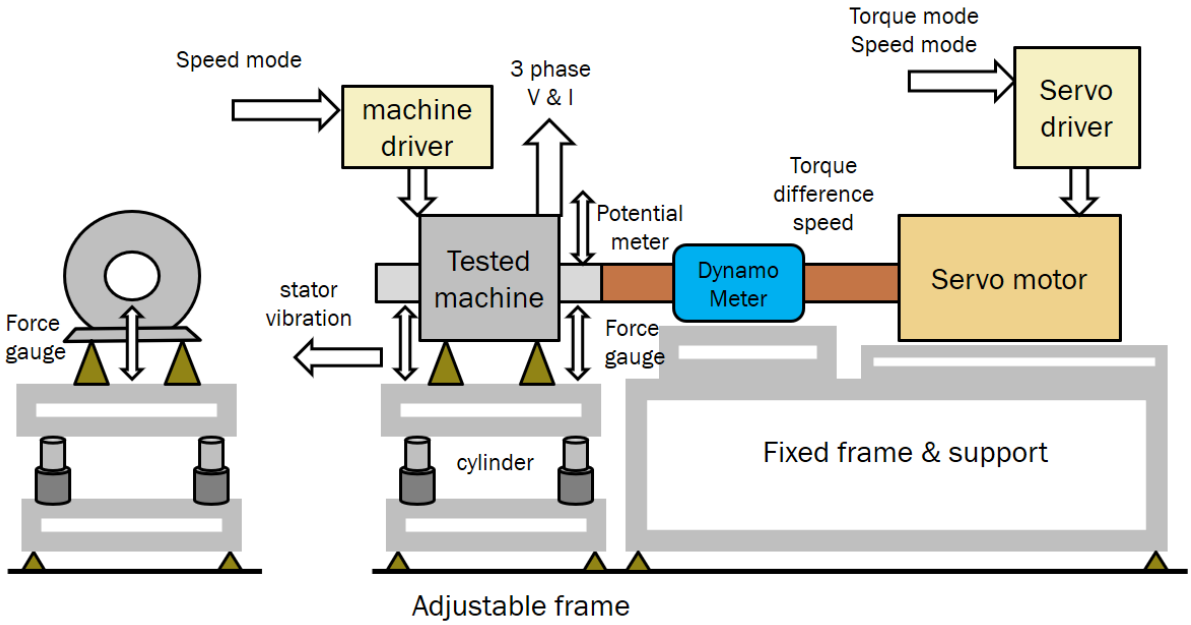

Figure 5-24 Schematic diagram for the full test rig

Figure 5-25 The adjustable micro-positioning platform before installing the tested generator

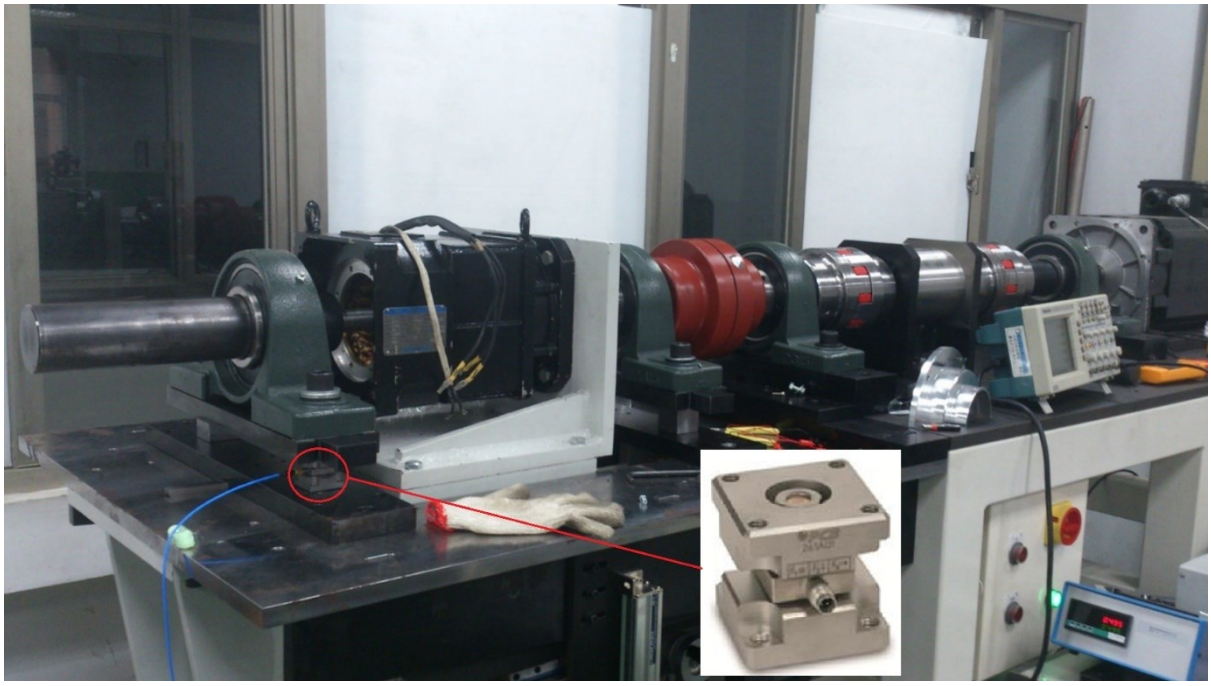

Figure 5-26 Full test rig with the tested 11 kW PM generator

Stator Position [mm]	Sensor Voltage [mV]	Force Applied on the Sensor [N]	Total Force on 4 Sensors [N]	UMP [N]
0.8	-331	-541.735	-2166.94	628.48
0.6	-359	-587.561	-2350.25	445.17
0.4	-385	-630.115	-2520.46	274.96
0.2	-401	-656.30	-2625.20	170.21
0	-427	-698.85	-2795.42	0
-0.19	-456	-746.32	-2985.27	-189.85
-0.4	-481	-787.23	-3148.94	-353.52
-0.6	-516	-844.52	-3378.07	-582.65
-0.78	-530	-867.43	-3469.72	-674.30

Table 5-4 UMP experimental results for different stator positions for 11kW PM generator. The machine gravitational force is 2795.42N

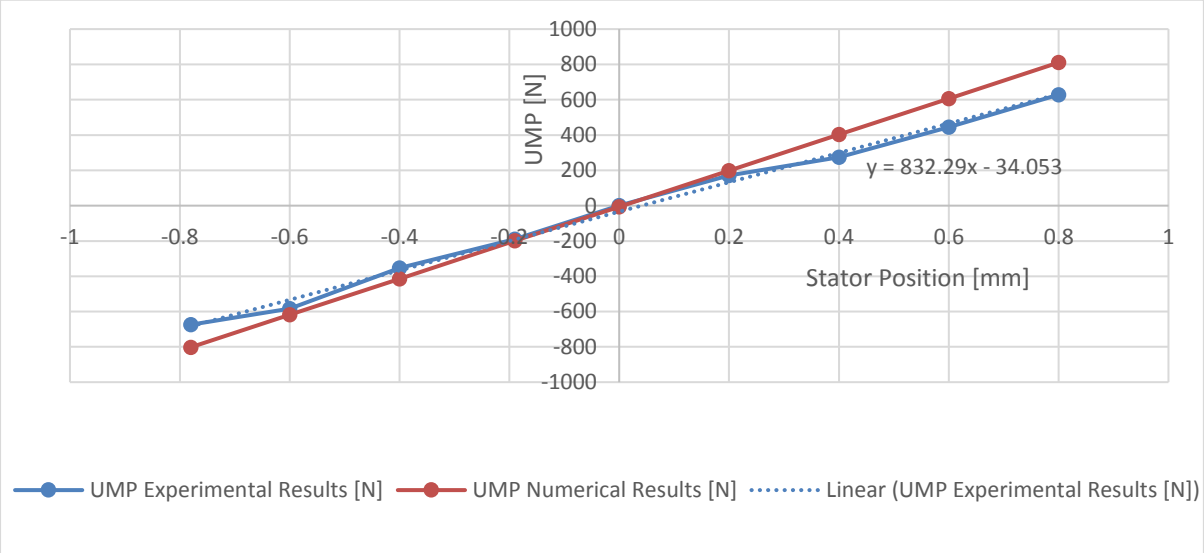

Figure 5-27 Comparison between the experimental and the numerical UMP results for stator displacement for 11kW PM generator

Even though, the concentration in this thesis is on PM generators, and for the sake of comparison, it is worth mentioning that the same UMP tests were repeated on a similar capacity (11kW) induction machine. The main goal was comparing the induced UMP for same relative eccentricity between the PM machine and the induction machine. Figures 5-28, 29, show the induction machine with the end cap removed. Similar to the PM machine, the original machine bearing is still located on the rotor shaft although it does not perform any function here. The induction machine was tested as a motor with rotor eccentricity and no load. The induction motor was fed by 50V and 15A alternating current. The voltage and current were limited because of the auto transformer specifications. The induction machine was not tested as a generator and the windings were not connected to the grid for safety reasons. The first attempt, as shown in Figure 5-28, was to balance the front side with one support that is the piezoelectric

force transducer. The main reason behind this attempt is increasing the results accuracy. This attempt was not successful because of the vibration. Therefore, the other support was installed back as shown in Figure 5-29 and in this case, the force transducer measured only one quarter of the total force.

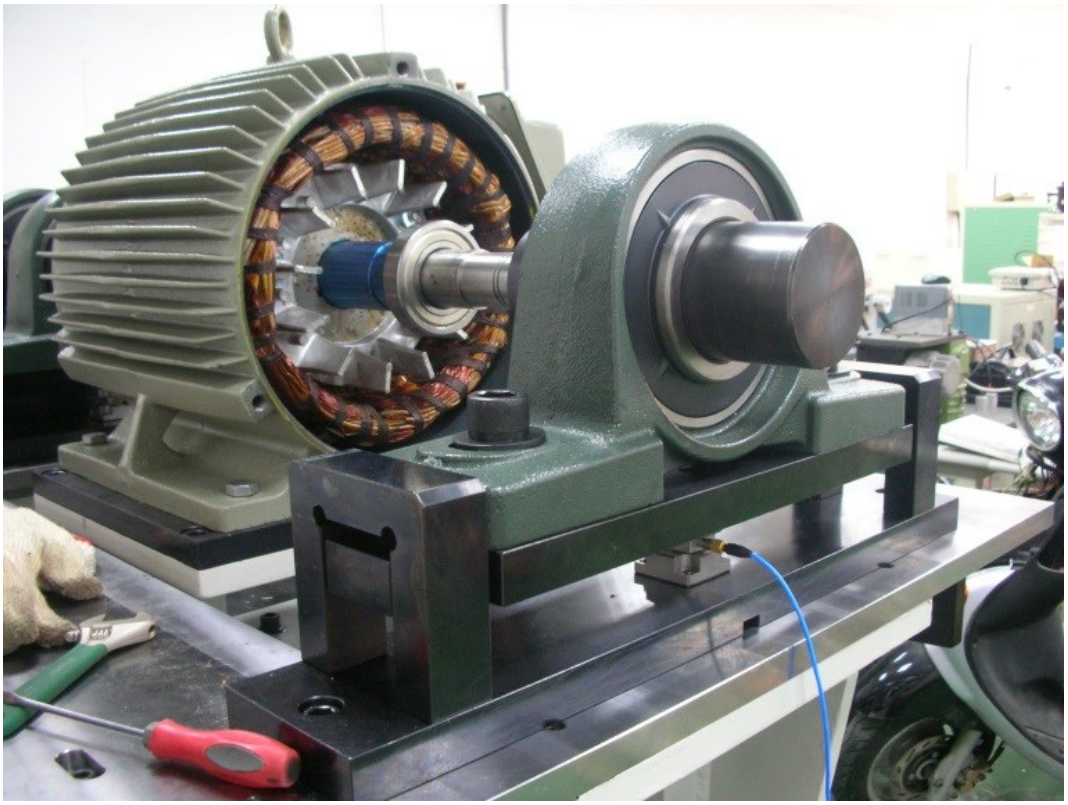

Figure 5-28 Induction generator replacing the PM generator in the test rig. Trying to balance one piezoelectric force transducer in the front side

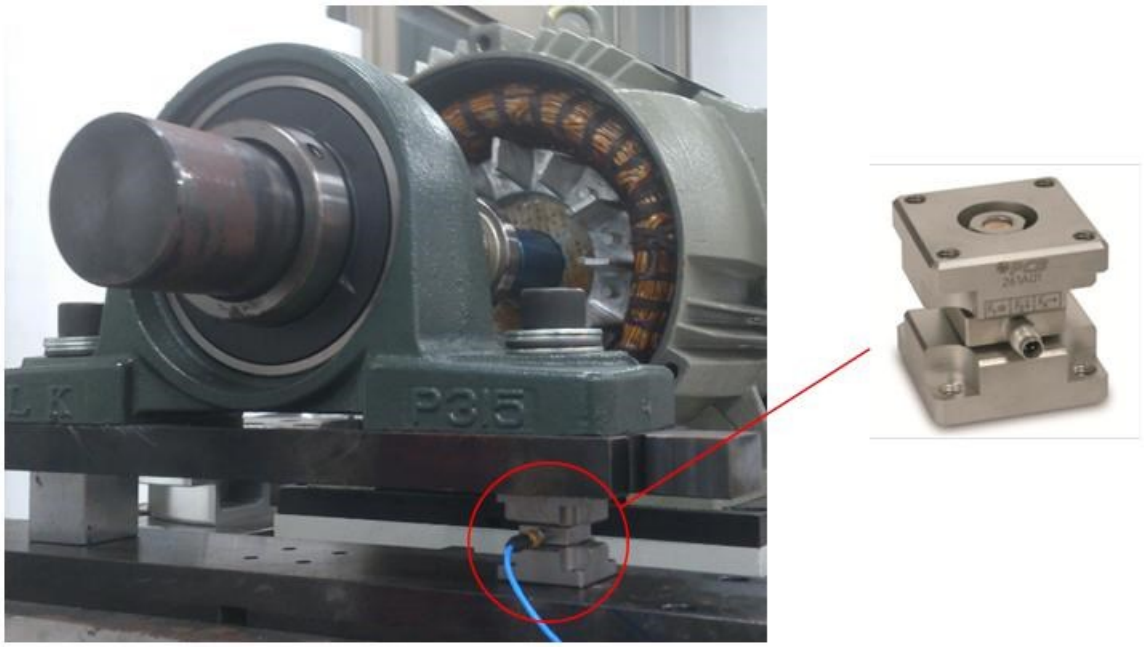

Figure 5-29 The induction generator having 4 supports, one of the supports is the piezoelectric force transducer measuring one quarter of the total force

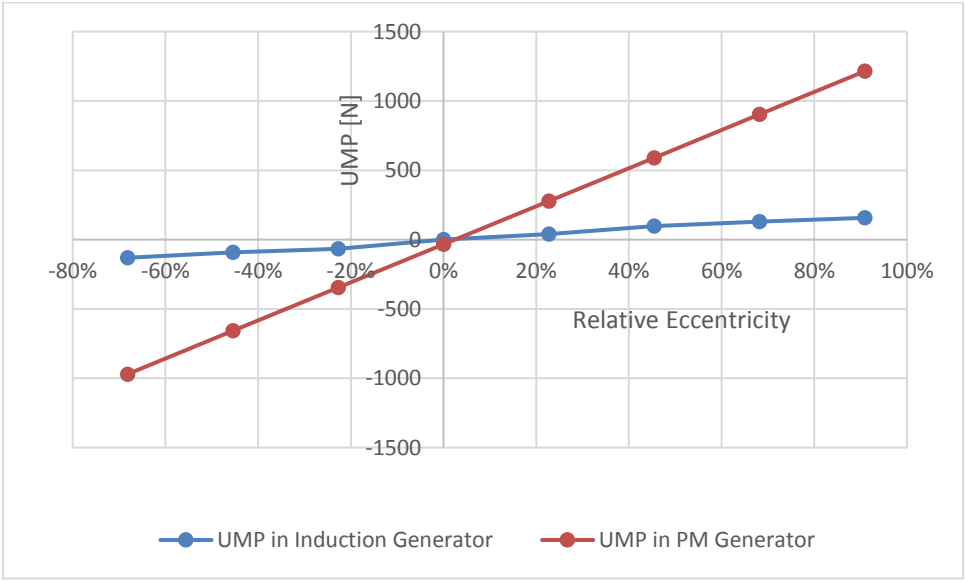

Figure 5-30 Comparison between the experimental UMP results for different relative eccentricities for 11kW PM and induction generators

The comparison results are shown in Figure 5-30. The induced UMP in the PM generator is about eight times bigger than the induced UMP in the induction generator for same relative eccentricities. That is mainly because of the high PM magnetic field in the PM generator that generates a big UMP for any relative eccentricity comparing to the induction generator airgap magnetic field and induced UMP.

5.6. Conclusion

The first part of this chapter provided a brief review about common methods that are used in numerical modelling for electrical machines. The second part provided numerical models using FEM to calculate UMP in two different PM generators namely, 47.7kW airgap winding PM generator and 11kW iron-cored PM generator. The main goal of the second part is verifying the analytical models presented in Chapter 4 and proving the linear relationship between the static rotor eccentricity and the induced UMP; moreover, estimating the induced UMP as percentage of the machine weight for both the airgap winding machine and the iron-cored machine. It is found that for 20% relative rotor eccentricity, the induced UMP is roughly equal to a third of the machine weight for both machines.

The third part provided details about the test rig and the experiments applied on 11kW iron-cored PM generator. The experimental results verified the numerical results. That gives the justification for adopting the numerical model results of the 5MW generators presented in Chapter 6 and using them as inputs for the 5MW direct-drive wind turbine multi-body model presented in Chapter 7.

Results of UMP test for 11kW induction generator were also presented in this chapter and the comparison with the PM generator experimental results showed big difference. For the same relative eccentricity, UMP in the PM machine is about eight times higher than that in the induction machine.

Chapter 6. Direct-Drive Permanent Magnet Generator Design for a 5MW Wind Turbine

6.1. Introduction

In the earlier analytical and numerical UMP calculations for the 11kW (iron cored) and 50kW (air-gap winding) machines, the main goal was extracting generalized verified analytical formulas. The work has primarily focussed on these smaller machines as they have immediate access in the laboratory environment and in the case of the 11kW machine test results were available.

In practice, however, the real value of direct-drive generators is for larger scale implementation. For this reason, this chapter introduces a design incorporating additional shaft, bearing and generator details into an existing conceptual study for a potential 5MW wind turbine, which was completed by NREL in 2009 [189]. NREL conceptual study was based on an existing real wind turbine: the REpower 5M machine shown in Figure 6-1. The main reason behind choosing the NREL study is that detailed modelling of most parts of a geared wind turbine are available. Some parts of the geared wind turbine are assumed to be the same in the proposed 5MW direct-drive wind turbine in this chapter. The main missing parts that required designing are the generator, bearing, shaft, and converter assembly. This chapter will focus on the first three with some discussion of the placement of the various components including the converter in the nacelle.

6.2. Proposed Design Additions

The NREL study [189] looked at a number of key wind turbine components. Among these were the following: blade, hub, nacelle, drive train and tower. Of these elements, given that only a direct-drive train is being considered in this thesis, the gearbox is eliminated and the drive train is redesigned. Furthermore, in order to accommodate the new direct-drive generator, the nacelle must be significantly modified.

Based on modelling efforts from chapters 4 and 5, three additional elements were added: the shaft, the bearing and the direct-drive permanent magnet generator. Moreover, the power

converter is also considered, albeit briefly. Through this research, the NREL report is being extended to cover a direct drive generator, and the impact of UMP.

Figure 6-1 The REpower 5M wind turbine used for the conceptual study by NREL and this study as well [190]

As with the previous chapters, two variations of generator are considered, namely: an air-gap winding generator and an iron-cored generator. Section 6.4 provides the generators design methodology and comparison. Table 6-1 below summarizes the essential modelling parameters for the NREL components (minus drive-train) [189][191] and Table 6-2 summarizes the components added by this study using prior studies as a basis [47], [68], [69], [171], [189],

[192]–[194]. The second table includes the parameterizations for the two generator types considered in this study.

Component Type	**Description**	***Variables & Relations***	***Value***
Blade	Cut-in wind speed	v_{iw}	3 [m/s]
	Cut-out wind speed	v_{ow}	25 [m/s]
	Rated wind speed	v_w	11 [m/s]
	Cut-in blade speed	ω_{ibl}	6.9 [rpm]
	Rated blade speed	ω_{bl}	12.1 [rpm]
	Rated blade tip speed	v_{tbl}	80 [m/s]
	Blade orientation	O_{bl}	Upwind
	Blade configuration	δ_{bl}	3 blades
	Blade swept Diameter	D_{bl}	126 [m]
	Blade precone	$\emptyset_{bl}$	2.5 [°]
	Blade length	l_{bl}	61.5 [m]
	Blade swept radius	r_{bl}	63 [m]
	Blade max chord length	l_{blch}	4.6 [m]
	Blade set & hub weight	m_t	110 [ton]
	Hub diameter	d_{hub}	3 [m]
	Hub height	h_{hub}	90 [m]
Tower	Tower weight	m_{tw}	347 [ton]

Table 6-1 Component critical values for NREL conceptual design. Data source: [189], [195]

The resulting wind turbine model described in the tables can be used to generate a detailed visualization of the complete wind turbine design. This detailed representation is shown in Figure 6-2 below.

A closer look at the various elements of the generated visualization is shown in Figure 6-3, which breaks down the earlier diagrams into the internal view of the nacelle assembly. This assembly is viewed as a cross-section in Figure 6-4 in order to gain a better understanding of how the various components may couple. It should be noted that the presented model has a level of abstraction and does not completely model all bolts, joints, etc. The design, however, is sufficient for the sake of this study. It is worthwhile to evaluate how the dimensional values provided in the tables were obtained. NREL wind turbine details in Table 6-1 were extracted from the actual physical parameters of the real REpower 5M (5MW) wind turbine shown in Figure 6-1. This leaves the need for a justification for generator, bearing, shaft dimensions, converter, nacelle and other related parameters.

Component Type	***Description***	***Variables & Relations***	***Air-gap winding machine***	***Iron-cored machine***
Generator, Nacelle/Housing & Converter	Turbine power	P_T	5 [MW]	5 [MW]
	Nominal generator power	P_g	5.56 [MW]	5.56 [MW]
	Input torque	$T_g = P_g/\omega_g$	4.5 [MNm]	4.5 [MNm]
	Aspect ratio of generator	$K_g = l_g/2r_g$	0.12	0.27
	Shear stress	$\sigma_g = \frac{T_g}{2\pi r_g^2 l_g}$	23.87 [kN/m^2]	41.05 [kN/m^2]
	Rotor radius	$r_g = \sqrt{T_g/2\pi l_g \sigma_g}$	5 [m]	3.185 [m]
	Axial length	$l_g = P_g/2\pi r_g^2 \sigma_g \omega_g$	1.2 [m]	1.72 [m]
	Air gap length (Mechanical Clearance)	l_{gap}	0.00636 [m]	0.00636 [m]
	Magnet height	h_{mg}	0.025 [m]	0.0159 [m]
	Stator slot pitch	τ_{sg}	-	0.033 [m]
	Pole pitch	τ_{rg}	0.125 [m]	0.1 [m]
	Number of pole pairs	$p_g = \pi r_{rg}/\tau_{rg}$	126	100
	Pole width	$w_{pg} = 0.8\tau_{rg}$	0.1 [m]	0.08 [m]
	Stator mass	m_{sg}	49 [tons]	76 [tons]
	Rotor mass	m_{rg}	33 [tons]	51 [tons]
	Converter mass	m_c	90 [tons]	90 [tons]
	Nacelle housing mass	m_{nh}	15 [tons]	15 [tons]
Shaft	Tilt	t_S	5 [°]	5 [°]
	Outer diameter	d_{oS}	2.62 [m]	2.62 [m]
	Inner diameter	d_{iS}	2.42 [m]	2.42 [m]
	Length	l_S	1.350 [m]	1.350 [m]
	Material	M_S	Steel	Steel
	Mass	m_S	8.3 [ton]	8.3 [ton]
	Shear stress	$\sigma_{US} = \gamma_{US}/\sqrt{3}$	318 [MPa]	318 [MPa]
	Ultimate tensile stress	γ_{US}	550 [MPa]	550 [MPa]
Bearing	Inner diameter	d_{ib}	2.62 [m]	2.62 [m]
	Outer diameter	d_{ob}	3.2 [m]	3.2 [m]
	Mass	m_b	6.5 [ton]	6.5 [ton]
	Basic Static load	C_{0b}	61000 [kN]	61000 [kN]
	Basic dynamic load	C_b	14000 [kN]	14000 [kN]
	Equivalent dynamic load	P_{ub}	2750 [kN]	2750 [kN]
	Total mass	m_{tot}	312 + 347 [tons]	357 + 347 [tons]

Table 6-2 Air-gap winding machine and iron-cored machine specifications [47], [171], [189], [192]–[194]

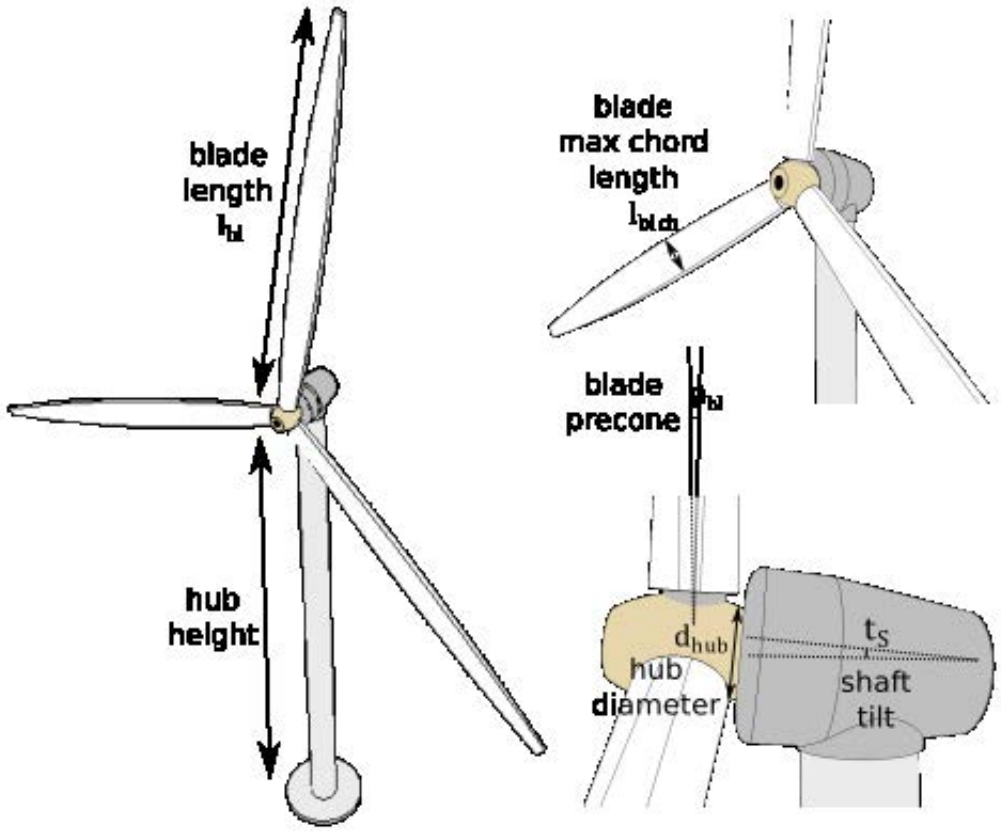

Figure 6-2 A proposed redesign of the REpower 5M machine

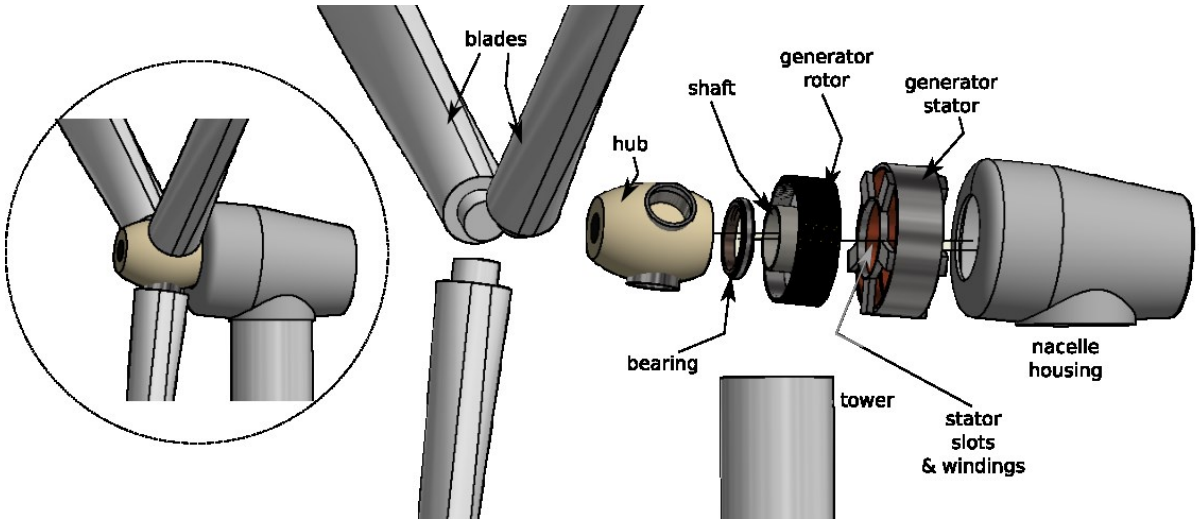

Figure 6-3 Looking inside the nacelle of the wind turbine

Considering that the discussion is related to direct-drive generator systems and these systems are being applied in the context of offshore wind energy where transportation and installation is an important issue, size and weight of the generator rotor combined with the turbine (blades and hub) is a key consideration for wind turbine design. In particular, it should be noted that

direct-drive generators are large and can require significant inactive mass to maintain structural stiffness.

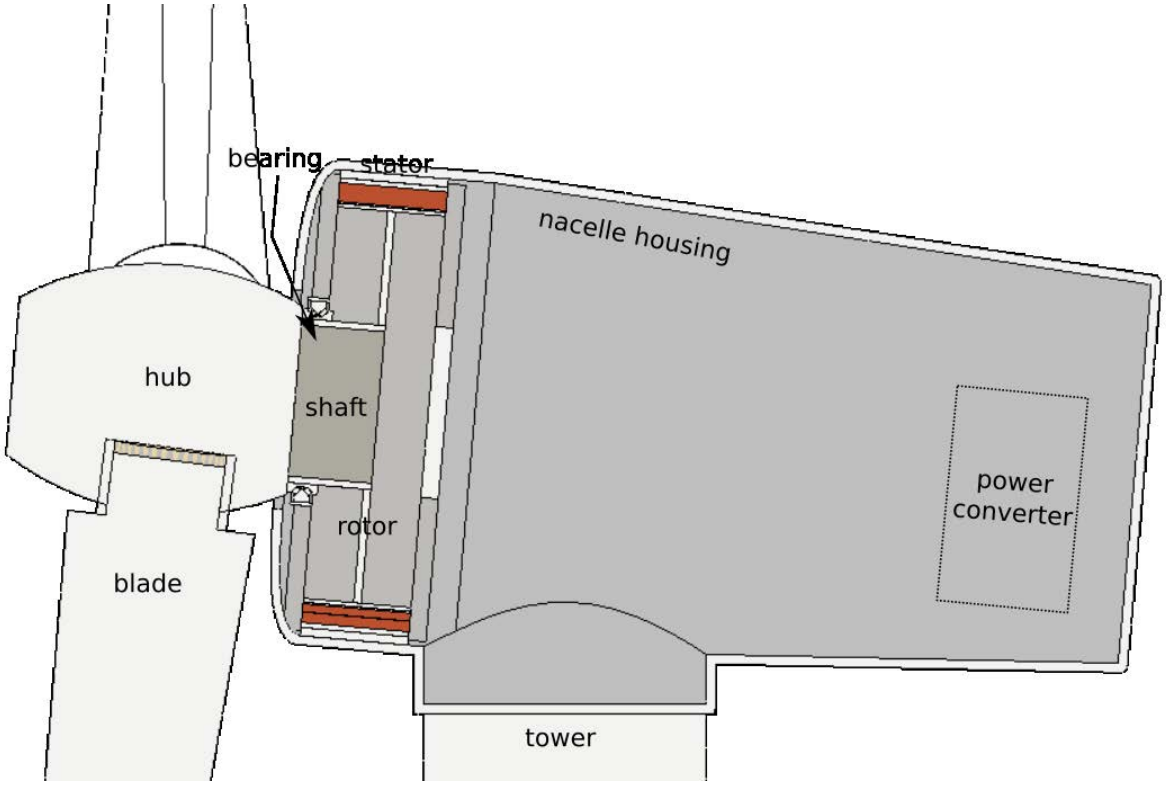

Figure 6-4 A cross-sectional view of the nacelle assembly showing the coupling between generator, shaft, bearing, hub and more. Note that for illustration reason, dimensions are exaggerated

Bang *et al* [196] have provided a rough relationship between generator torque, power rating and mass as shown in Figure 6-5. Mass for the entire generator assembly can vary between 20 tons and 325 tons for power ratings between 2MW and 10MW. Compared to weight concerns, machine diameter is less of an issue. Despite this, some considerations need to be made in the nacelle housing for the larger diameter. Diametric sizing of the connecting shaft that attaches the turbine (blades & hub) to the fixed structure would be determined by the particular bearing design. Generator rotors may vary in dimension between 2m and 6m in diameter for generators in the 5 to 20MW range. The mass of these generator rotors would vary between 13.3 tons and 65.4 tons once permanent magnets are taken into consideration [197].

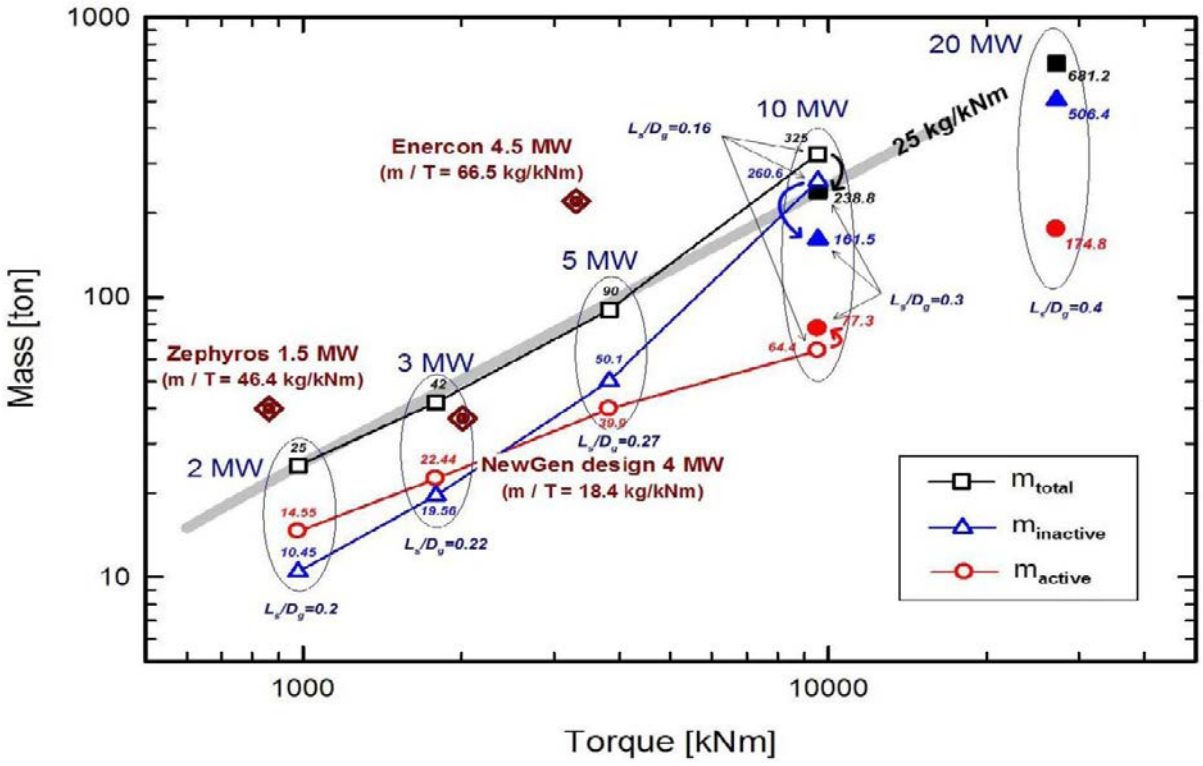

Figure 6-5 Relationship between mass, torque and power rating in direct drive generators [196]

Depending on the location, the turbine is being designed for offshore and onshore use, and tower dimensions may also need to be modified. Generally, tower height tends to be lower for offshore applications because of the higher wind speed. The structural elements of the tower will carry considerable loading so the nacelle and associated components should be positioned in such a way as to minimize the stress on the tower. This generally means a balance between the heaviest components, namely: the turbine, generator and power converter.

Further to this, the orientation of the blades (the blade precone) is significant in order to increase the clearance between the tower and the blades and prevent potential collisions. The shaft carrying the blades may also be tilted to account for wind force considerations, particularly for large turbines where the upper part of the turbine experiences higher wind speeds when compared to the lower part.

It should be noted that some effort has been made to relate the various parts of a wind turbine to each other and relate them to power output as shown in Figure 6-6.

The subsequent sections will talk about the considerations of the various components in greater depth, specifically focusing on the added component elements indicated earlier in this chapter.

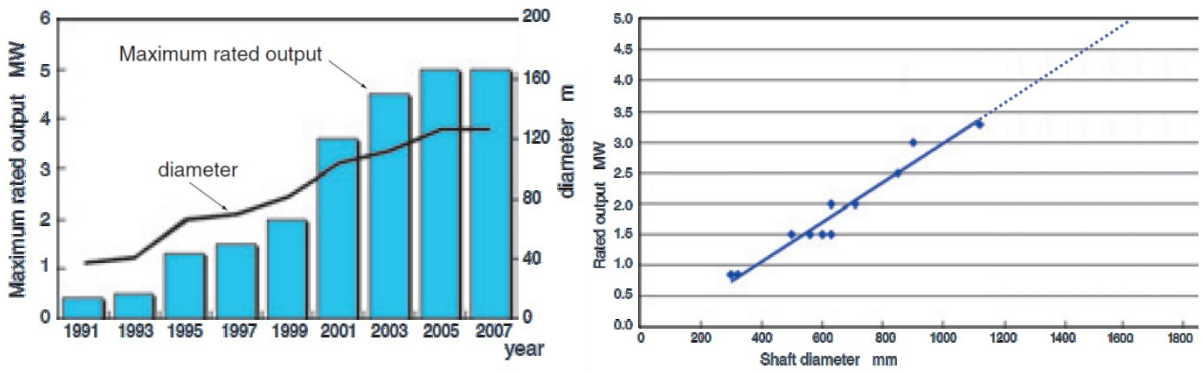

Figure 6-6 Turbine diameter, shaft diameter and their relationships to generator input power. Data source modified from: [198]

6.3. Nacelle & Tower

Forces applied on the nacelle components can be represented by their respective centres of gravity as shown in Figure 6-7. As mentioned earlier, it is important to position components to minimize the rotational torque at the joint where the nacelle and the tower connect. This reduces the net bending moment applied to the tower. Other important parameters should be considered here such as the wind force direction. The dominant wind direction will apply an axial force on the turbine blades shown in the figure below.

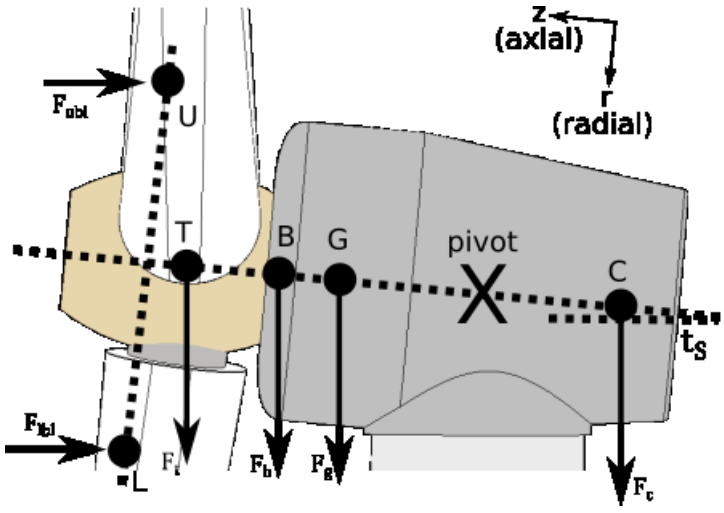

Figure 6-7 Considering the forces applied to the wind turbine nacelle and rotor as a result of the mass of the turbine, bearing, generator/shaft combo and converter

Assuming a three-dimensional cylindrical coordinate system (r, θ, z) with a centre point located at the pivot point shown in Figure 6-7, three torque components commonly known as (roll, yaw, pitch) at the pivot point can be distinguished. As shall be explained shortly, of these, roll and yaw are not considered and only pitch is given rigorous treatment. The variable T_n is used to represent this pitching torque associated with the wind turbine nacelle. The pivot point

represents the rotational centre point at the nacelle-tower joint. The added assumption here is that the centre of gravity of just the nacelle housing, which holds all the wind turbine components together, falls right at the pivot point.

A further assumption is that the wind force applied on the blades (of length l_{bl}) can be resolved to a single force at the centre of gravity of the blades. This point of application is given by the variable $\acute{l}_{bl}$. Similarly, $\acute{l}_t$, $\acute{l}_b$, $\acute{l}_g$, $\acute{l}_c$ are the distances of the centres of gravity of the turbine, bearing, generator/shaft combo and converter, respectively along the axial direction. The individual forces resulting from either the wind or the force of gravity for each of the components are given by the variables: F_{bl}, F_t, F_b, F_g and F_c. The axial and radial components of forces can be marked with subscript *z* (axial) or subscript *r* (radial), respectively relative to the pivot point. It should be noticed that the angle of orientation of the turbine blades is given by θ.

Looking more closely at the free body diagram of the setup can clarify the different force and length variables. The force variables can be broken down into component values along the axial (z) and radial (r) directions as shown in Figure 6-8. For the sake of clarity, the diagram shown on the right side of the figure, is shown without accounting for the nacelle angle (t_S) relative to the ground surface.

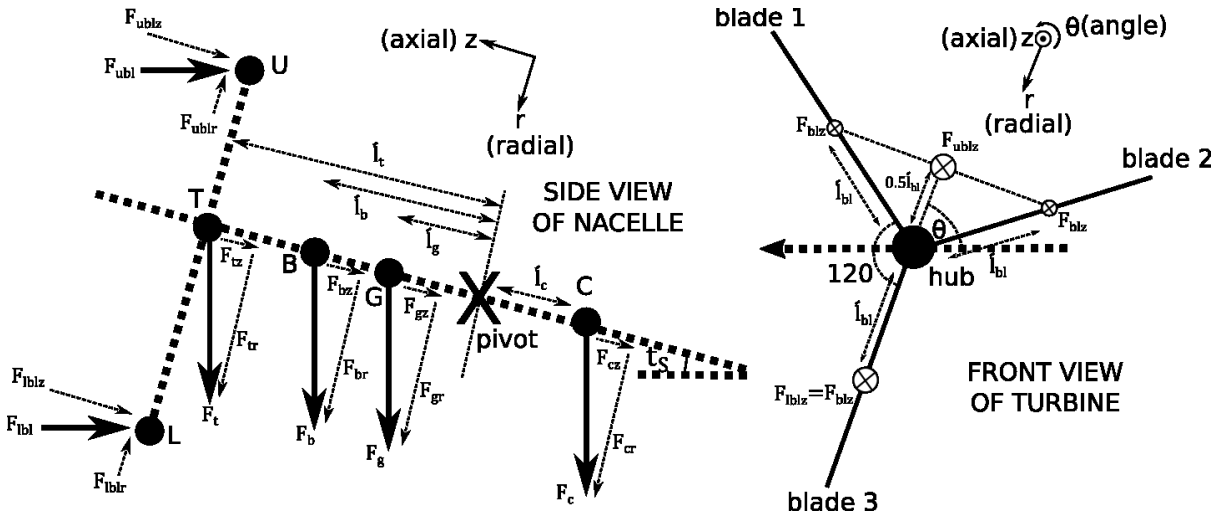

Figure 6-8 A closer look at the forces on the wind turbine nacelle. The left diagram shows a side view of the forces, while the right diagram shows a front view of the turbine (blades & hub) only.

The nacelle torque at the pivot point consists of two main components: (T_{nr}, T_{nz}). The first component, T_{nr}, is a result of the radially directed forces demarked by subscript *r*.

The second component, T_{nz}, is a result of axially (z) directed forces and is a result of the forward pressure of the wind. This component causes the nacelle to twist around the pivot point in the direction of angle t_S. It is important to note that in the case of gravity induced moments, the mass of the components is needed for computations. The mass of the various components are given by variables: m_t, m_b, m_g, m_c.

At this point, a quick note about rolling torque should be considered. The rolling torque on the nacelle is a result of the twisting action in the direction θ as a result of the turbine's rotation. For the purposes of this study, it will be assumed that this twisting is largely absorbed by the rotor assembly and does not contribute in any significant way to the moment at the pivot point. It is important to note that there is yet another torque. As the wind direction changes, the entire nacelle can experience a yaw force. For the purposes of this analysis, the assumption is made that this force is not significant. The assumption is based on the idea that the turbine presented would have a yaw control present at the tower-nacelle joint, which would ensure that the wind direction is perpendicular to the swept area of the turbine blades.

6.3.1. Blade Forces under Constant Wind Speed

Looking at the forces on the turbine itself, an assumption can be made that it is manufactured in a way that the centre of gravity of the turbine can be resolved to fall at the point T on the diagram. However, there is an added complication to the computation of forces that the force on the individual blades (F_{bl}), depending on the angular position of the turbine (θ) and can result in a difference in force on the upper part of the turbine (F_{ubl}) versus the lower part of the turbine (F_{lbl}). Here, the distinction between the upper part and lower part is made relative to whether the force is applied above the pivot point or below.

Considering the static case where one blade is directed completely downwards and two blades are directed upwards, it can be noted that while there would be twice the force applied on the upper region ($F_{ublz} = 2F_{blz}$) of the turbine when compared to the lower region ($F_{lblz} = F_{blz}$) of the turbine, this higher force will be applied at half the radial length ($l_{bl}cos(120/2) = 0.5l_{bl}$) from the pivot. That is the force F_{ublz} will be applied at radial distance $0.5l_{bl}$. This suggests that, at least in the static case, the moment (from axial forces - $T_{ubl\gamma}$) resulting from the upper force on the turbine will be equal to the moment on the lower part ($T_{lbl\gamma}$) and result in a net zero moment contribution from the turbine. In-fact, if a dynamic rotating turbine is considered, this relationship between the upper and lower torques would still remain true

regardless of the relative angle θ of the blades. This is because the ratio remains constant regardless of which blades are being considered and what angle is being considered.

6.3.2. Wind Speed Variability

The velocity of the wind on the turbine blades, v_{bl}, on the upper part (subscript u) and lower part (subscript l) of the turbine, will be different. More specifically what is seen is that $v_{ubl} > v_{lbl}$. This is a result of boundary conditions, whereby friction against the earth surface slows the wind speed at lower regions. For the large 5 MW turbine, it is important to take this into consideration given the vast difference in height of the lower blades versus the upper blades.

Looking at weather data for the UK [199], a variation in wind speed by height can be seen as shown in table 6-3. There is unfortunately only limited data for wind speeds available, and none at the requisite range over which the turbine blades sweep for the design presented in this chapter. In order to obtain height data beyond the available data an extrapolation approach may be used as shown in [200].

The extrapolation of wind speed beyond this 100m mark can be done using the power law formulation shown in Equation (6.1) below. In this equation, the value α is the WSC (Hellman or friction coefficient) that typically varies between 0.40 for urban environments to 0.10 for smooth flat terrain. The formulation is valid up to a height of around 150 - 200m. v_1, v_2 and h_1, h_2 are two velocities and related height points respectively.

$$v_2 = v_1 \left(\frac{h_2}{h_1}\right)^{\alpha} \tag{6.1}$$

The graph and table shown in Table 6-3 demonstrates the results of the extrapolation under smooth terrain approximation.

Given the 5MW turbine design considered in this chapter, the minimum height of a particular blade tip will fall at 27m while the maximum height will fall at 153m. This suggests a variation in wind speed between top and bottom of between 6.3m/s and 8m/s. While it was noted earlier that the force on the upper and lower sections of the turbine would effectively be zero, with this variation in wind speed this is no longer true.

Height	*Wind Speed*
10 [m]	5.6 [m/s]
25 [m]	6.4 [m/s]
45 [m]	7.1 [m/s]
100 [m]	7.69 [m/s]
125 [m]	7.86 [m/s]
150 [m]	8.00 [m/s]

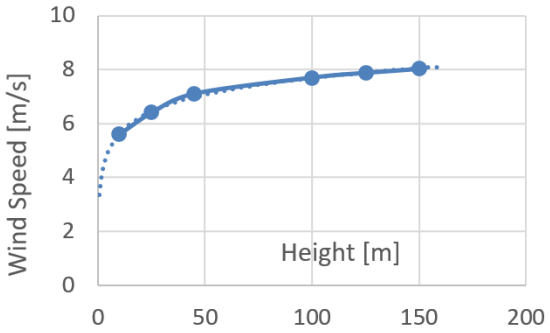

Table 6-3 The wind speed data with extrapolation for longitude: 3.17, latitude: 55.92. Data source: [199]

It can be seen that the actual wind speed will vary over the height in a continuous mode. So making use of the upper and lower bounds of the wind speed at the tips of the blade is not particularly representative. A better estimate can be obtained by averaging the wind speed above and below the turbine hub. The turbine hub sits at a height of 90m leading to a rough average speed below the hub of $v_{lbl} = 7.06$m/s and an average speed above the hub of $v_{ubl} = 7.85$m/s as calculated via the graph in Table 6-3.

6.3.3. Blade Forces under Variable Wind Speeds

The force on a given turbine blade (F_{bl}) can be computed by looking at the profile of the blade. Each blade can be presented as a classical aerofoil. Such an aerofoil at a given pitch will experience a lift and drag force as demonstrated by the diagram shown in Figure 6-9 below.

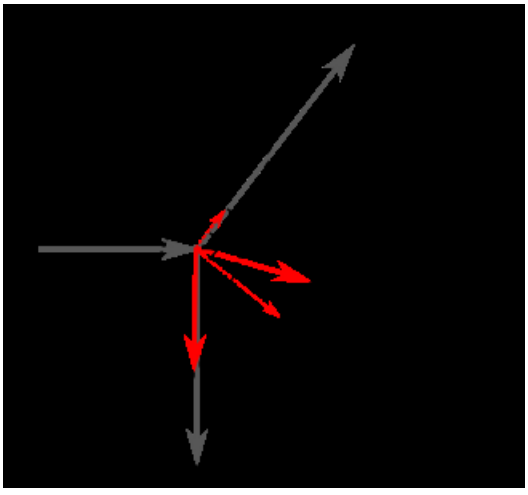

Figure 6-9 The forces on a single turbine blade from the wind.

From the diagram, it can be seen that the total axial force on the blade (F_{bl}) is the axial thrust of the blade and is a result of the projection of the total force (F_{bl-tot}) on the axial (z) axis. This total force is computed as the combination of the drag ($F_{bl-drag}$) and lift force ($F_{bl-lift}$).

In practice, turbines of the scale considered in this chapter will have some form of active pitch control. This means that the angle of attack of the aerofoil will change resulting in changing not only the angle of the lift and drag forces on the blade but also their magnitudes.

To simplify the problem, an assumption can be made about the pitch of the turbine blades and it can be assumed that the entire lift force of the blade is directed in the axial direction such that $F_{bl} = F_{bl-lift}$. From this assumption, it is relatively easy to determine the total axial force as shown in Equation (6.2) below [201].

$$F_{bl} = \frac{1}{2}\rho v_{bl}^2 \acute{A}_{bl} C_L \tag{6.2}$$

The value $\rho = 1.225\text{kg/m}^3$ represents the density of air, while $\acute{A}_{bl}$ represents the cross-sectional blade area for each individual blade of the wind turbine – the blade area is the cross-sectional area in the direction of the wind. The distinction of $\acute{A}_{bl}$ from the swept blade area A_{bl} should be noted. There is only marginal change in air density with height range considered for the turbine presented in this chapter.

C_L represents the lift coefficient – this coefficient is once more complicated to compute and varies over wind speed, blade pitch and blade profile. From [189], a range of coefficients for various blade profiles is possible as shown in Table 6-4.

Blade type	***Lift coefficient (C_L)***	***Drag coefficient (C_D)***	***Pitching moment coefficient (C_P)***
DU40	-0.9 to 1.9	0 to 1.8	-0.5 to 0.5
DU35	-0.75 to 1.7	0 to 1.4	-0.5 to 0.5
DU30	-1.25 to 1.5	0 to 1.4	-0.5 to 0.4
DU25	-1.0 to 1.5	0 to 1.4	-0.45 to 0.35
DU21	-1.1 to 1.4	0 to 1.5	-0.4 to 0.3
NACA64	-1.2 to 1.5	0 to 1.45	-0.4 to 0.3

Table 6-4 The minimum and maximum coefficient values for various 5 MW blade pitch angles. Pitch angles range from: -180° to 180° [189]

An example of the variation of the coefficients shown in Table 6-4 can be graphed as shown in Figure 6-10. The particular example represents the DU40 blade type. By using the maximum coefficient of lift of $C_L = 1.9$ for the DU40 blade type and combining it with an estimate of the averaged wind speed at height ranges: $h_{lbl} = 27\text{m}$ to $h_{ubl} = 153\text{m}$ it is possible to obtain an estimate of the force on the blade (F_{bl}).

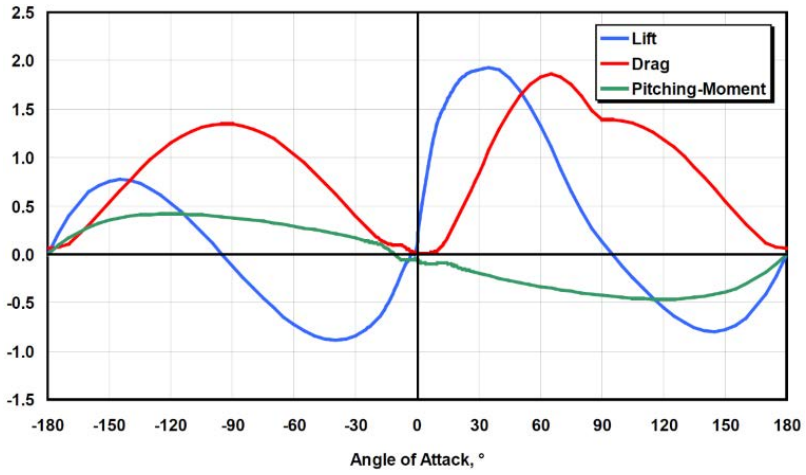

Figure 6-10 DU40 blade type coefficients of lift, drag and pitching moment vary over pitch angle of blades [189]

Equations (6.3) and (6.4) can be used to compute the lower and upper height ranges of the blades. The hub height is given as $h_{hub} = 90$m and the diameter is given as $d_{hub} = 3$m.

$$h_{lbl} = h_{hub} - \frac{d_{hub}}{2} - l_{bl} \tag{6.3}$$

$$h_{ubl} = h_{hub} + \frac{d_{hub}}{2} + l_{bl} \tag{6.4}$$

The 5 MW turbine under consideration has a maximum chord length given by $l_{blch} = 4.6$m and a blade length given by $l_{bl} = 61.5$m. This allows an estimate of the cross-sectional area as: $\acute{A}_{bl} = l_{blch} l_{bl} = 282.8\text{m}^2$. Given that the maximum chord length is used, this estimate will be an over-estimate.

From all this data, using Equation (6.2), the force on each turbine blade can be computed below and above the hub. This force is given as: $F_{bl-upper} = 20.2$kN (above hub) and $F_{bl-lower} = 16.4$kN (below hub). The presence of this variation in force complicates the earlier analysis somewhat in that the angular position (θ) of the blades now matters. To account for this the worst-case conditions are considered.

In the worst case, two blades will be located above the hub and one below. The reason for this is that when the two blades are at the highest height collectively, they will be under the greatest wind speed resulting in the greatest force. Under such conditions, two forces can be computed: F_{ubl} and F_{lbl} for the upper and lower parts of the turbine. Under such conditions $F_{ubl} = 2F_{bl-upper} = 40.4$kN directed at a distance $0.5\acute{l}_{bl}$ above the hub and $F_{lbl} = F_{bl-lower} = 16.4$kN directed at distance $\acute{l}_{bl}$ below the hub. This is an approximation once more in that the

height of the blades in the upper section will not quite reach the maximum height possible by an individual blade.

6.3.4. Computing torques and positions of components in nacelle

At this stage, it is possible to start estimating the position of components in the nacelle. For this computation, only a single bearing configuration and both an air gap winding and iron-cored generator were considered. Under typical rated conditions, the wind turbine nacelle should experience zero net torque in the combined radial (r) and axial (z) directions. Referring to Figure 6-8 with anti-clockwise direction representing negative torque, the net torque in both radial and axial directions can be given as shown in Equations (6.5) and (6.6) respectively.

$$\begin{aligned}
T_{nr} &= F_{ublr}\acute{l}_t + F_{lblr}\acute{l}_t - F_{tr}\acute{l}_t - F_{br}\acute{l}_b - F_{gr}\acute{l}_g + F_{cr}\acute{l}_c \\
&= F_{ubl}\,cos(t_S)\,\acute{l}_t + F_{lbl}\,cos(t_S)\,\acute{l}_t - F_t\,cos(t_S)\,\acute{l}_t - F_b\,cos(t_S)\,\acute{l}_b \\
&\qquad - F_g\,cos(t_S)\,\acute{l}_g + F_c\,cos(t_S)\,\acute{l}_c \\
&= 2F_{bl-upper}\,cos(t_S)\,\acute{l}_t + F_{bl-lower}\,cos(t_S)\,\acute{l}_t - m_t g\,cos(t_S)\,\acute{l}_t \\
&\qquad - m_b g\,cos(t_S)\,\acute{l}_b - m_g g\,cos(t_S)\,\acute{l}_g + m_c g\,cos(t_S)\,\acute{l}_c \\
&= \rho v_{ubl}^2 \acute{A}_{bl} C_L\,cos(t_S)\,\acute{l}_t + \frac{1}{2}\rho v_{lbl}^2 \acute{A}_{bl} C_L\,cos(t_S)\,\acute{l}_t - m_t g\,cos(t_S)\,\acute{l}_t \\
&\qquad - m_b g\,cos(t_S)\,\acute{l}_b - m_g g\,cos(t_S)\,\acute{l}_g + m_c g\,cos(t_S)\,\acute{l}_c \\
&= \rho \acute{A}_{bl} C_L\,cos(t_S)\,\acute{l}_t \left(v_{ubl}^2 + \frac{1}{2}v_{lbl}^2\right) + g\,cos(t_S)\left(-m_t\acute{l}_t - m_b\acute{l}_b - m_g\acute{l}_g + m_c\acute{l}_c\right)
\end{aligned} \tag{6.5}$$

$$\begin{aligned}
T_{nz} &= F_{ublz}0.5\acute{l}_{bl} - F_{lblz}\acute{l}_{bl} \\
&= F_{ubl}\,sin(t_S)\,0.5\acute{l}_{bl} - F_{lbl}\,sin(t_S)\,\acute{l}_{bl} \\
&= 2F_{bl-upper}\,sin(t_S)\,0.5\acute{l}_{bl} - F_{bl-lower}\,sin(t_S)\,\acute{l}_{bl} \\
&= \frac{1}{2}\rho v_{ubl}^2 \acute{A}_{bl} C_L\,sin(t_S)\,\acute{l}_{bl} - \frac{1}{2}\rho v_{lbl}^2 \acute{A}_{bl} C_L\,sin(t_S)\,\acute{l}_{bl} \\
&= \frac{1}{2}\rho \acute{A}_{bl} C_L\,sin(t_S)\,\acute{l}_{bl}(v_{ubl}^2 - v_{lbl}^2)
\end{aligned} \tag{6.6}$$

The total pitching torque resulting from these axial and radial components can be given as $T_n = T_{nr} + T_{nz}$. The two components together describe the pitching torque on the nacelle and should ideally fall at zero at the rated turbine velocity, that is $T_n = 0$Nm.

From this torque and fixing the position of the turbine ($\acute{l}_t = 6.83$m) and bearing ($\acute{l}_b = 4.34$m), it is possible to optimize the position of the generator ($\acute{l}_g$**)** and converter ($\acute{l}_c$). Table 6-5 lists all

the design variables and provides the $\acute{l}_g$ and $\acute{l}_C$ values needed to set torque on the nacelle to $T_n = 0$Nm. The unknown design variables can be optimized either manually or by some optimization algorithm aimed at minimizing nacelle length, for instance. For the purposes of this chapter, a manual approach to optimization has been taken.

Variable Description	***Variable***	***Value***	
		Air-gap	**Iron core**
Torque (radial)	T_n	0 [Nm]	0 [Nm]
Air density	ρ	1.225 [Kg/m^3]	1.225 [Kg/m^3]
Blade cross-sectional area	$\acute{A}_{bl}$	282.8 [m^2]	282.8 [m^2]
Blade lift coefficient	C_L	1.9	1.9
Nacelle/Shaft tilt	t_S	5 [°]	5 [°]
Wind velocity upper blade	v_{ubl}	7.85 [m/s]	7.85 [m/s]
Wind velocity lower blade	v_{lbl}	7.06 [m/s]	7.06 [m/s]
Gravitational acceleration	g	9.81 [m/s^2]	9.81 [m/s^2]
Blade centre of gravity position	$\acute{l}_{bl}$	30.75 [m]	30.75 [m]
Turbine centre of gravity position	$\acute{l}_t$	6.83 [m]	6.83 [m]
Single bearing centre of gravity position	$\acute{l}_b$	4.34 [m]	4.34 [m]
Generator rotor/stator/shaft centre of gravity position	$\acute{l}_g$	3.86 [m]	3.31 [m]
Power converter centre of gravity position	$\acute{l}_c$	11.13 [m]	13.18 [m]
Mass of turbine	m_t	110,000 [Kg]	110,000 [Kg]
Mass of single bearing	m_b	6,500 [Kg]	6,500 [Kg]
Mass of generator rotor/stator/shaft	m_g	90,300 [Kg]	135,300 [Kg]
Mass of converter	m_c	90,000 [Kg]	90,000 [Kg]

Table 6-5 Listing optimized design variables to achieve zero torque.

It should be noted that, given the very small mass associated with the shaft, it was neglected for computations related to the nacelle in this section.

With all nacelle components, positional considerations taken, a closer look at the generator, bearing and shaft in the following sections are presented.

6.4. Generator

The 5MW iron-cored PM generator used in this study was originally designed and structurally optimized by Zavvos [202]. The same design was also used by Sethuraman [192]. The specifications of this design is provided in Table 6-2. No design for an air-gap winding generator has been published yet, so a basic design for a 5MW air-gap winding generator is introduced here. This design could be improved and optimised, however, that is not the main aim of this research.

6.4.1. Electrical Design

The physical size of electrical machines is primarily determined by their torque capability. The generator input torque is set to the value of 4.5MNm. This torque is proportional to the product of the rotor volume and the shear stress. The shear stress is proportional to the product of the magnetic flux density (magnetic loading) and the stator current density (electric loading). For the sake of a fair comparison between the iron-cored generator and the air-gap winding generator, the electric loading is assumed to be similar. The magnetic loading, on the other hand, is higher in the iron-cored generator because of the smaller magnetic airgap, which means a higher shear stress. That is compensated by the higher volume for the airgap generator. The magnetic airgap length in the iron-cored generator equals the mechanical airgap clearance, whereas, it equals the sum of the mechanical clearance and the winding height in the airgap winding generator. The leakage flux density in the iron-cored generator has no benefit at all, whereas, most of the leakage flux density in the airgap winding generator pass through the stator coils and, hence, contribute in generating the electro-motive force. That should be taken in account when designing the generators and it is represented by the factor $K_{AW_{leak}}$ in this study. This factor has the value of 1 in the iron-cored generator, while it has the value of 1.1 in the air-gap winding generator. Giving the following assumptions:

- Similar mechanical airgap clearance (6.36mm) for the both generators.
- 30mm magnetic airgap length for the airgap winding generator, which means that the windings height l_c is 23.64mm. That also gives the advantage of lower attraction forces, which leads to easier manufacturing, installing and maintenance.
- The magnets height in the iron-cored generator $h_{mg_{IC}}$ is 15.9mm and in the airgap winding generator is 25mm. That is to generate more flux density in order to

compensate the larger magnetic airgap. The materials price, on the other hand, will increase. Comparing the manufacturing prices is recommended for a future study.

Description	***Air-gap***	***Iron-cored***
Number of phases	3	3
Number of coils N_{coils}	$\mathrm{N_{coils_{AW}}} = 189$	$\mathrm{N_{coils_{IC}}} = 99$
Number of coils/phase	63	33
Average flux density [T]	0.8	1.2
Number of slots per pole per phase	_	1
Coil pitch [m]	0.14	0.1
Axial length [m]	1.2	1.72
Coil area [m^2]	0.168	0.172
Flux density leakage factor $K_{AW\,leak}$	1.1	1
Coil magnetic flux [Weber]	0.148	0.2
Winding factor	0.96	0.96
Number of turns/coil $N_{turns/coil}$	$N_{turns/coil_{AW}}$=43	$N_{turns/coil_{IC}}$=40
Number of coils connected in parallel	63	33
Number of coils connected in series	1	1
Rated rotational speed [rpm]	12.1	12.1
Rated generated frequency [Hz]	25.4	20.17
Terminal voltage [V]	690	690
Total number of turns	N_{AW} =2713	N_{IC} =1327
Slot area [m^2]	_	$1.2e^{-3}$
Fill Factor	0.95	0.7
Coil cross section area [m^2]	$0.85e^{-3}$	$0.84e^{-3}$
Conductor cross section area [m^2]	$19e^{-6}$	$21e^{-6}$
Conductor diameter [m]	$5e^{-3}$	$5.17e^{-3}$
Conductor current [A]	38	72.7
Average coil length [m]	2.68	3.64
Coil resistance [Ω]	0.1	0.12
Coils losses [kW]	27.3	62.8
Total copper losses [kW]	82	188
Estimated iron, magnets, and stray losses [kW]	70	70
Efficiency	97%	95%

Table 6-6 Electrical design for the 5MW airgap-winding and iron-cored generators.

Comparing the magnetic loading B_{AW}, B_{IC} for the airgap winding and iron-cored generators respectively gives:

$$\frac{B_{AW}}{B_{IC}} = \frac{K_{AW\,leak}\ \dfrac{h_{mg_{AW}}}{h_{mg_{AW}} + l_{gap} + l_c}}{\dfrac{h_{mg_{IC}}}{h_{mg_{IC}} + l_{gap}}} = 0.69 \qquad (6.7)$$

Using Equation (5.10) to compare the fundamental electromotive forces E_{AW}, E_{IC} in the airgap winding and iron-cored generators respectively gives:

$$\frac{E_{AW}}{E_{IC}} = 0.5\ \frac{N_{AW}}{N_{IC}} \qquad (6.8)$$

For a similar electric loading, $E_{AW} = E_{IC}$, which means that the total number of turns in the generators are $N_{IC} = 0.5\ N_{AW}$. The number of coils in the airgap winding generator, however, is 189, while it is 99 coils in the iron-cored generator. That means the number of turns per coil for the both generators are different. They are determined by the generator terminals voltage design, which is normally 690V for a 5MW generator but choosing a higher voltage of 33kV will enhance the efficiency and may improve the total economics of the design [203]. If the generator terminal voltage is 690V, the phase current should be about 2.4kA. As shown in Table 6-6, which provides an electrical design for the both generators, the efficiency in the airgap-winding generator is 97% and in the iron-cored generator is 95%.

6.4.2. Mechanical Design

The generator position can be assigned based on the mass of components in the nacelle. In addition, the attached generator shaft length and diameter may also be affected by the distance to the bearing and the bearing diameter. For this reason, the generator shaft dimensions will vary based on the bearing arrangement, i.e. a single bearing nacelle approach or a double bearing nacelle approach. Discussions of the bearing and the shaft are presented in the next sections; however, the focus of this section is on torque related characteristics of the generator.

There are a number of parameters that can affect generator torque. The axial length of the generator or the type of the generator, for instance. Two particular 5MW generator designs are discussed here, namely: an air-gap winding generator and a slotted iron-core generator. Those two generators have different axial lengths and diameters but both have 5MW output power. Figure 6-11 elaborates on the design of both generators. The air-gap winding generator has a

shorter axial length and a wider diameter when compared to the iron-core generator. The stator of the iron-cored design is heavier, firstly as a result of the added iron from the slots and secondly because of the thicker support structure needed for the higher magnetic forces.

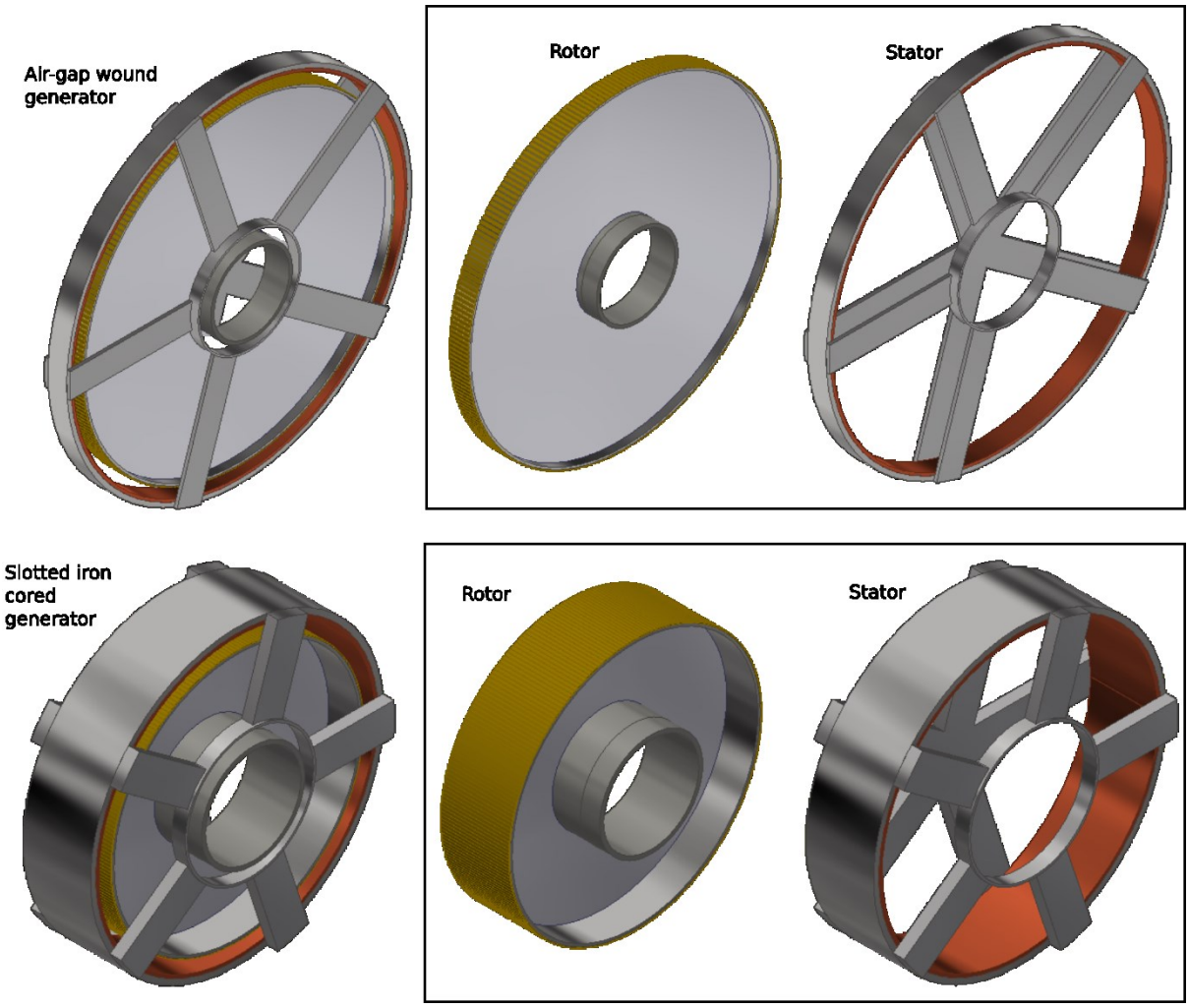

Figure 6-11 Structural visualizing of both the air-gap winding and the slotted iron-cored generators

The mass of the stator (m_{sg}) and rotor (m_{rg}) for the air-gap winding generator fall at: $m_{sg} =$ 49 tons and $m_{rg} = 33$ tons. Likewise, for the slotted iron-cored generator, the mass falls at: $m_{sg} = 76$ tons and $m_{rg} = 51$ tons. For each, air-gap winding and iron-cored generators, respectively, the axial lengths are $l_g = 1.2$m and $l_g = 1.72$m and the rotor radii are $r_g = 5$m and $r_g = 3.185$m.

6.4.3. Generator Power and Stress

The mechanical generator input power (P_{gm}) can be estimated as equal to the power produced by the turbine (P_t) itself disregarding the drive-train losses. This power is given as shown in

Equation (6.9) below. The equation is derived directly from the kinetic energy of the rotor and a detailed treatment can be found in [204].

$$P_t = P_g = \frac{1}{2}\rho v_w^3 A_{bl} C_p;\ \ A_{bl} = \pi r_{bl}^2 \tag{6.9}$$

Here, the variable ρ is the air density, v_w is the rated wind speed, r_{bl} is the turbine radius, and C_p is the power coefficient. The swept area of the turbine is given by A_{bl}. Note the distinction from the earlier use of the variable $\acute{A}_{bl}$ for the blade cross-sectional area. The rotational speed resulting from the wind (ω_{bl}) is the rotational speed of the generator rotor *(ω_g)* as well. This rotational speed is given by Equation (6.10).

$$\omega_{bl} = \omega_g = \frac{v_w\,\lambda}{r_{bl}};\ \lambda = \frac{v_{tbl}}{v_w} \tag{6.10}$$

The value λ is the tip speed ratio – the ratio of the velocity of the blade tips (v_{tbl}) and the velocity of the incoming wind (v_w). With careful optimization of λ it is possible to get an optimal value for the power coefficient. Typically, the optimal is chosen such that $C_p = 0.47$. In theory, the value is closely related to the Betz efficiency of 59.3%. Unfortunately, in practice, as a result of manufacturing and runtime inefficiencies, such a high coefficient cannot be obtained in practice so the indicated C_P is used as a slightly more realistic measure.

Given this, the input torque resulting from the action of the wind on the turbine blades (T_g) and resultant reaction of the generator to maintain a constant rotational velocity can be obtained as shown in Equation (6.11) below.

$$T_g = \frac{P_t}{\omega_g} = \frac{\rho v_w^3 \pi r_{bl}^3 C_p}{2 v_{tbl}} \tag{6.11}$$

The equation leads to a torque of $T_g = 4.5$MNm for the 5MW generator design as shown in Table 6-2. Once the input torque to the generator (T_g) is known, the shear stress between the generator rotor and stator (σ_g) can be determined. This stress is given in Equation (6.12) below.

$$\begin{aligned} T_g &= 2\pi r_g^2 l_g \sigma_g \\ \sigma_g &= \frac{T_g}{2\pi r_g^2 l_g} \end{aligned} \tag{6.12}$$

In reality, the shear stress of the PM generator is a combined effect of the shear stress contribution from the turbine (σ_t) and a reaction produced from the electromagnetic (σ_{em})

contributions of the generator magnets and windings. This additional and reactionary shear stress acts to counter the turbine's rotation and results in electrical generation [171]. Since the rotational speed of the rotor is already known, in practice the electrical shear stress (σ_{em}) is also known and assumed to be accounted for in Equation (6.12). The total shear stress would be given as: ($\sigma_g = \sigma_t + \sigma_{em}$). The calculated shear stress falls at: $\sigma_{g(a)} = 23.87\text{kN/m}^2$ for an air-gap winding generator and at $\sigma_{g(i)} = 41.05\text{kN/m}^2$ for the iron cored generator.

While unnecessary in the example used in this chapter, for the purposes of demonstration, the electrical stress can be computed as presented in Equation (6.13).

$$\sigma_{em} = \frac{1}{2} BK \cos\delta \tag{6.13}$$

In the equation, B[T] is the peak flux density and K[kA/m] is the peak electrical loading respectively [68]. δ is the relative angular displacement of the rotor relative to the stator. Combined with the use of Equation (6.14) it is possible to determine the rotor diameter.

$$\frac{r_g}{r_{bl}} = v_w \sqrt{\frac{\rho C_p}{\lambda\, BK \cos\delta\, (l/r_g)}} \tag{6.14}$$

The ratio, r_g/r_{bl}, was estimated as 0.285 in [68]. The ratio of generator active length to radius (l_g/r_g) was estimated as 0.02 for ironless PM generator in [68], 0.08 for the iron cored direct drive generator in [69], and 0.5 for radial flux PM machines in [47]. This allowed the determination of the rotor radius as $r_g = 5$ m for the air-gap winding generator and $r_g = 3.185$m for the iron-cored generator.

6.4.4. FEM of Generator Forces and UMP

At this stage, it is worth going further and moving from shear to UMP. Both types of PM generators (air-gap winding, slotted iron-core) were modelled in FEMM (see section 5.3). A two-dimensional diagram of the studied machines showing the flux density lines are presented in Figures 6-12 and 6-13.

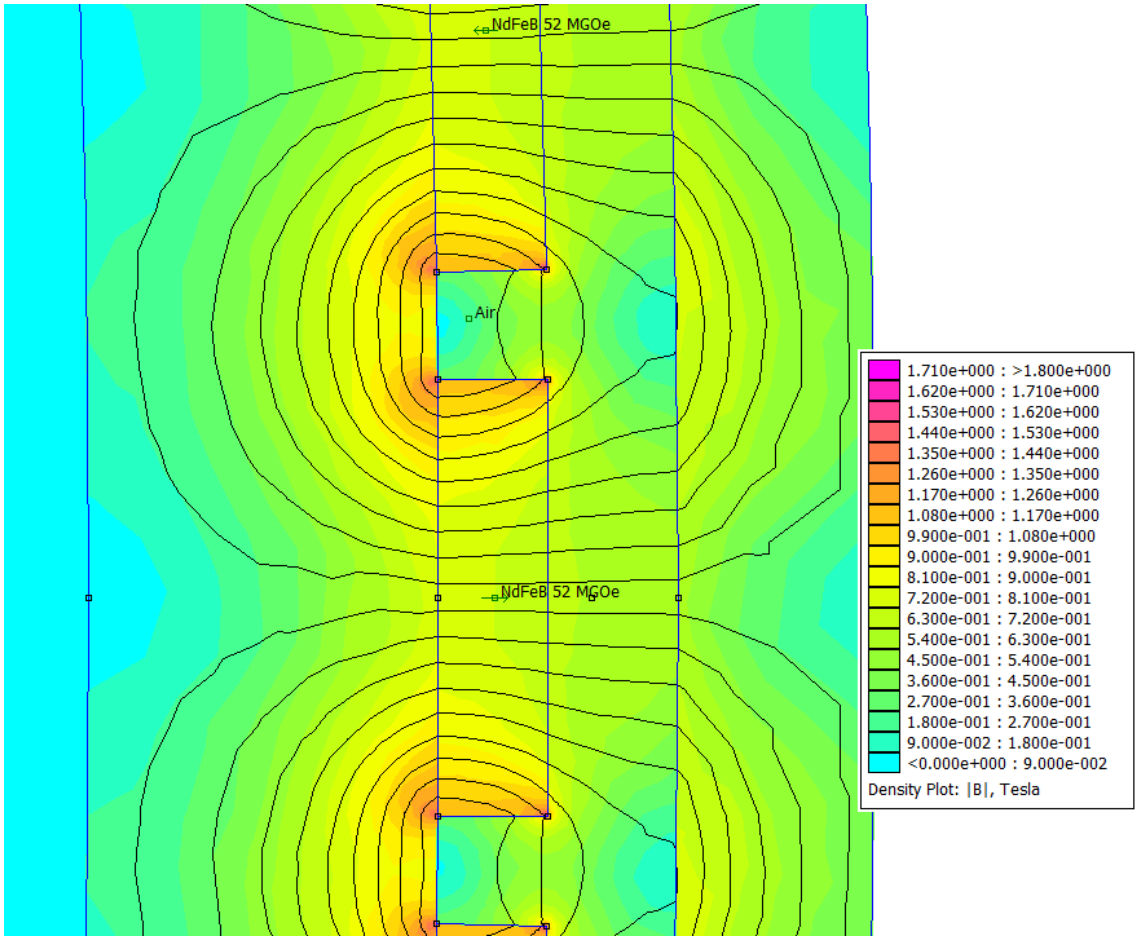

Figure 6-12 Magnetic flux density in 5MW air-gap winding machine using FEMM

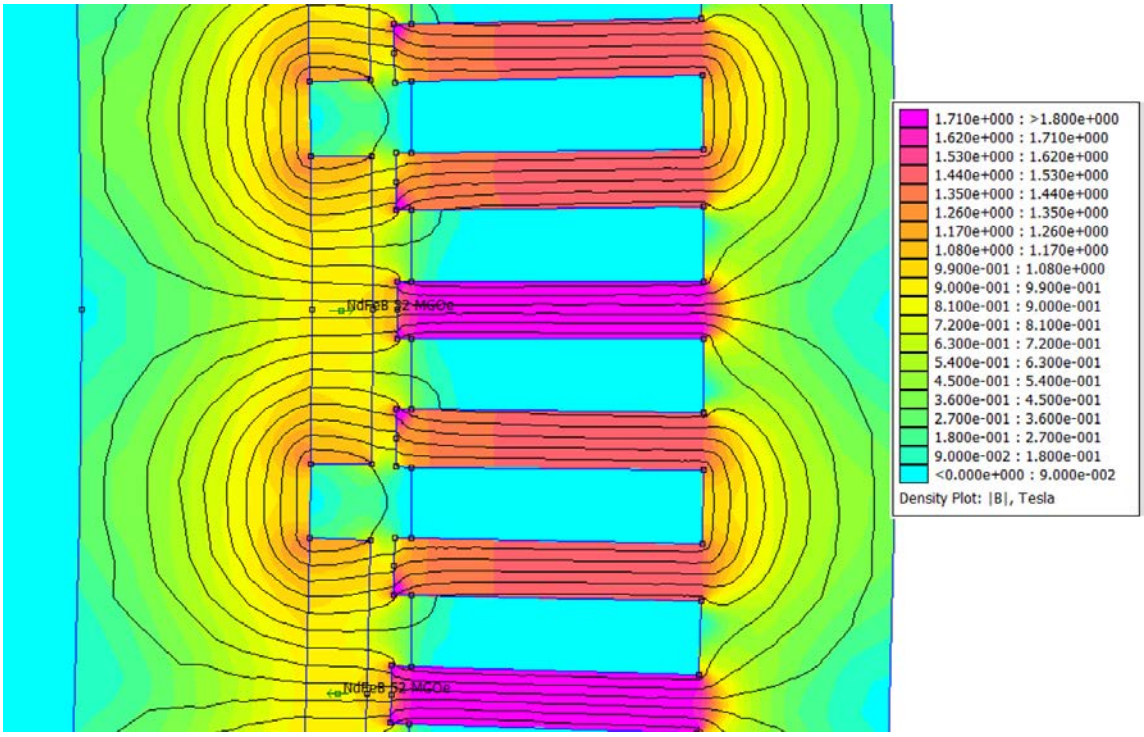

Figure 6-13 Magnetic flux density in 5MW iron-cored machine using FEMM

The earlier analysis of magnetic fields and UMP presented in chapters 4 and 5 can be applied to the generator designs in order to look at the effect of generator loading, rotor position, and associated induced UMP. Figure 6-14 demonstrates the unbalanced forces on the rotor of the air-gap winding machine induced by different relative rotor eccentricities in two cases: no-load case and loaded case.

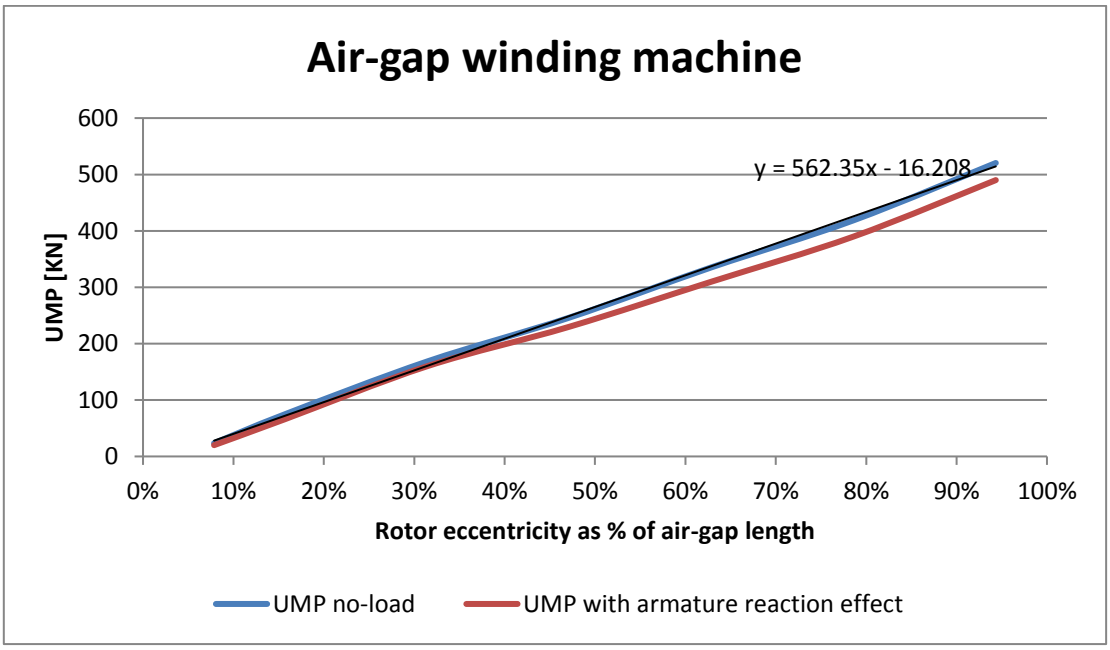

Figure 6-14 UMP induced in 5MW air-gap winding machine for different rotor eccentricities and different loading cases

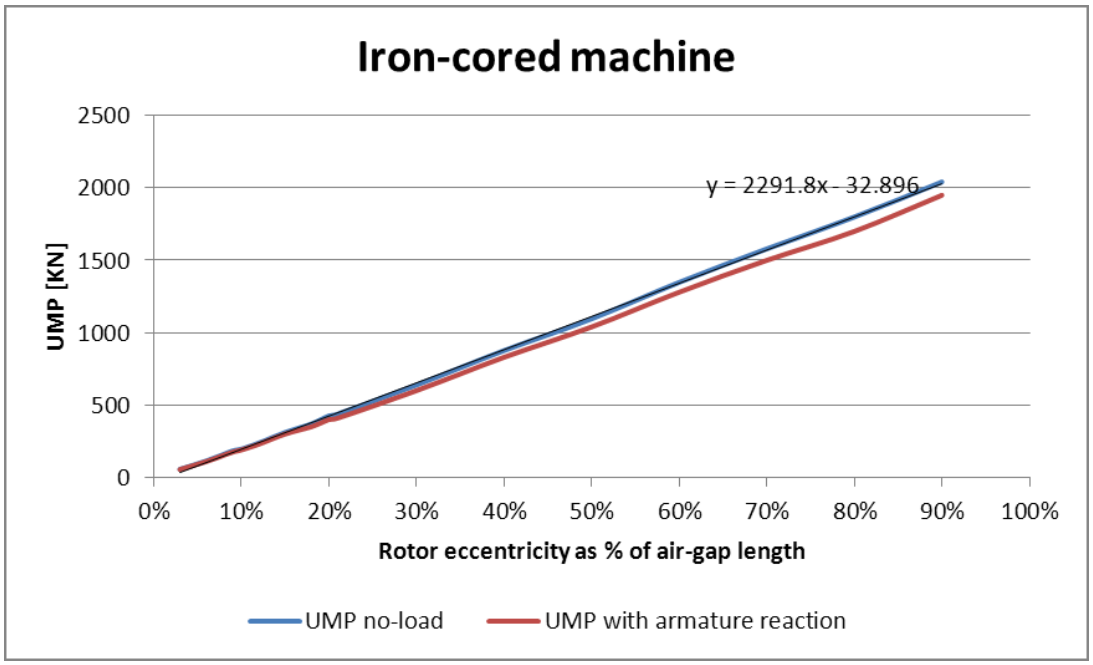

Figure 6-15 UMP induced in 5MW iron-cored machine for different rotor eccentricities and different loading cases

Going further and taking a look at the slotted iron-cored machine, the UMP in no-load and loaded conditions can be seen as shown in Figure 6-15. The first point of note is that the slotted iron-cored machine has significantly higher forces associated with it. The corresponding UMP is thus significantly higher (almost 5 times greater) than an air-gap winding based generator for same relative rotor eccentricity. The armature reaction appears to be very small in both types of PM generators, which can be justified by comparing the magnetic flux density generated by the PMs and the magnetic flux density generated by the induced currents in the windings. The FEA models show linear relationships between UMP and rotor eccentricity – refer to chapters 4 and 5.

6.5. Bearing and Shaft

With positional concerns addressed and with power, stress and UMP also discussed, a return can be made to a discussion of bearings. UMP force is transmitted to the bearing via the rotor shaft. The resultant variation in force leads to bearing wear. There are differences in the forces generated by the air-gap winding based generator and the slotted iron cored generator.

Of-course, bearing wear is not only a function of the generator UMP, but also a function of the forces applied on the bearing via the wind and the forces applied on the bearing as a result of weight related issues (as noted in the earlier subsection).

6.5.1. Bearing arrangement for a direct-drive generator

Unlike the conventional geared drive-train and because of the sheer size and weight of the generator, a direct-drive generator needs special consideration when designing support structure for the main shaft and the generator. One of the major challenges associated with direct-drive generators is maintaining the air-gap between the rotor and stator for optimal use of the rotational force. This is achieved by means of bearings arranged between the main shaft which is directly connected to the generator rotor and the generator stator which is connected to the nacelle housing. Of the many components that constitute the direct-drive generator, bearings are one of the most critical elements. They are not only responsible for carrying the main loads from the blade rotor but also responsible for maintaining the air gap between the rotor and stator. Assuming any structural deflection of the stator or the main shaft, the bearings would tilt from their desired position. Because of the heavy weight of the rotor, it requires a greater moment of resistance to this deflection. Since an optimal air gap is no longer maintained, bearing wear tends to increase. Conversely, the increased bearing wear affects the

stability of the air-gap. Therefore, bearing selection, design and arrangement is a critical to integration of direct-drive generator to a wind turbine as it determines the integrity, safety and life of the system.

Bearing faults constitute a significant portion of all faults in WTGs. The experience feedback from the wind energy industry corroborates that bearing failure is one of the typical failures in WTGs as shown in Figure 6-16 [18].

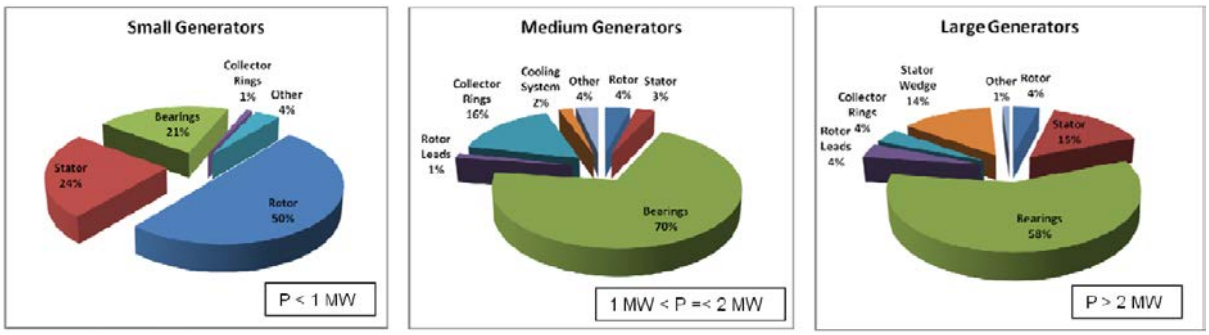

Figure 6-16 Survey of 800 failed wind turbine generators [18]

One explanation of the high bearing failure rates could be that the existing models used by the industry do not adequately account for the various loads and describe how the loads on the nacelle and bedplate structure are developed and then dissipated. These leads to under-estimated component sizes/ratings that fail much earlier than their intended design lives. An example was presented in subsection 6.3.3. when the wind turbine blades are loaded unevenly, a moment is applied to the spindle and main bearing. If the bearing stiffness is not adequately designed, causes deflections of the generator rotor potentially problematic variations in the gap. It is therefore essential to understanding the behaviour of the whole drivetrain under operating loads and also accurate estimation of loads.

Several solutions exist depending on the loads and intended load path. These employ either single, two, three or four bearing arrangements as shown in Figure 6-17 [205] which presents some of the interior rotor designs currently implemented in some of the commercially available wind turbines. The main shaft bearings are either located in front of, straddled, or behind the generator. Some turbines with two bearings use the hub as a housing. Each bearing arrangement has its own advantages and disadvantages.

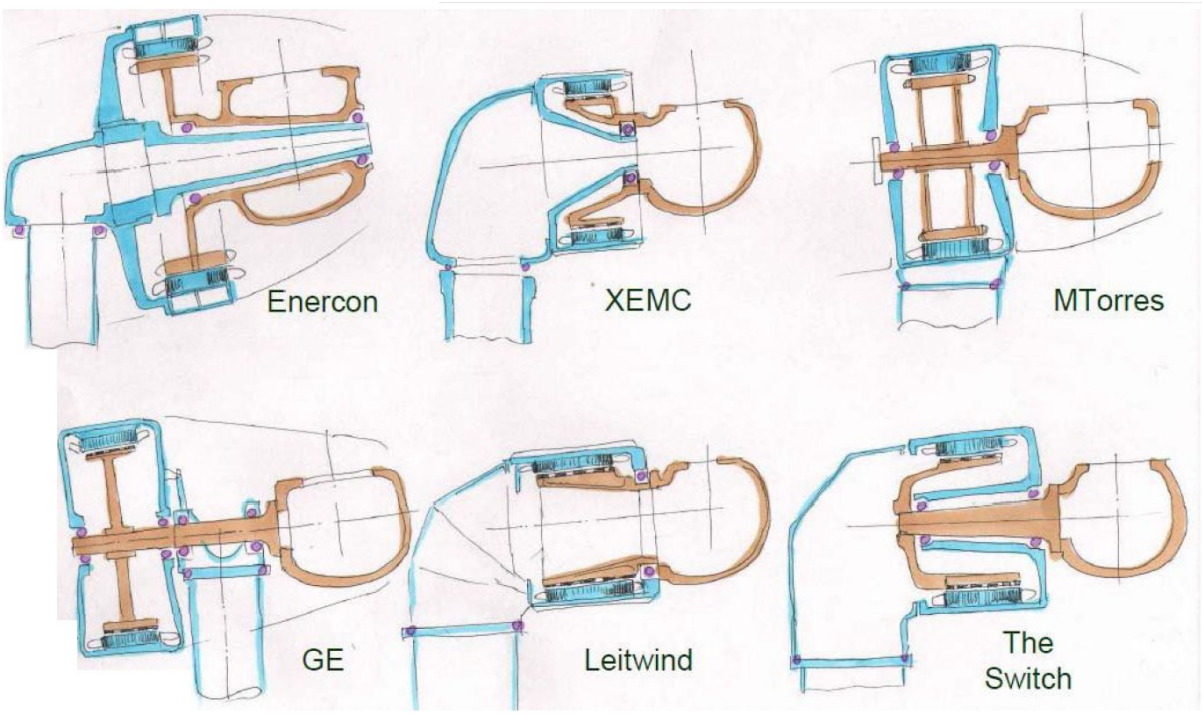

Figure 6-17 Bearing arrangements for inner-rotor direct-drive generator wind turbines [206] [207]

Stander *et al.* [208] also reviewed the bearing arrangements in direct-drive wind turbines as shown in Figure 6-18. The bearing location relative to stator is upwind in A1 (commercial examples are Leitwind and Zephyros [206] [209]), A2 (commercial examples are Simens and Goldwind [206]) and B2 (commercial example is Enercon [206]). The bearing location relative to stator is upwind & straddled in B1 (commercial example is Vensys [206]) and it is upwind and downwind in B6 and B7 (commercial examples are MTorres [206] and WERG-85 [210] respectively). The bearing location relative to stator is upwind, internal and downwind in C2 (example is Handler design [211]) and it is upwind and internal in B4, B8 and C1 (examples are Gensys [206], NewGen [212] and Handler design [211] respectively). The bearing location relative to stator is downwind and internal in B3 (commercial example is GE [206]).

Designs A1, B1, B2, B3, B6, C1 and C2 are inner rotor generators, while A2, B4, B7 and B8 are outer rotor generators.

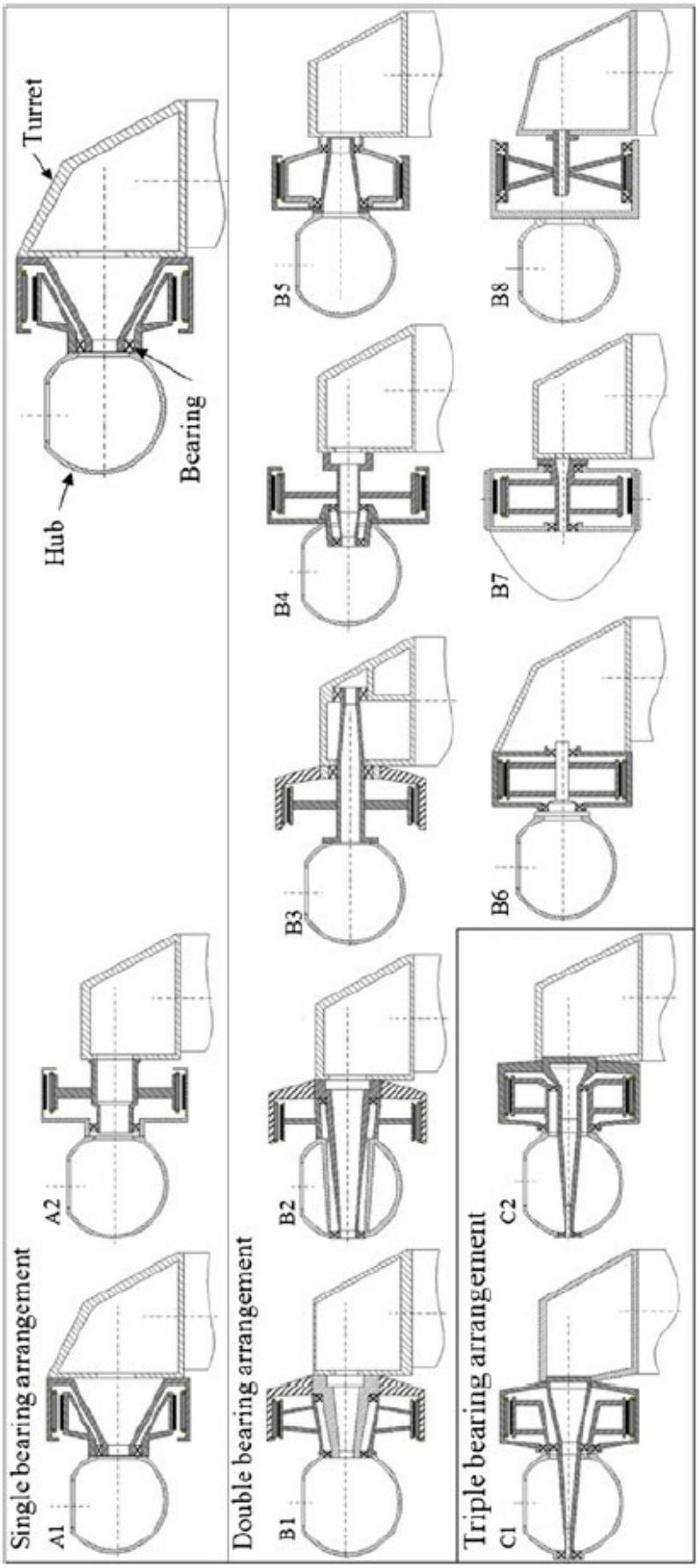

Figure 6-18 Representation of direct-drive wind turbine generator design configurations[213]

Bearings are characterised by their size, load rating and design life. The size and rating of the bearing supporting the main shaft of a wind turbine depends on the size of the shaft, the loading conditions, speed of operation and the design life required. Besides these requirements, bearings for direct-drive generators must allow for a power-dense arrangement managing the loads in compact space, with the level of stiffness and type of mounting are achievable [213]. The life of main shaft bearings for direct drive generators can be negatively affected by several factors. Operating stresses from inaccurate assessment of loading, shaft/housing misalignments, choice and efficiency of lubricant control system, thermal gradients, fatigue propagation rates and operating load zone [214]. Optimal bearing selection must balance of the factors affecting the load carrying capability, combining the predicted life, system stiffness, power loss and heat generation, load zone maintenance, setting, lubrication, handling and maintenance [213].

Main shaft bearings for a wind turbine come as a paired solution or a combination of bearings designed to carry different types of loads. These include Angular Ball Bearings (ABB), Spherical Roller Bearing (SRB), Cylindrical Roller Bearing (CRB) and Tapered Roller Bearings (TRB) with different locations and configurations. The thrust-to-radial loading ratio is important factor in selecting the type of fixed bearing [215]. Double row radial spherical roller bearings are the standard design choice for the fixed bearing as they have good alignment and load carrying abilities. Yet these bearings have lower bearing life when axial loads are significant. The studies [213] and [215] recommend the use of double row tapered roller bearings for the fixed end as they are better suited to address the concerns created by stiffness, skidding, smearing and roller load management that are difficult to achieve with spherical roller bearings.

In this study, the figure below (Figure 6-19) demonstrates the adopted bearing designs where (B) the typical bearing arrangement when a double bearing is used with the direct-drive generator based turbine. It also demonstrates (A) single bearing design. It should be noticed that traditional turbines make use of self-aligning spherical roller bearings as the main shaft bearing while making use of standard cylindrical roller bearings for the secondary support bearing [198]. In single bearing design, a tapered roller bearing is normally recommended as shown in Figure 6-20 and suggested by TIMKEN.

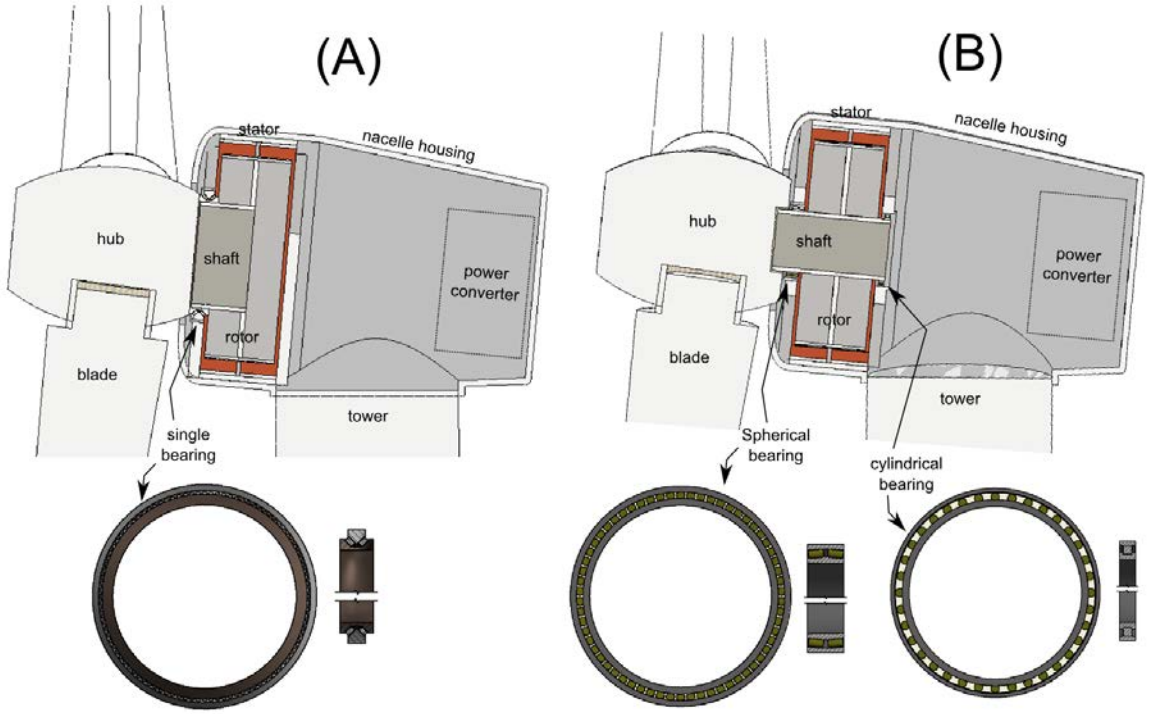

Figure 6-19 Approaches to setting up bearings for the proposed generators – an iron-cored generator is shown in the diagram. That air-gap and axial length of the generator has been exaggerated for visibility.

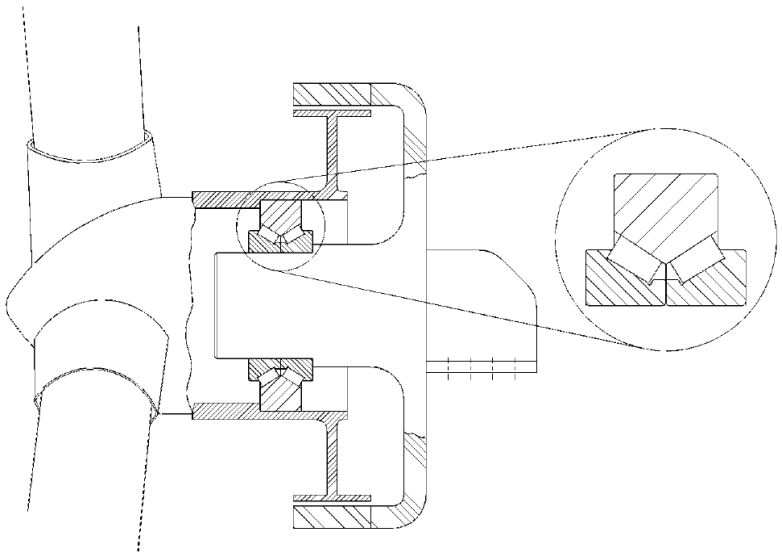

Figure 6-20 Typical direct-drive generator wind turbine design with a two-row tapered roller bearing as suggested by TIMKEN [215]

There are a number of key features to the use of direct drive turbines. While not completely independent of each other, in this section, features can be divided into considerations associated with the shaft and considerations associated with the bearings.

6.5.2. Shaft Twisting (torsional stress) Analysis

Compared to gearbox drivetrains, the shaft length is generally shorter in direct drive systems. There are simple mechanical reasons for this: one is that the long coupling length is not necessarily needed as it is for geared solutions. Of-course, this depends very much on the geometry of the wind turbine nacelle.

There is a pre-disposition to make the shaft length shorter to not only minimize weight, but also to take into account the high torque of the machine. In comparison to geared drivetrains, in direct-drive configurations this torque is directly applied to a single shaft. The torsional stress under these high torque conditions can be quite significant, and thus as a result, while the shaft length is short the shaft diameter tends to be wider. This diameter, however, is dependent on the particular type of bearing under consideration. For instance, the use of a single bearing requires a larger diameter shaft while that of a double bearing assembly generally involves the use of a smaller diameter shaft. This is largely because existing single bearing standards are restricted to relatively large minimum shaft diameters and existing spherical self-aligning bearings are restricted to relatively small diameters. Some length differences exist between single bearing variants vs. double bearing variants as well. Double bearings require longer shaft length to accommodate the back cylindrical bearing.

Torsional stress (σ_{S-tor}) can be considered as a result of the generator torque T_g. A shaft of inner diameter of d_{iS} =2.42m and outer diameter of d_{oS} =2.62m will experience some maximum torsional stress (σ_{S-tor}) from this torque for a single bearing configuration. Similarly, for a double bearing configuration, the shaft diameter is given as: $d_{iS} = 1.31$m and $d_{oS} = 1.51$m. The maximum stress must fall (within some shaft safety factor, s_S) under the maximum shear stress (σ_{US}) of the shaft material such that $\sigma_{US} > s_S\sigma_{S-tor}$. As will be seen, this maximum material shear is related to the yield stress of the material. There is, of-course an additional stress contribution (as seen in the previous sub-section) resulting from the unbalanced magnetic loading as the shaft rotates. This unbalance is a result of the eccentricity and can cause an increase in torsional stress at particular rotational angles of the rotor relative to the stator.

Figure 6-21 below elaborates and looks at the geometric considerations of the generator shaft under concentric rotational considerations. Generally, it is assumed that the rotor is made from one single structurally stiff material and all shear acts on the shaft. In some cases, especially where the shaft diameter is narrow and the shaft is a separate inserted piece, depending on the

attachment method, there may be slippage or shear between shaft and rotor. It is assumed that no such shear is present and that the wider shaft surface area prevents any slippage as well.

The total shear stress on the shaft is a product of the force ($dF = \tau dA$) at each elemental area ($dA = rdrd\emptyset$) given some lever arm length, r and arc length $rd\emptyset$. The value τ is the elemental shear stress for some small element shown in Figure 6-21. The relationship can be expressed as some elemental moment, dM, of the shaft material. The assumption here is that the relationship is valid for a shaft that is prismatic, i.e. has a circular cross-section. Equation (6.15) demonstrates that [216].

$$T_g = \int_A dM = \int_A dF \cdot r = \int_A \tau dA \cdot r \tag{6.15}$$

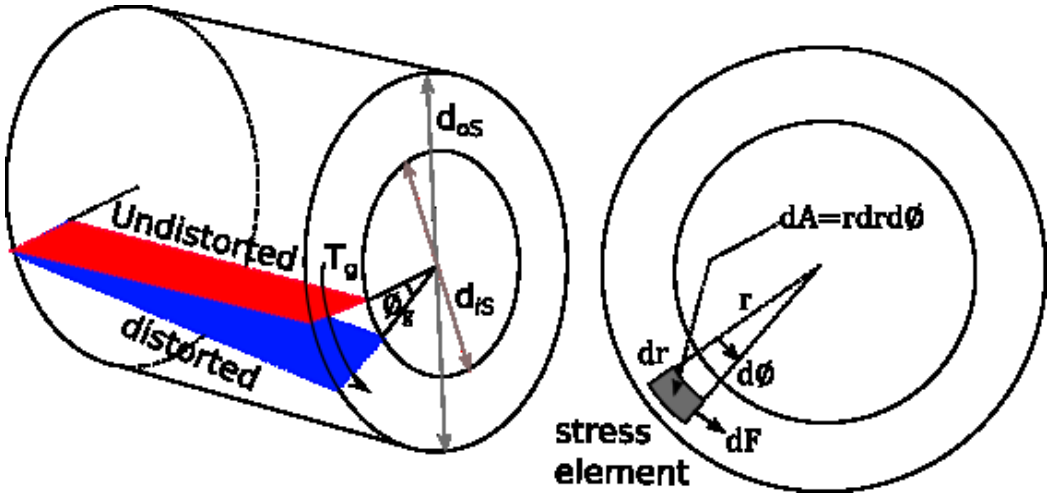

Figure 6-21 Defining torsional stress resulting from generator torque.

An added assumption can be made that the elemental shear stress (τ), itself, is linearly dependent on ratio of the radial position, r, and the total radius, R, such that: $\tau = \frac{r}{R}\sigma_{S-tor}$. This indicates an increasing percent contribution as the position r increases on the small infinitesimal element. The maximum stress on the shaft occurs when at the longest radius, $r = R = \frac{d_{oS}}{2}$. It can also be noted that the polar moment of inertia can be defined as: $J = \int_A r^3 drd\emptyset$. This moment for the hollow cylinder can further be calculated as: $J = \frac{1}{2}\pi\left(\left(\frac{d_{oS}}{2}\right)^4 - \left(\frac{d_{iS}}{2}\right)^4\right)$. This means that Equation (6.15) above can be re-written further as shown in Equation (6.16) [216].

$$T_g = \int_A \frac{r}{R}\sigma_{S-tor} r\, dA = \frac{\sigma_S}{R}\int_A r^2\, r dr d\emptyset$$

$$= \frac{\sigma_{S-tor}}{R}\int_A r^3\, dr d\emptyset = \frac{\sigma_{S-tor} J}{R} \tag{6.16}$$

$$\sigma_{S-tor} = \frac{T_g R}{J} = \frac{2T_g d_{oS}}{\pi\left(\left(\frac{d_{oS}}{2}\right)^4 - \left(\frac{d_{iS}}{2}\right)^4\right)}$$

Looking at steel as the structural material for the shaft, it is seen that the ultimate shear stress (σ_{US}) can be given by a simple relationship to the tensile yield stress (γ_{US}) as shown in Equation (6.17). This stress calculation is a common approach based on the Von Mises criterion [217]. Given the absence of experimental data on shear, the tensile yield stress can be used to make an estimate instead.

$$\sigma_{US} = \frac{\gamma_{US}}{\sqrt{3}} \tag{6.17}$$

From this equation, it is noted that the maximum shear stress on the shaft of the air-gap winding and slotted iron-core generators would be roughly $\sigma_{US} = 318$MPa. The generator torque in both cases is $T_g = 4.5MNm$. The resulting stress can thus be calculated for each of the generator types. Looking at a single bearing generator it is seen at a value of: $\sigma_{S-tor(s)} = 9.32$MPa and for a double bearing generator at the value of: $\sigma_{S-tor(d)} = 30.66$MPa.

6.5.3. Shaft Twisting (torsional stress) FEM

Going further than an analytical calculation and producing a simple numerical structural analysis of shaft shear stress and associated deformation to verify the analytical approach is possible. This is shown in Figure 6-22 below for an air-gap winding machine and in Figure 6-23 for a slotted iron-cored generator. It should be noted that in each case the stress value is estimated as: $\sigma_{S-tor(sa)} = 15.76$MPa and $\sigma_{S-tor(si)} = 18.64$MPa respectively. The subscript "*sa*" refers to the air-gap machine with a single bearing and the subscript "*si*" refers to the iron-cored machine with a single bearing. Equivalent subscripts "*da*" and "*di*" will be used to refer to these machines in a double bearing configuration. A question is raised at this point. The shear stress estimated via finite element analysis is lower than that produced from the analytical approach in the previous sub-section – why should this difference exist. In the purely analytical approach, it was assumed that as the shaft twists, the shear stress contributor would continue to be purely from twisting action of the shaft. However, this is not necessarily the case in a real

system. In a more realistic scenario, the twisting of the shaft will affect the nature of subsequent shear. The initial purely torsional shear may lead to a subsequent bending moment as well. The energy associated with the shear process would thus be divided between two shear components: the torsional and the bending shear. As a result, the torsional shear should be slightly lower than the analytical value computed.

Repeating the shear stress numerical analysis for a two-bearing system where the shaft diameter is narrower, Figure 6-24 and Figure 6-25 show the structural analysis and demonstrate the regions of high shear stress. The resulting value of the stress for the air-gap winding machine and the slotted iron-core machine are given as: $\sigma_{S(da)} = 25.4\text{MPa}$ and $\sigma_{S(di)} = 31.97\text{MPa}$ respectively.

Having addressed the issue of torsional stresses. It can be seen that there is significantly higher stress resulting from the two-bearing configuration. This suggests that the single bearing approach is better suited for lower shear stress in the generator shaft. In both cases, however, the stress on the shaft is less than the maximum allowable stress on the material. Further, it should be noted that for simplicity the effect of UMP has not been accounted for. It is likely however that for a given eccentricity the stress values in both single and double bearing configurations will maintain a similar relative relationship as for the case without UMP discussed in this section.

What remains to be addressed is the bending moment of the shaft. This is discussed in the next section.

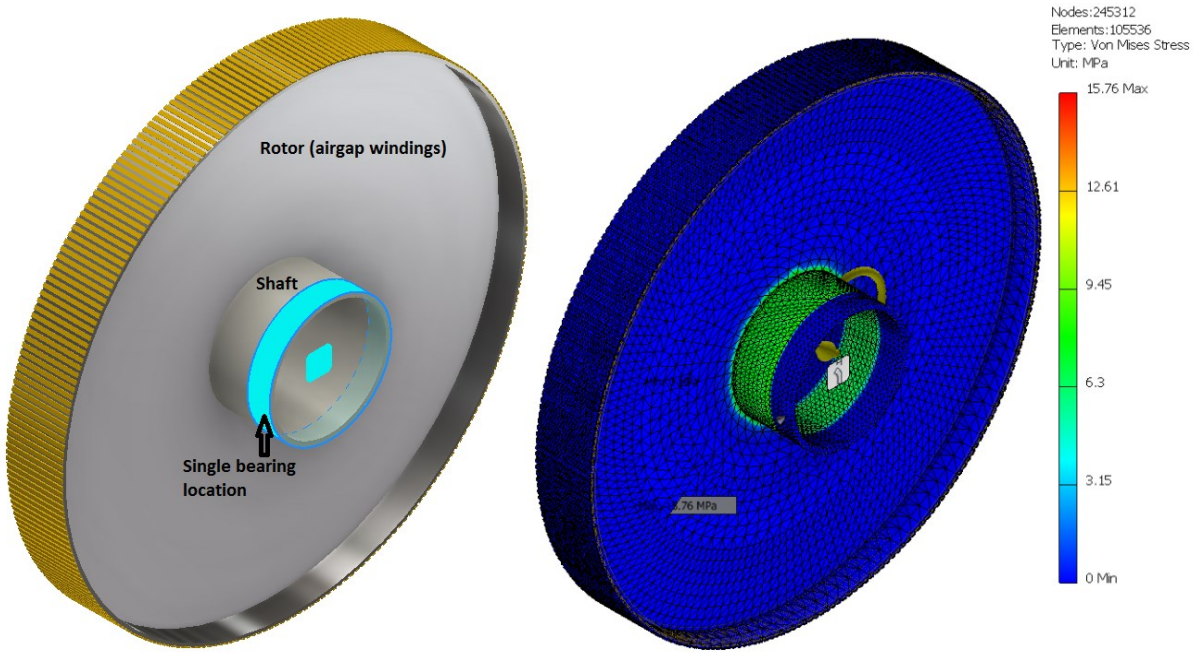

Figure 6-22 Structural analysis of shear stress using finite element modelling for an air-gap winding generator rotor in a single bearing configuration.

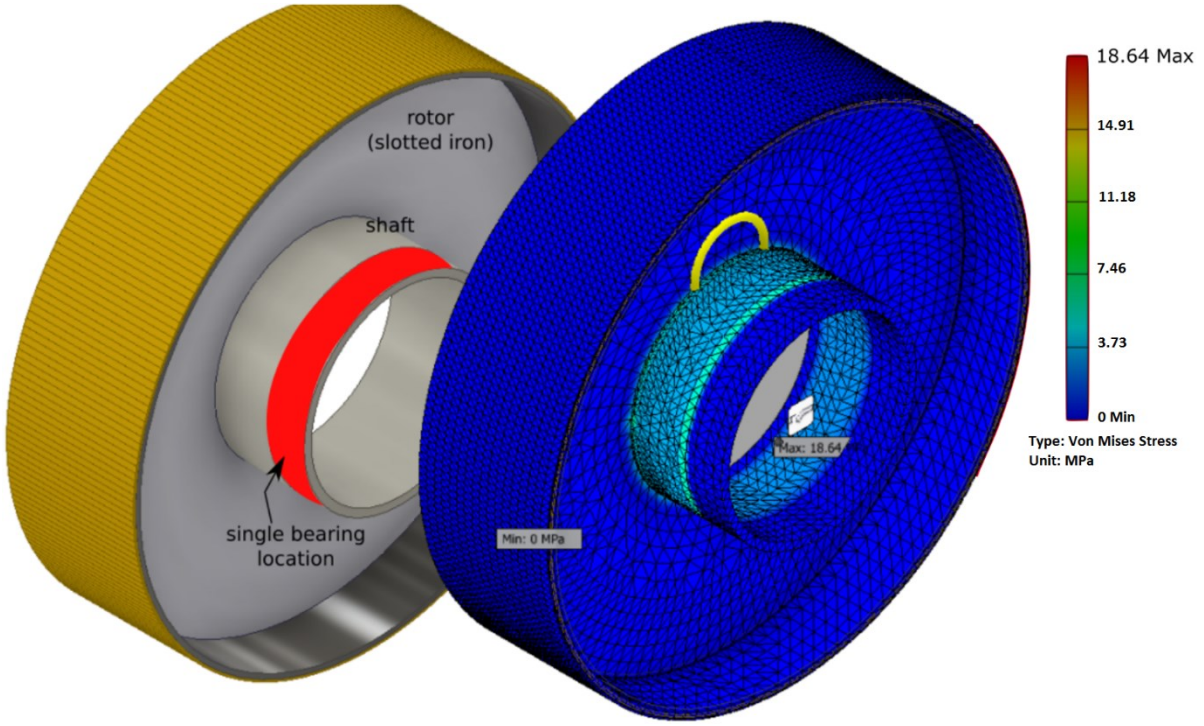

Figure 6-23 Structural analysis of shear stress using finite element modelling for a rotor in a slotted iron cored generator under a single bearing configuration.

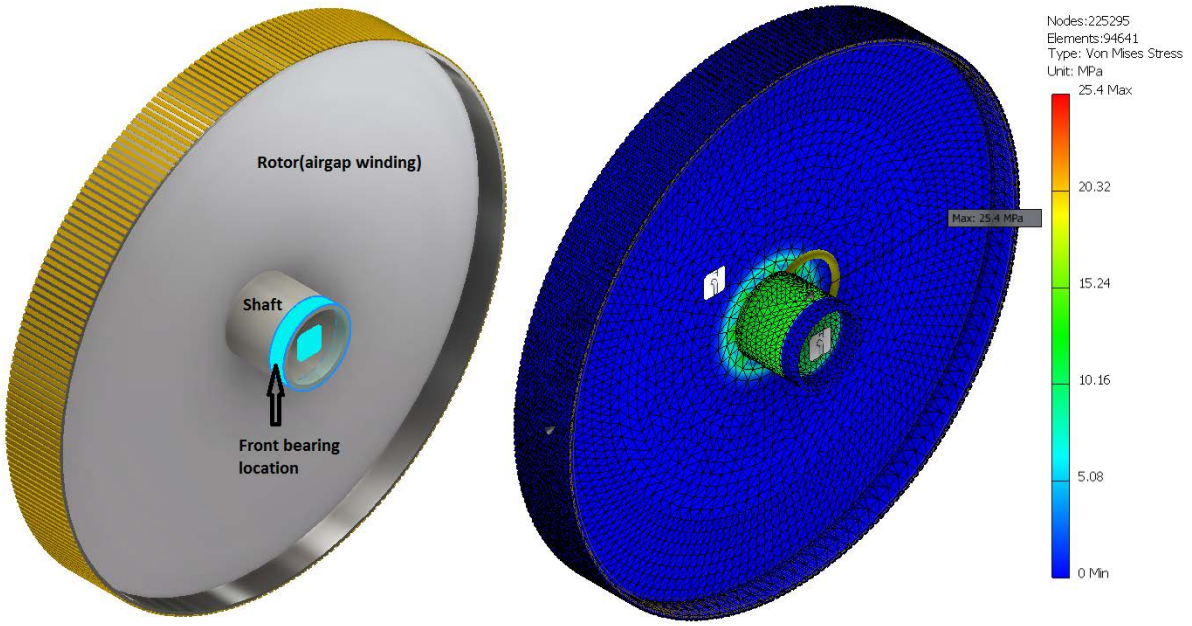

Figure 6-24 Structural analysis of shear stress using finite element modelling for a rotor in an air-gap wound generator under a double bearing configuration.

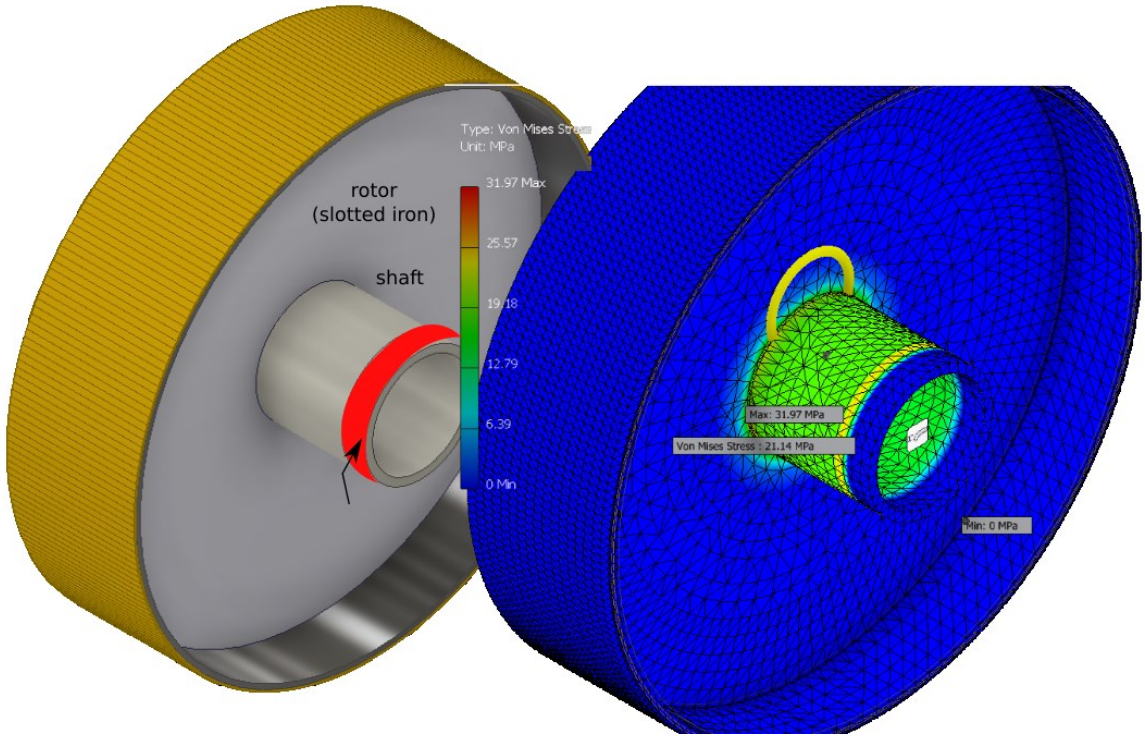

Figure 6-25 Structural analysis of shear stress using finite element modelling for a rotor in a slotted iron generator under a double bearing configuration.

6.5.4. Shaft Bending Analysis

Shaft length is an important consideration for the machine as well. For instance, the bending moment on longer and smaller diameter shafts, especially in geared systems, means that greater support is needed via multiple bearings. Generally, a two-bearing support is used for these shafts. Direct-drive systems allow the possibility of minimizing shaft length compared to geared systems. This means a potential reduction in bending moment applied to the rotor-turbine interface. Since a comparison between geared and direct-drive approaches is not appropriate here, the adopted comparison is for only a direct drive system using either a single bearing or a typical double bearing approach.

A key part of the bending moment is a result of the turbine or rotor weight. For the purposes of analysis, only the moment resulting from the weight of the rotor is looked at in this section. In practice, the UMP is considerable. This is necessary to do since the turbine-hub, at least, in the case of a single bearing system is fixed by the bearing. The weight of the rotor for an air-gap winding based generator is $m_{rg} = 33$ tons while the weight of the rotor in a slotted iron-cored generator is $m_{rg} = 51$ tons. Shaft lengths vary as follows for each of the air-gap single bearing, air-gap double bearing, slotted iron single bearing and slotted iron double bearing systems respectively: $L_{S(sa)} = 0.77$m, $L_{S(da)} = 1.5$m, $L_{S(si)} = 1.33$m, $L_{S(di)} = 2.76$m.

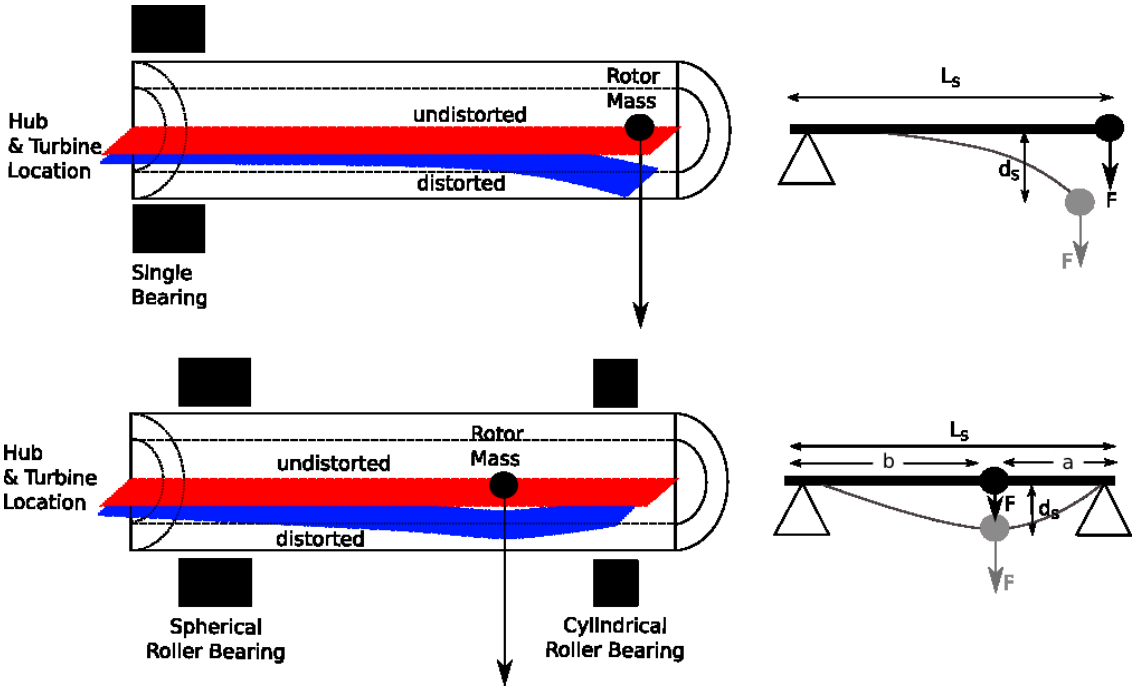

Figure 6-26 The geometry of a bending shaft in a generator with a single bearing (top) and a double bearing (bottom).

The choice of shaft length for the double bearing configuration was based on an existing generator design presented in [202].

As with the shaft torsional stress, the analysis can begin analytically by looking at the equations that define the bending stress considering the geometry shown in Figure 6-26.

There are two particular scenarios leading to two different representations of the bending moment. Two equations can be constructed [218]–[220] as shown in Equation (6.18) and Equation (6.19) for the single bearing and double bearing case respectively. While displacement was not particularly important for the analytical discussion of shaft torsional stress, it is more significant for bending stress. The bending shaft can lead to rotor contact with the stator. With this in mind, an estimate of the maximum displacement (d_S) can be set.

$$\sigma_{S-bend} = \frac{FL_S}{Z};\ d_S = \frac{F\ L_S^3}{3E\ J} \tag{6.18}$$

$$\sigma_{S-bend} = \frac{F\ a\ b}{ZL_S};\ d_S = \frac{F\ a^2 b^2}{3E\ J\ L_S} \tag{6.19}$$

In the equations, the value F is the force on the shaft as a result of the rotor mass. L_S is the length of the shaft and Z is the section modulus of the shaft. Adding to this E is the flexural modulus and J is the moment of inertia about the bending axis. Noting that the generator shaft is a hollow cylindrical tube, each of Z and J can be computed as follows in Equations (6.20) and (6.21).

$$Z = \frac{\pi\left(\left(\frac{d_{oS}}{2}\right)^4 - \left(\frac{d_{iS}}{2}\right)^4\right)}{2d_{oS}} \tag{6.20}$$

$$J = \frac{\pi}{2}\left(\left(\frac{d_{oS}}{2}\right)^4 - \left(\frac{d_{iS}}{2}\right)^4\right) \tag{6.21}$$

From these equations computing the bending stress for a single bearing system using either an air-gap winding machine or a slotted iron machine the following respective values are noted: $\sigma_{S-bend(sa)} = 0.52$MPa and $\sigma_{S-bend(si)} = 1.38$MPa. Likewise, the relative maximum displacements of the rotor in a single bearing machine are respectively, $d_{S-bend(sa)} = 0.13$mm and $d_{S-bend(si)} = 0.052$mm. Repeating this exercise for a double bearing machine it is seen that the following stress values: $\sigma_{S-bend(da)} = 0.76$MPa and $\sigma_{S-bend(di)} = 2.32$MPa and the following displacement values: $d_{S-bend(da)} = 0.017$mm and $d_{S-bend(di)} = 0.054$mm.

6.5.5. Shaft Bending FEM

Analysing the air-gap winding generator further using numerical analysis, the results shown in Figure 6-27 are noted. In this analysis for a single bearing system, the average bending stress is given as $\sigma_{S-bend(sa)} = 2.47$MPa. The displacement resulting from this stress is very small at $d_{S-bend(sa)} = 0.03$mm. Clearly very little effect occurs in a single bearing system.

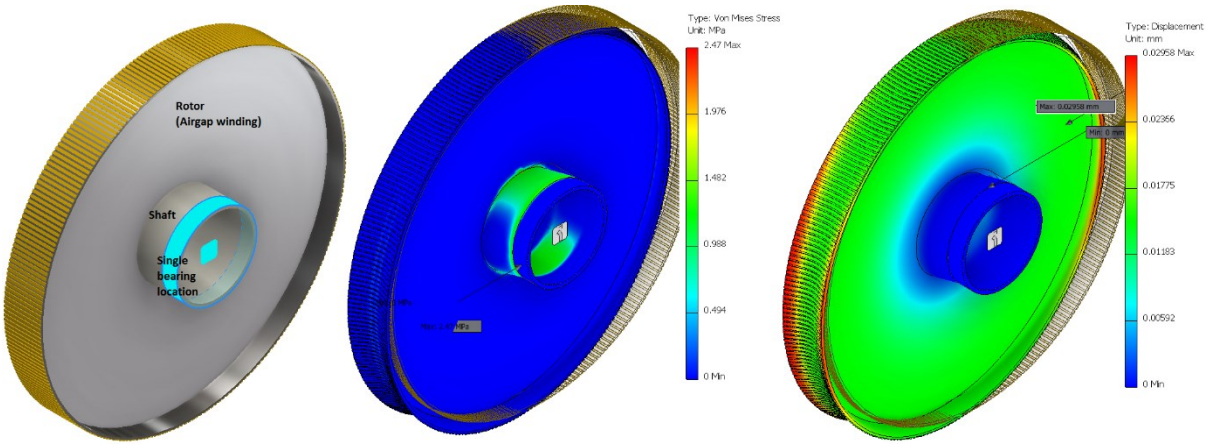

Figure 6-27 Structural analysis of bending stress using finite element modelling for a rotor in an air-gap winding generator under single bearing configuration.

Comparing this to a slotted iron-cored generator (Figure 6-28), it is noted that the bending moment is given as $\sigma_{S(si)} = 4.83$MPa while the maximum displacement of the rotor resulting from this moment is only $d_{S(si)} = 0.06$mm. The mass of the generator is higher in comparison to the air-gap winding version.

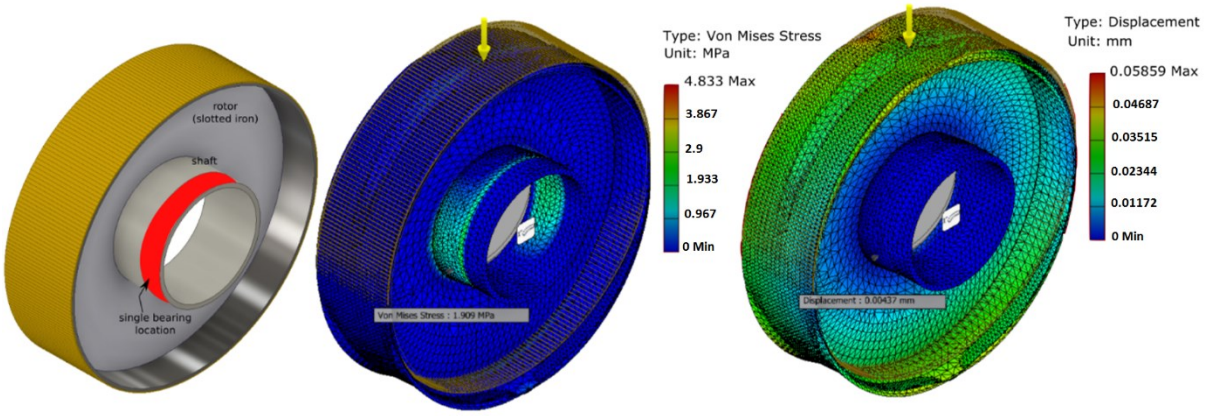

Figure 6-28 Structural analysis of bending stress using finite element modelling for a rotor in a slotted iron cored generator under single bearing configuration.

It is clearly seen that when switching to a double bearing system the stresses and displacements of the shaft are greater. This is a result of two particular reasons, the first of these is the

increased length of the shaft, and the second is the decreased diameter necessary to accommodate the double bearing configuration.

Figure 6-29 demonstrates the finite element modelling of a double bearing system for an air-gap winding machine. The bending stress in this system is given as $\sigma_{S(da)} = 1.66$MPa and the displacement of the rotor is $d_{S(da)} = 0.026$mm.

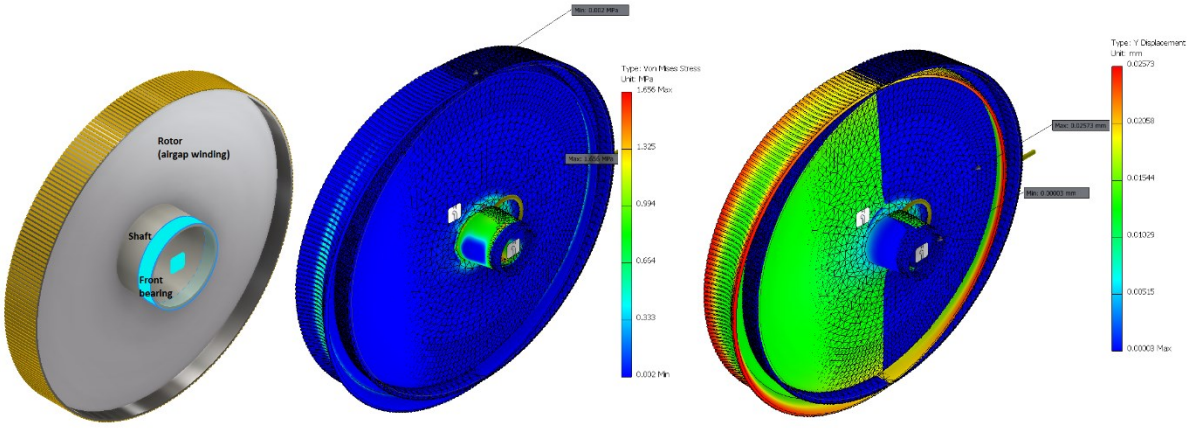

Figure 6-29 Structural analysis of bending stress using finite element modelling for a rotor in an air-gap winding generator under a double bearing configuration.

Likewise, Figure 6-30 demonstrates the finite element modelling of a double bearing system for a slotted iron cored machine. The bending stress in this system is given as $\sigma_{S(di)} = 2.89$MPa and the displacement of the rotor is $d_{S(di)} = 0.0522$mm.

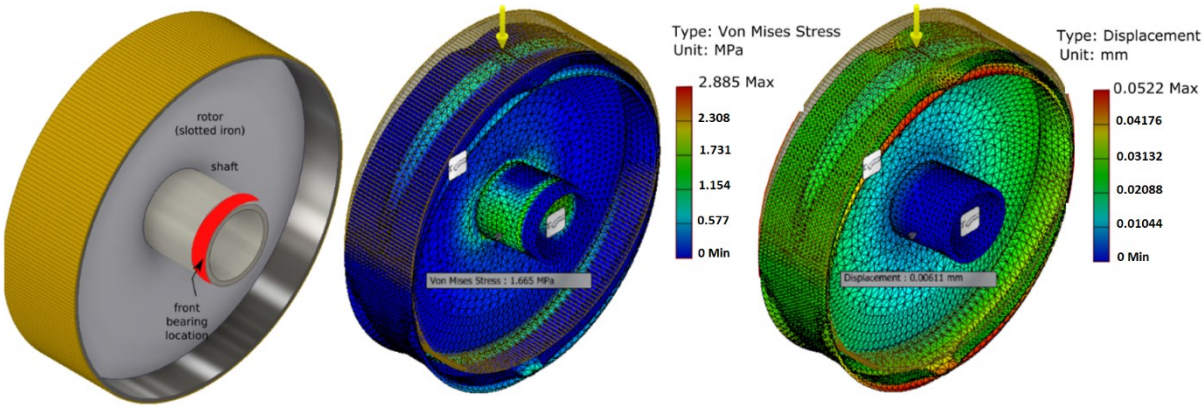

Figure 6-30 Structural analysis of bending stress using finite element modelling for a rotor in a slotted iron cored generator under a double bearing configuration.

6.5.6. Bearing Lifespans

At this stage, it is worthwhile having a discussion of the actual bearings that will hold the shaft in position. As noted in the previous section, the bearing plays a significant role in the configuration of generator, shaft and hub/turbine in the wind turbine. This study made use of two different types of bearing systems, namely: a single bearing and a double bearing system. Figure 6-31 demonstrates the two different bearing systems used.

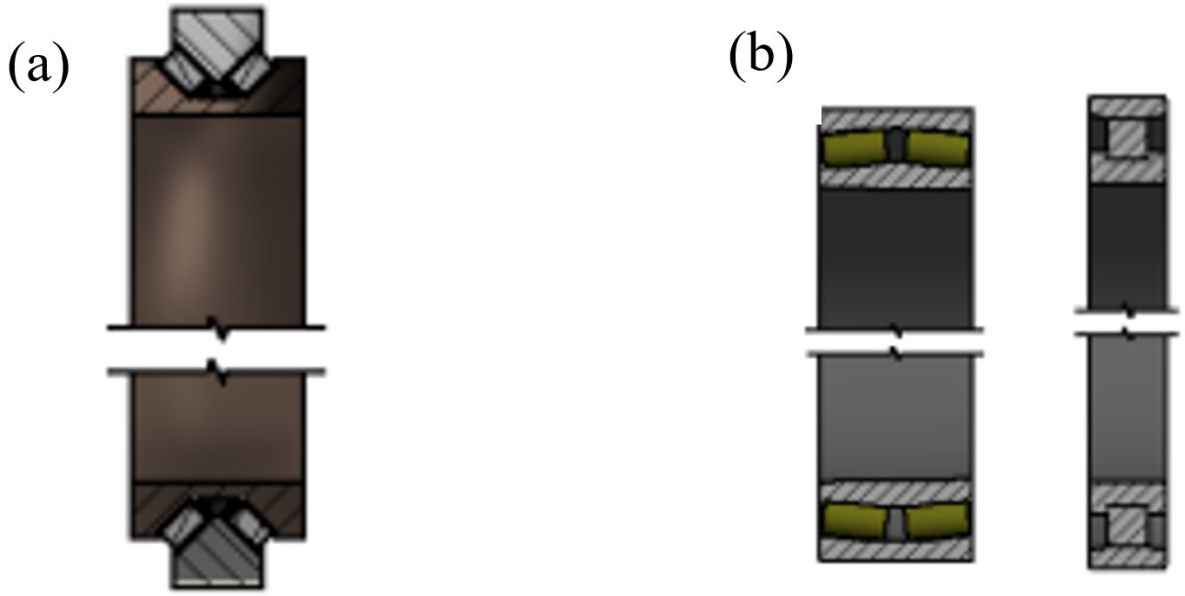

Figure 6-31 In (a) A single bearing model. In (b) a double bearing model.

The question of designing and selecting the appropriate kinds of bearings is an important one. This is especially true for larger direct drive generators where the challenges of maintaining air-gap uniformity play a significant factor in the resulting UMP and corresponding bearing wear. This matter is complicated by the fact that these large direct-drive generators also weigh significantly more than the gear-boxed generators.

Recall that structural connection between the rotor/hub combination with the stator structure via the bearing is accomplished by a short shaft. The diameter of this shaft will be controlled by the bearing dimensions. There are, however, other considerations. Thermal expansion and contraction in the rotor, stator, shaft and housing as well as issues of structural deformation can determine the type of bearing design used [193]. The generator system will generate significant amounts of heat changing the dimensions of the air gap and causing a variation in the UMP. Further expansion can occur at the shaft and in the housing. Humidity effects and moisture can

cause bearing materials to oxidize and degrade over time. Such considerations require sealing of bearing elements [221].

More can be added to these considerations of the speed of operation of the wind turbine. The specific bearing should be selected to accommodate the rated rotational speed of the turbine – in the case of our wind turbine; this is relatively slow at a rate of roughly 12.1rpm. Slow vs. fast speed has multiple impacts. For one the wear pattern on the bearing assembly changes. The lower speed implies a higher loading per roller over a given time frame that can lead to various issues such as flattened areas in rolling elements and indentations in raceways. Generally, such damage may also occur in an irregular fashion. Such deformations can also lead to higher vibration and noise levels as well as jamming. For large loads at slow speeds, the static load conditions should be a primary consideration when choosing or designing a bearing.

Consider the direct hub mountable single bearing, the spherical roller bearing and the simple cylindrical roller bearing shown in Figure 6-31. Referring to the datasheet, the following properties of these bearings are noted – listed in Table 6-7.

Bearing Type	***Basic Static Load (C_{0_B})***	***Basic Dynamic Load (C_B)***	***Equivalent Dynamic Load (P_U)***	***Life Span (air-gap)***	***Life Span (slotted iron)***
Double Bearing Configuration (Spherical Roller Bearing)	14684 [kN]	45000 [kN]	2400 [kN]	$3.13*10^8$ [h]	$1.68*10^8$ [h]
Double Bearing Configuration (Cylindrical Roller Bearing)	8000 [kN]	3300 [kN]	440 [kN]	$2.56*10^4$ [h]	$1.37*10^4$ [h]
Single Bearing Configuration (Tapered Rotor Bearing)	61000 [kN]	14000 [kN]	2750 [kN]	$1.99*10^6$ [h]	$0.53*10^6$ [h]

Table 6-7 The datasheet values for the static, dynamic and fatigue load. Additionally, the last two columns indicated computed lifespans for each machine type for the single and double bearings used.

It should be noted that the table lists the lifespans of the bearings. These lifespans are computed values based on the formulation of the cylindrical bearing formulation of lifespan. It should be noted that the complexity of loads of a rotating wind turbine makes calculations of dynamic lifespans quite complex [198], [222], [223]. Even though the offshore wind pattern is a lot more laminar than the onshore wind pattern, one reason for the complexity of the dynamic load calculation is that the real wind patterns are hard to be accurately forecasted in nature. This means quantification of dynamic life spans would require a-priori knowledge of weather

related data. Further complications occur when considering issues of humidity, temperature and lubrication.

The analytical formula for a cylindrical bearing is shown in Equation (6.22). Likewise, the formulation for the other two bearings can be represented as shown in Equation (6.23).

$$L_{cy} = \frac{10^6}{60n}\left(\frac{C}{P}\right)^p \tag{6.22}$$

$$L_{sp} = L_{tp} = 2\frac{10^6}{60n}\left(\frac{C}{P}\right)^p \tag{6.23}$$

For a cylindrical roller, the value of the exponent p is 10/3, the value n is the rated speed of operation of the turbine, C is the basic dynamic load rating and P is the equivalent dynamic load. The resultant lifespan is given in hours of operation.

This understanding can be used to further evaluate the life span of both the spherical and tapered single bearing using simple geometric considerations. These geometric considerations are shown in Figure 6-32.

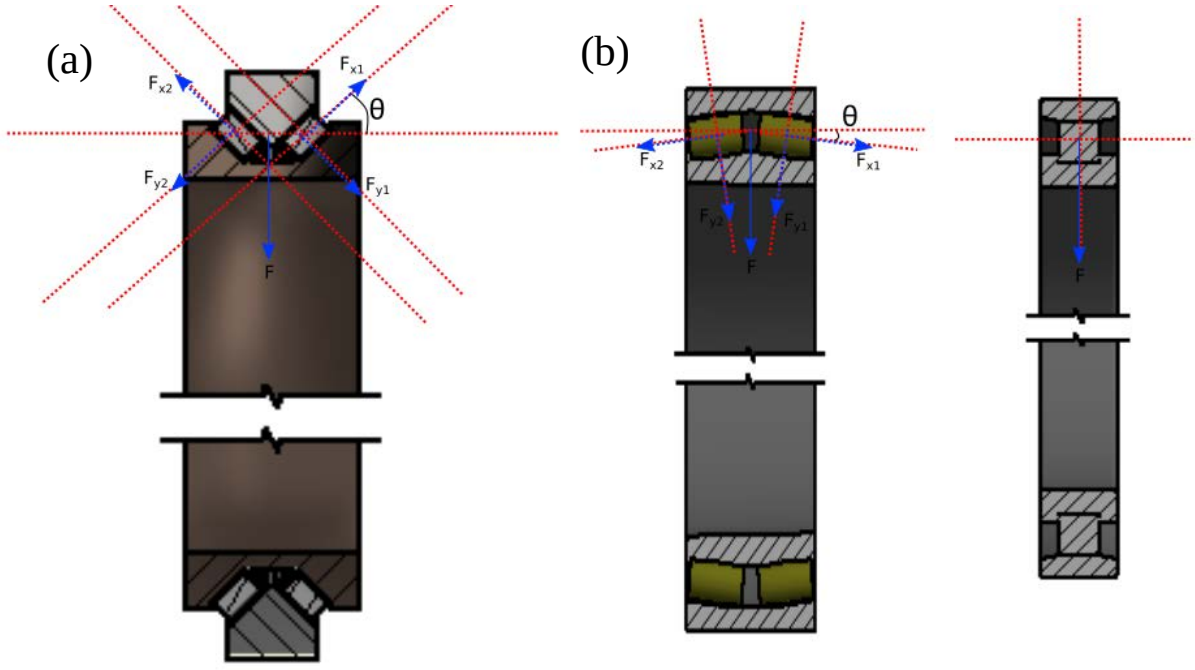

Figure 6-32 In (a) A single bearing model. In (b) a double bearing model.

The important point to note in the geometric representation is that the distinction between the single bearing and two bearing system is the geometric angle of the load force. For the single bearing this angle is $\theta = 45°$ and for the front bearing in the double bearing system this angle

is $\theta = 4.6°$. The force, F represents the loading of the bearing from the rotor weight. For the cylindrical bearing, this force can be directly translated in to the dynamic load, such that $P = F$. However, for the spherical bearing this force is better represented as $P = Fcos\theta$ and for the tapered single bearing $P = F/cos\theta$. A further argument can be made that since both these last two bearings distribute the dynamic load *P* across two different roller sets, the actual life span is likely to be double that of a single cylindrical roller bearing.

Given this understanding the lifespan of each of the bearing types can be computed. The dynamic load, *P* should ideally be determined experimentally, however for the purposes of this study the assumption is that this load is the weight of the rotating parts given as:

$$F_{(a)} = 151300\ x\ 9.81 = 1483\text{kN}$$

For an air-gap winding generator and as:

$$F_{(i)} = 1693000\ x\ 9.81 = 1661\text{kN}$$

The resulting loads in each of the three bearings is well under the maximum loading allowable by the bearing under static conditions.

6.6. Conclusion

In this chapter, a discussion of a real wind turbine design based on two direct drive generators, namely, an air-gap winding generator and a slotted iron cored generator was undertaken. This generator was put in the context of the other parts of the wind turbine such as the shaft, the bearing, the turbine, the converter, the nacelle housing and the tower.

The discussion of this design is divided into a discussion of the forces and moments associated with the various components and their positional considerations. It is then extended to a look at the generator itself. This focus is used to determine the torque and shear considerations of the generator and further extended to finite element modelling to determine forces between the rotor and stator. This work was then extended to the rotor and associated shaft related shear and bending stress. This chapter concluded with a final look at bearings and bearing life.

It was noted that between the two bearing types used and under the shaft loading conditions and under rated wind speeds both bearing configurations are sufficient for direct drive generators. The single bearing approach has the advantage of reduced weight.

Chapter 7. Multi-Body Modelling for Different 5MW Wind Turbine Designs

7.1. Introduction

The choice of permanent magnet generator and bearing design in a direct-drive wind turbine can be considered as the most critical step. The low speed operation requires a large generator size. Maintaining the uniformity of the generator airgap imposes stiffer generator support structure requirements. Variety of sources, such as shaft misalignment, bearing wear, structural deflection, and inaccurate bearing positioning during assembly, can result in generator airgap non-uniformity (rotor eccentricity). Eccentricity should not exceed 10-20% of the uniform airgap length in order to successfully keep the wind turbine in operation [192], [193], [224], [225]. The airgap length in a typical PMG design equals 1/1000 of the generator diameter [226], meaning that the 5MW iron-cored PMG design introduced in Chapter 6 with 6.36m diameter has a 6.36mm mechanical airgap length (equals the magnetic airgap length). That also means the eccentricity should not exceed 1.27mm otherwise the airgap flux density will increase significantly leading to an increase in normal stress and possibly leading to greater deflection [227]. In the case of airgap winding design, there is more flexibility in designing the mechanical airgap length (much smaller than the magnetic airgap length) because of the lower magnetic forces due to the large magnetic airgap. The mechanical airgap length for the airgap of the 5MW airgap winding generator was chosen to be 6.36mm similar to the iron-cored one. The uniformity of the generator airgap qualifies the structural integrity which is mainly related to the stiffness of the generator support structure and the bearings' design and bed-plate.

This chapter uses a multi-body simulation software (SIMPACK) to initiate investigations and comparison by providing assessments of electromagnetic interaction and internal drive-train loading for four possible designs for a 5MW direct-drive wind turbine in response to the loads normally seen by a wind turbine. The four designs include: (a) iron-cored PM direct-drive generator supported by two main bearings, (b) airgap winding PM direct-drive generator supported by two main bearings, (c) iron-cored PM direct-drive generator supported by a single main bearing, (d) airgap winding PM direct-drive generator supported by a single main bearing. The generator designs for each type were introduced in Chapter 6 and the choice of relevant bearing configurations were based on recommendations from a bearing manufacturer [221].

An aero-elastic simulation code (HAWC2) was used to extract the hub loads for different wind speeds corresponding to the normal operation of the wind turbine. The dynamic eccentricity and its influence on the electromagnetic interaction and consequential effects on bearing loading for all four designs is examined to determine the most optimal support structural configuration for a direct-drive system.

7.2. Multi-body simulation for wind turbines

Operational experience from existing direct-drive wind turbines to corroborate the claim of the possible consequences of the generator eccentricity and UMP on vibration, noise and bearing wear is not enough [194]. Designers, therefore, tend to rely on numerical simulation techniques to make inferences on the dynamics of the drive-train [228]. For such problems, multi-body simulation (MBS) techniques are commonly used in the industry. Wind turbine components, in this technique, are modelled as rigid or elastic bodies connected by kinematic constraints or force elements. The motion equations of the components, then, are solved using a set of computation algorithms. MBS tools deliver efficient understandings of the dynamic loading of the drivetrain taking in account all related loading conditions and system-wide interactions that exist in a wind turbine system [192].

Limited studies on the dynamics of direct-drive generators have been conducted in the past. Poore and Lettenmaier [229] in 2001 analysed and compared different drive-train and generator design combinations for wind turbines rated between 0.75-3MW. The proposed 1.5MW direct-drive design used two inverted-arrangement main-shaft tapered roller bearings engineered to meet the specified life as shown in Figure 7-1. A connection torque tube made of ductile iron is mounted on the bearings and connected to the main shaft through the bearings on one side and to the generator rotor on the other side. Even though, a single large-diameter bearing design would allow a direct connection between the rotor hub and the tower support structure, it was disregarded because the benefits were not obvious for the authors and the risk was seen as relatively high. Experimental tests on this design showed no vibration problems with the generator, although up to 50% eccentricity was permitted during extreme loads [230] [231].

Xing *et al.* [232][233] used MBS technique to de-couple gear behaviour from turbine dynamics in a 750kW floating wind turbine. Greater shaft and bearing loading and internal drive-train responses were noticed in the results caused by wave and pitch induced motions. Their study also suggested greater fatigue loads and therefore greater cost implications for floating wind

turbines. Sethuraman *et al.* [192], [194], [228], [234] also used MBS to study the dynamics of a 5MW direct-drive floating wind turbine. The results showed very small effect of the extra motions of the floating wind turbine on the rotor eccentricity and UMP with the generator design tolerances being fairly preserved. Extensive comparisons between land based wind turbine and floating wind turbine were presented showing additional excitation caused be extra axial loads and tilting moments in the floating wind turbine.

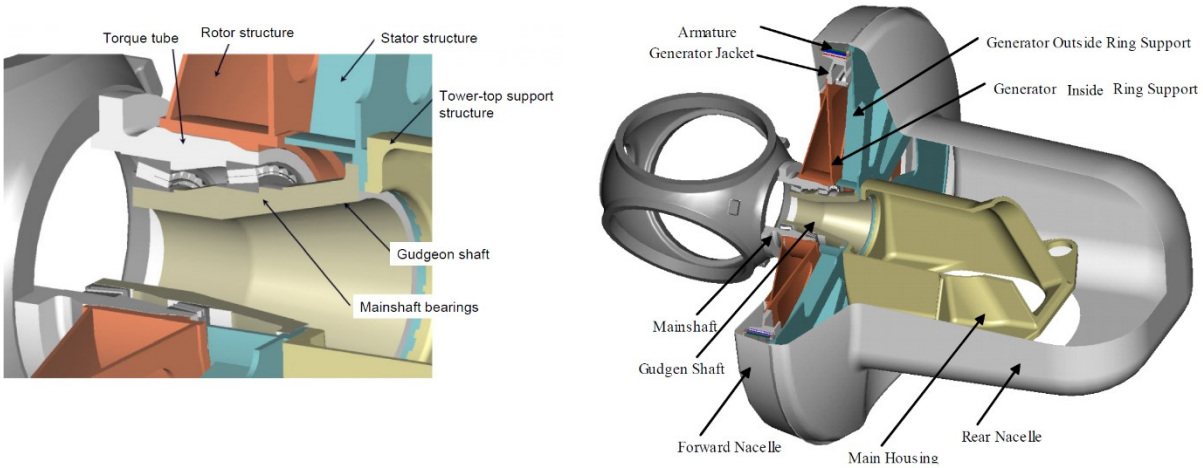

Figure 7-1 Section view of nacelle and main shaft area. Modified from: [229]

7.3. Methodology

Time-domain multi-body simulation tools namely HAWC2 [235] and SIMPACK [236] were used to examine the drive-train dynamic behaviour. HAWC2 is a multi-body simulation code that can simulate the time domain responses of a wind turbine by finite element modelling and coupling aero-elastic behaviour. SIMPACK, on the other hand, is a multi-body simulation software that generates detailed kinematic and dynamic analysis of drive-train components by means of integrated wind turbine simulation, incorporating the various forces and control elements.

The global motion response and drive-train loads are obtained by 1-hour simulations in HAWC2 and then fed to a detailed stand-alone drive-train model in SIMPACK as shown in the flow chart in Figure 7-2. The response statistics for shaft displacements, eccentricity, forces due to UMP, and the main bearing reactions were computed and compared for four designs include: (a) iron-cored PM direct-drive generator supported by two main bearings, (b) airgap winding PM direct-drive generator supported by two main bearings, (c) iron-cored PM direct-

drive generator supported by a single main bearing, (d) airgap winding PM direct-drive generator supported by a single main bearing.

For modelling the air-gap winding machine in SIMPACK, reference was made to [228]. The iron-cored generator model was replaced with the air-gap winding generator with suitable modifications of the mass and inertia properties. Specifications of both generators are detailed in Chapter 6. The bearing stiffness values were carefully tuned to accommodate a lighter structure such that the static deflection obtained for both the air-gap winding machine and the iron-cored machine were similar.

A simplified analytical model for UMP force was implemented based on [234] by measuring the eccentricity due to shaft displacement at every time-step. The analytical model relates the dynamic change in air-gap caused by radial shaft displacement to unbalanced magnetic forces, using a linear relationship as shown in Figures 6-14 & 6-15.

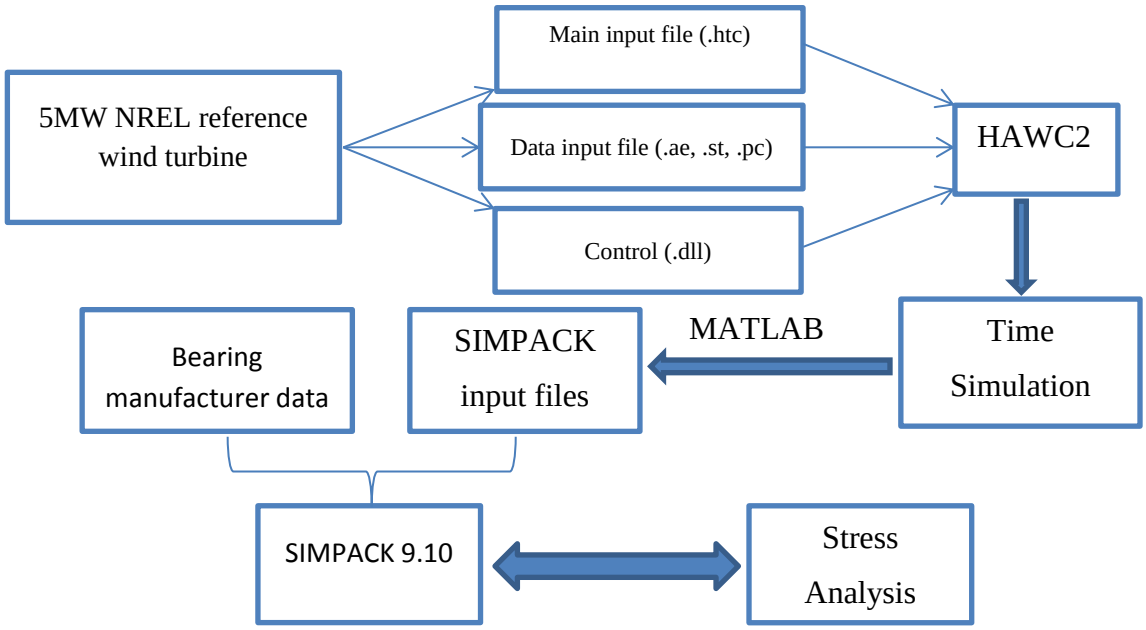

Figure 7-2 Flow chart showing the methodology of using a MATLAB code to transfer HAWC2 simulation output to force element inputs in SIMPACK model.

Two main reactions are included in SIMPACK model which are (a) eccentricity that induces unbalanced magnetic pull [237] and (b) shaft vibrations that appear as bearing load and torsional vibrations in the drive-train [238].

7.3.1. Unbalanced Magnetic Pull induced by rotor eccentricity

The stator and rotor in a large PMG are physically separated by a very small air-gap that does not exceed a few millimetres. The non-uniformity of this air-gap results in unbalanced magnetic pull inside the machine. The probability of radial shaft misalignment is quite high which can be the major contributor to eccentricity. Shaft misalignment gives rise to a dynamically eccentric rotor disturbing the equilibrium of the magnetic attraction forces that result in a periodical radial load on the bearings, undesirable noise and vibration due to the increase in space harmonics [176].

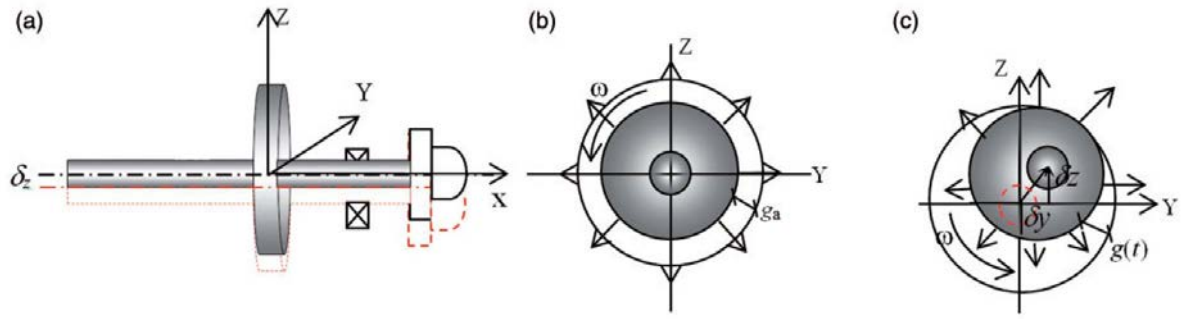

Figure 7-3 (a) Shaft displacement, (b) concentric rotor, (c) eccentric rotor. Reproduced from [194]

As shown in Figure 7-3, the rotor rotational direction is counter-clockwise around the x-axis and the eccentricity occurs in the Y-Z plane. Assuming $\delta y(t)$ and $\delta z(t)$ to be the incremental shaft displacements, in the Y-Z plane, measured at any instant *t*. Then the dynamic change in the air-gap, denoted as $g(t)$ can be obtained from the incremental shaft displacement along the Y and Z axis as

$$g(t) = \sqrt{\partial y^2(t) + \partial z^2(t)} \tag{7.1}$$

Analytical and numerical models to calculate the UMP in PMGs are presented in Chapters 4 & 5. Only static rotor eccentricity was considered in sub-section 6.4.2. in Chapter 6 for the considered 5MW generator designs. The unbalanced magnetic forces due to eccentricity were computed using magneto static simulations in Finite Element Methods Magnetics software (FEMM). Static eccentricity simulations were carried out as they represented the worst possible conditions that can be experienced by the rotor. The rotor was displaced from 3% up to 90% of the mechanical airgap length. The resultant force in the airgap winding generator was obtained from the airgap flux density variation and was approximated as a function of the static rotor eccentricity ($e_{static} = g(t)/g_a$) and given by:

$$UMP_{AW_{static}} = 562.35 \times e_{static} - 16.208 \quad [kN] \tag{7.2}$$

Similarly, the resultant force in the iron-cored generator was given by:

$$UMP_{IC_{static}} = 2291.8 \times e_{static} - 32.896 \quad [kN] \tag{7.3}$$

Armature reaction effect on UMP is very small, therefore, it was not considered in this model. A simple method for converting static eccentricity into dynamic eccentricity was done by considering the frequency of shaft displacements, w_s. The two different components of the resultant dynamic force along Y-axis and Z-axis were then resolved for the air-gap winding generator as:

$$UMP_{Y_{AW\,dynamic}} = (562.35 \times e(t) - 16.208)\cos w_s t \quad [kN] \tag{7.4}$$

$$UMP_{Z_{AW\,dynamic}} = (562.35 \times e(t) - 16.208)\sin w_s t \quad [kN] \tag{7.5}$$

Similarly, the resultant force in the iron-cored generator was given by:

$$UMP_{Y_{IC\,dynamic}} = (2291.8 \times e(t) - 32.896)\cos w_s t \quad [kN] \tag{7.6}$$

$$UMP_{Z_{IC\,dynamic}} = (2291.8 \times e(t) - 32.896)\sin w_s t \quad [kN] \tag{7.7}$$

It is quite important, on the other hand, to consider tilting eccentricity as well, especially when studying the single bearing designs. Section 4.5. introduces the analytical principle to calculate the UMP induced by tilting rotor eccentricity. Dividing the rotor of each generator into 100 slices then calculating the UMP induced in each slice due to a certain static eccentricity using FEMM and applying the analytical principle is the method adopted to obtain the tilting eccentricity UMP. Figures 7-4 & 7-5 show the UMP induced in one slice of the proposed 5MW air-gap winding and iron-cored generators respectively.

Assuming that the tilting is occurring around the centre of gravity of the machine's rotor, that means m, q, which are the generator slice numbers on the two sides of the tilting centre, are equals. Applying Equation (4.53) gives the total induced UMP because of different rotor tilting angles in each generator as shown in Figures 7-6 & 7-7. The resultant force in the air-gap winding generator due to $e_{tilt_{deg}}$ number of degrees was obtained from the air gap flux density variation of each slice and was approximated as a function of the tilting degree and given by:

$$UMP_{AW_{tilting}} = 218.87 \times e_{tilt_{deg}} - 15.106 \quad [kN] \tag{7.8}$$

Similarly, the resultant force in the iron-cored generator was given by:

$$UMP_{IC_{tilting}} = 1743.2 \times e_{tilt_{deg}} - 19.64 \quad [kN] \tag{7.9}$$

Considering the static eccentricity for the first slice $e_{tilt_{max}}$ which has highest eccentricity between all slices, Equations (7.8) & (7.9) can be rewritten as:

$$UMP_{AW_{tilting}} = 135.37 \times e_{tilt_{max}} - 14.944 \quad [kN] \tag{7.10}$$

$$UMP_{IC_{tilting}} = 754.7 \times e_{tilt_{max}} - 20.002 \quad [kN] \tag{7.11}$$

The two different components of the resultant dynamic tilting force along Y-axis and Z-axis were resolved for the air-gap winding generator as:

$$UMP_{Y_{AW\,tilting_{dynamic}}} = \left(135.37 \times e_{tilt_{max}}(t) - 14.944\right) \cos w_s t \quad [kN] \tag{7.12}$$

$$UMP_{Z_{AW\,tilting_{dynamic}}} = \left(135.37 \times e_{tilt_{max}}(t) - 14.944\right) \sin w_s t \quad [kN] \tag{7.13}$$

Similarly, the resultant force in the iron-cored generator was given by:

$$UMP_{Y_{IC\,tilting_{dynamic}}} = \left(754.7 \times e_{tilt_{max}}(t) - 20.002\right) \cos w_s t \quad [kN] \tag{7.14}$$

$$UMP_{Z_{IC\,tilting_{dynamic}}} = \left(754.7 \times e_{tilt_{max}}(t) - 20.002\right) \sin w_s t \quad [kN] \tag{7.15}$$

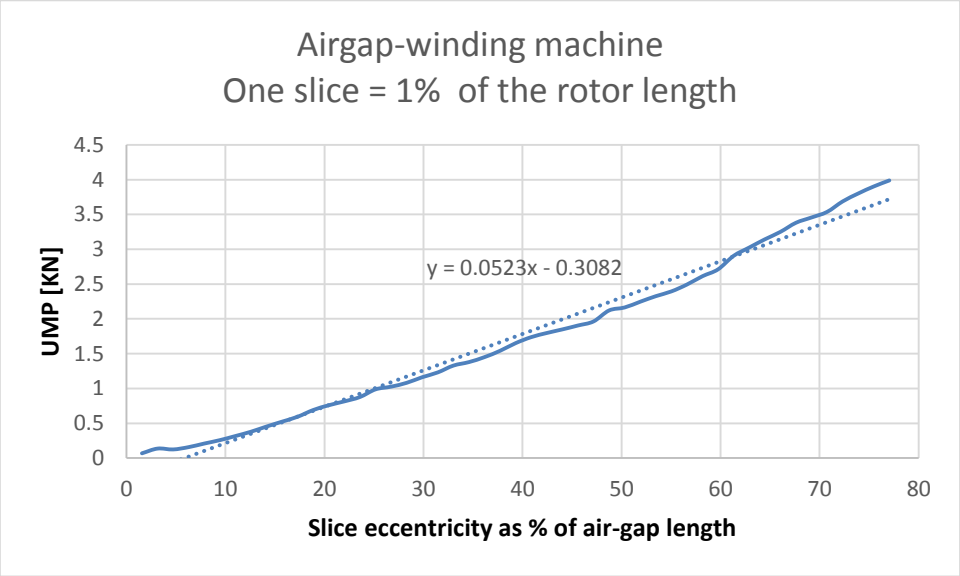

Figure 7-4 UMP induced in one slice of the air-gap winding machine's rotor due to static eccentricity showing the best fit line and equation

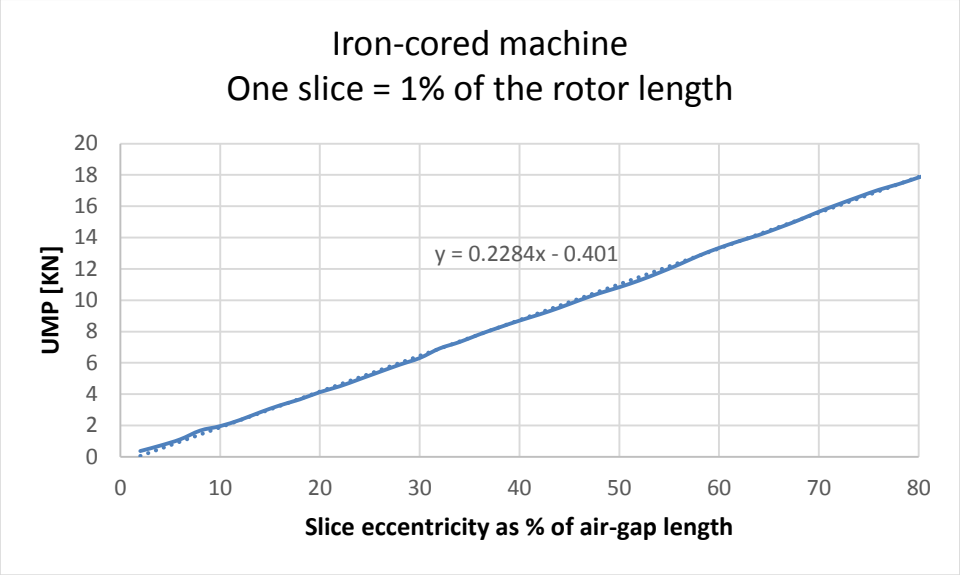

Figure 7-5 UMP induced in one slice of the iron-cored machine's rotor due to static eccentricity showing the best fit line and equation

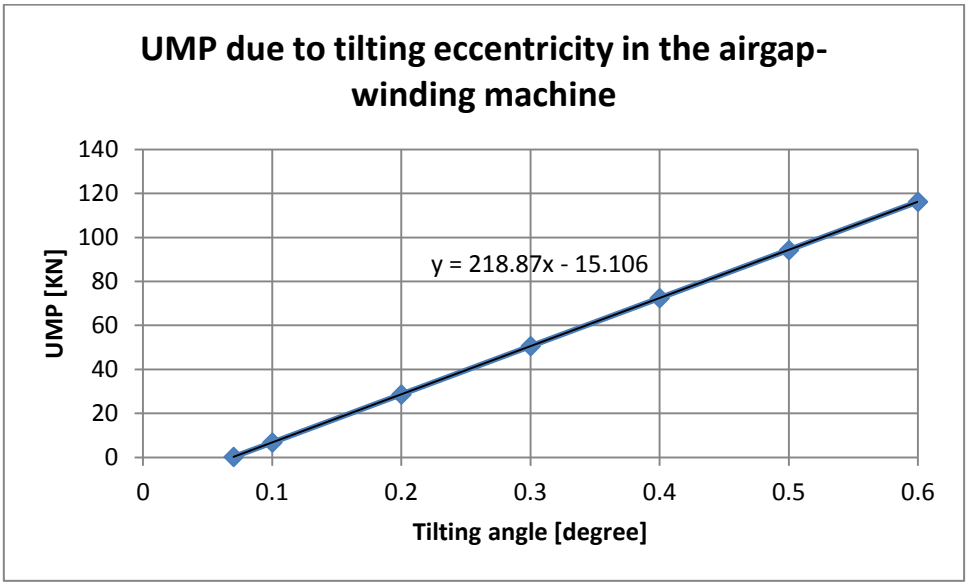

Figure 7-6 UMP induced in the air-gap winding machine due to tilting rotor eccentricity showing the best fit line and equation

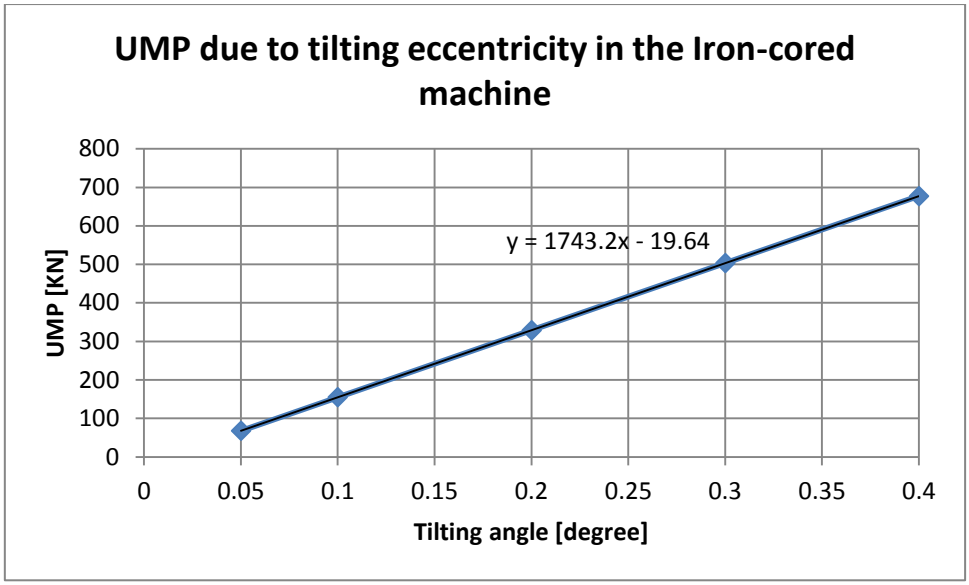

Figure 7-7 UMP induced in the iron-cored machine due to tilting rotor eccentricity showing the best fit line and equation

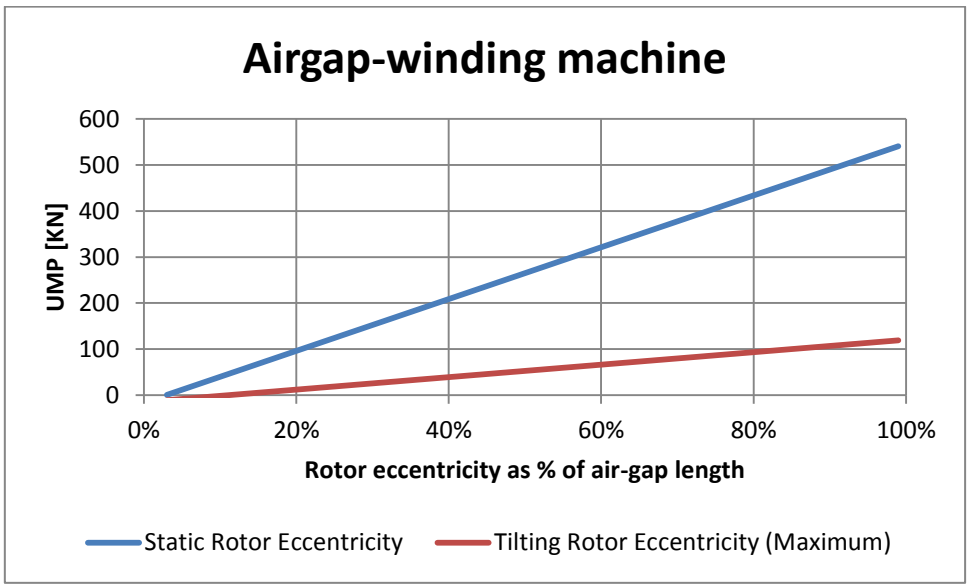

Figure 7-8 Comparison between the UMP induced in the 5 MW air-gap winding generator due to static and tilting rotor eccentricities

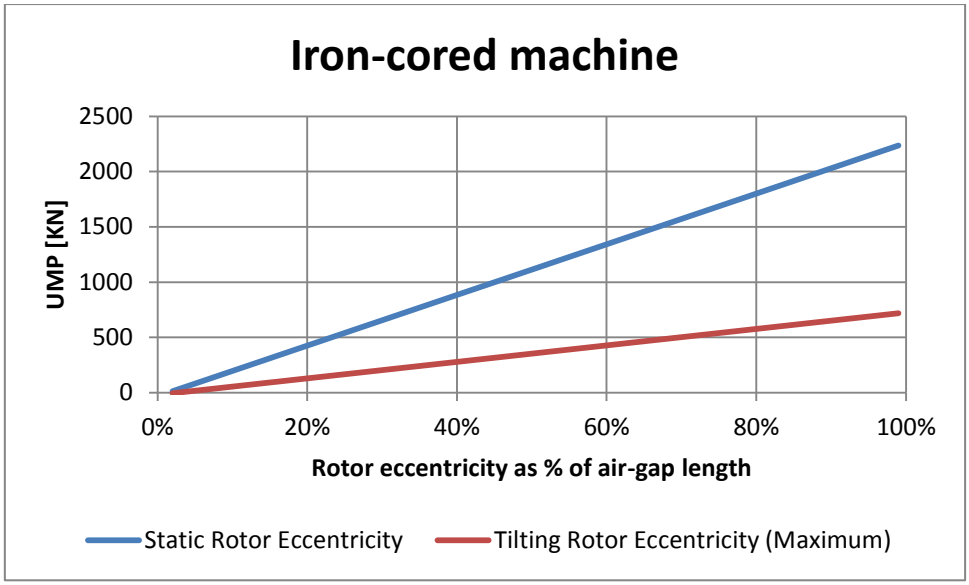

Figure 7-9 Comparison between the UMP induced in the 5 MW iron-cored generator due to static and tilting rotor eccentricities

Comparison of the UMPs induced in the airgap-winding machine because of similar static and tilting rotor eccentricities is shown in Figures 7-8. The same comparison in the iron-cored machine is shown in Figure 7-9. The comparisons clearly indicate that tilting rotor eccentricity in both machines generates much lower UMP than what is generated by the static rotor eccentricity. In the airgap-winding machine, the UMP induced by a static rotor eccentricity is about 4 times higher than the UMP induced by a similar maximum tilting rotor eccentricity. Whereas, in the iron-cored machine, the UMP induced by a static rotor eccentricity is about 3 times higher than the UMP induced by a similar maximum tilting rotor eccentricity.

In conclusion, as having the maximum effect, it is enough to consider the maximum static rotor eccentricity when it comes to bearing design.

7.3.2. Shaft displacement, vibratory torque and possible feedback effects

The shaft of a wind turbine experiences axial, radial and bending displacements due to external loads. If the shaft is out of balance, displaced from the centre or if the shaft rotates at a speed equal to the natural frequency of transverse vibration, then the shaft begins to whirl, causing it to resonate. This can be very damaging to the wind turbine generator and the bearings.

Assuming the shaft as a rigid body, as it is displaced from the location of the centreline; the bearing stiffness constantly attempts to return the shaft back to the centreline. This is very similar to a rotating mass that experiences a centrifugal force as it moves away from the centre of rotation, and returned by inward pull from bearings. If the displacement of the shaft $g(t)$ is

measured at every instant time *t*, then the centrifugal force on the rotor shaft assembly is given by [239]:

$$F_{centrifugal} = mw_s^2(g(t) + e) \tag{7.16}$$

where, w_s is the frequency of the shaft displacement, e is the static deflection. If m is the mass of the rotor shaft assembly, then the restoring forces from the bearings with stiffness, k must balance the centrifugal forces as:

$$mw_s^2(g(t) + e) = k.g(t) \tag{7.17}$$

$$w_s = w_{nat}\sqrt{\frac{g(t)}{g(t) + e}} \tag{7.18}$$

where, w_{nat} is the natural frequency of transverse vibrations $\left(\sqrt{\frac{k}{m}}\right)$. The available torque from the generator would be noticeably reduced if the frequency of shaft displacement is high and the bearing stiffness is not high enough.

The equation of a generator torque under rotor eccentricity can be derived from the kinetic energy equation. Assuming a mass with rotational moment of inertia I_1 rotating at an angular velocity w_1 when a torque T is applied. Assuming the shaft also experiences displacement, then in order that the kinetic energy (E) to be conserved during rotation [192]:

$$E = \frac{1}{2}I_1\left(w_1^2(t)\right) + \frac{1}{2}(I_2(t))\ (w_s^2(t)) \tag{7.19}$$

where, $I_2(t)$ is the moment of inertia of combined mass (shaft + rotor + turbine) displaced by a distance $g(t)$ from the centre. To compute the instantaneous torque, equation (7.19) is divided by time t and the intended frequency of rotation ω [194]:

$$T(t) = \frac{1}{2wt}I_1\left(w_1^2(t)\right) + \frac{1}{2}(I_2(t))\ (w_s^2(t)) \tag{7.20}$$

$$T(t) = T_1(t) + T_{vib}(t) \tag{7.21}$$

where T_1 is the available generator reaction after losses due to vibration T_{vib}.

7.3.3. Control of the generator torque

The control method of the torque of 5MW direct-drive PM generator was introduced by Sethuraman *et al.* [192], [234]. The method was originally implemented for the NREL 5MW geared-driven reference wind turbine [189]. According to this method and depending on the measured generator speed, the wind turbine operates according to five different control regions namely 1, $1\frac{1}{2}$, 2, $2\frac{1}{2}$ and 3 as shown in Figure 7-10.

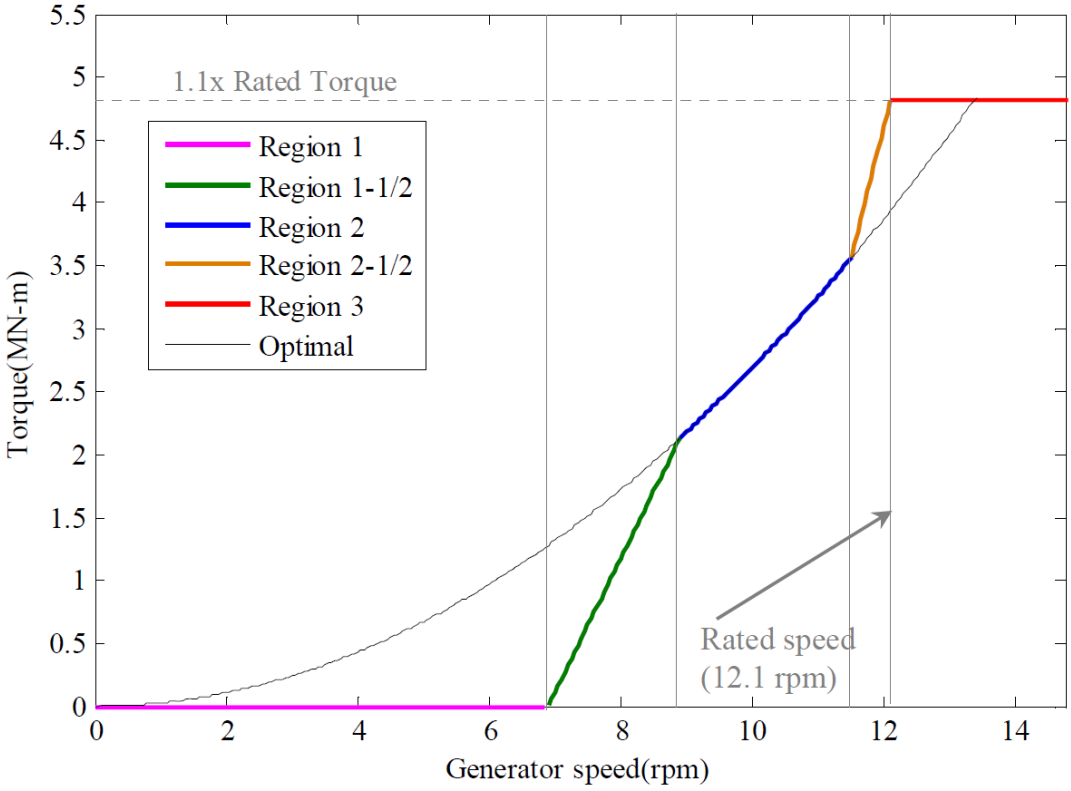

Figure 7-10 Speed-Torque characteristics of the 5 MW generator [192], [234]

The generator starting-up occurs in region 1 for speed between 0 rpm and 6.9 rpm and no generator torque in this region. In region $1\frac{1}{2}$, the generator torque starts to increase to reach the optimal torque-speed value and the electrical power is produced normally. Region 2 starts when the generator's torque-speed is optimal (8.9 rpm) and the turbine in this region operates at the peak of its $C_p - \lambda$ curve and follow the square law [192]:

$$T_{gen\,2} = \left(\frac{\pi}{30}\right)^2 k_T \Omega^2 \tag{7.22}$$

Where, $T_{gen\,2}$ is the generator torque in region 2, Ω is the generator speed in rpm, and k_T is the nominal optimal torque control gain (generator torque constant) in (Nms^2/rad^2) and given by:

$$k_T = \frac{1}{2}\,\rho\pi R^5 \frac{C_{p\,max}}{\lambda_{max}^3} \approx \frac{P_{rated}}{\Omega_0^3} \approx 2.45 \left[\frac{MNms^2}{rad^2}\right] \tag{7.23}$$

Where, R is the rotor radius, $C_{p\,max}$ is the maximum power coefficient, λ_{max} is the tip speed ratio at $C_{p\,max}$, and P_{rated} is the rated turbine mechanical power. The torque gain is set to about 90% of the optimal in order to account the wind speed turbulence and maximise the captured energy [240]. Region $2\frac{1}{2}$ is introduced in order for the generator torque to match the rated torque (1.1 * 4.5 MNm) at the rated speed (12.1 rpm) as the control law used in region 2 would result in a value below the rated torque at the rated speed. The generator torque equation in region $2\frac{1}{2}$ is given as [241]:

$$T_{gen\,2\frac{1}{2}} = T_1 + \left(\frac{T_{rated} - T_1}{\Omega_2 - \Omega_1}\right)(\Omega - \Omega_1) \tag{7.24}$$

Where, Ω is the measured generator speed which determines $T_{gen\,2\frac{1}{2}}$, T_1 is the torque at the rotor speed Ω_1 at the start of this region and Ω_2 is the rotor speed at the rated torque T_{rated}.

Region 3 represents the above rated wind speed and that is when the pitch control is active to avoid negative aerodynamic damping as recommended by [242]. Generator torque in region 3 is given as:

$$T_{gen\,3} = 1.1\,T_{rated} \tag{7.25}$$

This assumption is basically to protect the wind turbine components and avoid extreme generator overloading.

7.4. Multi-body simulation results

HAWC2 was used to compute the external wind turbine loads and feed them into a stand-alone SIMPACK model. HAWC2 results are similar to these used in [192], [194], [234]. The equations of motion were solved by a time integration scheme and the results were presented as time series of forces, moments, and deformations. HAWC2 outputs include 6 Degree of Freedom (DOF) motion elements that provide the instantaneous nacelle position, velocity, and accelerations while other sensors for the drivetrain provide the main shaft moments and forces.

Four arrangements include two generator designs (airgap winding and iron-cored generators) and two main bearing arrangements (two main bearings and single bearing) were modelled in SIMPACK. The dynamics from the rest of the drive-train including power electronics and

conversion equipment were lumped as passive elements contributing to the mass and inertia at the nacelle. As shown in Figure 7-11 for the two-main bearing design, the tower and platform action were simulated by a dummy body directed by a 6 DOF joint that accepts the position, velocity and acceleration inputs from the respective HAWC2 models. The shaft moments, forces and torque input from HAWC2 are applied as time excitations using force element FE-93. The two components of the UMP (Y and Z) (presented in subsection 7.3.1.) computed at each instant from the shaft displacements and applied between stator and rotor using force element FE-50. The generator reaction torque is modelled using force element FE-110, a proportional actuator which applies the generator torque determined by using the shaft speed from the HAWC2 simulations as the reference input (w_{ref}) as [192]:

$$T = K_p(w - w_{ref}) + K_I \int_0^t (w - w_{ref})dt \tag{7.26}$$

K_P and K_I are the proportional and integral gains for the controller.

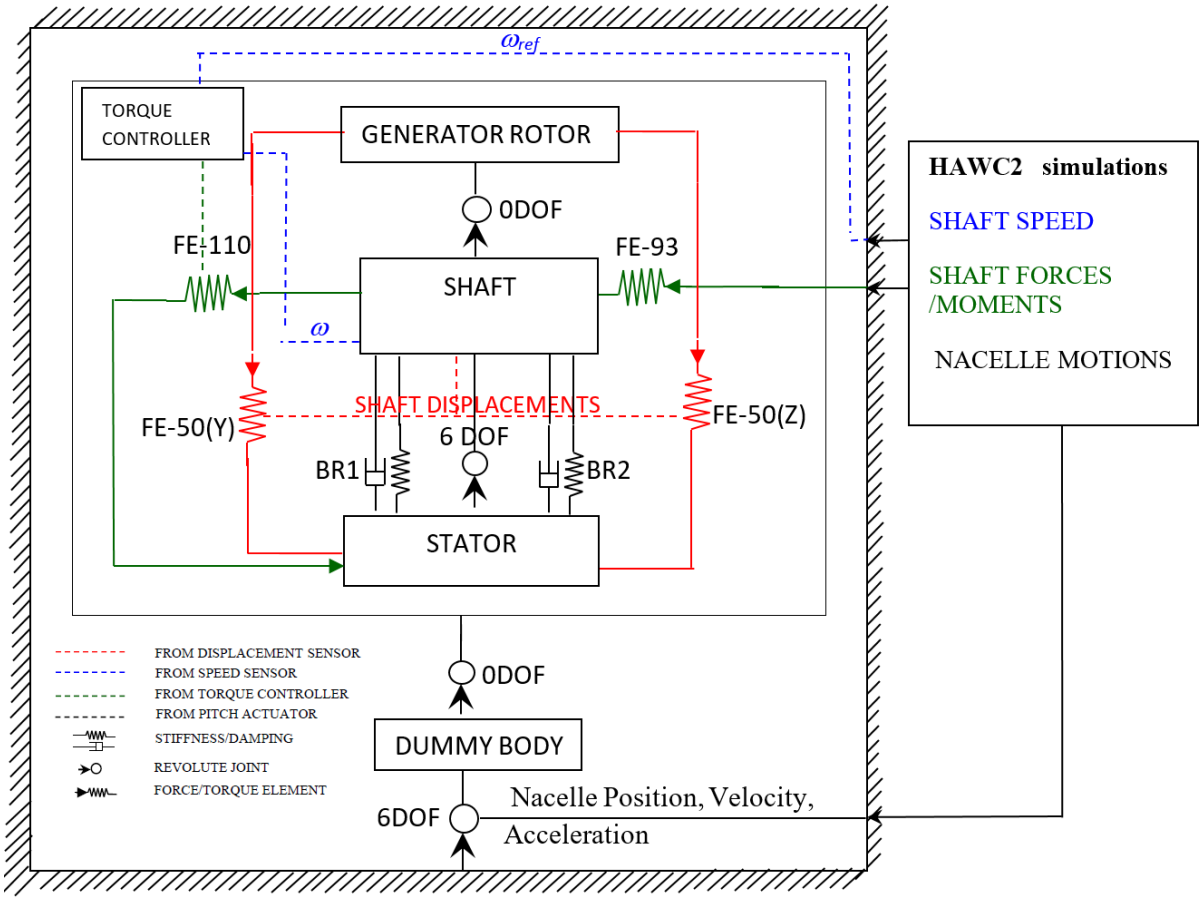

Figure 7-11 Multi-body model of the direct-drive generator two-bearings wind turbine in SIMPACK

The proportional gain of the controller was chosen to be the slope of region 2 of the respective torque-speed characteristics [192], [228], [234]. The integral gain was chosen to minimise the steady-state speed error to less than 0.5rad/s.

As the wind speed increases, the radial shaft displacements also increase. Figures 7-12, 7-14 and 7-16 show the time histories of the net UMP forces for the air-gap winding machine compared with the iron-cored machine for wind speeds of 4m/s, 15m/s and 25m/s respectively. Figures 7-13, 7-15, and 7-17, show the corresponding time histories for radial shaft displacements. For the air-gap winding machine, the mean values of UMP forces at 4m/s was 4.3kN and this increased to a value of 19.1kN and 43.8kN at 15m/s and 25m/s respectively. The iron-cored machine has substantially higher net UMP forces with a mean of 40kN, 98kN and 329kN at 4, 15 and 25m/s wind speed respectively. It is observed that the air-gap winding machine results in a substantially lower UMP forces compared to the iron-cored machine for the same shaft displacements.

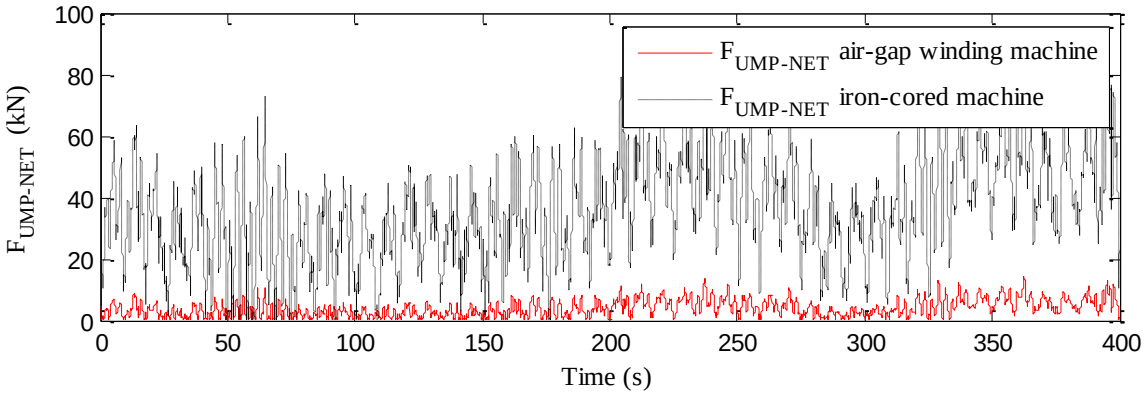

Figure 7-12 Net UMP forces measured at an average wind speed of 4m/s

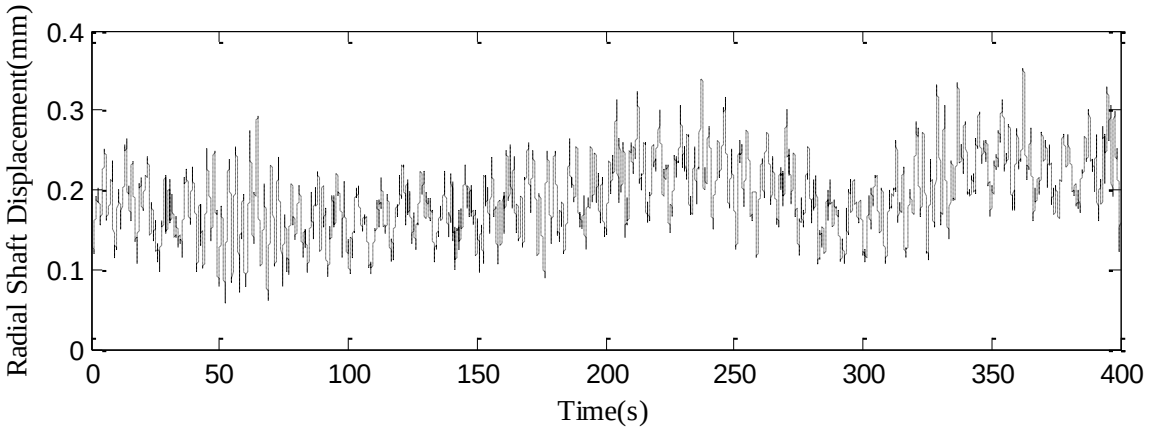

Figure 7-13 Shaft displacements measured at an average wind speed of 4m/s

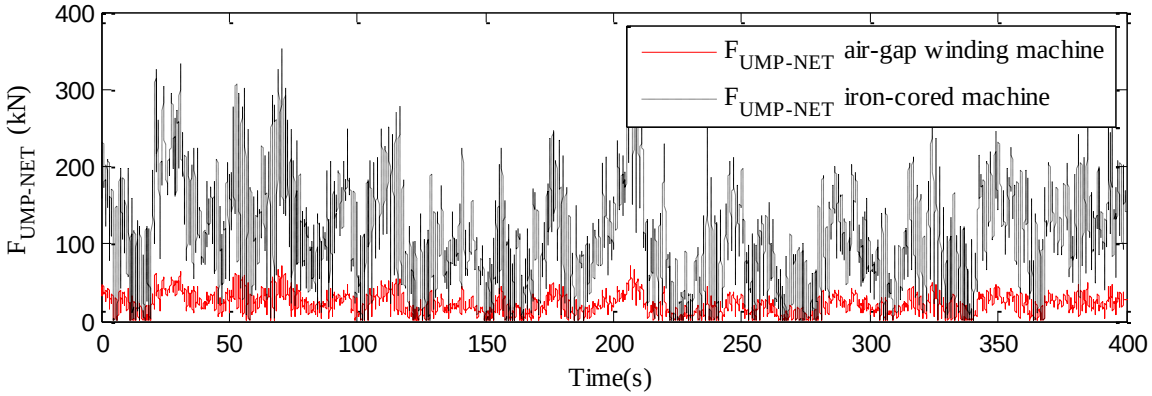

Figure 7-14 Net UMP forces measured at an average wind speed of 15m/s

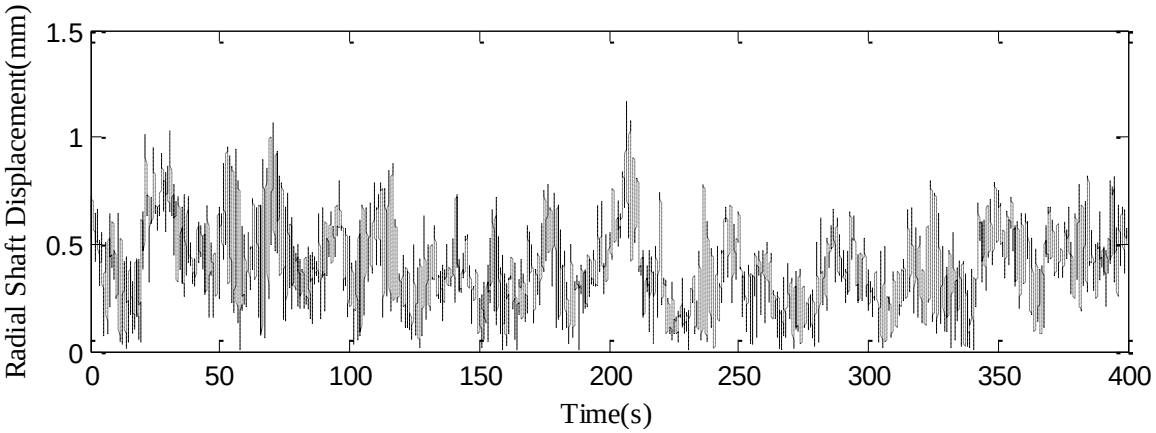

Figure 7-15 Shaft displacements measured at an average wind speed of 15m/s

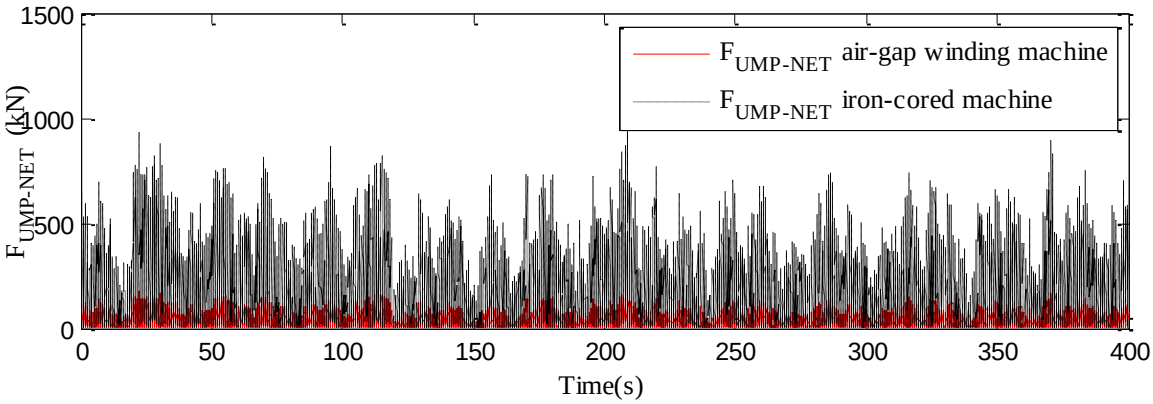

Figure 7-16 Net UMP forces measured at an average wind speed of 25m/s

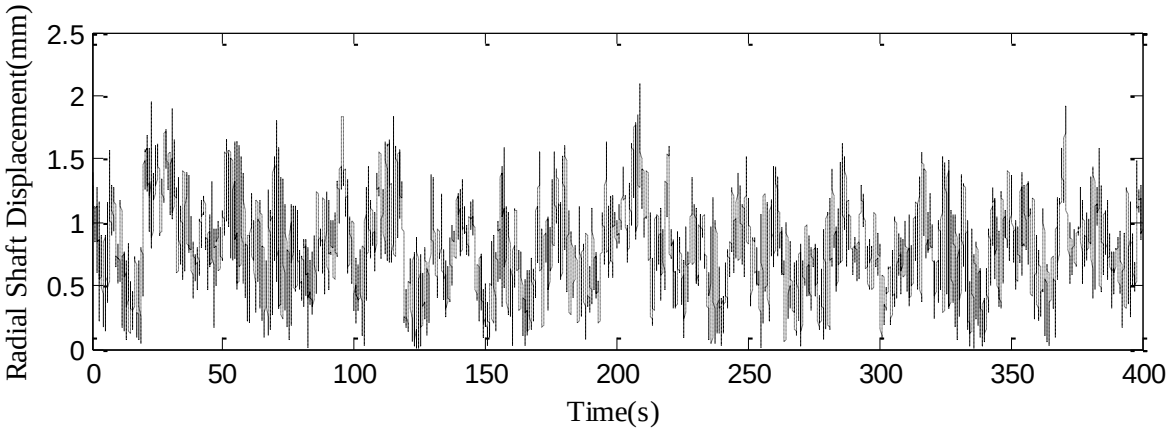

Figure 7-17 Shaft displacements measured at an average wind speed of 25m/s

7.4.1. Two main bearings arrangement

Figures 7-18, 7-19 and 7-20, illustrate the increase in bearing reaction with increase in wind speed. For the present study, a high value of bearing stiffness (case 1, shown in Table 7-1) has been assumed for the radial direction. As a result, UMP forces are substantially smaller when compared to bearing reactions even with high wind speed such as 25m/s.

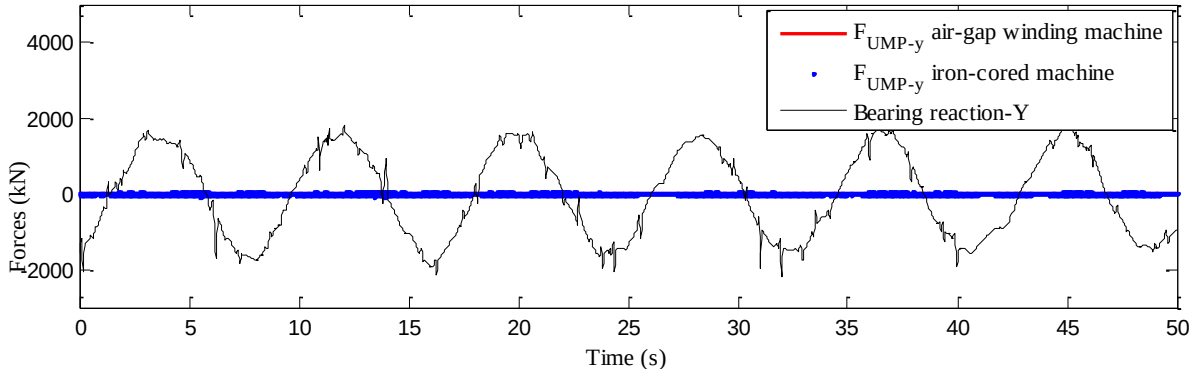

Figure 7-18 Comparison of UMP forces against bearing reaction at an average wind speed of 4m/s, bearing stiffness case 1

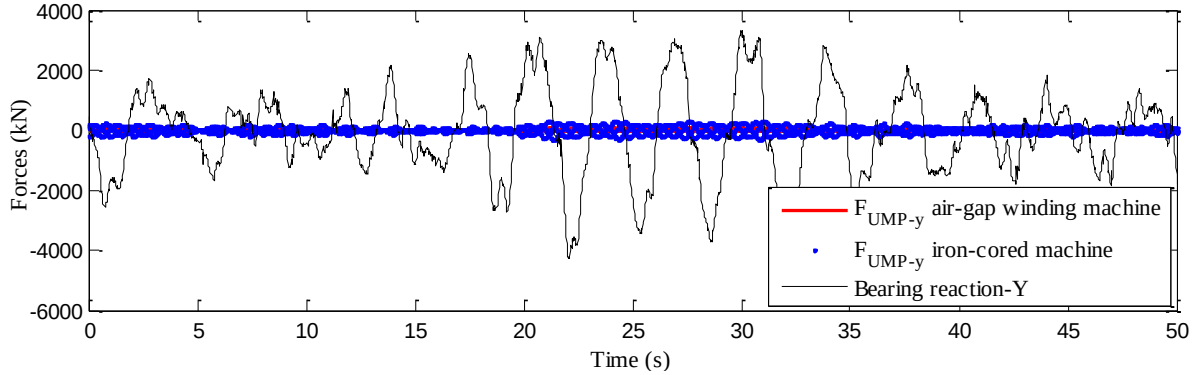

Figure 7-19 Comparison of UMP forces against bearing reaction at an average wind speed of 15m/s, bearing stiffness case 1

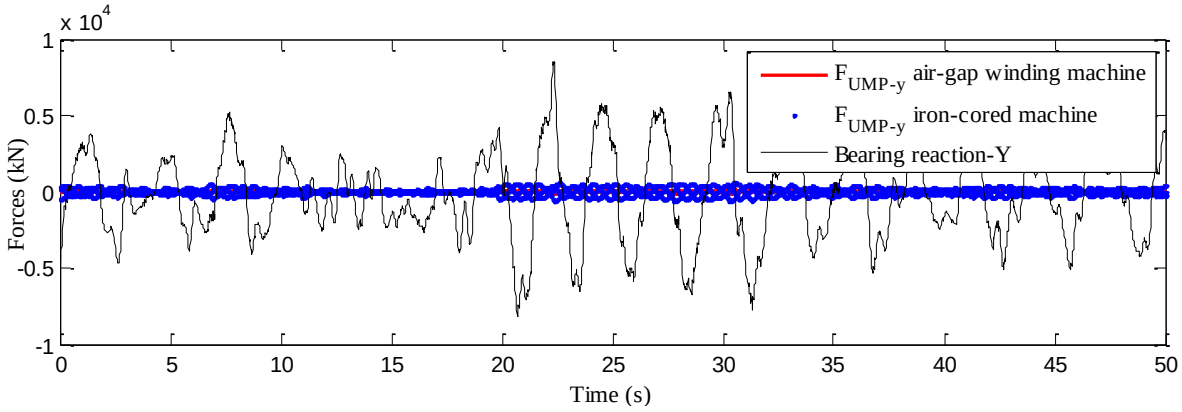

Figure 7-20 Comparison of UMP forces against bearing reaction at an average wind speed of 25m/s, bearing stiffness case 1

	Case 1	*Case 2*
Axial Stiffness [N/m]	3.74E+09	2.99E+09
Radial Stiffness [N/m]	3.81E+10	3.04E+10
Tilt Stiffness [Nm/deg]	7.21E+08	5.77E+08

Table 7-1 Bearing stiffness cases

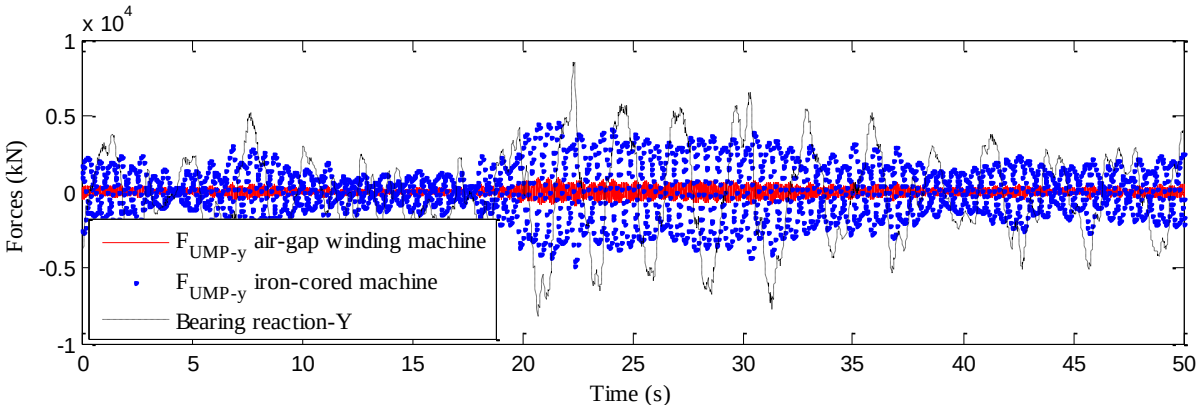

Figure 7-21 Comparison of UMP forces against bearing reaction at an average wind speed of 25m/s, bearing stiffness case 2

The UMP forces for the above case represent less than 2.5% of the bearing loads. For the UMP loads to have an effect on bearing response, the magnetic stiffness should be comparable with bearing stiffness and that is well explained in [228].

Applying case 2 of bearing stiffness to the MBS model then running the simulation shows that the lower bearing stiffness with air-gap winding generator is sufficient as shown in Figure 7-21 where the bearing reaction is significantly higher than the UMP. On the other hand, the reduced bearing stiffness is not sufficient to the iron-cored generator design because the bearing reaction is not enough to match the UMP as shown in Figure 7-21.

7.4.2. Single main bearing arrangement

The same methodology adopted in subsection 7.4.1. is used here with the following differences:

- One main bearing as shown in Figure 7-22 instead of two.
- Different bearing stiffness matrix. The single bearing stiffness matrix was obtained from SKF for Nautilus single bearing design [243]. Figure 7-23 shows the radial and axial stiffness for the single bearing.
- Different UMP expressions in the force elements FE-50(Y) and FE-50(Z) including UMP induced by static rotor eccentricity (see subsection 7.3.1.).
- Different component locations based on the study presented in Chapter 6.

The worst case scenario happens when the wind speed is maximum at 25m/s. Hence, a 25m/s wind speed is considered in the multi-body models. The simulation results showed no problem with the radial and axial bearing stiffness values obtained from the bearing manufacturer. Tilting stiffness, however, was the main issue. In a stiffness matrix, tilting stiffness is represented by the values of K(5,5) and K(6,6).

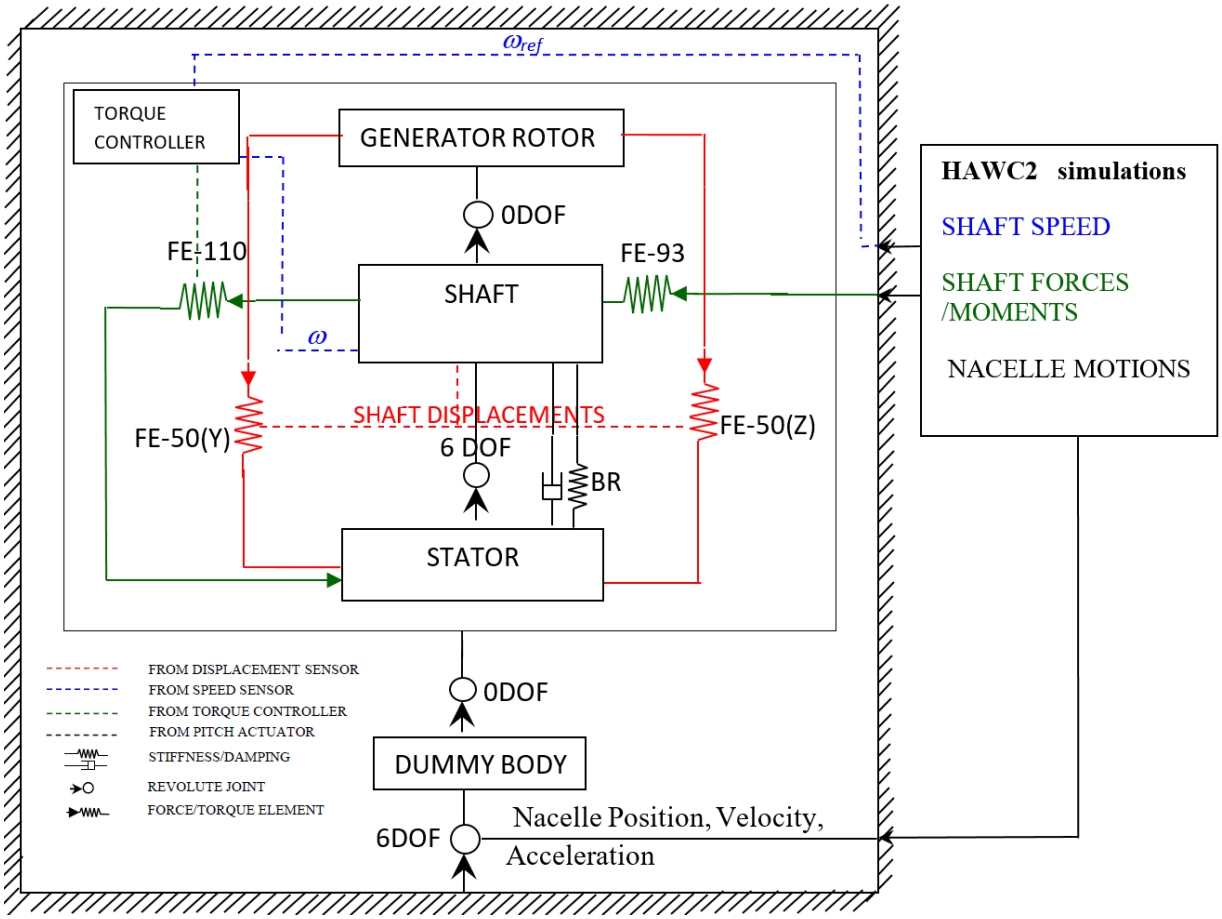

Figure 7-22 Multi-body model of the direct-drive generator single-bearing wind turbine in SIMPACK

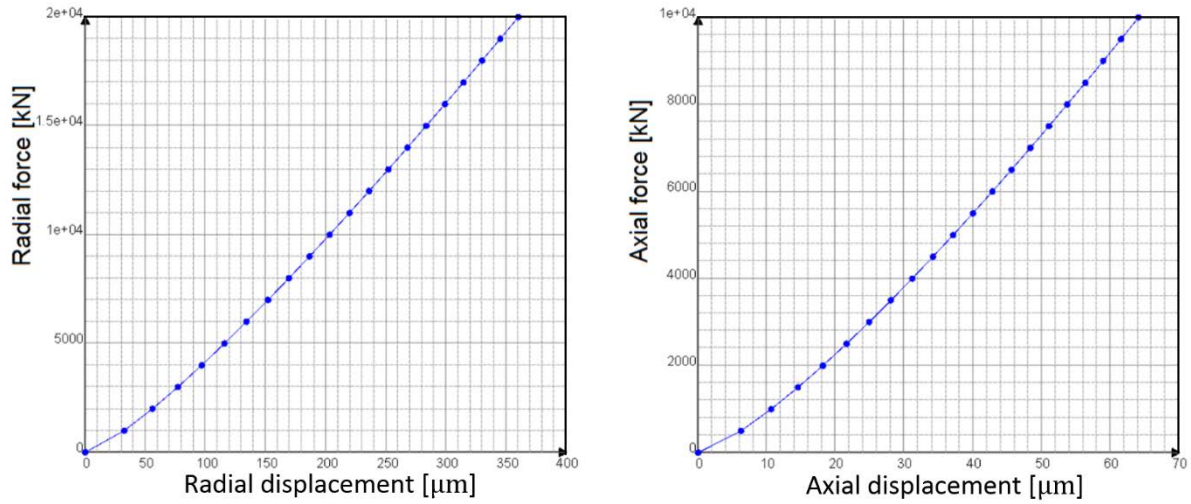

Figure 7-23 Radial and axial stiffness for single bearing

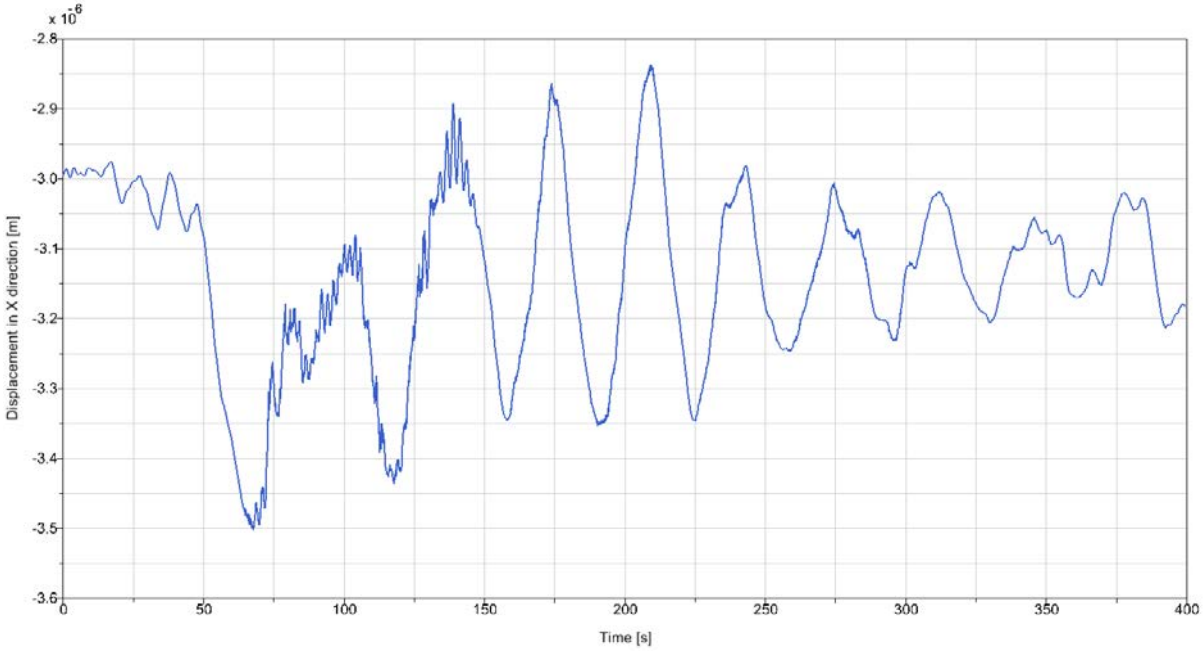

Figure 7-24 Shaft displacement in X direction when using a single bearing arrangement at an average wind speed of 25m/s

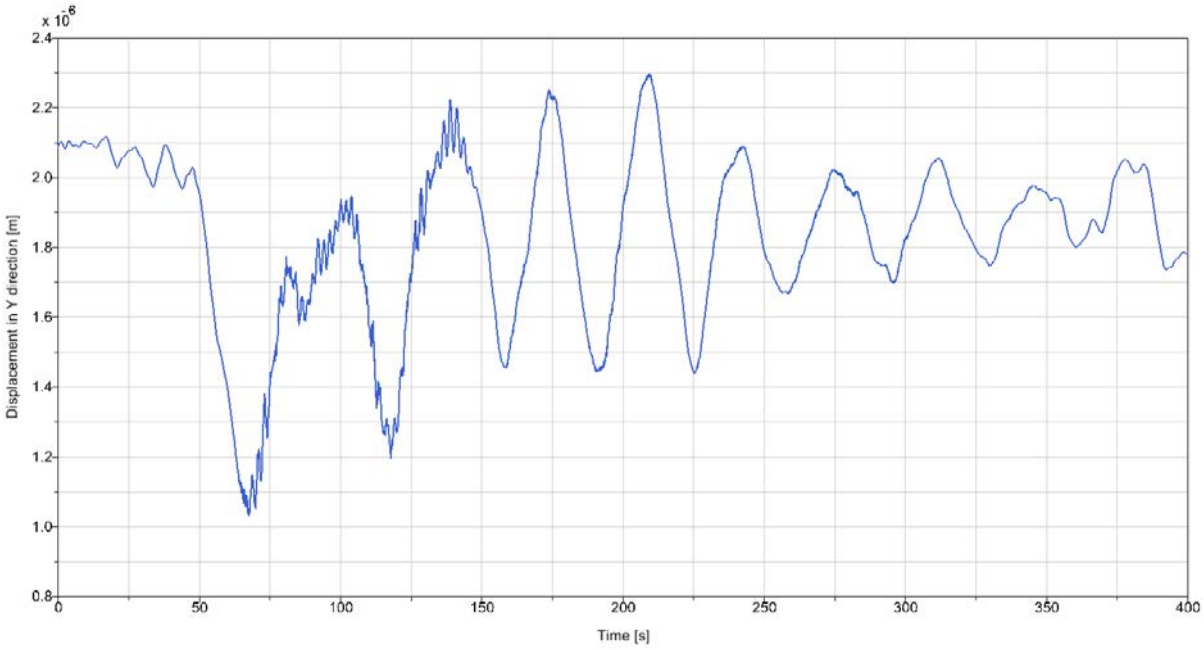

Figure 7-25 Shaft displacement in Y direction when using a single bearing arrangement at an average wind speed of 25m/s

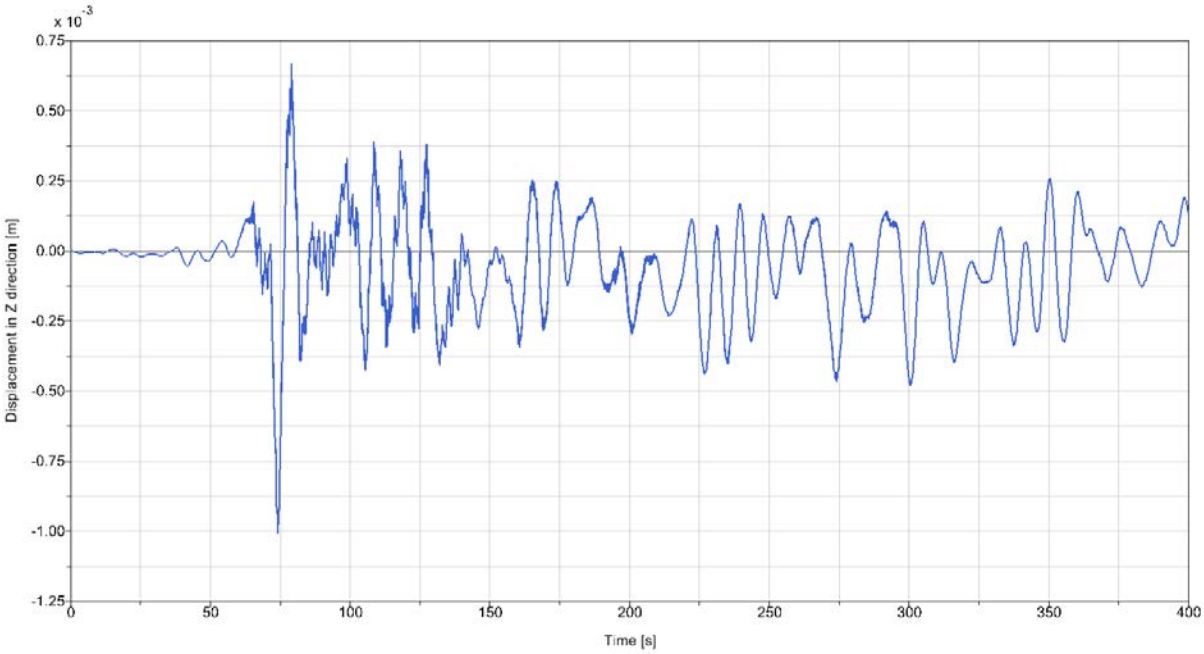

Figure 7-26 Shaft displacement in Z direction when using a single bearing arrangement at an average wind speed of 25m/s

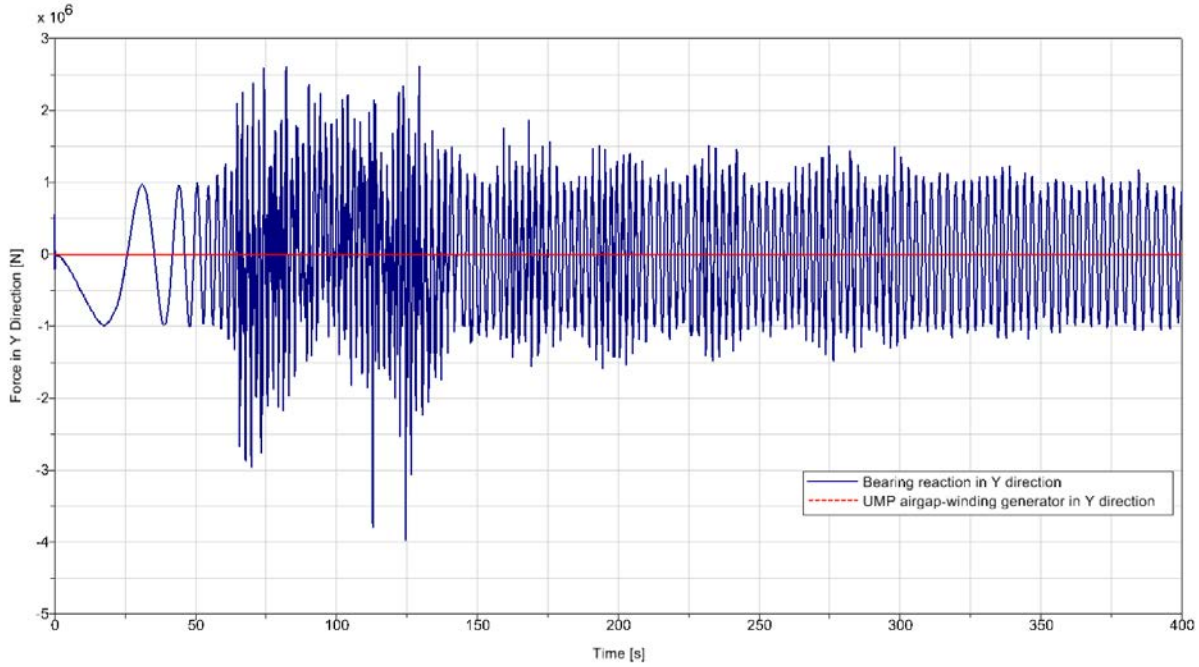

Figure 7-27 Comparison of UMP force against bearing reaction in Y direction at an average wind speed of 25m/s for the airgap winding PM direct-drive generator supported by a single main bearing arrangement

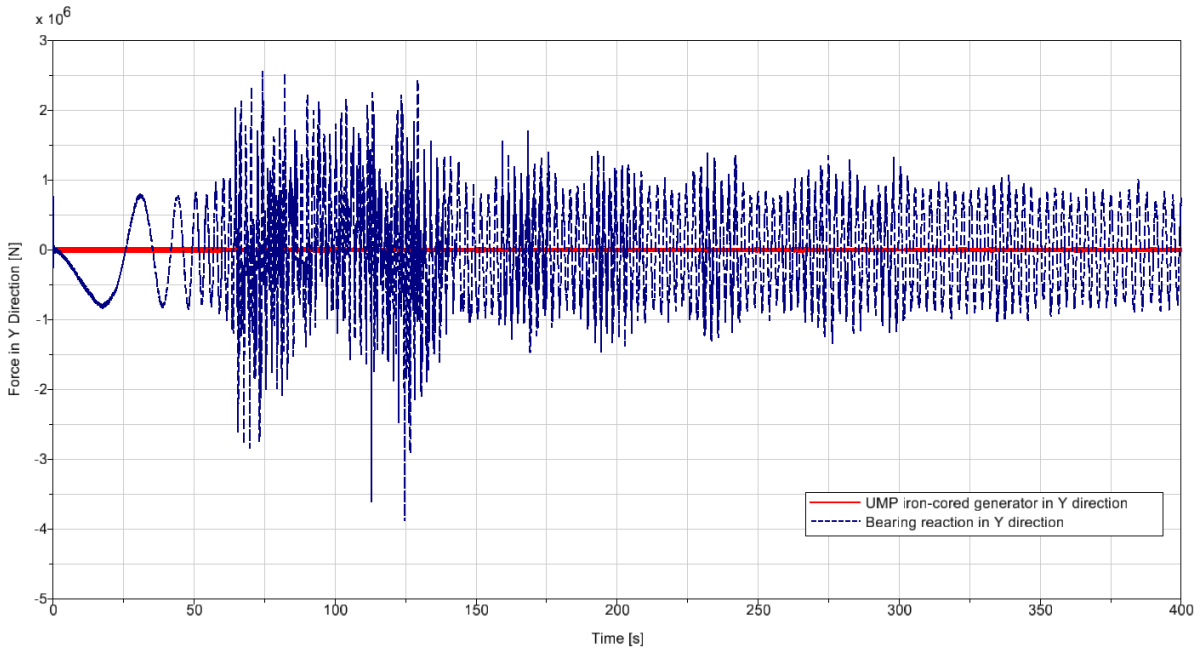

Figure 7-28 Comparison of UMP force against bearing reaction in Y direction at an average wind speed of 25m/s for the iron-cored PM direct-drive generator supported by a single main bearing arrangement

In order to keep the stability in the model, the shaft displacement has to be constrained. Shaft displacement should not exceed the generator airgap length, otherwise, the rotor and generator would have a contact causing a wind turbine failure. Figures 7-24, 7-25, and 7-26 show the shaft displacement in X, Y, and Z directions respectively at a wind speed of 25m/s.

The tilting stiffness of the single bearing design had to be increased significantly compared to the double bearing design in order to keep the model stability. The minimum tilting stiffness required to keep the stability in the 5MW airgap winding PM direct-drive generator supported by a single main bearing arrangement, regarding the multi-body simulation, was found to be in the range of 10^{14}kNm/deg as shown in Figure 7-27. Similarly, that value had to be slightly increased in order to keep the stability in the 5MW iron-cored PM direct-drive generator supported by a single main bearing arrangement as shown in Figure 7-28.

The slight increase in the value of the bearing tilting stiffness can be justified by the following:

1- The rotor weight in the 5MW iron-cored PM generator is more than the rotor weight in the airgap winding generator.
2- For similar static rotor eccentricity, the UMP induced in the iron-cored PM generator is about 5 times more than that induced in the air-gap winding generator. This UMP is directly applied on the single bearing.

In conclusion, when designing a direct drive wind turbine with single bearing arrangement, the generator design has a significant effect on the single bearing design. There is a rotor weight reduction in the 5MW airgap winding generator compared to the iron-cored generator, which means a reduction in the required bearing stiffness. Static rotor eccentricity was found to have the most significant UMP compared to the other types of eccentricities.

7.5. Conclusion

The outputs of Chapters 4, 5, and 6 were used as inputs for this Chapter. The 5MW direct drive wind turbine design presented in Chapter 6 was adopted for the multi-body design. UMP analytical and numerical models introduced in Chapters 4 and 5 were also used as extra force elements acting directly on the bearing. Tilting rotor eccentricity was reviewed in details. Comparing the UMP induced because of similar static and tilting rotor eccentricity clearly indicates higher impact of the static rotor eccentricity. It was found that the induced UMP because of a static rotor eccentricity in the studies iron-cored machine is about 3 times higher than that induced because of a similar tilting rotor eccentricity in the same machine. Similarly, in the airgap winding machine, a static rotor eccentricity induces 4 times higher UMP than a similar tilting rotor eccentricity.

Multi-body simulation software (SIMPACK) was used to initiate investigations and comparison by providing assessments of electromagnetic interaction and internal drive-train

loading for four possible designs for a 5MW direct-drive wind turbine in response to the loads normally seen by a wind turbine. The four designs include: (a) iron-cored PM direct-drive generator supported by two main bearings, (b) airgap winding PM direct-drive generator supported by two main bearings, (c) iron-cored PM direct-drive generator supported by a single main bearing, (d) airgap winding PM direct-drive generator supported by a single main bearing. The hub loads for different wind speeds corresponding to the normal operation of the wind turbine were obtained from an aero-elastic simulation code (HAWC2). The dynamic eccentricity and its influence on the electromagnetic interaction and consequential effects on bearing loading for all four designs was examined to determine the most optimal support structural configuration for a direct-drive system. The results disclosed an advantage of the single-bearing with airgap-winding PM generator arrangement over the single-bearing with iron-cored PM generator arrangement.

Chapter 8. Conclusions and Future Work

8.1. Summary and Conclusion

The objectives of this thesis can be divided into three, (1) presenting a suitable literature review for permanent magnet generators for direct drive wind turbines and the unbalanced magnetic forces induced in these generators because of different types of rotor eccentricities, (2) Introducing a novel analytical model to calculate the UMP in direct drive PM generators and verifying this model with numerical and experimental results, and (3) Using multi-body simulations to study the effect of UMP in direct drive PM generators on the arrangements of the main drive-train bearing.

The study starts with illustrating the huge potential of improving and expanding the wind energy industry, showing the advantages of direct drive wind turbines over geared wind turbines and pointing out the research gap. Nowadays, PM generators are the most common type to be used within direct drive wind turbines. The large diameters of direct drive generators in addition to the high PM attraction forces result in likely occurrence of rotor eccentricity. UMP is the main result of any rotor eccentricity and it is directly applied on the main bearing. That gave the spark for finding and adopting the research gap which is the effect of rotor eccentricity in direct drive PM generators on the main bearings in wind turbines.

After choosing the research area, a literature review for the PMG types for direct drive wind turbines was presented. Keeping in mind the UMP effect, the research has concentrated on two types of radial PMGs, namely: iron-cored PMG and airgap winding PMG. Working principle, comparisons, advantages, and disadvantages of PMG types were presented in Chapter 2.

Next step was explaining the types of rotor eccentricity and the induced UMP in electrical generators. Chapter 3, therefore, presented a literature review about analytical, numerical, and experimental methods to calculate UMP induced by the rotor eccentricity.

The following step included analytical studies for calculating UMP in radial flux PMGs. Calculating the UMP requires having the radial component value of the airgap flux density, which is a function of both the permeance and the PM magneto-motive force MMF. Air-gap

permeance cannot be determined without calculating the airgap length, which is variable when the rotor is eccentric. The type of the rotor eccentricity regulates the analytical equations to calculate the air-gap length. The analytical study in Chapter 4, therefore, started with calculating the spatial generator airgap length during different types of rotor eccentricity, namely: static, dynamic, and tilting eccentricity. Permeance, magnetic flux density, and UMP were calculated, then, depending on the eccentricity type. A novel simplified analytical model to calculate UMP in radial-flux airgap-winding PM generator depending on a magnetic circuit representation was also presented in Chapter 4.

Verifying and validating the analytical model was the main goal of the next step in Chapter 5. Two machines were analysed in this chapter: the first machine is a 47.7kW radial-flux airgap-winding PM generator and the second machine is an 11kW radial-flux iron-cored PM generator. Both machines were modelled using the 2-D open source finite element analysis software, FEMM. Validating both the numerical and analytical results required building a test-rig and comparing those results with the experimental results. The test-rig was introduced with the experimental results for only the 11kW iron-cored PM generator. The results clearly indicated a linear relationship between the static rotor eccentricity and the induced UMP in the proposed PM generators. Analytical and numerical results showed high level of similarity. Comparing the experimental results with the numerical modelling results for the tested 11kW PM generator displayed good level of similarity with slightly greater values for the numerical results. The results differences were justified because of the difficulty of taking very accurate measurements, the accuracy of the measuring instruments, and the possible extrinsic UMP that was not included in the analytical and numerical models. Results of UMP test for 11kW induction generator were also presented and the comparison with the PM generator experimental results showed big difference. For the same relative eccentricity, UMP in the PM generator is about eight times higher than that in the induction generator.

The main goal up to this point was extracting generalized verified analytical formulas in order to use in a large direct-drive wind turbine model. The work has primarily focussed on smaller machines as they have immediate access in the laboratory environment and in the case of the 11kW machine test-rig results were available. In practice, however, the real value of direct-drive generators is for larger scale implementation. For this reason, the next step in Chapter 6 introduced a design incorporating additional shaft, bearing and generator details into an existing conceptual study for a potential 5MW wind turbine, which was completed by NREL in 2009. The main reason behind choosing the NREL study is that detailed modelling of most

parts of a geared wind turbine are available. Some parts of the geared wind turbine are assumed to be the same in the proposed 5MW direct-drive wind turbine in this study. The main missing parts that required designing are the generator, bearing, shaft, and converter assembly. Therefore, Chapter 6 focused on the first three with some discussion of the placement of the various components including the converter in the nacelle. Two direct-drive radial-flux PM generators, namely, an air-gap winding generator and a slotted iron-cored generator were considered in the design. These generators were put in the context of the other parts of the wind turbine such as the shaft, the bearing, the turbine, and the converter. The discussion of this design was divided into a discussion of the forces and moments associated with the various components and their positional considerations. It was then extended to a look at the generator itself. This focus was used to determine the torque and shear considerations of the generator and further extended to finite element modelling to determine UMP induced by rotor eccentricity. This work was then extended to the rotor and associated shaft related shear and bending stress. Simplified look at bearing arrangements, namely, single bearing design and two-bearing design, and bearing life was also presented in this study. It was noted that between the two bearing types used, and under the shaft loading conditions and rated wind speeds, both bearing configurations are sufficient for direct drive generators. The single bearing approach has the advantage of reduced weight.

Final step of this study was using a multi-body simulation software (SIMPACK) to initiate investigations and comparisons by providing assessments of electromagnetic interaction and internal drive-train loading for four possible designs for the proposed 5 MW direct-drive wind turbine in response to the loads normally seen by a wind turbine. The four designs include: (a) iron-cored PM direct-drive generator supported by two main bearings, (b) airgap winding PM direct-drive generator supported by two main bearings, (c) iron-cored PM direct-drive generator supported by a single main bearing, (d) airgap winding PM direct-drive generator supported by a single main bearing. An aero-elastic simulation code (HAWC2) was used to extract the hub loads for different wind speeds corresponding to the normal operation of the wind turbine. The dynamic eccentricity and its influence on the electromagnetic interaction and consequential effects on bearing loading for all four designs was examined to determine the most optimal support structural configuration for a direct-drive system. The multi-body simulation disclosed an advantage of the single-bearing with airgap-winding PM generator arrangement over the single-bearing with iron-cored PM generator arrangement.

8.2. Contribution to Knowledge

The most significant scientific contributions of this study are briefly listed below:

1- A novel analytical model to calculate the UMP induced by rotor eccentricity in a radial-flux airgap-winding PM generator is developed and verified using numerical FEM model.
2- A novel test-rig to generate static rotor eccentricity and measure the induced UMP in 11kW PM generator and 11kW induction generator is introduced and the experimental results are presented.
3- The relationship between a static rotor eccentricity and the induced UMP is found to be linear in both airgap- winding and iron-cored radial-flux PM generators.
4- The armature reaction effect on the induced UMP in case of rotor eccentricity was found to be very small and can be disregarded in both airgap- winding and iron-cored radial-flux PM generators.
5- It is found that for 20% relative rotor eccentricity, the induced UMP is roughly equal to a third of the machine weight for both airgap- winding and iron-cored radial-flux PM generators.
6- For the same relative eccentricity, UMP in an iron-cored PM generator is found to be about eight times higher than that induced in a same power capacity induction generator.
7- A novel model to calculate the UMP induced by tilting rotor eccentricity is introduced.
8- Tilting rotor eccentricity is not as effective as static rotor eccentricity. In an iron-cored machine, a static rotor eccentricity induces about 3 times higher UMP than a similar tilting rotor eccentricity. In an airgap-winding machine, a static rotor eccentricity induces about 4 times higher UMP than a similar tilting rotor eccentricity.
9- A novel 5MW direct-drive wind turbine design is presented based on an existing conceptual study for a potential 5MW geared wind turbine completed by NREL in 2009 incorporating additional shaft, bearing and generator details.
10- Novel multi-body simulations are presented for four different 5MW direct- drive wind turbine designs include: (a) iron-cored PM direct-drive generator supported by two main bearings, (b) airgap winding PM direct-drive generator supported by two main bearings, (c) iron-cored PM direct-drive generator supported by a single main bearing, (d) airgap winding PM direct-drive generator supported by a single main bearing.

11- Iron-cored PM direct-drive generator supported by two main bearings design and airgap winding PM direct-drive generator supported by a single main bearing design are found to have advantages over the other two designs in this study.

8.3. Recommendations for Future Work

This study introduces some interesting possibilities for further investigations. Some recommendations for future work are listed here:

1- In Chapter 4 in this thesis, the redistribution of magnetic flux density due to fringing and saturation is not taken in account in the analytical model, which reduces the results accuracy by about 8% as shown in Figure 5-4. It is recommended, therefore, to consider the flux density redistribution in future studies.
2- The introduced UMP model for the airgap-winding PM machine uses a simplified magnetic circuit to generate a quick estimation of the magnetic force. The model can be improved by using more detailed magnetic circuits so it is recommended to adopt the more accurate magnetic circuit presented in Chapter 4 in future studies.
3- An interesting piece of work to be done in the future is to build a prototype for a radial-flux airgap-winding PM generator. The same test rig technique introduced in this study can be used to measure the induced UMP when applying different types of rotor eccentricity, then comparing the experimental results with the novel analytical model presented in this thesis.
4- The adopted technique, in this thesis, to calculate the UMP induced by tilting rotor eccentricity is based on: (a) dividing the rotor into large number of slices, (b) assuming that each slice has different static eccentricity, (c) calculating the UMP induced on each slice separately, and (d) calculating the total UMP in the machine by summing up the UMP values of all slices. It is recommended for further work to use a 3-D FEM software to verify the analytical method introduced in this study.
5- In this study, bearing lifetimes are approximate based on simplified lifetime model. More accurate calculations on reliability based on improved bearing models are highly recommended. The roller misalignments, coupled axial-radial-bending effects, lubrication condition, operating temperature, and other factors as mentioned in ISO-281 should be considered.
6- Cost comparison between the four different 5MW direct- drive wind turbine designs was not included in this study so it can be a potential future work.

7- Condition monitoring for the stator electrical currents to detect rotor eccentricity and bearing wear is a very interesting subject for further research. Some work on this subject was conducted by the author [175] but not included in this thesis.

8.4. Publications

1- J. Shek, D. Dorrell, M. Hsieh, I-H. Lin, K. Mostafa, M. A. Mueller, and Y-H. Yeh, "Unbalanced Forces in Electrical Generators for Wave and Tidal Devices," in European Wave and Tidal Energy Conference (EWTEC 2013), 2013.

2- K. Mostafa, L. Sethuraman, and M. A. Mueller, "Unbalanced Magnetic Pull Comparison of Air-gap Winding and Iron-cored Permanent Magnet Machines for Direct Drive Wind Turbines," in European Wind Energy Conference (EWEA 2014), 2014.

3- K. Mostafa, M. A. Mueller, and Q. Jiang, "Bearing Wear Detection and Rotor Eccentricity Calculation in Radial Flux Air-Gap Winding Permanent Magnet Machines," in 7th IET International Conference on Power Electronics, Machines and Drives (PEMD 2014), 2014, no. 1.

4- J. Wu, A. Butler, M. A. Mueller, and K. Mostafa, "Combining fatigue analysis information into reliability analysis using Bayesian hierarchical modelling method," in 2017 Annual Reliability and Maintainability Symposium (RAMS), 2017, pp. 1–7.

References

[1] G. Brown, “British power generation achieves first ever coal-free day,” *The Guardian*, 2017. [Online]. Available: https://www.theguardian.com/environment/2017/apr/21/britain-set-for-first-coal-free-day-since-the-industrial-revolution. [Accessed: 09-Oct-2017].

[2] “UK energy from coal hits zero for first time in over 100 years,” *The Guardian*, 2016. [Online]. Available: https://www.theguardian.com/environment/2016/may/13/uk-energy-from-coal-hits-zero-for-first-time-in-over-100-years. [Accessed: 24-Jul-2016].

[3] J. Shankleman, “Renewable energy just provided Germany with almost all of its power,” *Bloomberg*, 2016. [Online]. Available: http://www.independent.co.uk/environment/germany-just-got-almost-all-of-its-power-from-renewable-energy-a7037851.html. [Accessed: 24-Jul-2016].

[4] S. Narula, “Denmark’s wind farms generated 140% of the country’s electricity needs yesterday,” 2015. [Online]. Available: http://qz.com/450737/denmarks-wind-farms-generated-140-of-the-countrys-electricity-needs-yesterday/. [Accessed: 24-Jul-2016].

[5] W. Yang, P. J. Tavner, and M. R. Wilkinson, “Condition monitoring and fault diagnosis of a wind turbine synchronous generator drive train,” *Renew. Power Gener. IET*, vol. 3, no. 1, pp. 1–11, 2009.

[6] “GLOBAL WIND STATISTICS 2017,” *Global Wind Energy Council GWEC*, 2017. [Online]. Available: http://gwec.net/wp-content/uploads/vip/GWEC_PRstats2017_EN-003_FINAL.pdf. [Accessed: 06-Feb-2018].

[7] M. Lesser and J. Muller, “Superconductor Technology, Generating the Future of Offshore Wind Power,” in *Renewable Energy World Conference*, 2009, pp. 1–10.

[8] D. Bang, H. Polinder, G. Shrestha, and J. A. Ferreira, “Review of Generator Systems for Direct-Drive Wind Turbines,” in *European Wind Energy Conference & Exhibition, Belgium, 31 March–3 April*, 2008.

[9] J. Burchell, “Advancement of Direct Drive Generator Systems for Offshore Renewable Energy Production,” THE UNIVERSITY OF EDINBURGH, 2018.

[10] T. A. Rule, *Solar, Wind and Land: Conflicts in Renewable Energy Development*. Routledge, 2014.

[11] “Cost Reduction Monitoring Framework,” *CATAPULT*, 2017. [Online]. Available: https://ore.catapult.org.uk/our-knowledge-areas/knowledge-standards/knowledge-standards-projects/cost-reduction-monitoring-framework/. [Accessed: 22-Mar-2017].

[12] P. Clark, “Energy groups in pledge to slash cost of offshore wind farms,” *Financial Times*, 2016. [Online]. Available: https://next.ft.com/content/c0b56810-29b9-11e6-8b18-91555f2f4fde. [Accessed: 06-Jul-2016].

[13] P. Clark, “Dong Energy in offshore wind cost breakthrough,” *Financial Times*, 2016. [Online]. Available: https://www.ft.com/content/18b0f2b6-42db-11e6-b22f-79eb4891c97d. [Accessed: 22-Mar-2017].

[14] “Onshore Wind Energy UK,” 2014. [Online]. Available: http://www.lse.ac.uk/GranthamInstitute/wp-content/uploads/2014/03/PB-onshore-wind energy-UK.pdf. [Accessed: 12-Dec-2016].

[15] “Value breakdown for the offshore wind sector,” *Renewables Advisory Board*, 2010. [Online]. Available: https://www.gov.uk/government/publications/offshore-wind-sector-value-breakdown. [Accessed: 03-Apr-2018].

[16] “UK Renewable Energy Roadmap,” *Department of Energy & Climate Change*, 2011. [Online]. Available: https://www.gov.uk/government/...data/.../2167-uk-renewable-energy-roadmap.pdf. [Accessed: 06-Jul-2016].

[17] “Overview of Support for the Offshore Wind Industry,” *HM Government*, 2014. [Online]. Available: https://www.gov.uk/government/uploads/system/uploads/attachment_data/file/319026/bis-14-880-support-for-the-offshore-wind-industry-overview.pdf. [Accessed: 06-Jul-2016].

[18] M. WHITTLE, “Wind Turbine Generator Reliability: An Exploration of the Root Causes of Generator Bearing Failures,” Durham University. Available at Durham E-Theses Online: http://etheses.dur.ac.uk/9422/, 2013.

[19] J. K. Kaldellis and D. Zafirakis, “The wind energy (r)evolution: A short review of a long history,” *Renew. Energy*, vol. 36, no. 7, pp. 1887–1901, Jul. 2011.

[20] S. Mathew, *Wind Energy Fundamentals, Resource Analysis and Economics*. Netherlands: Springer Berlin Heidelberg New York, 2006.

[21] “POUL LA COUR MUSEUM.” [Online]. Available: http://www.poullacour.dk/index-uk.htm. [Accessed: 20-Nov-2014].

[22] P. Tavner, *Reliability , availability and maintenance Offshore Wind Turbines*, Renewable. London: IET The Institution of Engineering and Technology, 2012.

[23] “Global statistics,” *Global Wind Report - Global Wind Energy Council. Technical report,* 2015. [Online]. Available: http://www.gwec.net/publications/global-wind-report-2/global-wind-report-2014-annual-market-update/. [Accessed: 08-Apr-2015].

[24] J. Wu, A. Butler, M. A. Mueller, and K. Mostafa, “Combining fatigue analysis information into reliability analysis using Bayesian hierarchical modelling method,” in *2017 Annual Reliability and Maintainability Symposium (RAMS)*, 2017, pp. 1–7.

[25] P. J. Tavner, J. Xiang, and F. Spinato, “Reliability analysis for wind turbines,” *Wind Energy*, vol. 10, no. 1, pp. 1–18, 2007.

[26] W. Yang, P. J. Tavner, and M. Wilkinson, “Wind turbine condition monitoring and fault diagnosis using both mechanical and electrical signatures,” in *Advanced Intelligent Mechatronics, 2008. AIM 2008. IEEE/ASME International Conference on*, 2008, pp. 1296–1301.

[27] J. Schmid and H. P. Klein, *Performance of European Wind Turbines*. London and New York: Elsevier, Applied Science, 1991.

[28] D. Robb, “The gearbox challenge - the role of bearings in gearbox failure,” *Windpower*

Monthly magazine, pp. 53–60, Nov-2005.

[29] P. J. Tavner, F. Spianto, and G. J. W. VanBussel, “Reliability of Different Wind Turbine Concepts with Relevance to Offshore Application,” *Eur. Wind Energy Conf. Brussels*, 2008.

[30] F. Oyague, *Gearbox modeling and load simulation of a baseline 750-kW wind turbine using state-of-the-art simulation codes*. National Renewable Energy Laboratory Golden, CO, 2009.

[31] C. Walford, “O&M Cost Model Quantifying the Influence of Reliability, Wind Turbine Reliability Workshop,” *Global Energy Concepts Seattle, WA*, 2006.

[32] J. Ikäheimo, “Permanent magnet motors eliminate gearboxes,” *ABB Rev.*, vol. 4, pp. 22–25, 2002.

[33] M. A. Delucchi and M. Z. Jacobson, “Providing all global energy with wind, water, and solar power, Part II: Reliability, system and transmission costs, and policies,” *Energy Policy*, vol. 39, no. 3, pp. 1170–1190, Mar. 2011.

[34] S. Sheng and P. Veers, “Wind Turbine Drivetrain Condition Monitoring – An Overview,” in *Mechanical Failures Prevention Group: Applied Systems Health Management Conference*, 2011.

[35] ENERCON, “Brochure Technology & Services,” 2016. [Online]. Available: http://www.enercon.de/en/downloads/. [Accessed: 21-Jul-2016].

[36] B. Maples, M. Hand, and W. Musial, “Comparative Assessment of Direct Drive High Temperature Superconducting Generators in Multi-Megawatt Class Wind Turbines,” National Renewable Energy Laboratory/TP - 5000 - 49086, October, 2010.

[37] R. S. Semken *et al.*, “Direct-drive permanent magnet generators for high-power wind turbines: benefits and limiting factors,” *IET Renewable Power Generation*, vol. 6, no. 1. pp. 1–8, 2012.

[38] H. Polinder, F. F. A. van der Pijl, G. J. de Vilder, and P. Tavner, “Comparison of direct-drive and geared generator concepts for wind turbines,” *IEEE International Conference on Electric Machines and Drives, 2005.* pp. 543–550, 2005.

[39] T. Haring, K. Forman, T. Huhtanen, and M. Zawadzki, “Direct drive-opening a new era in many applications,” *Pulp and Paper Industry Technical Conference*. pp. 171–179, 2003.

[40] P. Tavner, L. Ran, J. Penman, and H. Sedding, *Condition Monitoring of Rotating Electrical Machines*. London: The Institution of Engineering and Technology, 2008.

[41] P. Tavner, J. Xiang, and F. Spinato, “Reliability analysis for wind turbines,” *Wind Energy*, vol. 10, no. 1, pp. 1–18, 2007.

[42] P. J. Tavner, “Review of condition monitoring of rotating electrical machines,” *Electr. Power Appl. IET*, vol. 2, no. 4, pp. 215–247, 2008.

[43] “ABB Generators Ltd. Permanent Magnet Generator (PMG) User’s Manual,” 2012.

[44] C. Lewis, “The Advanced Induction Motor,” *Power Engineering Society Summer*

Meeting, 2002 IEEE, vol. 1. pp. 250–253 vol.1, 2002.

[45] W. Soong, "Sizing of Electrical Machines," *Power Engineering Briefing Note Series*, pp. 17–18, Sep-2008.

[46] J. Pyrhönen, J. Nerg, P. Kurronen, J. Puranen, and M. Haavisto, "Permanent magnet technology in wind power generators," *The XIX International Conference on Electrical Machines - ICEM 2010*. pp. 1–6, 2010.

[47] D. Bang, "Design of transverse flux permanent magnet machines for large direct-drive wind turbines," *Delft University of Technology*, 2010. [Online]. Available: http://repository.tudelft.nl/view/ir/uuid:c6867c53-fc10-468d-b6d7-082b7a052f4b/. [Accessed: 04-Jan-2014].

[48] J. Wirtz, "Single Bearing Designs for Wind Turbines," 2011. [Online]. Available: http://www.ien.eu/article/single-bearing-designs-for-wind-turbines/. [Accessed: 30-Jan-2017].

[49] "Direct Drive Wind Turbine Market To Increase at Steady Growth Rate," *Offshore Wind Industry*, 2016. [Online]. Available: http://www.offshorewindindustry.com/news/direct-drive-wind-turbine-market-to-increase. [Accessed: 02-Mar-2018].

[50] J. O. Giæver Tande *et al.*, "DeepWind'2013 – Selected papers from 10th Deep Sea Offshore Wind R&D Conference, Trondheim, Norway, 24 – 25 January 2013High-power Generators for Offshore Wind Turbines," *Energy Procedia*, vol. 35, pp. 52–61, 2013.

[51] K. W. Klontz, T. J. E. Miller, M. I. McGilp, H. Karmaker, and P. Zhong, "Short-circuit analysis of permanent-magnet generators," *2009 IEEE International Electric Machines and Drives Conference*. pp. 1080–1087, 2009.

[52] "How does temperature affect neodymium magnets?," 2017. [Online]. Available: http://www.first4magnets.com/tech-centre-i61/information-and-articles-i70/neodymium-magnet-information-i82/how-does-temperature-affect-neodymium-magnets-i91. [Accessed: 30-Jan-2017].

[53] M. Dubois, "Optimized permanent magnet generator topologies for direct-drive wind turbines," Ph.D thesis, Delft University of Technology, Delft, The Netherlands, 2004.

[54] T. J. E. Miller, *Brushless Permanent-Magnet and Reluctance Motor Drives*, no. 21. Glasgow: Oxford Science Publications, 1989.

[55] "Materials Information System (MIS). Neodymium," *European Commission*, 2016. [Online]. Available: https://setis.ec.europa.eu/mis/material/neodymium. [Accessed: 30-Jan-2017].

[56] S. Eriksson and H. Bernhoff, "Rotor design for PM generators reflecting the unstable neodymium price," in *International Conference on Electrical Machines*, 2012, pp. 1419–1423.

[57] H. Sapiecha, "As the rare earth turns," 2015. [Online]. Available: https://www-globalcommodities.com/category/prices/. [Accessed: 20-Jan-2017].

[58] J. Horwitz, "Price of rare earth carbonate," *Quartz*, 2017. [Online]. Available:

https://www.theatlas.com/charts/SkurWnzjl. [Accessed: 20-Jan-2018].

[59] "Materials Information System (MIS). Neodymium," *European Commission*, 2016. .

[60] W. T. Benecki, T. K. Claggett, and S. R. Trout, *Permanent Magnets 2010-2020: A Comprehensive Overview of the Global Permanent Magnet Industry*. Walter T. Benecki LLC, 2010.

[61] T. Heikkilä, "Permanent Magnet Synchronous Motor for Industrial Inverter Applications - Analysis and Design," Ph.D Thesis. Lappeenranta University of Technology, Finland, 2002.

[62] A. Parviainen, "DESIGN OF AXIAL-FLUX PERMANENT-MAGNET LOW-SPEED MACHINES AND PERFORMANCE COMPARISON BETWEEN RADIAL-FLUX AND AXIAL-FLUX MACHINES," Ph.D Thesis, Lappeenranta University of Technology, Lappeenranta, Finland, 2005.

[63] O. Keysan, A. McDonald, M. Mueller, R. Doherty, and M. Hamilton, "C-GEN, a lightweight direct drive generator for marine energy converters," *5th IET International Conference on Power Electronics, Machines and Drives (PEMD 2010)*. pp. 1–6, 2010.

[64] P. Lampola, "Directly Driven, Low-Speed Permanent-Magnet Generators for Wind Power Applications," Ph.D. Thesis, Helsinki University of Technology, Finland, 2000.

[65] W. Wu, V. S. Ramsden, T. Crawford, and G. Hill, "A low speed, high-torque, direct-drive permanent magnet generator for wind turbines," *Industry Applications Conference, 2000. Conference Record of the 2000 IEEE*, vol. 1. pp. 147–154 vol.1, 2000.

[66] R. E. Hanitsch and M. S. Widyan, "Design, construction and test of a permanent-magnet prototype machine for wind energy applications," 2005.

[67] E. Spooner, P. Gordon, and C. D. French, "Lightweight, ironless-stator, PM generators for direct-drive wind turbines," *Power Electronics, Machines and Drives, 2004. (PEMD 2004). Second International Conference on (Conf. Publ. No. 498)*, vol. 1. p. 29–33 Vol.1, 2004.

[68] E. Spooner, P. Gordon, J. R. Bumby, and C. D. French, "Lightweight ironless-stator PM generators for direct-drive wind turbines," *Electric Power Applications, IEE Proceedings -*, vol. 152, no. 1. pp. 17–26, 2005.

[69] S. Engstrom and S. Lindgren, "Design of NewGen direct drive generator for demonstration in a 3.5 MW Wind Turbine," in *EWEC (European Wind Energy Conference & Exhibition), Milan, Italy, May 7-10*, 2007, no. 1.

[70] S. Engström, "NewGen generator," 2016. [Online]. Available: http://www.newgengenerator.com/contact. [Accessed: 12-Dec-2016].

[71] M. Valavi, A. Matveev, A. Nysveen, and R. Nilssen, "Multiple-airgap iron-cored direct-driven permanent magnet wind generators," *2014 International Conference on Electrical Machines (ICEM)*. pp. 578–584, 2014.

[72] M. A. Mueller and A. S. McDonald, "A lightweight low-speed permanent magnet electrical generator for direct-drive wind turbines," *Wind Energy*, vol. 12, no. 8, pp. 768–780, 2009.

[73] E. Borgan, “Introduction of the Sway Turbine ST10,” in *Drivetrain Concepts for Wind Turbines*, 2012.

[74] S. Nathan, “The next big things in renewables,” 2015. [Online]. Available: https://www.theengineer.co.uk/the-next-big-things-in-renewables/. [Accessed: 07-Jul-2016].

[75] “Boulder Wind Power,” 2017. [Online]. Available: http://www.boulderwindpower.com/testing/. [Accessed: 10-Jan-2017].

[76] “Permanent magnet generators,” *THE SWITCH*, 2017. [Online]. Available: http://theswitch.com/wind-power/permanent-magnet-generators/. [Accessed: 20-Mar-2017].

[77] A. Matveev, “High torque density electrical machine,” NO333170B1, 2013.

[78] L. Mach, “GOLIATH Wind,” 2017. [Online]. Available: http://www.goliath.ee/. [Accessed: 20-Jan-2017].

[79] “The Capella 3 wind turbine,” *Steelite Capella*, 2016. [Online]. Available: http://www.steelitecapella.com/index.html. [Accessed: 15-Feb-2018].

[80] G. Korouji, “Design, construction and test study of a wind energy generator with dual permanent magnet excitation,” Ph.D. Thesis, Berlin University of Technology, Berline, Germany, 2004.

[81] Y. Chen, P. Pillay, and A. Khan, “PM wind generator topologies,” *Industry Applications, IEEE Transactions on*, vol. 41, no. 6. pp. 1619–1626, 2005.

[82] Y. Chen and P. Pillay, “Axial-flux PM wind generator with a soft magnetic composite core,” *Industry Applications Conference, 2005. Fourtieth IAS Annual Meeting. Conference Record of the 2005*, vol. 1. p. 231–237 Vol. 1, 2005.

[83] E. Spooner, B. J. Chalmers, M. M. El-Missiry, W. Wei, and A. C. Renfrew, “Motoring performance of the toroidal permanent-magnet machine `Torus’,” *Electrical Machines and Drives, 1991. Fifth International Conference on (Conf. Publ. No. 341)*. pp. 36–40, 1991.

[84] E. Spooner and B. J. Chalmers, “`TORUS’: a slotless, toroidal-stator, permanent-magnet generator,” *Electric Power Applications, IEE Proceedings B*, vol. 139, no. 6. pp. 497–506, 1992.

[85] C. Boccaletti, S. Elia, and E. Nistico, “Deterministic and stochastic optimisation algorithms in conventional design of axial flux PM machines,” *Power Electronics, Electrical Drives, Automation and Motion, 2006. SPEEDAM 2006. International Symposium on*. pp. 111–115, 2006.

[86] H. Li and Z. Chen, “Overview of different wind generator systems and their comparisons,” *IET Renewable Power Generation*, vol. 2, no. 2. pp. 123–138, 2008.

[87] J. R. Bumby and R. Martin, “Axial-flux permanent-magnet air-cored generator for small-scale wind turbines,” *Electric Power Applications, IEE Proceedings -*, vol. 152, no. 5. pp. 1065–1075, 2005.

[88] J. Wang, K. T. Chau, J. Z. Jiang, and C. Yu, “Design and analysis of a transverse flux

permanent-magnet machine using three-dimensional scalar magnetic potential finite element method," *J. Appl. Phys.*, vol. 103, no. 7, pp. 07-10, 2008.

[89] L. H. Hansen, L. Helle, F. Blaabjerg, E. Ritchie, H. Bindner, and P. Sørensen, *Conceptual survey of Generators and Power Electronics for Wind Turbines*, vol. 1205, no. December. Riso-R-(EN), 2001.

[90] G. Kastinger and A. Schumacher, "Reducing torque ripple of transverse flux machines by structural designs," *Power Electronics, Machines and Drives, 2002. International Conference on (Conf. Publ. No. 487)*. pp. 320–324, 2002.

[91] D. H. Kang, Y. H. Chun, and H. Weh, "Analysis and optimal design of transverse flux linear motor with PM excitation for railway traction," *Electric Power Applications, IEE Proceedings -*, vol. 150, no. 4. pp. 493–499, 2003.

[92] D. Svechkarenko, "On Design and Analysis of a Novel Transverse Flux Generator for Direct-driven Wind Application," PhD Thesis, Royal Institute of Technology, Sweeden, 2010.

[93] D. j. Bang, H. Polinder, G. Shrestha, and J. A. Ferreira, "Ring-shaped transverse flux PM generator for large direct-drive wind turbines," *2009 International Conference on Power Electronics and Drive Systems (PEDS)*. pp. 61–66, 2009.

[94] Z. Wan, A. Ahmed, I. Husain, and E. Muljadi, "A novel transverse flux machine for vehicle traction aplications," *IEEE Power Energy Soc. Gen. Meet.*, vol. 2015–Septe, no. April, 2015.

[95] H. Guldemir, "Detection of airgap eccentricity using line current spectrum of induction motors," *Electr. Power Syst. Res.*, vol. 64, no. 2, pp. 109–117, Feb. 2003.

[96] J. Shek *et al.*, "Unbalanced Forces in Electrical Generators for Wave and Tidal Devices," in *European Wave and Tidal Energy Conference (EWTEC 2013)*, 2013.

[97] M. Bradford, "Unbalanced magnetic pull in a 6-pole induction motor," *Electr. Eng. Proc. Inst.*, vol. 115, no. 11, pp. 1619–1627, 1968.

[98] C. Bi, Q. Jiang, and S. Lin, "Unbalanced-magnetic-pull induced by the EM structure of PM spindle motor," in *Electrical Machines and Systems, 2005. ICEMS 2005. Proceedings of the Eighth International Conference on*, 2005, vol. 1, p. 183–187 Vol. 1.

[99] S. Lin, Q. Jiang, A. A. Mamun, and C. Bi, "Effect of drive modes on the acoustic noise of fluid dynamic bearing spindle motors," *Magn. IEEE Trans.*, vol. 39, no. 5, pp. 3277–3279, 2003.

[100] E. Starschich, A. Muetze, and K. Hameyer, "Analytical force calculation in brushless-DC motors I: An alternative approach," *2009 IEEE International Electric Machines and Drives Conference*. pp. 1200–1207, 2009.

[101] A. Gray and J. G. Pertsch, "Critical Review of the Bibliography on Unbalanced Magnetic Pull in Dynamo-Electric Machines," *American Institute of Electrical Engineers, Transactions of the*, vol. XXXVII, no. 2. pp. 1417–1424, 1918.

[102] E. Rosenberg, "Magnetic pull in electric machines," *Proceedings of the American Institute of Electrical Engineers*, vol. 37, no. 9. pp. 1069–1113, 1918.

[103] R. C. Robinson, “The Calculation of Unbalanced Magnetic Pull in Synchronous and Induction Motors,” *American Institute of Electrical Engineers, Transactions of the*, vol. 62, no. 10. pp. 620–624, 1943.

[104] E. W. Summers, “Vibration in 2-Pole Induction Motors Related to Slip Frequency [includes discussion],” *Power apparatus and systems, part iii. transactions of the american institute of electrical engineers*, vol. 74, no. 3. 1955.

[105] H. Frohne, “The practical importance of unbalanced magnetic pull, possibilities of calculating and damping it,” in *Conti Elektro Berichte*, 1967, vol. 13, pp. 81–92.

[106] D. G. Dorrell, “Experimental behaviour of unbalanced magnetic pull in 3-phase induction motors with eccentric rotors and the relationship with tooth saturation,” *Energy Conversion, IEEE Trans.*, vol. 14, no. 3, pp. 304–309, 1999.

[107] K. Kalita, “Integrating rotordynamic and electromagnetic dynamic models for flexible-rotor electrical machines,” PhD thesis, University of Nottingham, 2007.

[108] D. G. Dorrell and A. C. Smith, “Calculation of UMP in induction motors with series or parallel winding connections,” *IEEE Transactions on Energy Conversion*, vol. 9, no. 2. pp. 304–310, 1994.

[109] S. A. Swann, “Effect of rotor eccentricity on the magnetic field in the air-gap of a non-salient-pole machine,” *Electrical Engineers, Proceedings of the Institution of*, vol. 110, no. 5. pp. 903–915, 1963.

[110] S. Williamson, “Power-factor improvement in cage-rotor induction motors,” *IEE Proceedings B - Electric Power Applications*, vol. 130, no. 2. pp. 121–129, 1983.

[111] S. Williamson and M. A. S. Abdel-Magied, “Steady-state analysis of double-cage induction motors with rotor-cage faults,” *IEE Proceedings B - Electric Power Applications*, vol. 134, no. 4. pp. 199–206, 1987.

[112] S. Williamson and N. K. Adams, “Cage induction motors with inter-rings,” *IEE Proceedings B - Electric Power Applications*, vol. 136, no. 6. pp. 263–274, 1989.

[113] S. Williamson and K. Mirzoian, “Analysis of Cage Induction Motors with Stator Winding Faults,” *IEEE Power Engineering Review*, vol. PER-5, no. 7. pp. 50–51, 1985.

[114] S. Williamson, M. A. Mueller, J. F. Eastham, and L. H. Lim, “Transient unbalanced magnetic pull in change-pole induction motors,” *Electrical Machines and Drives, 1989. Fourth International Conference on (Conf. Publ. No. ??)*. pp. 261–265, 1989.

[115] S. Williamson and A. C. Smith, “Steady-state analysis of 3-phase cage motors with rotor-bar and end-ring faults,” *IEE Proceedings B - Electric Power Applications*, vol. 129, no. 3. p. 93, 1982.

[116] A. C. Smith and D. G. Dorrell, “Calculation and measurement of unbalanced magnetic pull in cage induction motors with eccentric rotors. I. Analytical model,” *IEE Proceedings - Electric Power Applications*, vol. 143, no. 3. pp. 193–201, 1996.

[117] D. G. Dorrell and A. C. Smith, “Calculation and measurement of unbalanced magnetic pull in cage induction motors with eccentric rotors. II. Experimental investigation,” *Electr. Power Appl. IEE Proc. -*, vol. 143, no. 3, pp. 202–210, 1996.

[118] O. Misir, F. Dobbert, and B. Ponick, “Analytical method for the air gap permeance calculation of salient pole synchronous machines,” *e {&} i Elektrotechnik und Informationstechnik*, vol. 133, no. 2, pp. 103–111, 2016.

[119] E. Ilhan, M. F. J. Kremers, E. T. Motoasca, J. J. H. Paulides, and E. A. Lomonova, “Spatial Discretization Methods for Air Gap Permeance Calculations in Double Salient Traction Motors,” *IEEE Transactions on Industry Applications*, vol. 48, no. 6. pp. 2165–2172, 2012.

[120] J. T. Li, Z. J. Liu, and L. H. A. Nay, “Effect of Radial Magnetic Forces in Permanent Magnet Motors With Rotor Eccentricity,” *Magnetics, IEEE Transactions on*, vol. 43, no. 6. pp. 2525–2527, 2007.

[121] U. Siraj, “How damper winding provides smooth starting to synchronous machine.,” *Electrical Engineering Blog*, 2012. [Online]. Available: http://eblogbd.com/what-is-damper-winding/. [Accessed: 10-Jan-2017].

[122] D. G. Dorrell, “Calculation of unbalanced magnetic pull in small cage induction motors with skewed rotors and dynamic rotor eccentricity,” *Energy Conversion, IEEE Trans.*, vol. 11, no. 3, pp. 483–488, 1996.

[123] D. G. Dorrell, “Calculation of unbalanced magnetic pull in cage induction machines,” Cambridge: University of Cambridge, 1993.

[124] D. G. Dorrell, J. K. H. Shek, and M.-F. Hsieh, “The measurement and indexing of unbalanced magnetic pull in electrical machines,” *Energy Conversion Congress and Exposition (ECCE), 2014 IEEE*. pp. 4827–4834, 2014.

[125] D. G. Dorrell, J. K. H. Shek, and M.-F. Hsieh, “The Development of an Indexing Method for the Comparison of Unbalanced Magnetic Pull in Electrical Machines,” *Industry Applications, IEEE Transactions on*, vol. PP, no. 99. p. 1, 2015.

[126] D. G. Dorrell, J. K. H. Shek, M. A. Mueller, and M.-F. Hsieh, “Damper windings in induction machines for reduction of unbalanced magnetic pull and bearing wear,” in *Energy Conversion Congress and Exposition (ECCE), 2011 IEEE*, 2011, pp. 1612–1619.

[127] D. G. Dorrell, J. Shek, M.-F. Hsieh, and M. A. Mueller, “Unbalanced Magnetic Pull in Cage Induction Machines for Fixed-Speed Renewable Energy Generators,” *Magn. IEEE Trans.*, vol. 47, no. 10, pp. 4096–4099, 2011.

[128] D. G. Dorrell, “Sources and Characteristics of Unbalanced Magnetic Pull in Three-Phase Cage Induction Motors With Axial-Varying Rotor Eccentricity,” *Ind. Appl. IEEE Trans.*, vol. 47, no. 1, pp. 12–24, 2011.

[129] D. G. Dorrell, “Sources and characteristics of unbalanced magnetic pull in 3-phase cage induction motors with axial-varying rotor eccentricity,” in *Energy Conversion Congress and Exposition, 2009. ECCE 2009. IEEE*, 2009, pp. 240–247.

[130] D. G. Dorrell, M.-F. Hsieh, and Y. Guo, “Unbalanced Magnet Pull in Large Brushless Rare-Earth Permanent Magnet Motors With Rotor Eccentricity,” *Magnetics, IEEE Transactions on*, vol. 45, no. 10. pp. 4586–4589, 2009.

[131] D. G. Dorrell, A. M. Knight, and R. E. Betz, “Issues with the design of brushless doubly-fed reluctance machines: Unbalanced magnetic pull, skew and iron losses,” in *Electric*

Machines & Drives Conference (IEMDC), 2011 IEEE International, 2011, pp. 663–668.

[132] D. G. Dorrell, A. M. Knight, and R. E. Betz, "Improvements in Brushless Doubly Fed Reluctance Generators Using High-Flux-Density Steels and Selection of the Correct Pole Numbers," *Magn. IEEE Trans.*, vol. 47, no. 10, pp. 4092–4095, 2011.

[133] D. G. Dorrell, M. Popescu, C. Cossar, and D. Ionel, "Unbalanced Magnetic Pull in Fractional-Slot Brushless PM Motors," *Industry Applications Society Annual Meeting, 2008. IAS '08. IEEE*. pp. 1–8, 2008.

[134] D. G. Dorrell, M. Popescu, and D. M. Ionel, "Unbalanced Magnetic Pull Due to Asymmetry and Low-Level Static Rotor Eccentricity in Fractional-Slot Brushless Permanent-Magnet Motors With Surface-Magnet and Consequent-Pole Rotors," *Magnetics, IEEE Transactions on*, vol. 46, no. 7. pp. 2675–2685, 2010.

[135] D. G. Dorrell, "The influence of rotor skew on unbalanced magnetic pull in cage induction motors with eccentric rotors," *Electrical Machines and Drives, 1995. Seventh International Conference on (Conf. Publ. No. 412)*. pp. 67–71, 1995.

[136] A. Burakov and A. Arkkio, "Low-order parametric force model for eccentric-rotor electrical machine equipped with parallel stator windings and rotor cage," *IET Electric Power Applications*, vol. 1, no. 4. pp. 532–542, 2007.

[137] A. Burakov and A. Arkkio, "Comparison of the Unbalanced Magnetic Pull Mitigation by the Parallel Paths in the Stator and Rotor Windings," *IEEE Transactions on Magnetics*, vol. 43, no. 12. pp. 4083–4088, 2007.

[138] A. Kallaste, A. Belahcen, A. Kilk, and T. Vaimann, "Analysis of the eccentricity in a low-speed slotless permanent-magnet wind generator," *Electric Power Quality and Supply Reliability Conference (PQ), 2012*. pp. 1–6, 2012.

[139] M. V. K. Chari and P. P. Silvester, *Finite elements in electrical and magnetic field problems*. New York: Chichester : Wiley, 1980.

[140] A. Tura, "A Review of Finite Element Analysis Method," *University of Victoria's faculty of engineering*, 2014. [Online]. Available: http://www.engr.uvic.ca/~mech410/lectures/FEA_Theory.pdf. [Accessed: 20-Jan-2017].

[141] J. P. A. Bastos and N. Sadowski, *Electromagnetic Modeling by Finite Element Methods*. CRC Press, 2003.

[142] S. Williamson, L. H. Lim, and M. J. Robinson, "Finite-element models for cage induction motor analysis," *IEEE Transactions on Industry Applications*, vol. 26, no. 6. pp. 1007–1017, 1990.

[143] A. Arkkio, "Analysis of induction motors based on the numerical solution of the magnetic field and circuit equations," Helsinki, 1987.

[144] A. Arkkio, "Unbalanced magnetic pull in cage induction motors with asymmetry in rotor structures," *Electrical Machines and Drives, 1997 Eighth International Conference on (Conf. Publ. No. 444)*. pp. 36–40, 1997.

[145] A. Arkkio, M. Antila, K. Pokki, A. Simon, and E. Lantto, "Electromagnetic force on a

whirling cage rotor," *IEE Proceedings - Electric Power Applications*, vol. 147, no. 5. pp. 353–360, 2000.

[146] A. Arkkio *et al.*, "Finite-Element Analysis for a Rolling-Rotor Electrical Machine," *IEEE Transactions on Magnetics*, vol. 46, no. 8. pp. 2727–2730, 2010.

[147] A. Arkkio and A. Hannukainen, "Proper finite-element discretization for torque computation of cage induction motors," *Power Electronics, Electrical Drives, Automation and Motion (SPEEDAM), 2012 International Symposium on*. pp. 1456–1461, 2012.

[148] M. Michon, R. C. Holehouse, K. Atallah, and G. Johnstone, "Effect of Rotor Eccentricity in Large Synchronous Machines," *Magnetics, IEEE Transactions on*, vol. 50, no. 11. pp. 1–4, 2014.

[149] C. Fumeaux, D. Baumann, P. Bonnet, and R. Vahldieck, "Developments of finite-volume techniques for electromagnetic modeling in unstructured meshes," *2006 17th International Zurich Symposium on Electromagnetic Compatibility*. pp. 5–8, 2006.

[150] H. Antes, "A Short Course on Boundary Element Methods," *Institut fur Angewandte Mechanik*, 2010. [Online]. Available: http://www.sci.utah.edu/~macleod/links/bem-shortcourse.pdf. [Accessed: 12-Jan-2017].

[151] Q. Wu, L. Zhang, and Z. Ma, "A model establishment and numerical simulation of dynamic coupled hydraulic--mechanical--electric--structural system for hydropower station," *Nonlinear Dyn.*, vol. 87, no. 1, pp. 459–474, 2017.

[152] J. Fruchtenicht, H. Jordan, and H. 0 Seinsch, "Running instability of cage induction motors caused by harmonic fields due to eccentricity. part 1: electromagnetic spring constant and electromagnetic damping coefficient, part 2: self excited transverse vibration of rotors," *Arch. Electrotech*, no. 65, pp. 271–292, 1982.

[153] R. Belmans, A. Vandenput, and W. Geysen, "Calculation of the flux density and the unbalanced pull in two pole induction machines," *Arch. für Elektrotechnik*, vol. 70, no. 3, pp. 151–161, 1987.

[154] D. GUO, F. CHU, and D. CHEN, "THE UNBALANCED MAGNETIC PULL AND ITS EFFECTS ON VIBRATION IN A THREE-PHASE GENERATOR WITH ECCENTRIC ROTOR," *J. Sound Vib.*, vol. 254, no. 2, pp. 297–312, 2002.

[155] T. Holopainen, A. Tenhunen, and A. Arkkio, "Electromechanical interaction in rotor vibrations of electric machines," in *Fifth World Congress on Computational Mechanics (WCCM V)*, 2002.

[156] R. Belmans, A. Vandenput, and W. Geysen, "Influence of unbalanced magnetic pull on the radial stability of flexible-shaft induction machines," *Electr. Power Appl. IEE Proc. B*, vol. 134, no. 2, pp. 101–109, 1987.

[157] G. Rai and M. Bradford, "Vibratory forces resulting from rotating air-gap eccentricity in a six-pole induction motor," 1971.

[158] A. Burakov and A. Arkkio, "Low-order parametric force model for eccentric-rotor electrical machine with parallel connections in stator winding," *IEE Proceedings - Electric Power Applications*, vol. 153, no. 4. pp. 592–600, 2006.

[159] M. A. Mueller, “Improved calculation methods for particular aspects of induction motor performance,” University of Cambridge, 1991.

[160] M. Michon, K. Atallah, and G. Johnstone, “Effects of unbalanced magnetic pull in large permanent magnet machines,” *Energy Conversion Congress and Exposition (ECCE), 2014 IEEE*. pp. 4815–4820, 2014.

[161] Z. Q. Zhu, D. Ishak, D. Howe, and J. Chen, “Unbalanced Magnetic Forces in Permanent-Magnet Brushless Machines With Diametrically Asymmetric Phase Windings,” *Industry Applications, IEEE Transactions on*, vol. 43, no. 6. pp. 1544–1553, 2007.

[162] M. Michon, R. C. Holehouse, K. Atallah, and J. Wang, “Unbalanced magnetic pull in permanent magnet machines,” *Power Electronics, Machines and Drives (PEMD 2014), 7th IET International Conference on*. pp. 1–6, 2014.

[163] M. Kimiabeigi and Z. Q. Zhu, “Modelling and analysis of airgap flux density in direct drive PM machines with rotor eccentricity,” *6th IET Int. Conf. Power Electron. Mach. Drives (PEMD 2012)*, pp. P397–P397, 2012.

[164] J. R. Cameron, W. T. Thomson, and A. B. Dow, “Vibration and current monitoring for detecting airgap eccentricity in large induction motors,” *Electric Power Applications, IEE Proceedings B*, vol. 133, no. 3. pp. 155–163, 1986.

[165] A. J. Ellison and S. J. Yang, “Effects of rotor eccentricity on acoustic noise from induction machines,” *Electrical Engineers, Proceedings of the Institution of*, vol. 118, no. 1. pp. 174–184, 1971.

[166] C. J. Moore, “The measurement and calculation of acoustic noise radiated by small electric machines,” Ph.D thesis, University of London, 1965.

[167] R. T. Coe and H. W. Taylor, “VIII. Some problems in electrical machine design involving elliptic functions,” *London, Edinburgh, Dublin Philos. Mag. J. Sci.*, vol. 6, no. 34, pp. 100–145, Jul. 1928.

[168] C. J. Carpenter, “Surface-integral methods of calculating forces on magnetized iron parts,” *Proceedings of the IEE - Part C: Monographs*, vol. 107, no. 11. pp. 19–28, 1960.

[169] B. Heller and V. Hamata, *Harmonic field effects in induction machines*. Elsevier Scientific Pub. Co., 1977.

[170] E. Spooner and A. Williamson, “Modular, permanent-magnet wind-turbine generators,” *Industry Applications Conference, 1996. Thirty-First IAS Annual Meeting, IAS ’96., Conference Record of the 1996 IEEE*, vol. 1. pp. 497–502 vol.1, 1996.

[171] A. S. Mcdonald, “Structural analysis of low speed, high torque electrical generators for direct drive renewable energy converters,” University of Edinburgh, UK, 2008.

[172] S. Chapman, *Electric Machinery Fundamentals*. McGraw-Hill Companies,Incorporated, 2005.

[173] H. Li, Z. Chen, and H. Polinder, “Optimization of multibrid permanent-magnet wind generator systems,” *IEEE Trans. Energy Convers.*, vol. 24, no. 1, pp. 82–92, 2009.

[174] A. C. Smith and D. G. Dorrell, “Calculation and measurement of unbalanced magnetic pull in cage induction motors with eccentric rotors. I. Analytical model,” *Electr. Power*

Appl. IEE Proc. -, vol. 143, no. 3, pp. 193–201, 1996.

[175] K. Mostafa, M. A. Mueller, and Q. Jiang, “Bearing Wear Detection and Rotor Eccentricity Calculation in Radial Flux Air-Gap Winding Permanent Magnet Machines,” in *7th IET International Conference on Power Electronics, Machines and Drives (PEMD 2014)*, 2014, no. 1.

[176] K. Mostafa, L. Sethuraman, and M. A. Mueller, “Unbalanced Magnetic Pull Comparison of Air-gap Winding and Iron-cored Permanent Magnet Machines for Direct Drive Wind Turbines,” in *European Wind Energy Conference (EWEA 2014)*, 2014.

[177] “‘Magnetic Properties of Ferromagnetic Materials’,‘ “Iron,”’” *C.R Nave Georgia State University*, 2016. [Online]. Available: http://hyperphysics.phy-astr.gsu.edu/hbase/Tables/magprop.html. [Accessed: 10-Dec-2016].

[178] K. Hameyer and R. Belmans, *Numerical modeling and design of electrical machines and devices*. Southampton, UK: WIT Press, 1999.

[179] O. C. Zienkiewicz and R. L. Taylor, *The finite element method volume 1: basic formulation and linear problems. Vol. 1.* McGraw-Hill Book Company, 1989.

[180] K. Bathe, *Finite element procedures. Vol. 1037.* Prentice-Hall, Inc, 1996.

[181] P. P. Sylvester and R. L. Ferrari, *Finite elements for electrical engineers, ed. 3rd.* Cambridge University Press, 1996.

[182] A. Burakov, “MODELLING THE UNBALANCED MAGNETIC PULL IN ECCENTRIC-ROTOR ELECTRICAL MACHINES WITH PARALLEL WINDINGS,” Helsinki University of Technology, 2007.

[183] J. Luomi, “Finite element methods for electrical machines. Lecture notes for a postgraduate course in electrical machines.” Chalmers University of Technology, Department of Electrical Machines and Power Electronics, Göteborg, 1993.

[184] “Finite Element Method Magnetics (Version 4.2),” 2010. [Online]. Available: http://www.femm.info/Archives/doc/manual42.pdf.

[185] K. B. Baltzis, “The finite element method magnetics (FEMM) freeware package: May it serve as an educational tool in teaching electromagnetics?,” *Educ. Inf. Technol.*, no. March, 2010.

[186] D. Meeker, “Finite Element Method Magnetics Version 4.2 User’s Manual,” 2013.

[187] “The programming language,” 2017. [Online]. Available: http://www.lua.org/home.html. [Accessed: 09-Jan-2017].

[188] “PCB PIEZOTRONICS MTS SYSTEMS CORPORATION,” 2017. [Online]. Available: https://www.pcb.com/products.aspx?m=261A01. [Accessed: 07-Jan-2017].

[189] J. Jonkman, S. Butterfield, W. Musial, and G. Scott, “Definition of a 5-MW Reference Wind Turbine for Offshore System Development,” 2009.

[190] “The World’s Largest Wind Turbine,” 2004. [Online]. Available: https://xpda.com/junkmail/junk164/repower5m.htm. [Accessed: 05-Feb-2017].

[191] “The Wind Power: Wind Energy Market Intelligence,” 2016. [Online]. Available:

http://www.thewindpower.net/turbine_en_14_repower_5m.php. [Accessed: 08-Feb-2017].

[192] L. Sethuraman, “Hydrodynamics and drive-train dynamics of a direct-drive floating wind turbine,” THE UNIVERSITY OF EDINBURGH, 2014.

[193] A. S. Mcdonald, M. A. Mueller, and H. Polinder, “Structural mass in direct-drive permanent magnet electrical generators,” *IET Renewable Power Generation*, vol. 2, no. 1. pp. 3–15, 2008.

[194] L. Sethuraman, Y. Xing, V. Venugopal, Z. Gao, M. Mueller, and T. Moan, “A 5 MW direct-drive generator for floating spar-buoy wind turbine: Drive-train dynamics,” *Proc. Inst. Mech. Eng. Part C J. Mech. Eng. Sci.*, vol. 231, no. 4, pp. 744–763, 2017.

[195] “5M Proven Technology in New Dimensions,” 2004. [Online]. Available: http://www.skf.com/binary/21-64162/Nautilus-Exp-Brochure-12744-EN.pdf. [Accessed: 08-Feb-2017].

[196] D. j. Bang, H. Polinder, G. Shrestha, and J. A. Ferreira, “Promising Direct-Drive Generator System for Large Wind Turbines,” *2008 Wind Power to the Grid - EPE Wind Energy Chapter 1st Seminar*. pp. 1–10, 2008.

[197] D. j. Bang, H. Polinder, J. A. Ferreira, and S. s. Hong, “Structural mass minimization of large direct-drive wind generators using a buoyant rotor structure,” *2010 IEEE Energy Conversion Congress and Exposition*. pp. 3561–3568, 2010.

[198] S. YAGI and N. NINOYU, “Technical Trends in Wind Turbine Bearings. NTN TECHNICAL REVIEW No.76,” 2008.

[199] “NOABL Wind Map,” 2017. [Online]. Available: http://www.rensmart.com/Weather/BERR. [Accessed: 15-Jan-2017].

[200] G. Gualtieri and S. Secci, “Methods to extrapolate wind resource to the turbine hub height based on power law: A 1-h wind speed vs. Weibull distribution extrapolation comparison,” *Renew. Energy*, vol. 43, pp. 183–200, 2012.

[201] M. Ragheb, “Aeorodynamics of Rotor Blades,” 2013. [Online]. Available: http://mragheb.com/NPRE 475 Wind Power Systems/Aeorodynamics of Rotor Blades.pdf. [Accessed: 03-Feb-2017].

[202] A. Zavvos, “Structural Optimisation of Permanent Magnet Direct Drive Generators for 5MW Wind Turbines,” The University of Edinburgh, PhD Thesis, 2013.

[203] M. Saeki, I. Tobinaga, J. Sugino, and T. Shiraishi, “Development of 5-MW Offshore Wind Turbine and 2-MW Floating Offshore Wind Turbine Technology,” *Hitachi Rev.*, vol. 63, no. 7, pp. 414–421, 2014.

[204] “Wind Turbine Power Calculations RWE npower renewables Mechanical and Electrical Engineering Power Industry,” *The Royal Academy of Engineering*, 2016. [Online]. Available: www.raeng.org.uk/publications/other/23-wind-turbine. [Accessed: 02-Feb-2017].

[205] “MERVENTO,” *Presentation given by Mervento 3rd May*, 2011. [Online]. Available: https://www.tut.fi/smg/tp/.../2011/Drive_train_technologies_20110503_part4.pdf.

[Accessed: 12-Jan-2017].

[206] F. Klinger, “Direct drive—the future in wind turbine design,” *Technik-Symposium Presentation*, 2010. .

[207] “MERVENTO,” *Presentation given by Mervento 3rd May*, 2011. .

[208] J. N. Stander, G. Venter, and M. J. Kamper, “Review of direct-drive radial flux wind turbine generator mechanical design,” *Wind Energy*, vol. 15, no. 3, pp. 459–472, 2012.

[209] J. Versteegh, “Design of the Zephyros Z72 wind turbine with emphasis on the direct drive PM generator,” in *Presentation at the IEEE Nordic Workshop on Power and Industrial Electronics (NORPIE)*, 2004, pp. 1–7.

[210] B. Theoblad and F. Klinger, “New direct drive turbine design using advanced cooling with evaporating CO2,” in *Proceedings of the 9th German Wind Energy Conference (Deutsche Wind Energie Konference—DEWEK)*, 2008, pp. 1–4.

[211] D. Handler, “Investigation on gearless wind turbine generator structures—calculation and optimisation of the 3- bearing-variants,” Technische Universität, Darmstadt, Germany, 1997.

[212] S. Engström, B. Hernnäs, C. Parkegren, and S. Waernulf, “Development of NewGen a new type of direct-drive generator,” in *Proceedings of European Wind Energy Conference and Exhibition*, 2004, pp. 1–10.

[213] J. N. Stander, G. Venter, and M. J. Kamper, “Review of direct-drive radial flux wind turbine generator mechanical design,” *Wind Energy*, vol. 15, no. 3, pp. 459–472, 2012.

[214] M. B. Turi and C. S. Marks, “BEARING SELECTION TECHNIQUES AS APPLIED TO MAINSHAFT DIRECT AND HYBRID DRIVES FOR WIND TURBINES,” *TIMKEN Technical Paper*. [Online]. Available: news.timken.com/file.php/42186/MainShaftTechPaper.pdf. [Accessed: 03-Feb-2017].

[215] M. B. Turi and C. S. Marks, “BEARING SELECTION TECHNIQUES AS APPLIED TO MAINSHAFT DIRECT AND HYBRID DRIVES FOR WIND TURBINES,” *TIMKEN Technical Paper*. .

[216] “TORSION OF CIRCULAR SECTIONS,” *Department of Aerospace Engineering Sciences University of Colorado*, 2012. [Online]. Available: http://www.colorado.edu/engineering/CAS/courses.d/Structures.d/IAST.Lect07.d/IAST.Lect07.pdf. [Accessed: 19-Jan-2017].

[217] “Derivation of von Mises Criterion,” *Department of Mechanical & Aerospace Engineering University of Florida*, 2017. [Online]. Available: http://web.mae.ufl.edu/nkim/eas4200c/VonMisesCriterion.pdf. [Accessed: 13-Jan-2017].

[218] “Bending Stresses for Simple Shapes,” *Advanced Technical Communications LLC*, 2017. [Online]. Available: http://www.atcpublications.com/Sample_pages_from_FDG.pdf. [Accessed: 06-Jan-2017].

[219] “Beam Deflection and Stress Formula and Calculator for Beam Supported on Both Ends Loaded at any Location,” *Engineer Edge*, 2017. [Online]. Available:

http://www.engineersedge.com/beam_bending/beam_bending3.htm. [Accessed: 20-Jan-2017].

[220] "Stiffness and Bending," 1997. [Online]. Available: http://www2.myoops.org/cocw/mit/NR/rdonlyres/Mechanical-Engineering/2-007Design-and-Manufacturing-ISpring2003/E175EAAA-B85C-428F-A728-1B45E71E592B/0/bending.pdf. [Accessed: 25-Jan-2017].

[221] "Rolling bearings and seals in electric motors and generators," *SKF*, 2013. [Online]. Available: http://www.skf.com/binary/68-134586/13459-EN-Rolling-bearings-and-seals-in-electric-motors-and-generators.pdf. [Accessed: 14-Feb-2017].

[222] "Selection of Bearing Size," *NSK*, 2017. [Online]. Available: http://www.nsk.com.br/upload/file/NSK_CAT_E1102m_A24-36.pdf. [Accessed: 20-Feb-2017].

[223] "Shaft and Bearing Calculation," *FLYGT*, 2004. [Online]. Available: http://www.xylemwatersolutions.com/scs/norway/nb-no/produkter/flygtknow-how/Documents/shaft n bearing.pdf. [Accessed: 20-Feb-2017].

[224] A. S. McDonald, M. A. Mueller, and H. Polinder, "Comparison of generator topologies for direct-drive wind turbines including structural mass."

[225] H. Polinder, D. Bang, R. P. J. O. M. van Rooij, A. S. McDonald, and M. A. Mueller, "10 MW Wind Turbine Direct-Drive Generator Design with Pitch or Active Speed Stall Control," *2007 IEEE International Electric Machines & Drives Conference*, vol. 2. pp. 1390–1395, 2007.

[226] A. Grauers, "Design of direct-driven permanent-magnet generators for wind turbines," PhD Thesis,Chalmers University of Technology, Goteborg, Sweden, 1998.

[227] A. S. McDonald and M. A. Mueller, "Mechanical design tools for low speed high torque electrical machines," *The 3rd IET International Conference on Power Electronics, Machines and Drives, 2006. PEMD 2006*. pp. 666–670, 2006.

[228] L. Sethuraman, Y. Xing, Z. Gao, V. Venugopal, M. Mueller, and T. Moan, "A multi-body model of a direct-drive generator for a wind turbine. In the Proc. of EWEA 2014," in *EWEA*, 2014.

[229] R. Poore and T. Lettenmaier, "Alternative Design Study Report: WindPACT Advanced Wind Turbine Drive Train Designs Study; November 1, 2000 -- February 28, 2002," United States, 2003.

[230] G. Bywaters *et al.*, "Northern Power Systems WindPACT Drive Train Alternative Design Study Report Northern Power Systems WindPACT Drive Train Alternative Design Study Report," *Nrel*, no. October 2004, 2005.

[231] G. Bywaters *et al.*, "Northern Power NW 1500 Direct-Drive Generator: April 12, 2001-September 30, 2006," National Renewable Energy Laboratory (NREL), Golden, CO., 2007.

[232] Y. Xing, M. Karimirad, and T. Moan, "Effect of Spar-Type Floating Wind Turbine Nacelle Motion on Drivetrain Dynamics," in *In the Proc. of EWEA 2012 Annual Event, Copenhagen, Denmark, 16-19 April*, 2012.

[233] Y. Xing, M. Karimirad, and T. Moan, “Modelling and analysis of floating spar-type wind turbine drivetrain,” *Wind Energy*, vol. 17, no. 4, pp. 565–587, 2014.

[234] L. Sethuraman, V. Venugopal, A. Zavvos, and M. Mueller, “Structural integrity of a direct-drive generator for a floating wind turbine,” *Renew. Energy*, vol. 63, no. 0, pp. 597–616, Mar. 2014.

[235] T. J. Larsen and A. M. Hansen, “How 2 HAWC2, the user’s manual Risø National Laboratory,” in *Technical University of Denmark*, 2012.

[236] “Dassault Systèmes SIMULIA and Simpack,” 2017. [Online]. Available: http://www.simpack.com/about-us.html. [Accessed: 01-Feb-2017].

[237] Y. K. Chin, P. Kanninen, P. Maki-Ontto, R. Sakki, and H. Lendenmann, “Phenomenon of magnetic force in permanent magnet wind turbine generators,” *Electrical Machines and Systems, 2009. ICEMS 2009. International Conference on*. pp. 1–6, 2009.

[238] M. Whittle, W. Shin, J. Trevelyan, and J. Wu, “A Parametric Study of the Effect of Generator Misalignment on Bearing Fatigue Life in Wind Turbines,” in *EWEA*, 2011.

[239] S. Dunkerley, “On the Whirling and Vibration of Shafts,” *Philos. Trans. R. Soc. London.*, vol. 185, p. 279 LP-360, Jan. 1894.

[240] K. Johnson, L. Fingersh, M. Balas, and L. Pao, “Methods for Increasing Region 2 Power Capture on a Variable Speed HAWT,” in *Proceedings of the 23rd ASME Wind Energy Symposium*, 2004.

[241] A. D. Wright and L. J. Fingersh, “Advanced Control Design for Wind Turbines . Part I: Control Design, Implementation, and Initial Tests,” in *NREL/TP-500-42437 (March)*, 2008.

[242] T. J. Larsen and T. D. Hanson, “A method to avoid negative damped low frequency tower vibrations for a floating pitch controlled wind turbine,” *J. Phys.*, vol. 75, 2007.

[243] M. Hofmann, “Rotor bearing SKF Nautilus D=3200mm, Working Document,” 2016.